INVESTIGATING THE MECHANISTIC FEATURES OF ParABS-MEDIATED *Vibrio cholerae* CHROMOSOME 2 SEGREGATION

by

Satpal Singh Chodha

A thesis submitted in conformity with the requirements for the degree of

Doctor of Philosophy

Department of Molecular Biology and Biotechnology

University of Sheffield

October 2020

ABSTRACT

In all cell types, stable generational viability is dependent on the faithful inheritance of genomic material in daughter cells. This entails replicated DNA being segregated to opposing sides of the cell prior to cell division at mid-cell. In bacteria, a minimal ParABS (partitioning) system is used to correctly localise DNA cargos and is found on the chromosomes of up to 70% of species. A centromere-like site, *parS*, is bound by the CTP-binding protein, ParB. An ATPase with DNA-binding activity, ParA, acts as a motor protein to drive segregation of the ParB-*parS* complex, along with the attached DNA cargo. The underlying mechanism has been derived mostly from studies on plasmid Par systems. However, despite recent progress for Par-mediated chromosome segregation, the exact mechanism(s) of their action have yet to be deciphered. *Vibrio cholerae*, the causative agent of cholera, has two chromosomes, with one using a Par system closely related to those found on plasmids, making it an ideal chromosomal Par model to study. The goal of this thesis was to biochemically characterise the ParABS system of *V. cholerae* chromosome 2. First, each step in the ATPase cycle of ParA2 was examined and it was shown that there are key differences to plasmid ParA proteins, with an overall faster ATPase cycle likely responsible for driving translocation of a much bigger DNA cargo. Secondly, the formation of the ParA2-ParB2-*parS2* complex was investigated, and dynamic self-assembly was seen in the presence of ATP and CXP. Throughout the study, findings were compared with known plasmidal and chromosomal Par systems in order to contribute to a greater understanding of the mechanism(s) of bacterial chromosome segregation.

ACKNOWLEDGEMENTS

I would like to express sincere gratitude to my supervisor Dr. Ling Chin Hwang for the opportunity to undertake an amazing project that has widened my perspectives on science and life in general. It has been a privilege to work alongside my fellow lab members, Adam Brooks and Alexandra Parker, as well as the lab alumni, and I am grateful to have been part of a lab that has produced a high level of research. I am very thankful to Dr. Egbert Hoiczyk, Prof. Jeffrey Green, and Dr. Alexander Webb for their advice and guidance, especially during the last part of my PhD and write-up period. I would also like to show my appreciation to the members of the Green and Hoiczyk labs for their valuable suggestions during lab meetings, as well as for providing perspectives from the field of synthetic biology; in particular, thanks to Dr. Michael Cartron, Dr. Vijay Raghavedran, and Dr. Joseph Webb for being model scientists and for continually demonstrating an infectious appetite for learning and giving back to the next generations. A special acknowledgement goes to Dr. Stephane Mesnage and Linda Harris, who were always so approachable and supportive in providing me with additional funding for my write-up period, which fell in the unprecedented year of 2020.

I would also like to thank the following people who have helped me to acquire the data presented in this thesis. Dr. Svetlana Sedelnikova and Dr. Amanda Brindley for their insights into, and for, the purification of the proteins used in this work. Dr. Peter Davies for performing the SEC-MALS experiments and for making time to answer any questions I had. Dr. Jim Reid and Dr. Derren Heyes for providing technical assistance with the spectrofluorometer, and for discussions regarding the design of stopped-flow experiments. And lastly, the Green, Mesnage/Fagan, Hunter, Staniforth, Gilmour, Gray/Casson, Bose, and Leggett labs for use of their lab space and equipment. To all those mentioned above, and the whole of MBB, thank you for providing me with a stimulating, positive, and an invaluable academic experience. The training and guidance that I have received have been of the highest quality and I have learned what is required to be a scientist.

I am indebted to the support from my family and I would like to thank my mum and dad for encouraging me whenever I needed it. To the best sister Mandeep, my brother-in-law Mandip, and of course my niece Manali, thanks for your emotional support and light-hearted times; having you all stay over in my tiny flat was a highlight of my time in Sheffield. To my brother and friend Rajhan, and my sister-in-law Jasneet, thanks for supporting me in your unique way; the kart races kept me sane through these four years.

Finally, I would like to thank the Engineering and Physical Sciences Research Council (EPSRC) and the Microbiology Society for providing funding and making the research presented here possible.

TABLE OF CONTENTS

List of Figures

List of Tables

Chapter 2

Chapter 3

APPENDIX

List of Abbreviations

Ab^R	Antibiotic resistance
AMPPnP	Adenosine-5'-[(β,γ)-imido]triphosphate
ATPγS	Adenosine 5'-(γ-thiotriphosphate)
AU	Arbitrary units
AXP	Adenosine nucleotide (ADP, AMPPnP, ATP, ATPγS)
Biotin-PE	1-oleoyl-2-(12-biotinyl(aminododecanoyl))-*sn*-glycero-3-phosphoethanolamine
BME	β-Mercaptoethanol
bp	Base pairs
Bs	*Bacillus subtilis*
CBP	Centromere-binding protein
Cc	*Caulobacter crescentus*
CD	Circular dichroism
Chr1	Chromosome 1
Chr2	Chromosome 2
CV	Column volume
Cy	Cyanine
CTD	C-terminal domain
CXP	Cytidine nucleotide (CDP, CTP)
DBD	DNA-binding domain
DOPC	1,2-dioleoyl-*sn*-glycero-3-phosphocholine
dsDNA	Double stranded DNA
Ec	*Escherichia coli*
EDTA	Ethylenediaminetetraacetic acid
EMSA	Electrophoretic mobility shift assay
ESKAPE	*Enterococcus faecium, Staphylococcus aureus, Klebsiella pneumoniae, Acinetobacter* species*, Pseudomonas aeruginosa, and Enterobacter* species
GFP	Green fluorescent protein
Gr	Group
HDR	High-density chromosomal region
HTH	Helix-turn-helix
IPTG	Isopropyl β-D-thiogalactoside
kDa	Kilo-Dalton
K_D	Equilibrium dissociation constant
k_{obs}	Observed pseudo-first-order rate constant
k_{off}	First-order dissociation rate constant

k_{on}	Second-order association rate constant
LB	Luria-Bertani liquid medium
MANT	*N*-methylanthraniloyl
MANT-ADP	2'-(or-3')-*O*-(*N*-Methylanthraniloyl) Adenosine 5'-Diphosphate
MANT-ATP	2'-(or-3')-*O*-(*N*-Methylanthraniloyl) Adenosine 5'-Triphosphate
Mb/kb	Megabase pairs/kilobase pairs
Mw	Molecular weight
Mx	*Myxococcus xanthus*
NAC	Nucleoid-adaptor complex
NAP	Nucleoid-associated protein
NO	Nucleoid occlusion
nsDNA	Non-specific DNA
NTD	N-terminal domain
NTP	Nucleotide triphosphate
ORF	Open reading frame
ori/oriC	Origin of replication/chromosomal origin of replication
Ori	Chromosome macrodomain that encompasses the *oriC*
Par	Partitioning
ParABS2	*Vibrio cholerae* Chromosome 2 partitioning/segregation system
parOP	*par* operon operater
Par^{PD}	Propagation defective
PMT	Photomultiplier tube
RFU	Relative fluorescence units
RHH	Ribbon-helix-helix
Rtp	Room temperature and pressure
SBS	SlmA-binding site
SD	Standard deviation
SEC-MALS	Size exclusion chromatography-multiple angle light scattering
sssDNA	Sonicated salmon sperm DNA
τ (tau)	Time constant
ter	Replication terminus
Ter	Chromosome macrodomain that encompasses the *ter*
TIRF	Total internal reflection fluorescence
T_m	Melting temperature
Vc	*Vibrio cholerae*

CHAPTER 1

LITERATURE REVIEW: BACTERIAL GENOME ORGANISATION and DYNAMICS

1.1 INTRODUCTION

The faithful inheritance of replicated chromosomal DNA in daughter cells prior to cell division is a vital process in all cell types. Whereas the eukaryotic mitotic spindle is well characterised, the exact mechanism, or mechanisms, responsible for chromosome segregation in prokaryotes is less well understood. Roughly 70% of bacterial chromosomes encode a DNA partitioning (ParABS) system, which was first discovered and investigated in plasmids (**Livny et al., 2007; Austin and Abeles, 1983; Funnell, 1991**). It is a minimal system comprising two proteins, ParA and ParB, and a centromere-like sequence, *parS*, proximally located to the origin of replication (*ori*). ParB is a centromere-binding protein that binds *parS* to form a dense partition complex. ParA is a Walker-box ATPase with DNA-binding activity and utilises the nucleoid itself as a matrix to drive plasmid partitioning. Briefly, the underlying mechanism relies on ParA activities being mediated by the ParB-*parS* complex, which in turn provides the means for ParB-*parS* segregation and the attached plasmid cargo (**Vecchiarelli et al., 2010; Hwang et al., 2013**). The main distinction for the segregation of chromosomes is that they are much larger molecules than plasmids. Like eukaryotic DNA, bacterial chromosomes need to be compacted by 1000-fold to fit within cells. The tightly packed nucleoid thus formed needs to be compatible with processes such as DNA replication, transcription, and repair (**Junier et al., 2010; Bouet et al., 2014)**. Moreover, the characterisation of bacterial chromosome segregation is complicated by the fact that it occurs in parallel to DNA replication as opposed to being restricted temporally, as in eukaryotes with designated cell-cycle phases.

A further consideration confounding bacterial chromosome segregation in around 10% of bacterial species is that they have more than one chromosome, of which *Vibrio cholerae* is a model multipartite genome organism (**Fogel and Waldor, 2005; 2006**). *V. cholerae* maintains two circular replicons, with a ~3 Mb primary chromosome, and a 1.1 Mb secondary chromosome. A distinct Par system is located on each chromosome and, as with all chromosomal Par systems, they function in a chromosome-specific fashion. The secondary chromosome is believed to be derived from a domesticated megaplasmid, and in support of this is that the ParABS system is more closely related to plasmidal systems than chromosomal homologues (**Egan et al., 2005; Fogel and Waldor, 2006; Yamaichi et al., 2007a**). Replicated plasmids are generally equi-positioned along the cell length and occupy quarter-cell positions prior to cell division while chromosome origins of replication (*oriCs*) display a range of dynamics. Duplicated chromosome 2 (Chr2) *oriCs* are positioned similarly to plasmids, moving from mid-cell to quarter-cell. The Chr2 ParABS system (*Vc*ParABS2) is therefore an intriguing model system to investigate the differential mechanisms between closely related Par systems that localise very different DNA cargos with distinct segregation

parameters. This study will thus contribute to understanding how chromosomal Par systems function mechanistically.

In this chapter, the aspects that are relevant to the mechanism of Par-mediated chromosome segregation in a multi-chromosomal bacterium will be introduced. To best elucidate if and how *Vc*ParABS2 can utilise genomic DNA within the nucleoid to correctly localise the secondary chromosome, global nucleoid organisation will be discussed in relation to the cell-cycle. The emphasis of the chapter will be on *V. cholerae*, reviewing features of its genome, with detailed descriptions of chromosomal and extrachromosomal DNA. General genome structure and maintenance are then summarised, followed by chromosome dynamics. Non-Par-mediated segregation systems are considered in this section since the mechanisms are closely linked to chromosome structure and/or DNA replication. The different classes of Par systems (best studied in plasmids) are then described, leading to the type 1a class that includes *Vc*ParABS2. The features of individual Par components are reviewed in detail, before the different models to describe the type I mechanism of action are described, and finally the thesis rationale is outlined.

1.2 BACTERIAL GENOME STRUCTURE

1.2.1 Multipartite genomes

The primary bacterial chromosome is a large DNA molecule (on average 3.65 Mb) that represents the primary replicon of the cell and comprises all of the housekeeping genes required for survival and replication (**diCenzo and Finan, 2017**). Plasmids are extra-chromosomal, self-replicating genetic packages that are devoid of essential genes and are therefore not required for cell viability. There are genomic signatures that differ from the primary chromosome, such as codon usage, and dinucleotide relative abundance (**Marbouty et al., 2015**). The term ‘multipartite genome’, however, refers to the feature of having additional larger replicons, in the form of ‘megaplasmids’ and ‘chromids’. A megaplasmid is essentially a plasmid but with the distinction of being, on average, ten times larger (~0.77 Mb) (**diCenzo and Finan, 2017**). Another key characteristic of megaplasmids is that they are usually maintained at one copy per cell due to the cellular burden of maintaining such a large additional replicon. Chromids are termed as such to represent a ‘middle-ground’ between megaplasmids and chromosomes, in that they display features common to megaplasmids but also hold at least one essential gene. Further differences are that chromids are around twice as large as megaplasmids; chromid (plasmid-like) replication systems are integrated into the cell-cycle via regulatory mechanisms; and finally, codon usage and dinucleotide composition

shift towards being chromosome-like. Chromids are therefore interchangeably referred to as secondary chromosomes, as is the case with *V. cholerae* (**Harrison et al., 2010**).

Currently, it is unclear why some bacteria like *V. cholerae* possess two chromosomes. One feasible driving factor for a multipartite genome was thought to be faster cell division (and thus faster bacterial growth). In fact, some split genomes undergo faster DNA replication by way of multiple replicons replicating in parallel (**Srivastava and Chattoraj, 2007**), but while *V. cholerae* is an example of a fast replicating species, many other multipartite genome species are much slower-growing. Conceptually, the fastest way to replicate the genome would be to have an even distribution of essential genes on the available replicons. This would give rise to roughly similar sized chromosomes; however, secondary chromosomes are always smaller than the primary replicons, and typically only possess a few essential genes (**Egan et al., 2005**). Therefore, the more likely scenario is that secondary chromosomes are most probably not the result of an ancestral chromosomal splitting-event, but the acquirement and domestication of a megaplasmid. Maintaining the increased genome length would be accompanied by fitness costs that would have to be overcome. Faster genome replication is therefore likely to be an auxiliary feature that has emerged to facilitate maintenance of secondary chromosomes, notably in the *Vibrio* genus (**Harrison et al., 2010; Ramachandran et al., 2018**).

V. cholerae Chr2 harbours only four putative essential genes and this is a key reason why secondary chromosomes are thought to be derived from megaplasmids as opposed to a genome-splitting event. Megaplasmids acquire core genes from the primary chromosome and consistent with this statement is that the *V. cholerae* Chr2 essential genes are normally located on the primary chromosome in related species (**Sozhamannan and Waldminghaus, 2020**). Other clusters of genes have also been found to have transferred from the primary replicon, although the exact mechanism for inter-replicon gene transfer has not been identified (**diCenza and Finan, 2017**). One hypothesis for acquiring a second chromosome would be to attain an overall larger genome via gene accumulation. On average, multipartite genomes are slightly larger than mono-chromosomal genomes, and this is also true for *V. cholerae*, however, most of the largest genomes are mono-chromosomal (**Egan et al, 2005**). In the establishment of a chromid, the megaplasmid undergoes a high rate of evolution to offset the costs of its maintenance. Megaplasmids rapidly accumulate genes via horizontal gene transfer such that they benefit the cell sufficiently to overcome their potential high maintenance costs. If the megaplasmid is not lost, then co-residing with the primary replicon would eventually lead to the transfer of essential genes such that a chromid forms (**diCenza and Finan, 2017**).

The primary selective pressure for the establishment of multipartite genomes is thought to be adaptation to new environments (**diCenza and Finan, 2017; Sozhamannan and Waldminghaus, 2020**). In response, the genomic signatures of the chromid shift towards being more chromosome-like. GC content increases in an established chromid since there is no longer the need to select against high energy expenditure, which is more applicable to plasmids. Codon usage of highly expressed genes matches the available tRNAs for a given species and, correspondingly, codon usage bias on secondary chromosomes is regularly observed to shift away from that of megaplasmids and towards that of chromosomes. Extra replicons also differ from the primary chromosome in terms of dinucleotide composition. Gene clusters located on separate replicons could thus coordinate regulation by codon usage, but also from unevenly distributed transcription factors in the cell (**Junier et al., 2010; diCenza and Finan, 2017**).

The positioning and regulation of the particular genes acquired by chromids are conducive to facilitating their expression in new environments. Specifically, additional chromosomes are more prevalent in species that have mutually beneficial or pathogenic interactions with eukaryotic organisms (**diCenza and Finan, 2017**). Accordingly, there was higher expression of *V. cholerae* Chr2 genes in rabbit intestines than when grown aerobically (**Xu et al., 2003**). These are niche-specific genes that were also expressed in stools of cholera patients (**Merrell et al., 2002**). Alternatively, extrachromosomal replicons without essential genes can prove to be near impossible to remove. For instance, many plasmids like the pSymA megaplasmid in *Sinorhizobium meliloti*, encode 'plasmid addiction' toxin-antitoxin systems, which are linked to post-segregational killing as the encoded toxin is more stable than the antitoxin (**Milunovic et al., 2014; Yuan et al., 2011**). Bacterial genome organisation is thus not random and embodies functional and regulatory purposes (**Junier et al., 2010**).

1.2.2 Chromosome condensation and packaging

Bacterial genomes are tightly packed into nucleoids which comprise the primary chromosomal DNA, additional replicons, RNA, and protein. Prokaryotic chromosomes are most often covalently closed, circular DNA molecules, and are thus topologically constrained. The well-studied chromosome of *Escherichia coli* has been shown to be compacted into negatively supercoiled structures, called 'plectonemic loops' that extend out into the cytoplasm (**Figure 1.1A**). *V. cholerae* is closely related to *E. coli*, and chromosome 1 (Chr1) is a derivative of the mono-chromosomal ancestor of both species, as reviewed in **Sozhamannan and Waldminghaus, 2020**. Specifically, the activities of DNA gyrase (absent in eukaryotes) and topoisomerases I, III, and IV contribute to maintaining an average negative superhelicity of

chromosomal DNA. Nucleoid-associated proteins (NAPs) work alongside DNA gyrases and topoisomerases to generate and maintain plectonemic loop organisation, and to achieve an overall DNA-condensation of three-orders of magnitude (**Talukder and Ishihama, 2015)**. NAPs act on the scale of around 1 kb by bending, bridging, and looping DNA. The plectonemic loops form at the scale of 10 kb which associate to form Mb-scale macrodomains with an overall architecture that influences gene transcription (**Verma et al., 2019**). As illustrated in **Figure 1.1A**, the nucleoid assumes a helical ellipsoid structure, with areas of DNA that are highly condensed, called high density regions (HDRs) (**Fisher et al., 2013; Marbouty et al., 2015; Le Gall et al., 2016**).

1.2.3 Nucleoid-associated proteins

Global nucleoid structure is maintained by hundreds of NAPs. Five major proteins populate up to 70% of the total *E. coli* nucleoid in exponential phase, mostly via non-specific binding, as summarised in **Figures 1.1B-F**: heat-unstable nucleoid protein (HU), histone-like nucleoid structuring protein (H-NS), factor for inversion stimulation (Fis), suppressor of td- phenotype A (StpA), and host factor for phage Qβ (Hfq) (**Talukder and Ishihama, 2015**). Alternatively, during stationary phase DNA-binding protein from starved cells (Dps) binds up to half of the nucleoid (**Talukder and Ishihama, 2015**). Single molecule imaging, AFM, biochemical studies, and functional studies have given insight into the individual activities of these proteins, the best characterised of which are described briefly below.

HU is a small protein that binds across the genome. It can bind DNA with an existing kink (such as from single-stranded breaks) with high affinity to stabilise the bend structure, while it can also wrap linear DNA around itself in a manner similar to eukaryotic histones, (**Azam et al., 1999**). HU has also been shown to form filaments at high concentrations that act to linearise DNA, and HU then oligomerises to bunch many DNA fragments together (**Hammel et al, 2016**). Integration host factor (IHF) from *E. coli* is conserved among gram-negative bacteria and is structurally similar to HU where it can bind specific sequences to bend DNA. IHF is an example of NAPs being integral to various cell processes and it participates in transcription, replication, and recombination (**Goodman et al., 1999**). Although it is not required for *V. cholerae* chromosome segregation, IHF is also involved in P1 plasmid ParABS functionality as it binds P1 *parS* and recruits ParB, which in turn acts as an adaptor between the partition complex and ParA (**McLeod et al., 2006; Bouet and Funnell, 1999**). Fis is similar to IHF in that it initiates a slight bend in DNA. It is also similar to ParB as it binds specific sequences via a HTH motif and exerts a similar condensation force in DNA magnetic tweezer experiments (**Taylor et al., 2015**).

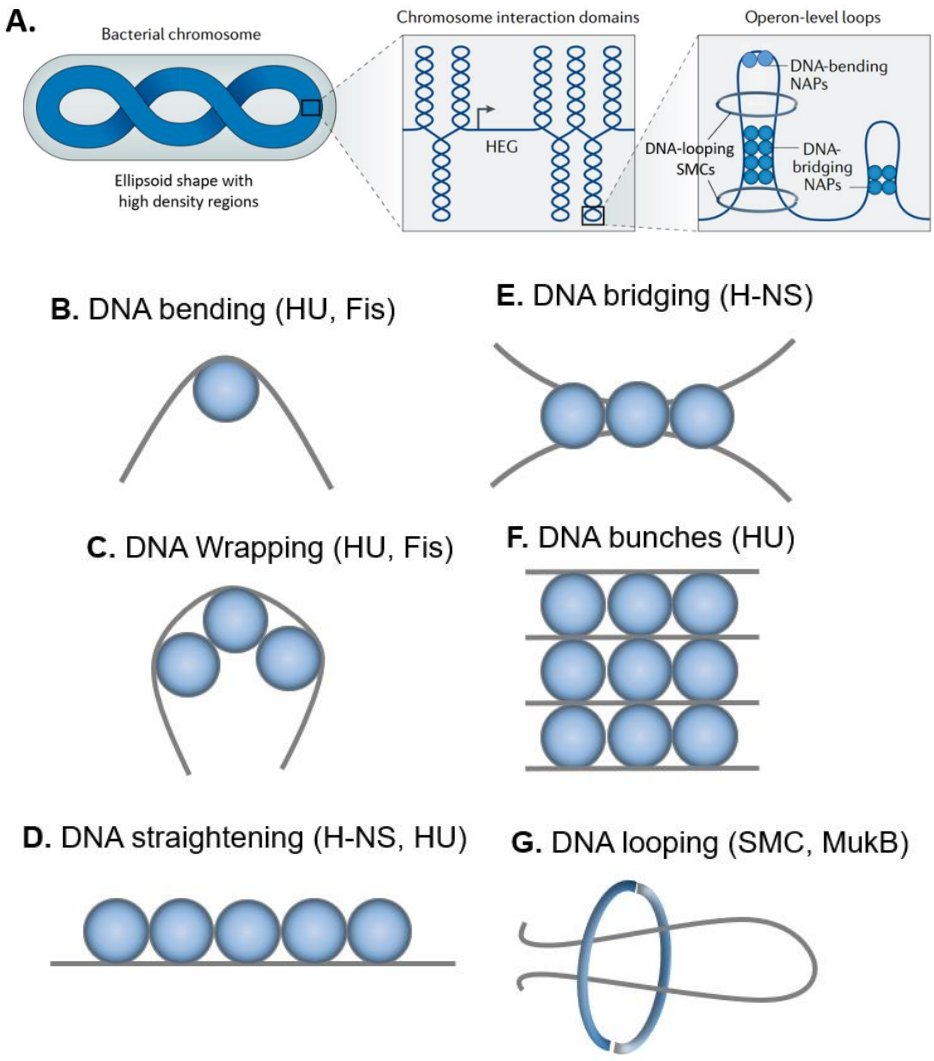

Figure 1.1. Hierarchal packaging of bacterial chromosomes. A) Chromosomes are condensed 1000-fold into the nucleoid with a helical-ellipsoid structure to fit in the cell. The middle panel shows adjacent chromosomal regions interacting at the scale of ten to hundreds of kb of DNA to form plectonemic loop domains called chromosome interaction domains (CIDs). Highly expressed genes (HEGs) insulate CID regions. The right panel shows that base-level plectoneme loops are maintained by various nucleoid-associated proteins (NAPs). **B)** Heat-unstable nucleoid protein (HU) binds DNA to introduce and stabilise up to 180° bends in DNA, and Fis introduces up to 75° bends. **C)** Sequentially placed HU or Fis can wrap DNA akin to eukaryotic histones. **D)** H-NS spreads along DNA to effect DNA stiffening. **E)** H-NS is an example of a NAP being able to bridge DNA, alone or when spread along DNA. **F)** At high concentrations, HU can straighten DNA by oligomerising and then 'bunch' multiple DNA segments. **G)** Structural maintenance of chromosomes (SMC), or MukB, loop DNA and maintain CID macrodomains. Adapted from **Dame et al., 2020** and **Verma et al., 2019**.

H-NS cooperatively binds to AT-rich regions of DNA and has the effect of straightening DNA, much like HU can. H-NS primarily consolidates loop regions as it has been found to colocalise with supercoils. H-NS also functions as a transcriptional repressor of 'spurious' genes where RNA polymerase promiscuity on the nucleoid would otherwise affect cell function, and primarily growth rate (**Wade and Grainger, 2017**). Without NAPs, replicons would assume a more relaxed default topological state (**Verma et al., 2019**). To summarise, the extent of chromosomal negative supercoiling is dependent on protein composition, and there are similarities to ParB in some specific condensation activities of NAPs. Considering that *V. cholerae* is closely related to *E. coli*, it can be seen that *V. cholerae* chromosome segregation would be affected by changing protein composition on the nucleoid where both ParA1 and ParA2 would compete with NAPs for available DNA. Indeed, this was shown directly for *Bacillus subtilis* ParA (Soj) where overexpression lead to DNA condensation but also premature cell division, along with guillotining of the nucleoid. This was due to Soj competing with a NAP responsible for inhibiting the formation of the cell division contractile-ring until after chromosome segregation is completed (**Hester and Lutkenhaus, 2007).**

1.2.3.1 Chromosome interacting domains and macrodomains

The method of capturing chromosome conformation (3C) allows the detection of interactions between two genomic loci using cross-linking and PCR amplification (**Dekker et al., 2002**), and 'Hi-C' is an adaptation for identification of chromatin interactions across an entire genome by employing high-throughput sequencing (**Lieberman-Aiden et al., 2009**). Hi-C has revealed that the *E. coli* chromosome is organised into around 400 independent plectonemic loop domains, and each segment is referred to as a chromosome interacting domain (CID), ranging from 30 to 400 kb (**Lioy et al, 2018**). As shown in **Figure 1.1A**, 'diffusion barriers' define CIDs based on the action of RNA polymerase whereby highly transcribed regions have lower NAP densities (**Booker et al., 2010**). Similar observations have been described for other studied organisms, including *V. cholerae* (**Val et al., 2016**).

There are occasional abrupt changes in the frequency of long-range chromosome contacts, and this shows the existence of larger domains (**Lioy et al., 2018**). Macrodomains are Mb-sized domains of coalesced CIDs, and are isolated from each other, as shown by various approaches including Hi-C, as well as fluorescence *in situ* hybridisation (FISH), and recombination-based studies (**Duigou and Boccard, 2017; Verma et al., 2019**). CIDs within a macrodomain interact with each other more frequently, and macrodomains are generally more flexible and structured than chromosomal regions that fall outside of these domains (non-structured domains). There are typically six chromosomal macrodomains in total, with four ~1

Mb macrodomains (Ori, Ter, Right, and Left), and two non-structured domains flanking the Ori (**Figure 1.2A**). Ori encompasses the *oriC*, the Ter includes the replication terminus (*ter*), while the Right and Left macrodomains flank the Ter. The positioning of *oriC* determines macrodomain formation as the architecture described above repositions around the new *oriC* upon relocation (**Duigou and Boccard, 2017)**. In support of this is that the *oriC* of the linear *Streptomyces coelicolor* chromosome is also centrally located (**Jakimowics et al., 2002**).

1.2.3.2 Proteins that maintain macrodomains

Organisation of macrodomains relies mainly on Macrodomain Ter protein (MatP) and structural maintenance of chromosomes (SMC) (**Figure 1.1G**). These proteins are widely conserved, with MatP found to have roles for both *V. cholerae* replicons (**Demarre et al., 2014**), while the *E.coli* SMC (MukB) has been identified in other gamma-proteobacteria, including *Vibrionaceae* (**David et al., 2014**). The Ter macrodomain is condensed by MatP-binding to numerous *matS* sequences located within the Ter (**Lioy et al., 2018**), and this activity excludes MukB from this domain (**Duigou and Boccard, 2017)**. SMCs are highly conserved ATPases (present in eukaryotes) that loop DNA upon interaction with accessory proteins called kleisins. SMCs are thought to be able to consolidate looped-DNA segments, or act in *cis* to initiate loop formation via a loop-extrusion mechanism, with proper functionality thought to be dependent on concerted action with ParB bound to *parS* (**Baxter et al., 2019**; **Makela and Sherratt, 2020**). *E. coli* MukB has a globular ATPase head-domain that it is separated from the dimerisation domain by a long coiled-coil ‘arm’. A flexible hinge forms at the dimer interface and the ATPase head domains interact with MukE and MukF (accessory protein and kleisin-like protein, respectively) to form a large ring-like structure (**Makela and Sherratt, 2020**). The dimer complex alone could potentially encompass two DNA segments with the enclosed ‘arms’. Alternatively, a ‘dimer of dimers’ complex could function in a ‘handcuffing’ mechanism, with each dimer-ring enclosing only one of the DNA segments brought together (**Dame et al., 2020**). Unlike SMCs, the MukBEF system functions independently of ParB, and is involved in the accurate segregation of *E. coli oriC*s in the absence of a ParABS system altogether (**Hofmann et al., 2019**). The mechanism could be influenced by MatP displacing MukBEF from the Ter domain (**Makela and Sherratt, 2020**).

As described, stochastic DNA-binding of NAPs is organised by transcription-mediated diffusion barriers, and the established plectonemic loop CID regions are also maintained by the MukBEF/SMC complex. Interestingly, some diffusion barriers exist at regions without highly transcribed genes (**Booker et al., 2010**). Furthering understanding of the molecular nature of CID diffusion barriers is a major goal for building a model of the dynamic prokaryotic

nucleoid (**Booker et al., 2010; Lioy et al., 2018**). In concert with DNA gyrase and topoisomerases, NAPs can supercoil and relax sections of the nucleoid individually to affect overall nucleoid dynamicity (**Verma et al., 2019**). It is still unclear how macrodomains are maintained with multipartite genomes. However, as illustrated in the next section, *Vc*Chr2 is spatially and temporally regulated with Chr1 throughout the cell-cycle. The helical nature of the packaged bacterial nucleoid, with fluctuating longitudinal HDRs, would be integral to the segregation of *Vc*Chr2, with ParA2 activity directly affected as proposed in later Chapters.

1.3 CHROMOSOME DYNAMICS

1.3.1 Transverse, 'left-*ori*-right' orientation, and non-Par segregation mechanisms

Bacterial chromosomes assume iterations of two broad spatial patterns: a transverse organisation, where the Left and Right macrodomains occupy opposite halves of the cell (left-*ori*-right configuration); or with the Ori and Ter macrodomains positioned longitudinally at opposite poles of the cell (*ori-ter* configuration) (**Figure 1.2**). Slow growing *E. coli* is the best studied model for the left-*ori*-right orientation. Bacterial chromosome segregation is coordinated with DNA replication and cell division and as such, a factory chromosome segregation mechanism was originally postulated where genomic DNA is spooled into centrally-held replisomes and replicated DNA is discharged to opposite cell poles (**Dingman, 1974**). It has since been shown that *E. coli* replisomes in fact oscillate at a central cell position and represent the process of tracking along chromosomal arms (replichores) (**Bates, 2008**).

E. coli lacks a chromosomal Par system, and instead the MukBEF system interacts with HU to correctly package and move the replicated *oriC*s to quarter cell positions prior to cell division (**Lioy et al., 2018**). MukBEF also interacts with Topisomerase IV (TopoIV) to promote segregation of replicated DNA. Newly replicated, hemi-methylated DNA is held together for several minutes by a protein called SeqA and this is necessary to prevent replisome stalling and disintegration. SeqA-mediated cohesion of DNA is resistant to TopoIV activities (**Joshi et al., 2013**). The majority of TopoIV was observed to be required for efficient decatenation as part of a MukBEF-TopoIV complex (**Zawadzki et al., 2015**). As sister chromosomes eventually become topologically un-entangled by TopoIV, there is an effective bidirectional force exerted on sister chromosomes, termed 'snapping' (**Joshi et al., 2013**). This periodic build up and release of mechanical tension could drive chromosome segregation. These collective activities cause initial segregation of *oriC* followed by the bulk of the *E. coli* chromosome (**Badrinarayanan et al., 2015**).

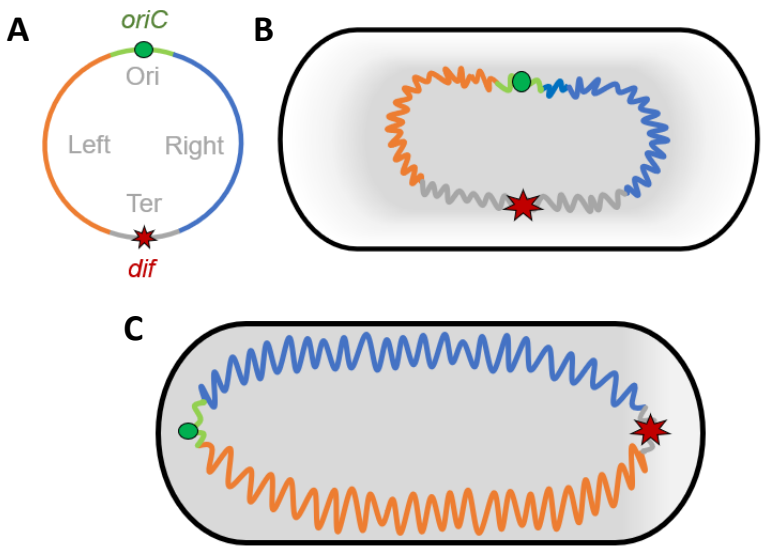

Figure 1.2. Chromosome orientations. A) The four macrodomains of Ori, Left, Right, and Ter, are represented in map format. *oriC* and *ter* (*dif*) sites are also depicted. **B)** A 'left-*ori*-right' organisation exhibited by slow growing *E. coli*. **C)** An '*ori-ter*' chromosome organisation is shown for a typical bacterial primary chromosome. Grey signifies the general region of the cell inhabited by the entire nucleoid. High level chromosome compaction is depicted by weaving. Adapted from **Badrinarayanan et al. 2015.**

Similar positioning of vegetative *B. subtilis oriCs* is mediated by the SMC-ParB-*parS* complex, but a mutated *parB* gene results in impaired SMC loading (**Sullivan et al., 2009**). Crucially, *par* genes are non-essential for *B. subtilis oriC* segregation, as is often the case in bacteria with one chromosome (**Lee and Grossman, 2006; Bouet et al., 2014**). While there is less accurate chromosome segregation without the Par system, this shows that there is some redundancy in primary chromosome segregation. A polymer physics parameter was introduced where it was suggested that entropy can contribute to chromosome segregation (**Jun and Wright, 2010**). A single overlapping chain representative of a chromosome was shown to have fewer degrees of conformational freedom (or conformation entropy) than chains that are completely separate. Entropic forces therefore actively segregate mixed DNA molecules from one another in a process termed 'demixing'. It was thus suggested that proteins involved in chromosome organisation segregation, such as TopoIV introducing double stranded (ds) DNA cuts, have a supporting role in entropy-driven chromosome segregation (**Jun and Wright, 2010**). Moreover, the cylindrical confinement of the cell acts to apply tension which pulls and stretches the chromosomes (**Jun and Wright, 2010**). In support of this, a study on *B. subtilis* proliferation, had cell wall-deficient variants (FtsZ independent

cell division) grown in narrow, linear cell configurations via microfluidics chambers. The study demonstrated that an elongated, cylindrical cellular geometry played a primary role in the movement of chromosomes, and there was greatly improved efficiency of chromosome segregation (**Wu et al., 2020**). Entropic demixing is therefore another parameter to consider for chromosome segregation, and not only for species exhibiting a left-*ori*-right organisation.

1.3.2 Longitudinal, '*ori-ter*' orientation

The most common chromosomal organisation is the *ori-ter* configuration (**Figure 1.2C**). *In vivo* imaging using fluorescently labelled operator arrays, and DNA-binding proteins, have demonstrated that bacteria with complex cell-cycles (exhibiting differentiated phenotypes as the cell matures) often fall into this category. It was first shown that sporulating *B. subtilis* has a chromosome oriented along the length of the cell, with the *oriC* at the old cell pole and the *ter* close to the new pole. Replicated chromosomes then adopt an *ori-ter-ter-ori* organisation during stationary phase of sporulation (**Wang et al., 2014**)**.** *Caulobacter crescentus* is another well characterised species, and operator arrays throughout the genome were used to visualise a longitudinal orientation (**Viollier et al., 2004**). Chromosome segregation was shown to be an ordered multistep process as the duplicated *oriC* is localised to the new pole (**Shebelut et al., 2010; Toro et al, 2008**). As the cell elongates, the *ters* adopt a more central localisation, and an *ori*-ter orientation in both daughter cells is resumed upon cell division. It is a similar case for *Myxococcus xanthus.* These species utilise polar interactions via their ParABS machinery to tether the old *oriC* whilst the replicated *oriC* is translocated to the opposite pole. The polar anchors are used to effectively maintain the *ori*-ter organisation (**Lin et al., 2017; Trojanowski et al., 2018**).

Alternatively, *E. coli* growing in optimal conditions displays a variant of an *ori-ter* orientation. Fast growing cells are born with partially replicated chromosomes (**Youngren et al., 2014**), as the chromosome triggers replication more than once, in a phenomenon known as multi-fork replication. The single *ter* retains a central cellular localisation, but both replichores deviate from the normal left-*ori*-right pattern to an *ori-ter* orientation. This could be facilitated by a different cellular phenotype that can only adopt an *ori-ter* in a fast-growing state (**Youngren et al., 2014**). It has been suggested that the multi-chromosomal species, *Agrobacterium tumefaciens* and *S. meliloti*, also assume *ori-ter* arrangements via polar *oriC* localisations (**Kahng and Shapiro, 2003**), and it has been shown to be the case for *V. cholerae*, as outlined below.

1.3.3 Segregation dynamics of the two *V. cholerae* chromosomes

V. cholerae Chr1 and Chr2 have distinct *ori-ter* based dynamics during a cell-cycle (**Figure 1.3A**) conferred by their specific ParABS systems, and this is also seen for other multi-chromosomal species such as *B. cenocepacia* (**Dubarry et al., 2006**). The contribution of Par systems to chromosomes in general is unclear and it has been suggested that they are only needed for initial *ori* segregation. They could prevent entanglement of sister *oris* and minimise resistance when moving through the cell (**Lee and Grossman, 2006**). Numerous chromosomal Par systems have been shown to stabilise an unstable variant of F plasmid in a heterologous host (*E. coli*) (**Yamaichi and Niki, 2000, Godfrin-Estevenon and Lane, 2002, Jakimowicz et al., 2002, Bartosik et al. 2004, Dubarry et al., 2006, Yamaichi et al., 2007b**). Par systems are essential for *C. crescentus, M. xanthus,* and *Hyphomonas neptunium* (**Toro et al., 2008; Iniesta et al., 2014; Jung et al., 2019**). Other species display varying degrees of growth defects and anucleate cells when the Par system is inactivated (**Kawalek et al., 2020**). *parABS1* is not essential for *Vc*Chr1, with *par* gene deletions causing disrupted polar localisation with no growth defect (**Saint-dic et al., 2006; Yamaichi et al., 2007a; Kadoya et al., 2011**). *V. cholerae* encodes MukB and interestingly, it did not alter the Chr1 *ori-ter* arrangement to match that of *E. coli* in *parAB1* deletions. Moreover, *mukB* deletion was said to not appreciably affect Chr1 segregation and indicates higher complexity for primary chromosome segregation amongst a multipartite genome (**Kadoya et al., 2011**). In contrast, *Vc*ParABS2 is essential, with no apparent redundancy for Chr2 segregation; *parABS2* deletion mutants caused Chr2 mislocalisation and a high proportion of anucleate and non-viable cells (**Yamachi et al., 2007b**). This shows Par systems can contribute to independent segregation of a much larger DNA cargo than plasmids.

Fluorescently labelled operator arrays positioned at *V. cholerae oriC1* revealed localisation at the old pole and it is held there by a polar tether (**Fogel and Waldor, 2005; Yamaichi et al., 2012**). The duplicated *oriC1* is segregated asymmetrically to the opposite (new) pole. HubP is a protein that acts as a junction-point to underlie the perpetuation of the polar domain, and ParA1 interacts with HubP to anchor *oriC1* (**Fogel and Waldor, 2006; Yamaichi et al., 2012**). *oriC2*, on the other hand, is positioned at mid cell in new cells, and duplicated *oriC2*s are symmetrically segregated to the quarter cell positions (¼ and ¾) (**Figure 1.3A**) (**Fogel and Waldor, 2005; 2006; Fiebig et al., 2006; Srivastava and Chattoraj, 2007; Yamaichi et al., 2007b**). Fluorescently labelled Chr1 *ter* behaves like that of *E. coli*, in that it retains its position but appears to move toward mid-cell as the cell grows. Duplicated *ters* remain associated and differentiate only just prior to cell division. In contrast, duplicated Chr2 *ters* can segregate away slightly from mid-cell well before cytokinesis ensues (**Srivastava et al., 2006; Demarre et al., 2014**).

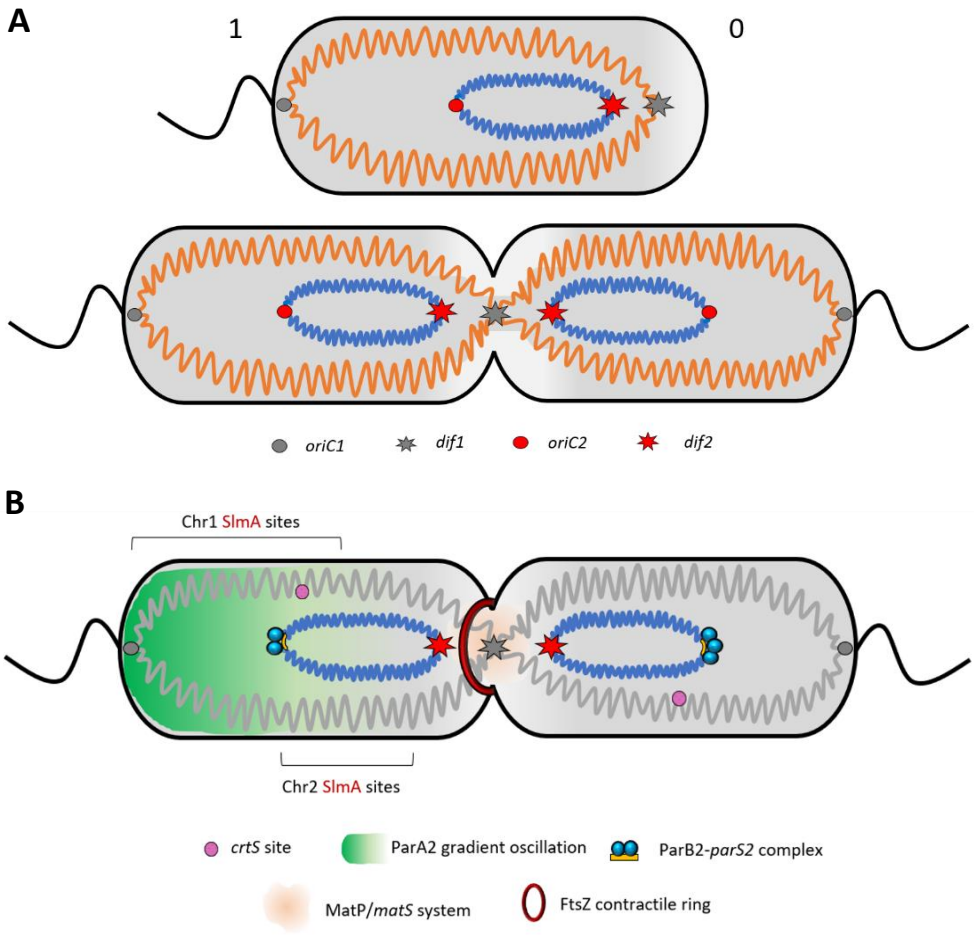

Figure 1.3. Distinct chromosome dynamics within *V. cholerae*. A) The top panel is a schematic of Chr1 and Chr2 arrangement relative to each other in a newly divided cell. The old pole is denoted by '1', and the new pole by '0'. As in Figure 1.2, grey represents the region of the cell taken up by the nucleoid. Chr1 is in orange. *oriC1* and *dif1* are represented by the grey circle and star, respectively. Chr2 is in blue, with *oriC2* and *dif2* represented by the red circle and star, respectively. *oriC1* is tethered to the old pole by the polar perpetuation protein, HubP, which also maintains the positioning of the flagellum. Inactive FtsZ sequesters in the small region at the new pole that is nucleoid-free (white). As the cell divides, the duplicated *oriC1* site moves asymmetrically to the new pole with HubP slowly localising to the new pole to facilitate translocation. Alternatively, sister *oriC2s* localise from mid cell to ¼ and ¾ positions. **B)** As in (**A**), but with Chr1 greyed out and Chr2-relevant subcellular localisation systems highlighted. Duplication of *crtS* site triggers Chr2 replication, upon which sister chromosomes are segregated symmetrically by *Vc*ParABS2. MatP resolves *dif2* before *dif1* and Chr2 SlmA sites delays the FtsZ ring. Septum formation re-establishes mid-cell positioning of *oriC2s* in daughter cells. *Vc*ParABS1 system not shown. Adapted from **Badrinarayanan et al. 2015** and **Galli et al., 2016**.

Coordinated positioning of both chromosome *ters* with cell division is facilitated by the MatP/*matS* macrodomain organisation system, although it is currently not completely understood how activity is differentiated for the distinct *ter* patterns exhibited. Since bacterial chromosomes are usually circular, *ter* is generally defined as being opposite *oriC*, but replication forks do not necessarily meet at this point. The significance of this region is that it is the last region to be resolved between sister chromosomes regardless of the chromosome orientation patterns. The region consequently contains a specific recombination site, called *dif*, dedicated to the resolution of chromosome dimers. Crossover of intertwined sister chromosomes is achieved by two tyrosine recombinases, XerC and XerD at this site (**Val et al., 2008; Kono et al., 2011**). In *E. coli,* the process is coordinated by a DNA pump, FtsK, which brings together duplicated *dif* sites for resolution. Many plasmids also use this host-encoded dimer-resolution mechanism, but independently of FtsK. FtsK is used for crossover events for both *V. cholerae* chromosomes through divergent dimer-resolution sites, *dif1* and *dif2* (**Val et al., 2008**). Distinct *ter1* and *ter2* patterning likely occurs from differential activities at *dif1* and *dif2* sites, and the MatP/*matS* system (**Figure 1.3B**).

The bulk of both chromosomes have been tracked in *V. cholerae.* Plasmid ParB fluorescent fusion proteins have been utilised as markers of chromosomal loci, with *parS* inserted throughout both chromosomes (**Fiebig et al., 2006; David et al., 2014**). Longitudinal orientations were observed for both chromosomes (**Fiebig et al., 2006**), and the markers were segregated sequentially as they were replicated (**David et al., 2014**). *Ori-ter* positioning for each chromosome is Par-dependent, however replication can also contribute to longitudinal organisation, as shown for *par*-deletion *V. cholerae oriC1* localisation. Chr1 was demonstrated to extend along most of the cell, as is the case for *C. crescentus* and *M. xanthus*, whereas Chr2 only fills half of the cell. It is unclear what causes Chr2 to be constrained to the newer half of the cell where it overlaps with the terminal part of Chr1 (**David et al., 2014**).

V. cholerae exhibits fast growth under optimal conditions with a minimum doubling time of 18 min (**Rasmussen et al., 2007**). Like *E. coli*, genome replication is concluded before cell division, with replication initiated more than once in a single cell-cycle. Genes encoding transcription and translation are located close to *oriC1*, and thus subsequent increased gene dosage facilitates multi-fork replication during exponential phase (**Soler-Bistue et al., 2020**). Interestingly, the partially replicated *oriC1*s demonstrated some pre-segregational behaviour of separation and then coming back together, before committing to segregate to opposite poles (**Srivastava and Chattoraj, 2007**). This behaviour has echoes of sister chromosome snapping, as postulated for *E. coli* (**Joshi et al., 2013**).

Fittingly, sister chromosome cohesion has recently been investigated for both *V. cholerae* chromosomes. An alternate 3C high-throughput method was recently developed for monitoring the relative frequency of sister-chromosome contacts (Hi-SC2) behind replisomes over the entire genome (**Espinosa et al., 2020**). There was comparable cohesion at both *oriCs* to that detected in *E. coli.* This was not expected since both chromosomes have a ParABS system for active sister *ori* segregation. Both *dif1* and *dif2* specific recombination sites were also highly cohesive. Various lysogenic filamentous phages integrate at *dif1* preferentially over *dif2*, including CTXΦ which encodes the cholera toxin (**Das, 2014**). Crucially, the H-NS NAP was revealed to extend the duration of cohesion at a 39.5 kb *Vibrio* pathogenicity island (VPI-I), located on CTXΦ (**Espinosa et al., 2020**). The aggregate cohesion of *dif1* and VPI-I relative to *dif2* alone could account for the two distinct *ter* patterns. The active segregation of both *oriC*s by their respective ParABS systems would therefore initiate after individualisation via the ensuing sister chromosome snapping events.

1.3.3.1 Initiation of *Vc*Chr2 replication is dependent on a *Vc*Chr1 locus

Each *V. cholerae* chromosome is replicated in a process linked to the cell-cycle (**Egan et al., 2005; Val et al. 2016**). As in *E. coli*, *oriC1* replication is initiated by the protein DnaA binding to multiple sites located within *oriC1* and unwinding DNA for replisomes to subsequently bind (**Egan and Waldor, 2003**). There are various regulatory mechanisms, including SeqA binding to 'persistent' hemi-methylated sites within the *oriC1* to repress initiation (**Lu et al., 1994**). For *oriC2*, there is a single DnaA binding site that is similarly complemented by the antagonistic activities of SeqA. A key distinction, however, is that the predominant *oriC2* initiator of replication is plasmid-like and is under the control of the RctB protein. RctB binds to an array of sites (12-mers) to initiate replication, which act as the equivalent of iterons found on plasmids; plasmids have various iteron-based 'initiator-titration' mechanisms for the control of replication initiation (**Chattoraj et al., 1984**). This alone is not enough to maintain only one copy of Chr2, and RctB also has the ability to bind three alternative sequences located within the *oriC2* (39-mers) to, in effect, sequester RctB away from 12-mers (**Venkova-Canova et al., 2006**). In an intriguing mechanism to illustrate the intricate interplay between DNA replication and segregation, ParB2 can bind 39-mers to compete with RctB. Furthermore, one 39-mer coding region includes a *parS*2 site which causes transcription repression when ParB2 binds, while another 39-mer coding region is occluded by ParB2 spreading from a nearby *parS*2 site (**Yamaichi et al., 2011; Kadoya and Chattoraj, 2012**; **Ramachandran et al., 2017**). Overall, the tight regulation ensures that *oriC2* is essentially inactive until a cell signal 'checkpoint' is reached (**Val et al., 2016**).

Chr2 is appropriately adapted and integrated into the *V. cholerae* genome with replication termination coordinated to finish at the same time as Chr1. Initiation of Chr1 before Chr2 in exponential growth conditions allows only Chr1 to be partially replicated in new-born cells, as described earlier. Raising Chr2 copy number decreased growth rate, suggesting that the necessary genes present on this chromosome come with high cost and are maintained in a specific balance (**Srivastava and Chattoraj, 2007**). The overriding initiation of *oriC2* replication is triggered by the duplication of a 150 bp sequence located on Chr1, called *crtS* (**Figure 1.3B**) (**Val et al., 2016**). As a major cell-cycle regulator, *crtS* acts to remodel RctB so that affinity for 39-mers is reduced and is increased for 12-mers. The exact mechanism has been shown to be more complex since increasing RctB bypasses the need for *crtS* duplication (**Ramachandran et al., 2018**). It has also been shown that RctB binding to *crtS* is weak and it could be that a higher RctB concentration causes more binding to *crtS*, and subsequent RctB remodelling. Nevertheless, it has been confirmed that Chr1 licences initiation of *oriC2* replication by doubling the gene dosage of *crtS* via replication of the locus, and this is a critical regulatory switch for Chr2 replication timing (**de Lemos Martins et al. 2018; Ramachandran et al., 2018**).

1.3.3.2 Coordinating nucleoid organisation with the end of the cell-cycle

The *E. coli* cell division apparatus and their regulators are also present in *V. cholerae*. The tubulin-like protein, FtsZ, associates with the membrane at mid-cell and polymerises into a contractile ring structure to bring about septation (**Figure 1.3B**) (**Galli et al., 2016**). In *E. coli*, this process is comprised of two main stages: FtsZ associates at mid-cell around a third of the way into the cell-cycle; the other cell division proteins, including FtsK, are then recruited half-way into the cell-cycle to begin septation. *V. cholerae* exhibits delayed FtsZ membrane association (mid-cell-cycle) with full assembly of the contractile ring occuring at 80% of the cell-cycle (**Galli et al., 2016**). Actual septation is constrained to the last 10% of the cell-cycle and importantly influences the polar organisation of the nucleoid (**Galli et al., 2017**).

The MinCDE system controls the spatiotemporal positioning of FtsZ in *E. coli.* MinC inhibits FtsZ polymerisation and interacts with MinD, a ParA-like ATPase that in turn associates to the membrane by interaction with MinE. Fluorescent MinCD has been observed to oscillate from pole-to-pole in a mechanism that chases FtsZ from the poles (**Lutkenhaus, 2007**). As the cell elongates, the relative concentration at the centre of the cell decreases such that FtsZ begins to polymerise. Meanwhile, SlmA is part of another regulatory system, termed the nucleoid occlusion (NO) system, which inhibits FtsZ-ring formation when the bulk of the chromosome is present at mid-cell (**Bernhardt and de Boer, 2005**). SlmA binds to specific

DNA sequences across the genome, called SlmA-binding sites (SBSs). *V. cholerae* has distinct requirements for cell division control due to the presence of Chr2 and longitudinal chromosome orientations. Premature septation at 50% of the cell-cycle would risk guillotining the nucleoid. MinCDE is thus deemed as a complementary system to NO regulation of FtsZ polymerisation (**Galli et al., 2016**).

The distribution of *V. cholerae* SBSs were defined in a whole genome binding analysis (**Galli et al., 2016**). SBSs are located across the length of both genomes but, crucially, there are various higher affinity SBSs close to both *oriC*s. There is also a major SBS located in the *ter* of Chr1; as described above, this is the last region of the nucleoid to resolve and facilitates septation to the last 10% of the cell-cycle. As there are lower strength sites located in the terminal half of Chr1, the positioning of Chr2 in the same vicinity (younger half of the cell) ensures the NO is functional across the entire length of the nucleoid. Essentially, NO in the older half of the cell is governed by the SBSs on *oriC1*, and by SBSs on *oriC2* and on *ter1* in the newer half of the cell (**Figure 1.3B**) (**Galli et al., 2016**).

Polar tethering of *oriC1* is brought about by HubP and the mechanism for *oriC1* recruitment has been investigated by determining the subcellular localisation of a fluorescent HubP fusion. In newly divided cells, HubP is almost entirely localised to the old pole but there is a slow increase of HubP at the new pole towards the end of cell growth (**Galli et al., 2017**). This is correlated to the choreography of Chr1 asymmetric segregation, with duplicated *oriC1* (along with Par proteins) colocalising with HubP at the new pole. Delaying septation to the last 10% of the cell-cycle means that the HubP does not have enough time to bind to the septum (**Galli et al., 2017**). Accordingly, this accounts for newly born cells being bound at the old pole by HubP, and for why Chr1 adopts a longitudinal orientation. The nucleoid assumes an asymmetric organisation and Chr1 *ter* is positioned slightly away from the new pole. The subsequent lack of NO results in FtsZ sequestration in this region until later in the cell-cycle (**Galli et al., 2016; 2017**). The longitudinal arrangement for the secondary chromosome could be due to equi-positioning of *oriC2s* akin to that of low copy plasmids, in addition to the MatP/*matS* system being used for *ter1* and *ter2*. Another possibility is put forward in Chapter 3, where *Vc*ParABS2 complex assembly is investigated in the presence of ATP and CXP (cytidine nucleotides).

As outlined for *E. coli* and *V. cholerae*, there are significant differences in cell division among different species. *B. subtilis* also utilises the MinCDE system alongside NO. These are absent in other organisms such as *C. crescentus*, for which MipZ functions instead (**Adams et al., 2014; Toro-Nahuelpan et al., 2019**). Interestingly, even with these distinctions, *V. cholerae* exhibits a more similar cell division phenotype to *C. crescentus* than *E. coli*. The best characterised systems that coordinate *Vc*Chr2 DNA replication, segregation, and cell division

are depicted in **Figure 1.3B**, with the *crtS* replication checkpoint, the *Vc*ParABS2 system, SlmA nucleoid occlusion, MatP/*matS ter* positioning, and FtsZ-mediated cell division. The current understanding of ParABS systems will next be reviewed in detail.

1.4 DNA SEGREGATION SYSTEMS

1.4.1 Plasmid partitioning systems

ParABS DNA partitioning systems were first observed on plasmids and are important mediators of plasmid stability (**Austin and Abeles, 1983**). Plasmids are pervasive in most bacterial species and are integral drivers of gene flux. In being extrachromosomal, the cost of their maintenance must not be outweighed by their associated benefits. Plasmids are the preferred vectors of mobile antibiotic resistance (Ab^R) genes, and the conjugative F plasmid is the main carrier of Ab^R genes in human associated commensal *E. coli* (**Stephens et al., 2020**). Virulence genes of pathogenic bacteria are also carried on plasmids, such as the shiga toxin in *Shigella flexneri*, and heat-labile enterotoxin (cholera toxin-like) in *E. coli* (**Venkatesan et al., 2001; Echeverria and Murphy, 1980**). Furthermore, the P1 prophage confers a reproductive growth advantage to *E. coli* lysogenic strains (**Edlin et al., 1977**). Many of these plasmids are relatively large (>50 kb) and the genes pose a burden to the host cell and they are therefore maintained at a low copy number (<5 per cell) to minimise the fitness costs (**Sengupta and Austin, 2011**). Various classes of ParABS systems are described in the following sections. In plasmids, ParABS systems represent one of several mechanisms involved in ensuring the stable maintenance of plasmids in host cells at a constant copy number. Dimer/multimer resolution has been alluded to in the previous section for chromosomes, and both high and low copy plasmids also utilise the host encoded dimer resolution mechanism (**Val et al., 2008**). Initiation of replication in plasmids, however, is very different from that of chromosomes with various iteron-based 'initiator-titration' mechanisms utilised (**Chattoraj et al., 1984; Park et al., 2001**). If these mechanisms were to in some way fail then post-segregational killing can intervene and, in combination, these mechanisms reduce plasmid loss to less than 1 in 10^8 cells (**Sengupta and Austin, 2011**).

Post-segregational killing refers to toxin-antitoxin (TA) systems that kill daughter cells lacking the relevant plasmid. Their mechanism relies on a pervasive, stable toxin (commonly targeting DNA or protein synthesis), and a relatively short-lived antitoxin that can only be synthesized by cells carrying the plasmid. One theory of TA systems is that they are 'selfish genes' that only exist to promote their own vertical transmission. There are thirteen TA loci in *V. cholerae* and all of them are located on Chr2, which explains the essential role of *parABS2* for Chr2 segregation and *V. cholerae* viability. These are likely a relic of the pre-domesticated

megaplasmid that Chr2 is derived from. There are, however, alternative theories for chromosomal TA loci, as they are present in nearly all sequenced bacterial genomes. For example, they could be important for stabilisation of dispensable primary chromosomal regions (**Yuan et al., 2011**).

Some plasmids have a high copy number (>20 per cell) and appear to have stochastic replication initiation (**Reyes-Lamothe et al., 2014).** The rate of loss is reduced further than that seen for low copy plasmids, simply due to there being more copies (**Sengupta and Austin, 2011**). As such, high copy plasmids do not encode ParABS systems. A ColE1-type plasmid was tracked in *Klebsiella pneumoniae* during microscopy experiments where it was found to be highly mobile and able to traverse the cell as individual elements. As the cell reached the final stages of the cell-cycle, plasmids became localised to the cell poles (**Reyes-Lamothe et al., 2014**). Although the plasmids are free to roam, they are excluded from the tightly packaged nucleoid as it acts as a barrier to the diffusion of other large DNA molecules. Entropic demixing thus influences the subcellular clustering of plasmids (**Jun and Wright, 2010**). ParABS systems are therefore necessary for the faithful transmission of low copy plasmids to daughter cells. This section will outline plasmid ParABS systems, starting briefly with the well characterised type II and type III systems. The pervasive type I system, as found on *V. cholerae* Chr2 and most bacterial chromosomes, will then be reviewed comprehensively.

1.4.2 Par system classes

Partitioning of DNA in bacteria requires three elements: a centromere-like signal sequence, CTPase centromere binding protein (CBP), and an NTPase protein that acts as a motor protein to drive partition **(Gerdes et al., 2010, Soh et al., 2018**). The two proteins are arranged in an operon with the centromeric element located close to it (**Figure 1.4**). This minimal cassette composition is conserved for the three classes of partitioning systems, although they differ in terms of sequence and underlying mechanisms. The three partition classes are defined based on the associated NTPase that drives partition: type I Par systems encode deviant Walker-type P-loop ATPases, type II systems encode actin-like ATPases, and the type III systems encode tubulin-like GTPases. Type I systems are further subclassified as type Ia or Ib. Type Ia ATPase proteins are typically larger than their type Ib counterparts, and have an N-terminal domain (NTD) for binding motifs within the *par* operator (*parOP*), to repress transcription of the *par* operon (**Figure 1.4B**). Type Ib ATPase proteins lack this feature and the CBP carries out the function of transcriptional repression by binding to centromeres located in the same region (**Figure 1.4C**) (**Dunham et al., 2009; Schumacher, 2012**).

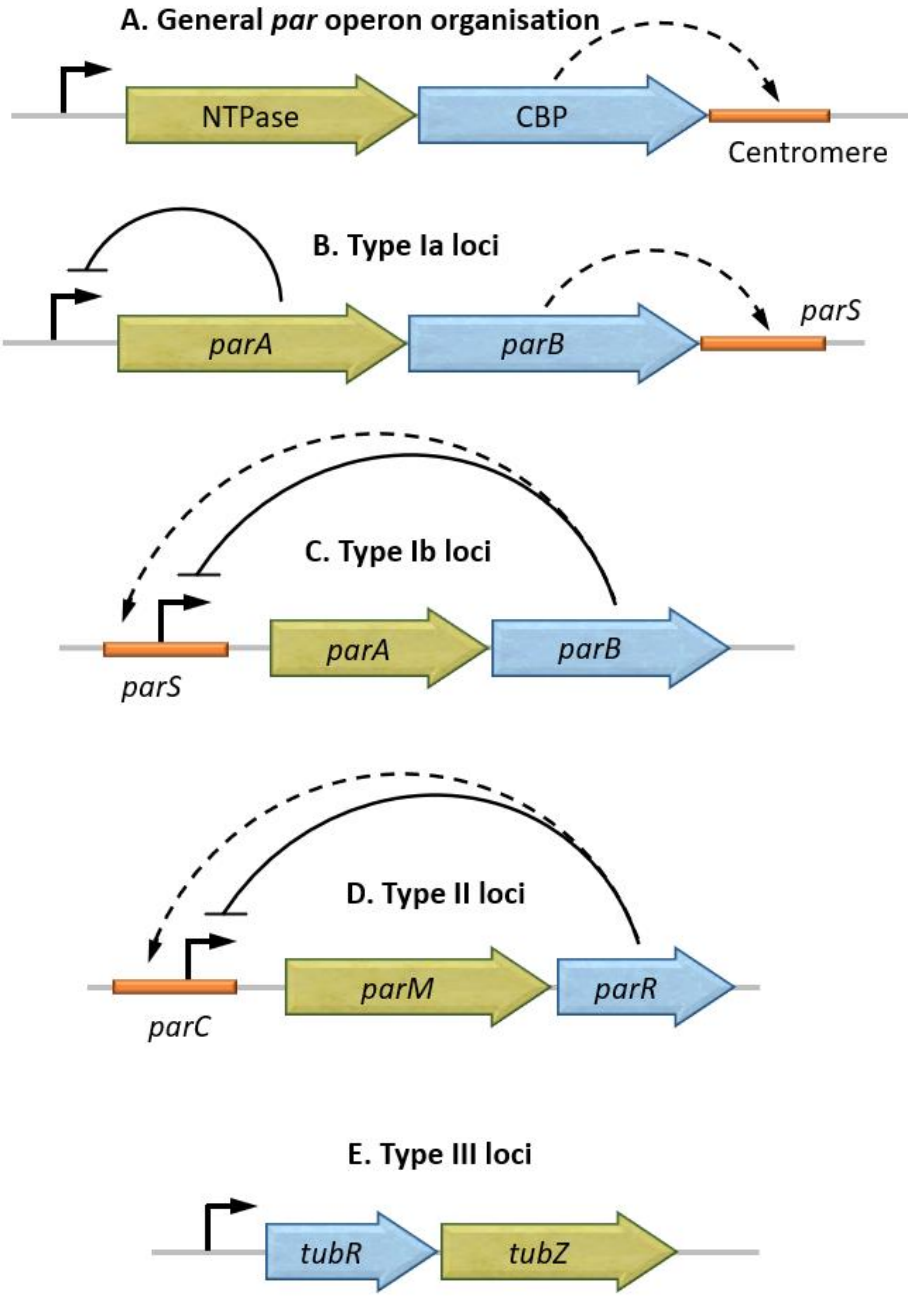

Figure 1.4. Organisation of *par* loci. A) General *par* operon organisation showing the arrangement of genes for the NTPase and the centromere binding protein (CBP), as well as the centromere-like site. The dashed arrow depicts the translated CBP protein binding to the centromere. **B)** Type Ia operons are present on most plasmids and *Vc*Chr2. ParA binds *parOP* upstream of the *par* locus promoter to repress transcription (solid bar). **C)** Type Ib operons are on most primary chromosomes and some plasmids. ParB represses transcription of the *par* locus by binding to *parS* located around the *par* promoter. Type Ib Par proteins are typically smaller than Type Ia proteins, as depicted with the comparative ORF lengths. **D)** Type II *par* operons encode actin-like homologues. **E)** Type III operons encoding for tubulin-like homologues are less well characterised. Adapted from **Gerdes et al., 2010**.

1.4.2.1 Type II systems

The archetypal type II Par system is encoded by the *parMRC* operon of the *E. coli* multi-Ab^R plasmid R1 (**Figure 1.4D**) (**Gerdes and Molin, 1986**). The centromere-like sequence, *parC*, is found as two arrays of five direct-repeats flanking the *parMRC* operon promoter. The CBP ParR, forms a U-shaped complex at *parC* sites as DNA is folded back on itself 150 º (**Hoischen et al., 2008**). In the presence of the ParRC complex, the ATPase, ParM, forms left-handed double-stranded helical filaments that polymerise with ParM-ATP monomers being inserted between ParRC complexes on sister plasmids. Structural studies and total internal reflection fluorescence (TIRF) microscopy studies showed that a single polar ParM filament is stabilised by ParRC (**Gayathri et al., 2012; Bharat et al., 2015**). The ParRC U-shaped complex caps the end of a ParM filament and is the site at which polymerisation occurs. Filament polarity is intrinsic to ParM oligomeric architecture as two filaments associate in an antiparallel orientation to form a bipolar polymer (**Gayathri et al., 2012**). The action of bidirectional filament elongation drives plasmid partitioning in a mechanism akin to elongation of unbranched actin filaments (**Jensen and Gerdes, 1999**).

The ParMRC mechanism was determined using fluorescent operator arrays (**Campbell and Mullins, 2007**). Plasmids are free to roam in newly divided cells and upon meeting become tethered to one another as ParR binds *parC* in a plasmid pairing event. Bipolar ParM filaments then extend to push plasmids apart along the length of the cell. Copies take around 20 s to be pushed to opposing poles with ParM polymerising until the ends of the cell are reached (**Campbell and Mullins, 2007**). ParRC dissociates from ParM filaments leaving them to rapidly depolymerise as ParM hydrolyses ATP. There are usually multiple rounds of plasmid partitioning as released plasmids resume random diffusive motion and likely encounter each other again. As plasmid partitioning is independent of the host cell-cycle, repeated processes of plasmid pairing and partitioning increases the probability of transmission to both daughter cells (**Campbell and Mullins, 2007; Garner et al., 2004**). There are variations of the type II Par system mechanism as some ParMs form only a single filament, while others have a wider filament that contacts the ParRC complex (**Schumacher, 2012**). An interesting observation is that a virulence plasmid in *E. coli*, pB171, has a type II system as well as a type Ib system, with both being functional for partition (**Sengupta and Austin, 2011)**.

1.4.2.2 Type III systems

In contrast to the well-characterised type II Par systems, the mechanism of type III systems has only recently been described for the partition of virulence plasmids in the genus *Bacillus*. TubZ is a GTPase necessary for both DNA replication and segregation (the reason for the

former being unclear) (**Figure 1.4E**) (**Ni et al., 2010**). DNA transport occurs as TubZ interacts with TubR, itself a homologue of ParB that can bind to two sets of *tubC* repeats located upstream of the *tubZRC* operon. A tubulin-like mechanism was first proposed for the action of TubZ since there is sequence homology to FtsZ which itself is known to have a nucleotide-binding motif similar to tubulin (**Aylett et al., 2010**). Structural studies have indicated similar features to other classes of Par system. Helical filaments are observed in bacterial cells to organise cellular processes in time and space as cytoskeletons. Indeed, the structural basis of filament formation is largely conserved even if the physiological functions are divergent (**Wagstaff and Lowe, 2018**). There seems to be some convergent evolutionary architecture between type II and type III cytomotive filaments, as TubZ forms double-stranded helical filaments similar to ParM, and GTP hydrolysis weakens polymerisation (**Aylett et al., 2010**). In terms of the CBPs, type II systems have a RHH motif, whereas TubR has a winged-HTH domain, with both features found in type I ParB proteins. Finally, *tubC* patterning is similar to that seen for *parC* in type II systems (**Ni et al., 2010**).

In vivo observations and a recent reconstitution of TubZRC have revealed that this system operates in a pulling mechanism (**Fink et al., 2015**). TubZ polymerises at a plus-end but intrinsic instability causes disassembly from the minus-end. This behaviour is termed 'treadmilling' and is otherwise only seen for eukaryotic kinetochore functionality (**Ni et al., 2010**). The reconstitution experiments showed that TubR bound to *tubC* can promote nucleation of TubZ polymerisation, after which TubZ freely polymerises at the plus-end. TubRC then stabilises TubZ depolymerisation and progressively tracks along the TubZ filament at the minus-end. Plasmids are deposited at the poles where the curvature of the cell at these regions is thought to act as a drop-off switch (**Ni et al., 2010; Fink et al., 2015**).

The mechanisms described so far – for the passive positioning of high copy plasmids and active positioning of low copy plasmids – result in polar localisation upon cell division. Type I systems effect polar positioning of sister *oriCs* and equi-positioning of duplicated plasmids along the long axis of the cell.

1.4.2.3 Type I systems

Deviant Walker-type P-loop ATPases are termed as such since they have a loop conformation ATP-binding motif, with a signature sequence of KGGXXK[ST] that deviates from the classical GXXGXGK[ST] fingerprint (**Walker et al., 1982; Koonin et al., 1993a; 1993b**). This domain is generally conserved within a long C-terminal domain (CTD). A short NTD for dimerisation is similarly conserved. On the other hand, type Ia ParA proteins have an elongated NTD comprising a helix-turn-helix (HTH) motif used for specific binding to the *parOP*

(**Figure 1.5A**) (**Dunham et al., 2009**). This activity is mediated by ADP-binding. Alternatively, ATP is required for non-specific (ns) DNA-binding activity that is integral for DNA partitioning in both type I systems.

1.4.2.4 The initial filament-based model

The type I Par system is the most prevalent among plasmids, as well as being present on up to 70% of sequenced bacterial chromosomes. It is, however, the least well understood class of DNA partitioning system. A retracting mitotic-like spindle mechanism was initially proposed based on *in vitro* findings of various type Ia and Ib ParA proteins polymerising in the presence of ATP. Light scattering, sedimentation and electron microscopy were used to detect large, self-sustaining filaments in the absence of DNA for P1 ParA and P7 ParA (**Dunham et al., 2009),** pSM19035 δ (**Pratto et al., 2008**), TP228 ParF (**Barilla 2005; Schumacher et al., 2012**), pB171 ParA (**Ebersbach et al., 2006**), and F SopA (**Hatano et al., 2007; Bouet et al., 2007).** These findings seemed to correlate well with how *V. cholerae oriC1* appears to be mitotically pulled to the opposing cell pole **(Fogel and Waldor, 2006**), while retracting filaments of ParA were thought to enable chromosome segregation in *C. crescentus* (**Shebelut et al., 2010; Ptacin et al., 2010**).

ParA filaments, however, have not been observed *in vivo* and the dynamic subcellular chromosome ParA localisations are in fact more cloud-like, as is the case for plasmid ParA proteins (**Hatano et al., 2007; Lim et al., 2005; Sengupta et al., 2010; Pratto et al., 2008; Ebersbach 2006; and Castaing et al 2010**). It was questioned whether self-associating SopA (the ParA for *E. coli* plasmid F) filaments would form independently of DNA *in vivo*, and they could be an artefact of using higher than physiologically relevant concentrations that were required for their stable formation *in vitro* (**Bouet et al., 2007**). Moreover, other ParA proteins form filaments around DNA, as seen for *B. subtilis* Soj and *V. cholerae* ParA2 (**Hester and Lutkenhaus, 2007; Hui et al., 2010**). This is likely due to cooperative DNA-binding, which has been shown in DNA footprint assays and gel shift assays for P1 ParA and Soj (**Davis et al., 1992; Leonard et al., 2004**). The biochemical and structural insights of Par components will next be reviewed before describing the most up to date models for type I Par systems.

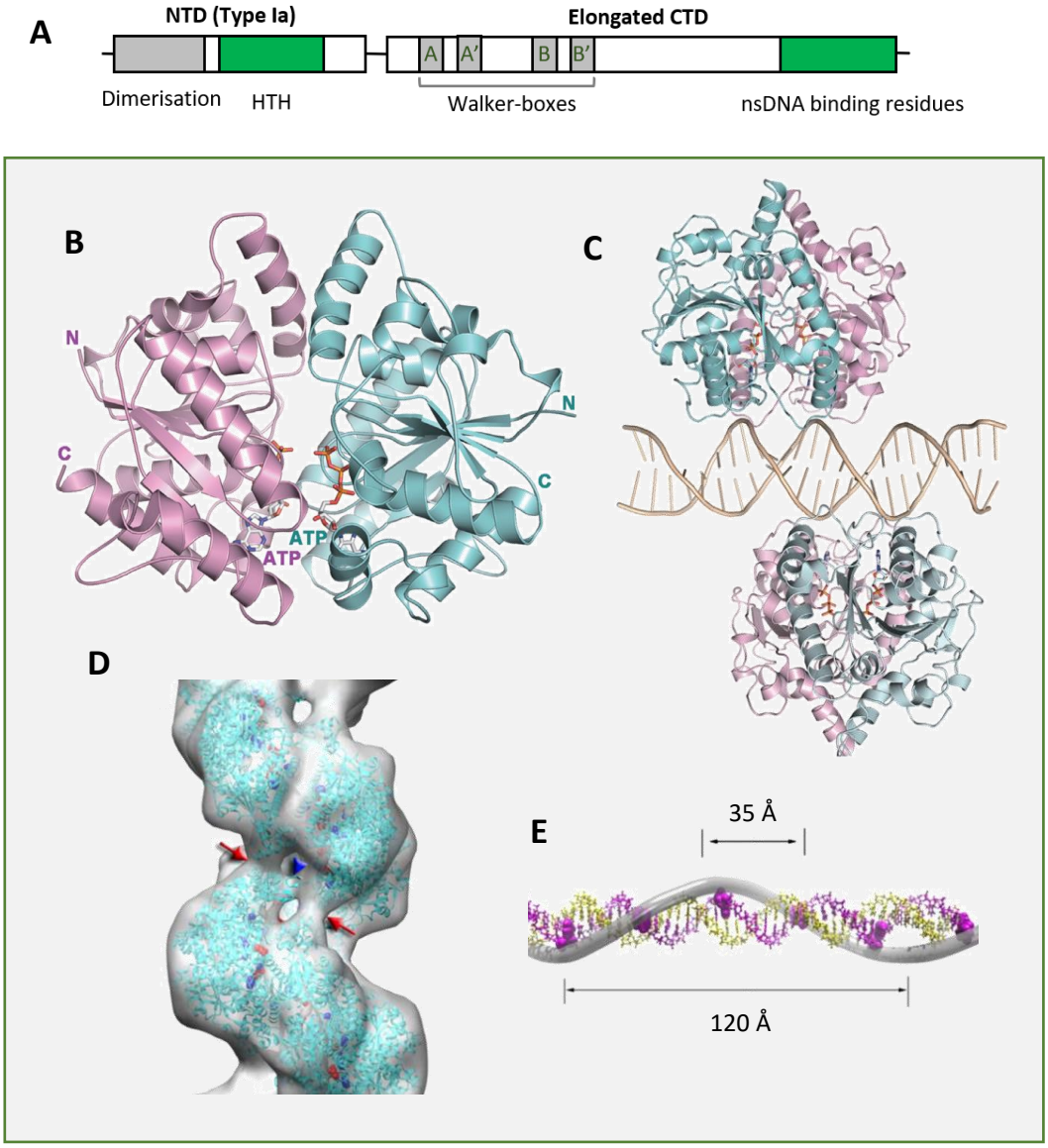

Figure 1.5. ParA structures and activities. A) Conserved domains and motifs. Type Ia ParA proteins are larger (321-420 residues) than type Ibs (192-308 residues). An elongated N-terminal domain (NTD) is present for the former and is used for binding to the *parOP* promoter for transcriptional control as characterised for plasmid ParA proteins. A long C-domain (CTD) comprises the conserved ATP-binding motif and nsDNA- binding region. Adapted from **Dunham et al, 2009; Schumacher, 2012. B)** Ribbon structure for *H. pylori* Soj (*Hp*Soj) dimer (type Ib). ATP-binding forms a sandwich dimer as for *E.coli* plasmid P1 ParA. The inner β-strands are framed by α-helices (**Chu et al., 2019**). **C).** *Hp*Soj-ATP-DNA ribbon structure with conserved basic residues located within the end of the CTD contacting the DNA phosphate backbone (**Chu et al., 2019**). **D)** *V. cholerae* ParA2 (*Vc*ParA2) (type Ia) forms filaments on DNA. Arrows show equivalent basic residues for nsDNA-binding. The elongated NTD is used for making contacts between dimers (**Hui et al., 2010**). **E)** The helical pitch of ParA2 filaments is represented on a DNA duplex shown in yellow and pink (**Hui et al., 2010**).

1.5 STRUCTURAL AND BIOCHEMICAL ASPECTS OF TYPE I Par COMPONENTS

1.5.1 ParA

1.5.1.1 Structural insights upon ATP-binding

Sequence similarity across ParA proteins of type 1 systems can be as low as 20%, even with the conserved Walker motifs, and poses the question of whether there are different mechanisms of action or if this simply allows specificity between plasmids and chromosomes (**Fu et al, 2010**). A number of structural studies have helped to elucidate conserved structural features among the type I ParA proteins. As mentioned, type Ia ParA proteins are larger than in type Ib systems. There are generally more structures determined for type Ib than type Ia ParA proteins, due to the former being smaller with fewer flexible regions and therefore easier to crystallise. Type Ia ParA proteins consist of 321-420 residues in comparison to 192-308 residues for type Ib ParA proteins (**Dunham et al., 2009**). The deviant Walker A P-loop NTP-binding motif has a conserved lysine residue (**K**GGXXK[ST]) that is integral to adenosine nucleotide-binding in all type I ParA proteins. There are further motifs that are significant for nucleotide-binding in the form of the Walker A' (switch 1) and Walker B (switch 2) motifs, each with conserved polar aspartic acid residues (**Koonin, 1993a; Fung et al., 2001**). ATP-binding is the first step in the type I ParA ATPase cycle and leads to dimerisation (**Figure 1.5B**), and slow structural changes that mediate DNA-binding, as well as segregation activities in concert with ParB (**Vecchiarelli et al., 2010; 2014b**).

The first type I ParA to have the crystal structure determined in the apo-, ADP-, ATP-states, was the type Ib ParA *Tt*Soj from *Thermos thermophilus*. In a similar manner to all studied type I ParA proteins, *Tt*Soj monomers undergo Rossman folding that is typical of ATPases, with a series of β-strand–α-helix–β-strands forming a twisted core of β-strands framed by α-helices (**Figure 1.5B**) (**Leonard et al., 2004; Pratto et al., 2008; Dunham et al., 2009; Zhang and Schumacher, 2017; Mcleod et al., 2017; and Chu et al., 2019**). A study on P1 and P7 ParA proteins showed that an N-terminal α-helix could be a conserved dimer interface. These plasmid ParA proteins were said to dimerise at physiological concentrations in the absence of nucleotide (**Dunham et al., 2009**). However, it was found previously that P1 ParA exists predominantly as a monomer in a mixed monomer:dimer population for the empty (apo)- and ADP-bound-states, and shifts to a dimer population with ATP (**Davey and Funnell, 1994; Vecchiarelli et al., 2010**). Other ParA proteins, such as pSM19035 δ, *Bs*Soj, *Tt*Soj, *Hp*Soj, and *Cc*ParA dimerise in the presence of ADP and ATP, although there are slight structural differences between the two bound-conditions (**Pratto et al., 2008; Scholefield et al., 2011; Leonard et al., 2004; Hester and Lutkenhaus et al., 2007; Lee and Grossman, 2006; Lim et al., 2014**). The main dimerisation domain for *Tt*Soj was found to be the P-loop

motif and to reflect this, *Tt*Soj forms a 'sandwich' dimer with ATPγS (**Leonard et al., 2004**). This is the case for all bacterial ParA structures studied thus far (**Figure 1.5B**) (**Pratto et al., 2008; Dunham et al., 2009; Zhang and Schumacher, 2017; Mcleod et al., 2017; and Chu et al., 2019**).

The *Tt*Soj P-loop motif undergoes a conformation change to accommodate ADP as a monomer (**Leonard et al., 2004**). The ATP-bound form was attained with an ATPase mutant, and indicated a symmetrical U-shaped dimer assembly. The active ATP-binding site was formed by the conserved lysine residues of both monomers contacting, and stabilising, the negative charges on opposing ATP molecules. Specifically, the α- and β-phosphates were stabilised by the lysine residues and the γ-phosphate was accommodated without any structural rearrangement (**Leonard et al., 2004**). On the other hand, another type Ib ParA, pSM19035 δ, forms dimers with ADP and Mg^{2+} (**Pratto et al., 2008**). This could be due to different conditions being used to attain crystals, or it could be a case of δ simply being more stable as a dimer at the concentrations used. In any case, pSM19035 δ was able to assemble as a dimer assembly with ADP, and ATPγS, nucleotide exchange was permitted without dissociation to monomers. There was extensive hydrogen-bonding between all ATP-binding motifs. This was also observed for the other characterised type Ib ParA proteins: *Tt*Soj, *Hp*Soj-ATP, and TP228 ParF-AMPPnP (non-hydrolysable ATP analague) (**Leonard et al., 2004; Chu et al., 2019; Zhang and Schumacher, 2017**). Walker-type ATPases usually have a water molecule positioned with a functional aspartic acid residue within Walker B motif for attack on the γ-phosphate. Interestingly, the water molecule in the δ-ATP dimer was positioned such that additional hydrogen-bonding was required to engage ATPase activity. This was deemed to explain the relatively low rates of ATPase activities documented for the deviant Walker-type ATPases (**Pratto et al., 2008**). ATPγS-bound δ exhibited a structurally different dimer to that formed with ADP (**Pratto et al., 2008**).

The ATP-bound form for plasmid P7 ParA was not attainable and instead ADP was found to cause large-scale folding of four regions that hydrogen-bond to the β-phosphate of ADP, which caused new α-helices to form on each monomer (**Dunham et al., 2009**). The result is linked to an increased helicity for P1 ParA when in the presence of ADP, as detected by circular dichroism (**Davey and Funnell, 1997**). This conformation corresponds to the high affinity binding for type Ia ParA proteins to the *parOP* region (**Davey and Funnell, 1997; Bouet and Funnell, 1999**). The conserved lysine contacted the β-phosphate of the opposing monomers ADP, underscoring its importance, and various ATP hydrolysis mutants have been made to show this directly. The mutation of the conserved lysine in P1 ParA (K122E) resulted in an effective deletion of the Walker A motif (**Davis et al., 1996**). Six further mutagenesis products were made and showed three classes of phenotypes (**Fung et al., 2001**). The first

included K122Q and resulted in variants that intriguingly became super-repressors of the P1 *parABS* operon. The second and third categories were weak repressors. Critically, the third group (including K122R) were declared to be 'propagation defective (Par^{PD})' and 'worse than null' variants, since they appeared worse than the *parA* null mutant; K122R can bind but not hydrolyse ATP and so there is a lack of initial unpairing of plasmid for segregation to proceed. All of the mutagenesis products had little to no ATPase activity and did not support plasmid stability (**Fung et al., 2001; Libante et al., 2001**). Moreover, K16Q and K20A mutants of *Bs*Soj and *Tt*Soj, respectively, abolished *in vivo* oscillations (**Quisel et al., 1999**). These studies collectively highlight the importance of ATPase activity for DNA segregation.

1.5.1.2 Stimulation of ParA ATPase activity

The presence of both ParB and DNA stimulates ParA ATPase activity far beyond the basal level for all type I ParA proteins analysed biochemically (**Libante et al., 2001; Davis et al., 1992; Easter and Gober, 2002; Barilla et al., 2005; Leonard et al., 2004; Lee and Grossman, 2006; Chu et al., 2019; Hui et al., 2010; Lim et al., 2014**). The ParB interaction with ParA, and subsequent stimulation of ATPase activity, has been probed in several structural studies. The ParA-ParB interaction was first mapped to the ParB N-terminal region in biochemical studies for *C. crescentus*, and then for *P. aeruginosa*, as well as for the P1, F, and pSM19035 plasmids (**Radnedge et al., 1998; Surtees and Funnell, 1999; Figge et al., 2003; Bartosik et al., 2014; Volante and Alonso, 2015**). An attempt was made to find the exact region of ParB responsible using a twenty amino acid N-terminal peptide. There was 8% stimulation of ATPase relative to full length ParB, whereas another study found that longer N-terminal peptides can function as well as full length SopB (**Leonard et al., 2004; Ah-seng et al., 2009**). It was theorised that the context of the interaction is relevant and that ParB acts as an arginine finger in stimulating ParA (**Leonard et al., 2004**), as indicated by the *Mx*ParA interaction with PadC-CTP (**Osorio-Valeriano et al., 2019**).

An intriguing study investigated the fine-tuning of ParA-ATP hydrolysis rates (**Dobruk-Serkowska et al., 2012**). A triplet of residues that lie outside the conserved motifs outlined above were revealed to play a role in shaping the TP228 ParF ATP-binding pocket. Mutations lead to hyperactive ParF ATPase activities for the variants produced, and significantly, they were unable to be stimulated by the N-terminal region of ParG (TP228 ParB) (**Dobruk-Serkowska et al., 2012**). This was investigated further to find that one hyperactive ParF mutant was able to oscillate more often *in vivo* (every 2-3 min) versus WT ParF (every 4-6 min). This mutant was able to slightly respond to ParG but segregation was disrupted as a result of the hyperactivity (**McLeod et al., 2017**). *Hp*Soj was tested for ATPase stimulation

with DNA-bound *Hp*Spo0J (ParB) and it was theorised that N-terminal regions of a ParB dimer could be brought together adequately to insert into the appropriate two regions of a *Hp*Soj dimer (**Chu et al., 2019**). This context could account for the stimulation of ATPase activity. The region on TP228 ParF of the ParA-ParB interaction was mapped to be close to the signature lysine residue with cross linking experiments (**Volante and Alonso, 2015**). A recent study made an aspartic acid substitution within the Walker B motif to a non-polar alanine residue in ParF. Amongst the segregation defects, there was an impaired interaction with ParG as monitored by two-hybrid analyses and ATPase assays (**Caccamo et al., 2020**). The binding of an arginine residue on a ParB helix close to the ParA active site could act as an arginine finger to further stabilise ATP-binding, and thus stimulate ATPase activity.

1.5.1.3 DNA-binding activity

ATP-binding for P1 ParA is slower than simple ligand-docking would necessitate, and tryptophan fluorescence assays show slow conformational changes in the presence of ATP (**Vecchiarelli et al., 2010**). The ATP-bound state is more stable relative to adenosine nucleotide analogues as detected by circular dichroism (**Vecchiarelli et al., 2010; Libante et al., 2001; Scholefield et al., 2011**). Indeed, structural insights show that ParA-ATP assumes a dimer conformation that is distinct from ADP-bound forms. These conformations represent the active versus inactive nsDNA-binding states in Brownian-ratchet-like mechanisms, respectively (**Vecchiarelli et al., 2010; Lim et al., 2014; Le Gall et al., 2016**). The increase in helicity of type Ia P1 ParA when bound to ADP corresponds to a HTH motif of each monomer binding to AT-rich regions of DNA within the operator region of the *parABS* operon such that transcription cannot proceed (**Dunham et al., 2009; Davey and Funnell, 1997; Bouet and Funnell, 1999; Castaing et al., 2008**). Each HTH element bound to major grooves of 40 bp DNA, which caused the DNA to bend (**Dunham et al., 2009**). Mutated HTH motifs in SopA had no effect on nsDNA-binding in the presence of ATP, and suggested separate DNA-binding domains (**Castaing et al., 2008**).

ParA crystal structures with DNA have revealed variations in basic surface residue distributions that are utilised for interacting with nsDNA. The (inverted) U-shape of bacterial type I ParA proteins, such as for pSM19035 δ ParF, has positive surface charges at the tips of the arms of the U-shaped dimer (**Pratto et al., 2008; Volante and Alonso, 2015**). Accordingly, *Tt*Soj has arginine residues that suitably orientate from dimerisation (**Hester and Lutkenhaus., 2007**). SopA has lysines required for nsDNA-binding and, although not identical, sequence alignment shows similar arginine and lysine residues within the corresponding region of *Tt*Soj (**Castaing et al., 2008**). The crystal structure of *Hp*Soj-ATP-

DNA (**Figure 1.5C**) identified a basic DNA-binding patch of arginine and lysine residues in this region that is conserved for *Tt*Soj, *Sp*ParA, and ParF (**Chu et al., 2019**). Interestingly, multiple basic residues that coat the surface of ParF were said to be able to make contacts with the DNA backbone based on comparisons to the crystal structure of an archael ParA (pNOB8) (**Zhang and Schumacher, 2017; McLeod et al., 2017**). The DNA-bound form showed a single pNOB8 ParA dimer is able to bridge two DNA fragments together via multiple contacts of basic residues with the DNA backbone (**Zhang and Schumacher, 2017**). Comparison to *Hp*Soj-ATP-DNA revealed the mode of DNA-binding is different, and that bacterial ParA proteins bind nsDNA at one surface formed from the tips of the U-shaped dimer. The bacterial superfamily might therefore have a conserved nsDNA-binding mode (**Chu et al., 2019**).

1.5.1.4 Filament formation on DNA

A number of plasmid ParA proteins form long polymer bundles *in vitro* and this has also been observed for *Cc*ParA, although these are not thought to be physiologically relevant (**Lim et al., 2005; Barilla et al., 2005; Ringaard et al., 2009; Ptacin et al., 2010; Vecchiarelli et al., 2014b; Chu et al., 2019**). Based on crystal structures with DNA, self-sustaining ParA polymerisation is not required in segregation. Interestingly, *Tt*Soj, *Bs*Soj, and *Vc*ParA2 do not form self-sustaining filaments and instead form nucleoprotein filaments on DNA, as shown by negative stain electron micrographs (**Leonard et al., 2004; Hester and Lutkenhaus, 2007; Hui et al., 2010**). Furthermore, pSM19035 δ only forms higher order structures in the presence of DNA and ATP (**Pratto et al., 2008**). Soj is said to bind DNA cooperatively with ATP to form filamentous structures that coat DNA (**Hester and Lutkenhaus, 2007**). In contrast, ParA2 forms distinct bipolar, left-handed filaments on DNA without nucleotide, with ADP, and with ATP (**Figure 1.5D, E**) (**Hui et al., 2010**). Features of the filaments were determined by fitting the crystal structure of P1 ParA. The filament formed with ATP was shown to bind nsDNA with similar regions to SopA and Soj, suggesting use of the patch of basic residues (**Figure 1.5D**) (**Hui et al., 2010; Castaing et al., 2008; Hester and Lutkenhaus, 2007**).

Intriguingly, the ParA2 HTH domain was predicted to contact other subunit NTDs to form the filament structure. The ATP-bound filament was more ordered than without nucleotide cofactor or ADP, which points towards more regular contacts being made with DNA to form a more stable nucleoprotein structure (**Hui et al., 2010**). The fact that the same basic patch is being utilised suggests there may be some relevance to segregation for the oligomers. The cooperative binding seen for Soj could also apply to ParA2, and therefore a link could be made with *in vivo* oscillatory patterns seen for ParA2, Soj, and several plasmid ParA proteins (**Ebersbach et al., 2006; Hester and Lutkenhaus, 2007; Castaing et al., 2008; Ringaard**

et al., 2009; McLeod et al., 2017). It was proposed that since ParA proteins have nsDNA-binding activity, they could all form filaments on DNA mediated by highly cooperative binding. The missing N-terminal HTH motif for type Ibs ParA proteins may mean that nucleoprotein filaments are not as stable as those formed by ParA2, and this permits multiple means for ParA proteins to oligomerise on DNA (**Hui et al., 2010**). Cooperative ParA2-DNA-binding is investigated in detail in Chapter 2, as part of a comprehensive biochemical characterisation of *V. cholerae* ParA2.

1.5.2 *parS*

Type Ib Par systems located on primary chromosomes have largely conserved *parS* sites, with 8 bp inverted repeats similar to the *B. subtilis parS*: 5'-**TGTTTCAC**GTGAAACA-3' (**Figure 1.6A**). Eight *parS* sites were identified in *B. subtilis* using a chromatin immunoprecipitation (ChIP) assay to detect SpoOJ (ParB) binding (**Lin and Grossman, 1998**). Other species have been experimentally confirmed to possess similar *parS* sequences, including *P. aeruginosa, P. putida, B. cenocepacia, S. coelicolor, H. pylori, C. crescentus, and V. cholerae* (**Bartosik et al., 2004; Dubarry et al., 2006; Godfrin-Estevenon and Lane, 2002; Kim et al., 2000; Mohl et al., 2001; Yamaichi et al., 2007a**). Phylogenetic bioinformatic analyses were then performed to search for putative *parS* sites on 400 sequenced chromosomes. Just two gram-positive species were used to derive a consensus sequence where putative *parS* sites were found in 69% of the available strains and representative species were found on all branches of prokaryotes. Additionally, at least one Par component was present in 75% of strains. This included some strains encoding for just ParA and ParB, or only ParA (**Livny et al., 2007**). As described earlier, the Ori domain is sufficient for segregation in the absence of *parS* sites via non-Par-mediated segregation.

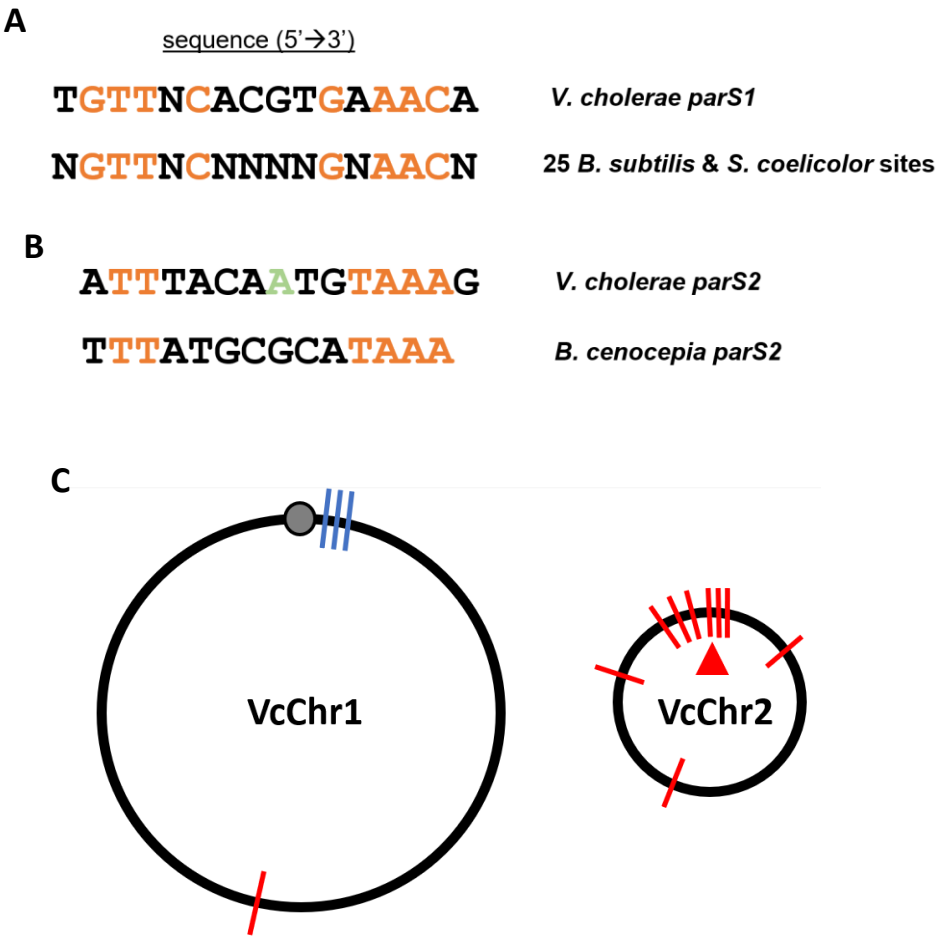

Figure 1.6. *parS* site patterning between the two *V. cholerae* chromosomes. A) The conserved nature of 16 bp (8 bp inverted repeat) primary chromosome *parS* sites are illustrated with a relevant comparison. Direct matches are shown to the *V. cholerae parS1* consensus. **B)** A similar comparison is made between just two secondary chromosome *parS* sites, showing markedly less conservation. A further distinction is that the *VcparS2*-1 7 bp palindrome is separated by a spacer bp (green). **C)** The 3 verified *parS1* sites (cyan) for Chr1 segregation, are proximal to *oriC1* (grey circle). For Chr2, 10 *parS2* sites (red) are shown, with one located in the Ter domain of Chr1; 6 are relatively close to *oriC2* (red arrowhead). Adapted from **Livny et al., 2007** and **Yamaichi et al., 2007a**.

Palindromic sequences are a defining feature of all *parS* sequences. ParB forms a dimer, with each monomer able to recognise half of the palindromic sequence (**Leonard et al., 2004**). Primary chromosomes have imperfect inverted repeats but with the same structure and length of the *B. subtilis parS* sequence (**Livny et al., 2007**). Secondary chromosome *parS* sites were found to have less overall conservation (**Figure 1.6B**), and are more plasmid-like in their variability (**Livny et al., 2007**). Characterised plasmid type Ia *parS* sites seemingly lack conservation beyond the involvement of imperfect inverted repeats, and the sequences can be complex. For instance, *E. coli* P1 plasmid has an 80 bp *parS* site comprised of four Box-A (hexameric) and two Box-B (heptameric) binding sites situated close to an IHF-binding site. Meanwhile, *E. coli* F plasmid has a 518 bp site made up of twelve 43 bp direct repeats, which are themselves comprised of 7 bp inverted repeats **(Mori et al., 1986; Bouet and Funnell, 1999)**. Various experimentally derived secondary chromosome sequences were thus used to form consensus sequences for identification of putative secondary chromosomal *parS* sites, with similar motifs and palindromic sequence structures (**Livny et al., 2007**).

Putative *parS* sites were distributed close to *oriC*s, irrespective of being present on primary or secondary chromosomes. The more diverse patterning and complexity of secondary chromosomal *parS* sites was demonstrated by 25.8% of secondary chromosomal *parS* sites being found outside of a 15% region close to the *oriC*, compared to 7.9% of *parS* sites on primary chromosomes being located outside of equivalent regions. Furthermore, only 14.5% of secondary chromosomes encoded one *parS* site, compared to 31.1% of primary chromosomes. There were regions on Left and Right domains of secondary chromosomes that appeared to contain the additional *parS* sites (**Livny et al., 2007**).

The sequences of primary chromosomes are so well conserved that a broad 16 bp consensus *parS* sequence was derived from 1030 predicted sites: 5'-**NGTTNCAN**NTGNAACN-3'. In contrast, secondary chromosome *parS sites* varied in sequence and length (**Livny et al., 2007**). The diverse, family-specific *parS* sites found on secondary chromosomes are best characterised in *V. cholerae.* DNase I protection assays were used to determine six putative *parS1* sites close to *oriC1* (5'-**TGTTNCAC**GTGAAACA-3'), of which three were verified to support YFP-ParB1 foci formation (**Yamaichi et al., 2007a**). Interestingly, there is one putative Chr1 *parS1* site on Chr2 which is not bound by YFP-ParB1. In total, there are fifteen putative *parS*2 sites with a consensus 7 bp inverted repeat: 5'-**NTTTACA**NTGTAAAN-3'. Ten *parS*2 sites are distributed on Chr2 and five on Chr1. Ten *parS*2 sites were verified with YFP-ParB2 foci forming *in vivo* and most of the verified *parS*2 sites are located within 70 kb of *oriC2*. However, there are a few that are more than 100 kb away, and intriguingly, the one located on Chr1 is close to the Ter domain, as shown in **Figure 1.6C** (**Yamaichi et al., 2007a**). It is feasible that there is a tethering mechanism between the

two chromosomes for spatially adjacent *parS*2 sites within the cell to contribute to the positioning of Chr2 in the newer cell half. Alternatively, *Vc*ParABS2 could contribute to translocation of Chr1 Ter domain just prior to cell division.

The distinctive *parS* patterns of the two chromosomes supports the earlier description of separate evolutionary histories. Deletion of *parAB2* causes a segregation defect with anucleate cells and degradation of the chromosome via post-segregational killing (**Yuan et al., 2011**). This shows that there is no redundancy for Chr2 segregation as opposed to that observed for most primary chromosomes. The unifying aspect of *parS* sites is in acting as a loading site for ParB for the demarcation of a partition complex for segregation. One site is enough to support chromosome segregation (**Livny et al., 2007**). However, *Vc*Chr2 has many *parS* sites close to *oriC*2 that is likely important for condensation of the Ori domain with ParB forming a dense partition complex, as outlined in the next section. Some species have many more *parS* sites, such as *S. coelicolor* with over 20 sites proximally distributed to the *oriC* (**Jakimowicz et al., 2002**). Excess *parS* sites on primary chromosomes could also increase the efficiency and robustness of chromosome segregation in acting as a site for the recruitment of SMC-like condensation and bulk segregation systems in relevant species (**Bohm et al., 2020**). A further function for *parS* sites is in acting as a global NAP nucleation point as it was recently found that *P. aeruginosa* ParB binds to hundreds of half-*parS* sites that are potentially used for changing chromosome topology (**Kawalek et al., 2018**). This activity has been implicated to apply to other species, including *V. cholerae* (**Jalal et al., 2020b**).

1.5.3 ParB

There is little sequence homology between ParB proteins and this illustrates the varying complexities involved in the formation of species-specific partition complexes. However, structural studies have shown that there is a conserved overall structure to ParB proteins (**Figure 1.7A**). Firstly, ParB proteins have an extended central DNA-binding domain (DBD) and adopt one of two motifs to recognise cognate *parS* sequences (**Funnell, 2016; Schumacher et al., 2010**). Most ParB proteins have a HTH motif to bind *parS* sequences with high affinity (**Chen et al., 2015; Schumacher et al., 2010**). Plasmid P1 ParB has an additional DNA-binding ‘wing’ region that enables bridging of DNA molecules (**Schumacher et al., 2007**). Type Ib plasmids (TP228, pB171) on the other hand, have a ribbon-helix-helix (RHH) motif for *parS* recognition (**Pratto et al., 2008; Murayama et al., 2001**). Flexible linkers connect the core DBD to the NTD and CTDs. The CTD encompasses conserved leucine residues that interdigitise to act as a leucine zipper and effect dimerisation (**Kawalek et al.,**

2020). The CTD can also be used for nsDNA-binding, and for dimer-dimer interactions to bridge DNA molecules (**Schumacher et al., 2007; 2010; Fisher et al., 2017**). The NTD is used for interaction with ParA with two conserved lysine residues that mediate stimulation of ParA ATPase activity (**Scholefield et al., 2011**). The NTD it is also critical for the conserved property of 'spreading' on DNA adjacent to *parS* sites to form a condensed partition complex. There are two conserved motifs, boxes I and II, which are intrinsic to ParB-ParB interactions, and box II contains an arginine patch (GxRRxRA) to facilitate this (**Funnell, 2016**). The arginine patch is one of the most conserved elements in ParB sequences and has very recently been discovered to form contacts with the ribonucleotide CTP (**Funnell, 2016; Soh et al., 2019**).

Several mechanisms for ParB-*parS* complex assembly have been suggested. The initial indication for spreading in *cis* was the repression of genes adjacent to *parS* sites from the overexpression of F plasmid SopB, although this was only observed chromosomally for *P. aeruginosa* (**Lynch and Wang, 1995; Kawalek et al., 2018**). ParB foci, initially observed within the *ori*-distal region of *C. crescentus*, naturally implied spreading from *parS*, and they have now been seen for the chromosomes of many other species, as well as for plasmids (**Mohl and Gober, 1997; Jakimowicz et al., 2002; Bartosik et al., 2009; Li et al., 2015; Graham et al., 2014; Attaiech et al., 2015; Sanchez et al., 2015; and Debaugny et al., 2018**). The extent of ParB-spreading has been determined in a species-specific manner (including *V. cholerae*) using quantitative genome-wide surveys (ChIP-seq and ChIP-microarrays), whereby the permissive zone for ParB can be up to 50 kb from *parS* sites (**Breier et al., 2007; Baek et al., 2014; Minnen et al., 2011; Bohm et al., 2020; Tran et al., 2018; Lagage et al., 2016; Debaugny et al., 2018**).

It was suggested that spreading to this extent cannot occur from 1D spreading alone based on how much DNA is condensed for a given ParB dimer (**Graham et al., 2014**). Single molecule experiments with *B. subtilis* SpoOJ showed bridging of DNA in *trans* through ParB-ParB interactions, and suggested the recruitment of SMC complexes as a limited number of ParB molecules per *parS* site (~20) can spread over many kilobases (**Graham et al 2014**). A computational simulation proposed 1D and 3D interactions were required for a coherent partition complex (**Broedersz et al., 2014**). A 'nucleation and caging' model was then proposed based on a combination of biochemistry, ChIP-seq, super-resolution microscopy, and computational modeling for plasmid F SopB; the stochastic nature of self-assembling ParB proteins on nsDNA surrounding *parS* was said to give rise to a network of synergistic ParB-ParB and ParB-DNA interactions (**Figure 1.7D**) (**Sanchez et al., 2015**). This model also applies to chromosomes, as demonstrated for *V. cholerae*. ParB resides within ParB foci clusters much longer than outside of them. At the same time, ParB is highly dynamic and able

to interchange between opposing partition complexes. A high diffusion constant of ~1 $\mu m^2 s^{-1}$ within cells is key parameter for ParB self-assembly into clusters (**Debaugny et al., 2018**).

The hierarchical nature of ParB-*parS* assembly has been inferred from gel shift assays and single molecule experiments. Specific ParB-*parS* binding species have been observed in gel shift assays with ParB concentration increased relative to a fixed *parS* concentration. Further increasing ParB results in a nucleocomplex that is immobile, and represents a larger complex forming through nsDNA-binding (**Funnell, 1991; Murray et al., 2006; Taylor et al., 2015**). Flow-stretched nsDNA was demonstrated to slowly condense upon SpoOJ binding (**Graham et al., 2014**). Magnetic tweezer experiments, which measured the condensation force by ParB-DNA interactions, showed that *parS* and nsDNA facilitated condensation and that *parS* marginally increased the stretching force required to reverse complexes (**Taylor et al., 2015**). P1 ParB was shown to have a 10,000-fold higher affinity for *parS* than nsDNA, which suggests the complexes in the magnetic tweezer experiments are poorly defined and comprised of relatively weak protein-protein interactions (**Figure 1.7B**) (**Funnell, 2016; Taylor et al., 2015**).

1.5.3.1 ParB-DNA structures

Structural studies have given insight into the molecular mechanisms underlying the ParB networks. Full-length structures have been so far unobtainable since the flexible domain linkers confer instability (**Schumacher, 2012; Funnell, 2016**). Specific binding to *parS* via the HTH motif has been determined for P1, F, and RP4 plasmid ParB proteins, in addition to *Bs*SpoOJ, *Tt*SpoOJ, HpSpoOJ, and *Cc*ParB (**Schumacher et al., 2007; 2010; Leonard et al., 2004; Chen et al., 2015; Fisher et al., 2017; Jalal et al.,. 2020b**). ParB proteins have been shown dimerise in solution (**Jakimowicz et al., 2002; Sanchez et al., 2015**). Unusually, P1 ParB makes contacts with *parS* half-sites on different DNA molecules in an effective pairing event. It binds inverted repeat A- (7 bp) and B-box (6 bp) motifs within the full length 80 bp *parS* site (**Schumacher et al., 2007**). Specificity is conferred from arginine residues of recognition helices contacting a guanine in position 4 of the inverted repeat (G4). Most of the contacts with the HTH and the inverted repeats are via the phosphate backbone. Residues outside of the HTH (within the CTD wing motif) make anchoring contacts with nsDNA. P1 ParB is therefore a flexible dimer with four potential bridge sites. The high variability of *parS* sites for different plasmids means that there are different *parS* and nsDNA-binding modes. RP4 ParB, for example, utilises residues outside the HTH motif to make specific contacts with both halves of its 13 bp palindrome (**Khare et al., 2004**). Alternatively, selective residues of the F SopB HTH contact a 9 bp palindrome at various positions (**Schumacher et al., 2010**).

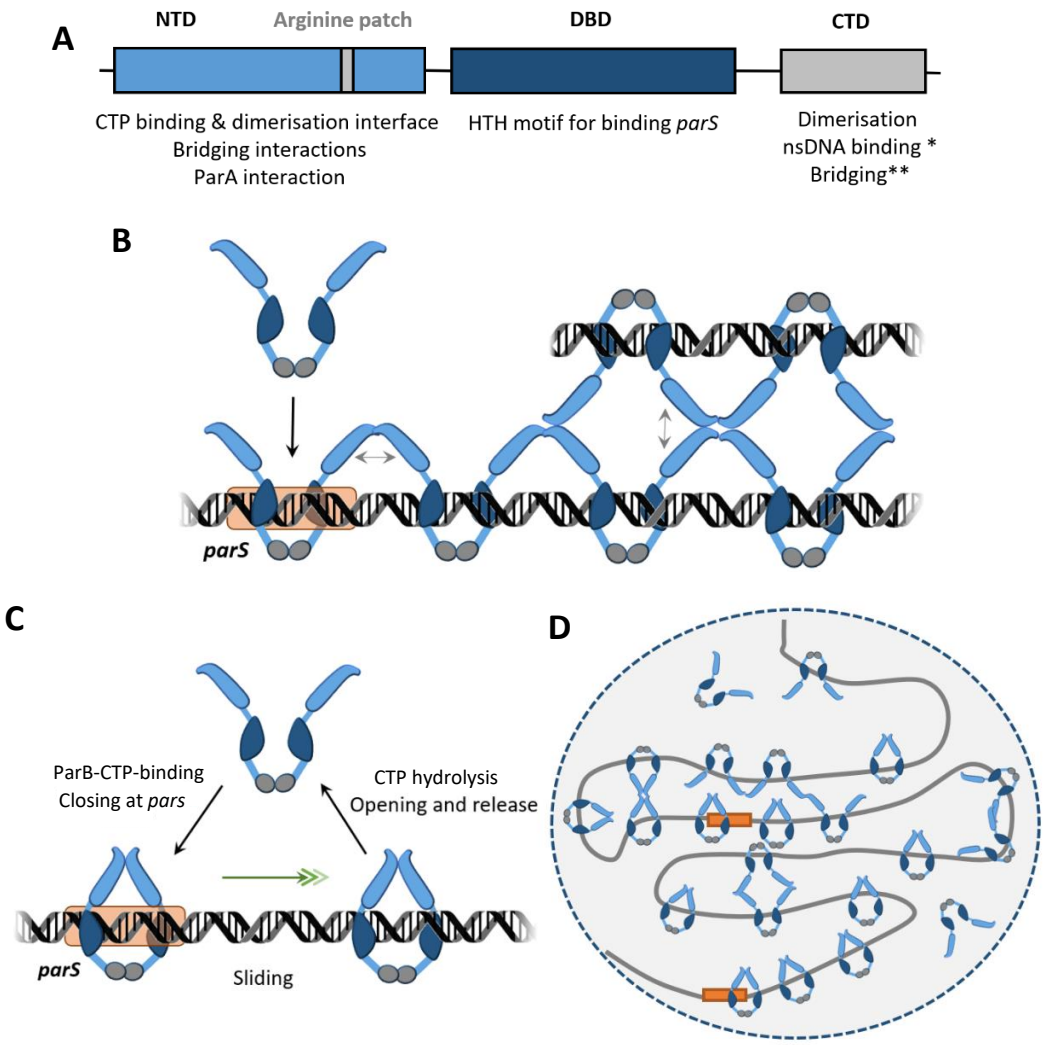

Figure 1.7. ParB structure and function. A) Conserved domains and motifs are depicted. Colours are representative of function with the multifunctional N-terminal domain (NTD) in blue, dark blue for DNA-binding domain (DBD) with a helix-turn helix (HTH), and grey dimerisation regions. The NTD is implicated in weak bridging interactions and ParA interaction. It also acts as a (second) dimerisation interface upon CTP-binding (grey arginine patch). The C-terminal domain (CTD) is involved in dimerisation, and for *Bs*SpoOJ, has been associated with nsDNA-binding (*) and bridging (**) (**Fisher et al., 2017**). **B)** ParB binding to *parS* via HTH-motif making species-specific contacts with *parS*; leads to 1D spreading and 3D bridging through weak NTD interactions. **C)** ParB-CTP loads onto *parS* with high efficiency. A closed conformation is attained such that the HTH motif disengages from parS and the sliding clamp allows more ParB-CTP to nucleate. **D)** Stochastic ParB activities lead to a dense partition complex on and around *parS* sites. Type Ia ParB proteins are typically larger (312-342 residues) than type Ibs (46-131 residues). Differences lie in a ribbon-helix-helix (RHH) in place of the HTH motif for a few plasmid ParB proteins, and longer CTDs for Type Ia ParB proteins. Adapted from **Song et al., 2017, Jalal et al., 2020a**, **Kawalek et al., 2020**.

Chromosomal ParB structures have shown more similarities in DNA-binding than those exhibited by plasmid ParB proteins, such that *Hp*SpoOJ is able to bind *Bs*SpoOJ *parS* sites (**Lee and Grossman, 2006**). Like plasmid ParB proteins, most contacts with the *parS* site are with the phosphate groups. Truncated DBDs (monomers) of *Cc*ParB showed the HTH-motif inserting into the major groove of *parS* and arginine and glycine residues contacting bases G1 and A6 of one half of the inverted repeat duplex (**Jalal et al., 2020b**). The study showed these positions confer specificity and a SlmA-like protein, Noc, was able to recognise different bases in the same positions (**Jalal et al., 2020b**). In addition, position 6 within primary chromosome *parS* sites (**Figure 1.6A**) correspond to differences between species. NsDNA-binding is also mediated by the HTH motif, as shown by F plasmid SopB substitutions affecting both *parS* and nsDNA-binding (**Ah-seng et al., 2009**). *Bs*SpoOJ CTD peptides have been uniquely shown to bind nsDNA upon dimerisation via a suite of lysine residues, with native mass spectrometry showing one 15 bp DNA fragment per dimer. (**Fisher et al., 2017**).

1.5.3.2 ParB-ParB bridging interactions

Whereas P1 ParB can bridge two 16 bp DNA duplexes as a single dimer, F SopB has a unique dimer-dimer interface in the CTD that is used between specific and nsDNA duplexes (**Schumacher et al., 2010**). The CTD of *Bs*SpoOJ has additionally been inferred to be a bridging interface where a solution NMR dimer SpoOJ structure formed DNA bridging interactions to condense DNA (**Fisher et al., 2017**). Free CTD exerted a dominant negative effect on ParB condensation activity that was later confirmed to be due to heterodimerisation of full length ParB with the free CTD (**Fisher et al., 2017; Madariaga-Marcos et al., 2019**).

The NTD has also been implicated in *trans* interactions between DNA-bound ParB proteins (**Figure 1.7B**). The NTD conserved arginine patch was deemed necessary for interactions in *cis*, as alanine screening of R79, R80, and R82 residues were spreading defective (**Graham et al., 2014**). Crystal structures of CTD-truncated *Hp*SpoOJ monomers were bound to separate inverted repeats of *parS* sites were solved to reveal that the flexible NTDs were exposed in an open conformation (**Chen et al., 2015**). Interactions between adjacent DNA-bound *Bs*SpoOJ proteins were defined via the arginine patch and also lead to a heterodimer complex of bridged ParB-DNA fragments (**Chen et al., 2015**). Although monomers were able to form transverse interactions, DNA condensation was dependent on the presence of the CTD dimerisation domain. As the CTD was missing, small angle X-ray scattering (SAXS) allowed a full-length model to be proposed (**Chen et al., 2015**). A follow up study showed asymmetry in the heterodimer interactions. A map of interacting residues was constructed from an alanine screening. The arginine patch was found to coordinate of an array of residues

involved in hydrogen-bonding and hydrophobic interactions responsible for ParB bridging (**Song et al., 2017**). *Tt*SpoOJ has a similar structure but the crystal structure adopted a closed conformation at the flexible NTD linker (**Leonard et al., 2004**). This implicated CTP-binding at the NTD interfaces in the network of *cis* and *trans* interactions.

1.5.3.3 ParB-CTP-binding

Chromosome and plasmid ParB proteins were recently discovered to bind and hydrolyse CTP (**Soh et al., 2019**). This came about from the observation that a functionally unrelated eukaryotic enzyme, sulfiredoxin (Srx), has an NTD arginine patch that constitutes an ATP-binding pocket. Biochemical assays confirmed that *Bs*SpoOJ bound CTP instead of ATP. The crystal structure of *Bs*SpoOJ with CDP was thus solved, with glycine and arginine residues of the conserved arginine patch (box II) contacting the β-phosphate group. Plasmids F and P1 ParB proteins were also confirmed to bind CTP in the same study, further illustrating the conserved feature (**Soh et al., 2019**). The crystal structure of a ParB-like protein from *M. xanthus*, PadC, was obtained with a CTP ligand. This protein acts to recruit inactive ParA molecules to the cell pole (**Osorio-Valeriano et al., 2019**). There were various contacts with the γ-phosphate of CTP in the arginine patch, but box I was determined to shape the main binding pocket conferring specificity for CTP (**Osorio-Valeriano et al., 2019**). There was a much higher affinity for CTP over CDP as determined for *Bs*SpoOJ, *Mx*ParB, and also for *Cc*ParB (**Soh et al., 2019; Osorio-Valeriano et al., 2019; Jalal et al., 2020a**). Indeed, CTPγS was used to show that cytidine triphosphate stabilises the *Mx*ParB CTP-binding pocket (**Osorio-Valeriano et al., 2019**). Cooperative CTP-binding was stimulated by the presence of cognate *parS*, while CTPase activity was stimulated up to 7-fold with *parS* at sub-stoichiometric amounts (**Soh et al., 2019; Osorio-Valeriano et al., 2019; Jalal et al., 2020a**).

Both crystal structures displayed a sandwich dimer interface akin to P-loop NTPases, where the active site of CTP-binding and hydrolysis is comprised of opposing monomer ParB proteins (**Soh et al., 2019; Osorio-Valeriano et al., 2019**). The *Bs*SpoOJ dimer structure showed that this leads to the formation of a second dimer interface (**Figure 1.7C**). Single molecule imaging and cross-linking assays showed key residues in the NTD dimer interface to contact upon binding *parS*, and it was said that gate closure is much slower in the absence of *parS*. ParB-CTP dimers were thus theorised to be in an open conformation until binding to *parS*. Superimposed *Bs*SpoOJ-CDP with *parS* suggested there would be steric hindrance of HTH motifs of opposing monomers in a closed conformation. This would cause release from *parS* and sliding, or spreading, to adjacent nsDNA (**Soh et al., 2019**). A reconstitution of ParB spreading in real-time was performed using *Cc*ParB-CTP where DNA substrate had to be

enclosed at either end to prevent a run-off (**Jalal et al., 2020a**). Furthermore, DNA-binding proteins were used as road-blocks to attenuate spreading and could represent NAPs *in vivo* restricting spreading beyond the Ori domain (**Soh et al., 2019; Osorio-Valeriano et al., 2019; Jalal et al., 2020a**). It has been suggested that sliding away from *parS* sites facilitates a high rate of ParB recruitment. This also corresponds to sub-stoichiometric amounts of *parS* stimulating ParB CTPase, since there is only a transient interaction before gate closure. In turn, gate closure forms the active CTPase site, thereby constituting a higher turnover of CTP in the closed conformation (**Soh et al., 2019; Osorio-Valeriano et al., 2019**).

CTP hydrolysis is slow and is most likely not responsible for spreading laterally from *parS* (**Soh et al., 2019**). This was corroborated by the fact that CTPγS promoted the closed conformation. On the other hand, CDP was not able to promote cross-linking of residues at the NTD dimer interface and suggest that it supports the open conformation. The *Bs*SpoOJ-CDP structure was prepared with CTP but was hydrolysed during crystallisation (**Soh et al., 2019**). This suggest that the closed conformation is at least stable even upon CTP hydrolysis and this could further promote spreading to adjacent nsDNA. Finally, CTP-binding affected PadC interactions with *Mx*ParA as CTP binding mutants caused aberrant subcellular ParA localisations. The interaction was monitored in real time by biolayer interferometric analysis, where CTP-bound PadC had a 3-fold higher binding intensity (**Osorio-Valeriano et al., 2019**).

The models for ParB spreading upon nucleating at *parS*, with and without CTP, have recapitulated *in vivo* observations of ParB. The finding that ParB proteins have CTP-binding and hydrolysis activities further demonstrates the underlying complexity for ParB-*parS* complex formation, as well as for the ParABS mechanism of action itself. These aspects are investigated with light-scattering assays in Chapter 3.

1.6 MODELS FOR THE TYPE I Par SYSTEM MECHANISM OF ACTION

1.6.1 The Brownian-ratchet model

Molecular ‘self-organisation’ gives rise to dynamic pattern formation from an initial homogenous mixture and functions to correctly distribute cellular content (**Ramm et al, 2019)**. This knowledge was derived from Alan Turing’s original reaction-diffusion theory of morphogenesis, which described how interactions between as few as two proteins, or reactants originally termed ‘morphogens’, within a relevant catalytic environment could give rise to the complex patterns observed in nature (**Turing, 1952**). The specific parameters for patterning depend on the system being studied. In eukaryotes, there are applications for developmental biology and the theory can also explain the formation of zebra stripes, for example (**Kondo & Miura, 2010; Wertheim & Roose, 2019**). However, many of these

systems are comprised of complex networks of reactants and therefore prokaryotes are more readily used for investigations. There are many parameters to explore in characterising the conditions required for pattern forming of minimal systems and as such, cell-free reconstitutions with TIRF microscopy facilitate this endeavour.

The minimal MinCDE system was the first to demonstrate 'Turing patterns' in cell-free reconstitutions, and the mechanism was used to derive the ParABS 'Brownian-reaction' model (**Lutkenhaus, 2007; Vecchiarelli et al., 2010**). There are three proteins in the MinCDE system that interact to control cell division (**Ramm et al., 2019**). The ATPase MinD has a low basal rate of ATP hydrolysis, much like ParA, except that it uses the inner membrane as the catalytic environment. A MinE ring chases the membrane-bound MinD, with the interaction stimulating MinD ATPase activity and MinD is released from the membrane. As MinD rebinds to the membrane ahead of the chasing MinE ring, a Turing pattern emerges. MinC is a passenger in the dynamics where it associates to MinD and functions to inhibit FtsZ formation. A new-born cell has a high average MinCD concentration across the cell but as the cell grows, the average concentration decreases from mid-cell such that an FtsZ ring forms (**Ramm et al., 2019**). ParABS systems are said to function similarly in that many ParAs oscillate from pole-to-pole, with the lowest concentration at mid-cell. As proposed in Chapter 3, this activity could give rise to mobile ParB-*parS* partition complexes relative to ¼ and ¾ cell positions.

A Brownian-ratchet mechanism was first proposed for Par systems from biochemical studies on P1 ParA, and cell-free reconstitution experiments were performed to further substantiate a cytoskeletal-free model (**Figure 1.8A**) (**Vecchiarelli et al., 2010; 2013; 2014a; and Hwang et al., 2013**). The model states that asymmetric ParA distributions on the nucleoid drive a directed motion of plasmid cargo. The first step in the Brownian-ratchet mechanism is ParA reaching the nsDNA-binding competent state and is accomplished by ATP-binding, dimerisation, and a slow conformational change (**Vecchiarelli et al., 2010**). ParA coats the outer surface of the nucleoid and there is an effective slowing of ParA subcellular diffusion relative to free-roaming ParA (**Vecchiarelli et al., 2014b**).

As a plasmid is replicated, ParB dimers load onto and around *parS* to form a dense partition complex (**Figure 1.8A**). This is enabled by *cis*-spreading along DNA from *parS*, and by *trans*-bridging interactions (**Graham et al., 2014, Taylor et al., 2015, Soh et al., 2019**). As such, plasmids can be translocated as solitary or paired DNA cargos due to ParB bridging activity. A segregating cargo unit is then tethered to the nucleoid itself by interacting with nucleoid-bound ParA. A nsDNA-ParA-ParB-*parS* complex has been demonstrated biochemically by gel shift and light-scattering assays (**Bouet and Funnell, 1999; Havey et al., 2012**).

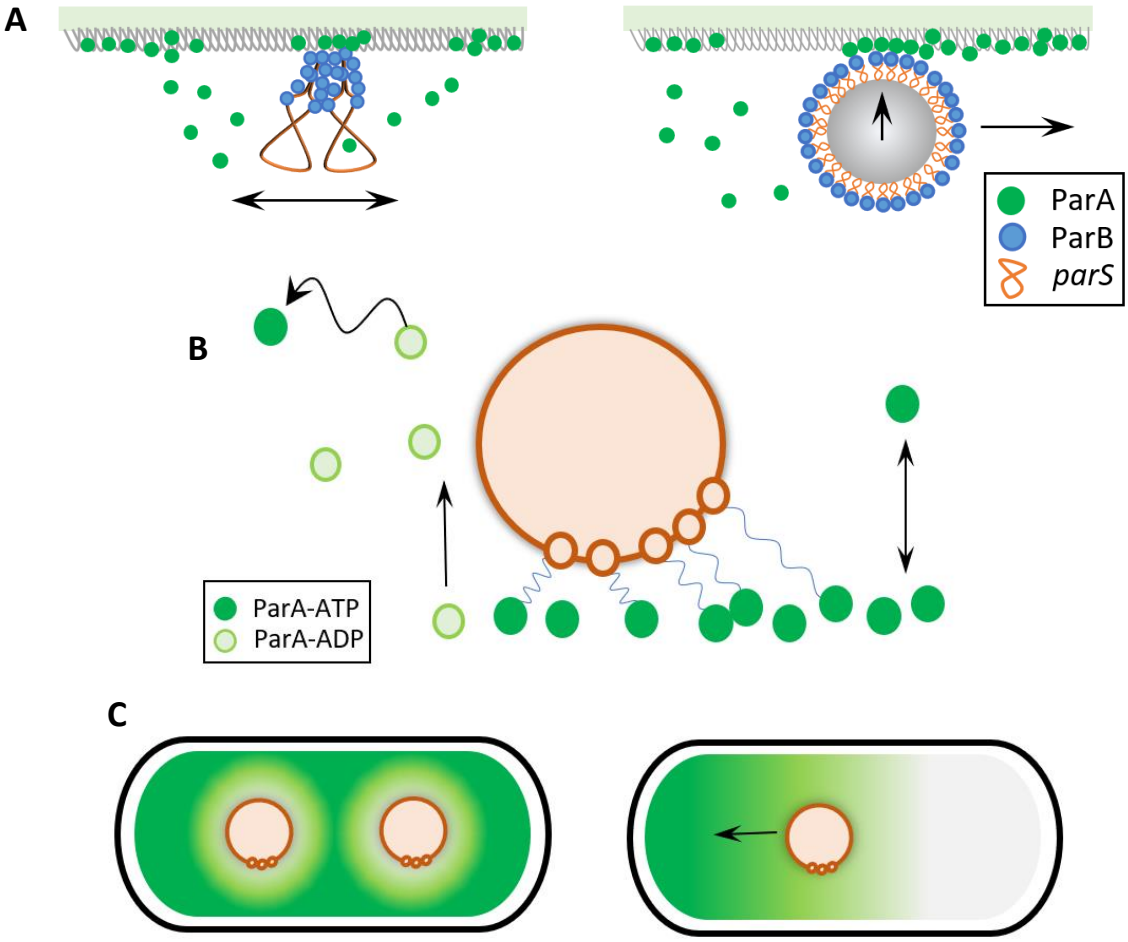

Figure 1.8. The Brownian-ratchet model for plasmid segregation. A) Cell-free, 2D reconstitutions of the P1 (left) and F (right) plasmid ParABS systems. Labelled plasmid and ParA were utilised to interrogate P1 ParABS interaction dynamics, whereas for the F plasmid, labelled proteins were used. A magnetic bead represented confinement in the cell between the nucleoid surface and the inner membrane for directed motion. **B)** Computer simulations introduced bond elasticity (blue zig-zags) as the predominant parameter for forward motion. A time delay for re-acquiring the active nsDNA-binding state is represented by the weaving arrow to ParA-ATP. **C)** Simulations show equi-positioning of two or more plasmid DNA cargo, as opposed to oscillating back and forth for a single plasmid. Figures adapted from **Brooks and Hwang, 2016; Vecchiarelli et al., 2014a; Jindal and Emberly, 2019**.

The interaction between ParA and ParB proteins initiates the break in ParA symmetry on the nucleoid, as a weak innate ParA ATPase activity is stimulated up to 13-fold (**Fung et al., 2001**). ParA-ADP dissociates from the nucleoid and diffuses away. This action is coupled with a time-delay to regain the nsDNA-binding conformation to cause the formation of a ParA depletion zone at the trailing edge of the partition complex (**Figure 1.8B**). Directed motion of the released partition complex then ensues as it interacts with another nucleoid-bound ParA at the leading edge (**Hwang et al., 2013; Vecchiarelli et al., 2014b**). Thus, uneven distributions of ParA on the nucleoid are initiated by the partition complex, which are in turn used by the partition complex for translocation as it moves up local ParA concentration gradients.

The 'diffusion' aspect of the model refers to the partition complex undergoing random Brownian diffusion from thermal fluctuations (**Peskin et al., 1993; Vecchiarelli et al., 2014b**). A critical feature is confinement of the partition complex upon being released from the nucleoid, such that it does not release into the cytoplasm but is held in the vicinity of the nucleoid surface in order to make contact for further transient ParA tethers. The confinement in this initial iteration of the Brownian-ratchet model was postulated to arise from the fact that the nucleoid takes up most of the subcellular volume, and consequently, there would be a small available space between the surface of the nucleoid and the inner membrane (**Hwang et al., 2013; Vecchiarelli et al., 2014a**). The released partition complex therefore diffuses in a restricted, two-dimensional local area. This was demonstrated in a reconstitution of the F plasmid ParABS system (**Figure 1.8A**). A two-dimensional biomimetic nucleoid was constructed in the form of a DNA carpet within a microfluidics device, and magnetic beads were coated with *parS*-DNA. Fluorescently tagged ParA and ParB coated the DNA carpet and the beads, respectively. ParA ATPase is stimulated via interaction with the partition complex and this was shown when the beads began to 'wiggle' through Brownian motion as they increasingly became less anchored to the DNA carpet. The beads were eventually released and, with spatial confinement via a magnet, demonstrated lateral directed movement representative of diverging plasmids between the membrane and the nucleoid (**Vecchiarelli et al., 2014a**).

The 'ratcheting' feature of the model is fundamentally dependent on the formation of a depletion zone at the trailing edge of the partition complex as it acts as an interval or boundary region. The diffusing partition complex ratchets up the highest local ParA concentrations even though it can diffuse in all directions. There are effectively more tethering bonds forming at the leading face than at the rear of the moving cargo. Type I Par systems thus utilise the energy of ATP to establish asymmetric ParA distributions on the nucleoid to rectify the random

diffusing motion of partition complexes towards directed motion (**Vecchiarelli et al., 2014a; Hu et al., 2017a**).

Coordinated motion of the P1 partition complex as a macromolecule in a ParA protein gradient was later computationally studied to authenticate that the chemical energy cycle of the ParABS system is directly coupled to useful (uni-directional) mechanical motion, in a principle designated as a chemophoresis force (**Figure 1.8B**) (**Sugawara and Kaneko, 2011; Hu et al., 2015; 2017a**). Rates were varied for the dissociation of the ParA-ParB protein tethering bond, and for ParA replenishment within the depletion zone. Each tethering bond is said to have an elasticity. Contrary to what was initially stated for this model, a low estimated diffusion constant was derived from the fact that the cytoplasm is a highly viscous environment (**Hu et al., 2015**). The momentum of the partition complex would thus drop immediately after being released at the trailing edge. As such, the elasticity of the chemical ParA-ParB proteins bonds being released would function as the predominant (transient) force to effect uni-directional motion (**Sugawara and Kaneko, 2011**; **Hu et al., 2017a**). The effects of altering rates of bond dissociation and ParA replenishment on partition complex positioning were comprehensively documented. Motility patterns fell under the following categories: completely diffusive, pole-to pole oscillations, minimal excursions and static (**Figure 1.8C**). Accordingly, there was a significant window of opportunity that supported pole-to-pole oscillations akin to those seen *in vivo* (**Hu et al., 2017a**). This was the case for a single partition complex or for two-partition complex motility.

The Brownian-ratchet model as described thus far has been defined by biochemical characterisations of Par components and the basis of the mechanistic model has been corroborated with cell-free reconstitutions. However, an all-encompassing operational mechanism responsible for the equi-positioning of plasmid cargo, and equally for the asymmetric translocation of some replicated primary chromosome *oris* via a gradual retracting ParA cloud, are still not clear. There are also significant distinctions between closely related Par systems. For example, it is still not understood why some plasmid ParA proteins exhibit pole-to-pole oscillations *in vivo* while others appear more stable. Alternate models and iterations of the Brownian-ratchet model have been proposed in attempts to address various unresolved aspects of the model.

1.6.2 Variations of the Brownian-ratchet model

1.6.2.1 The 'DNA-relay' model

Inherent chromosome dynamicity, or elasticity, was introduced as a new parameter in ParA-dependent translocation in a study on *C. crescentus* chromosome segregation (**Lim et al., 2014; Surovtsev et al., 2016a**). Biochemical characterisation, quantitative imaging, and computational modeling were utilised to determine that *in vivo* observations of segregation timings could not be explained by a ParA-ParB chemophoresis force alone. It was stipulated that although DNA-bound ParA-ATP dimers maintain an average subcellular position, they could actually be mobile. This activity would arise from the dynamicity of highly compacted and ordered DNA which could be exploited by Par systems to achieve active partitioning. Computational modeling of translocation properties with the additional parameter resulted in similar dynamics to those observed *in vivo* (**Lim et al., 2014**).

In this mechanism, ParA-ATP dimers fluctuate at apparent steady DNA loci. Upon encountering a partition complex, ParA-ATP is in a 'stretched' state. At the same time, the donor ParA at the trailing edge of the cargo undergoes ATP hydrolysis to release the partition complex. The elastic force 'relays' the partition complex from one ParA-ATP bound nucleoid region to another (**Figure 1.9A**) (**Lim et al., 2014**). Motion is directed by a preformed ParA-ATP concentration gradient and an apparently unique biochemical feature of *Cc*ParA is the requirement of a very high concentration of ParB (~five-fold higher than P1 ParA or SopA) to stimulate ParA ATPase activity beyond its low basal rate (**MacCready et al., 2018; Lim et al., 2014**). ATPase activity was believed to be optimal for a DNA-relay mechanism in *C. crescentus*, and would enable ParA-ATP dimers to be sequestered on the nucleoid at the opposite end of the cell to that of the ParB proteins complex; a spontaneous ParA-ATP gradient could thereby form with the concerted action of the HubP-like polar protein, PopZ (**Lim et al., 2014**). This proposed mechanism was said to be a key distinction to *B. subtilis* Soj, where there is a relatively premature stimulation of ATPase activity such that Soj largely dissociates to monomers. As an aside, it was postulated that this could explain why Soj oscillates *in vivo*. *Cc*ParA, on the other hand, has slow mobility on the nucleoid and is primed in a concentration gradient for ParB-*parS* complex translocation (**Lim et al., 2014; Surovtsev et al., 2016a**).

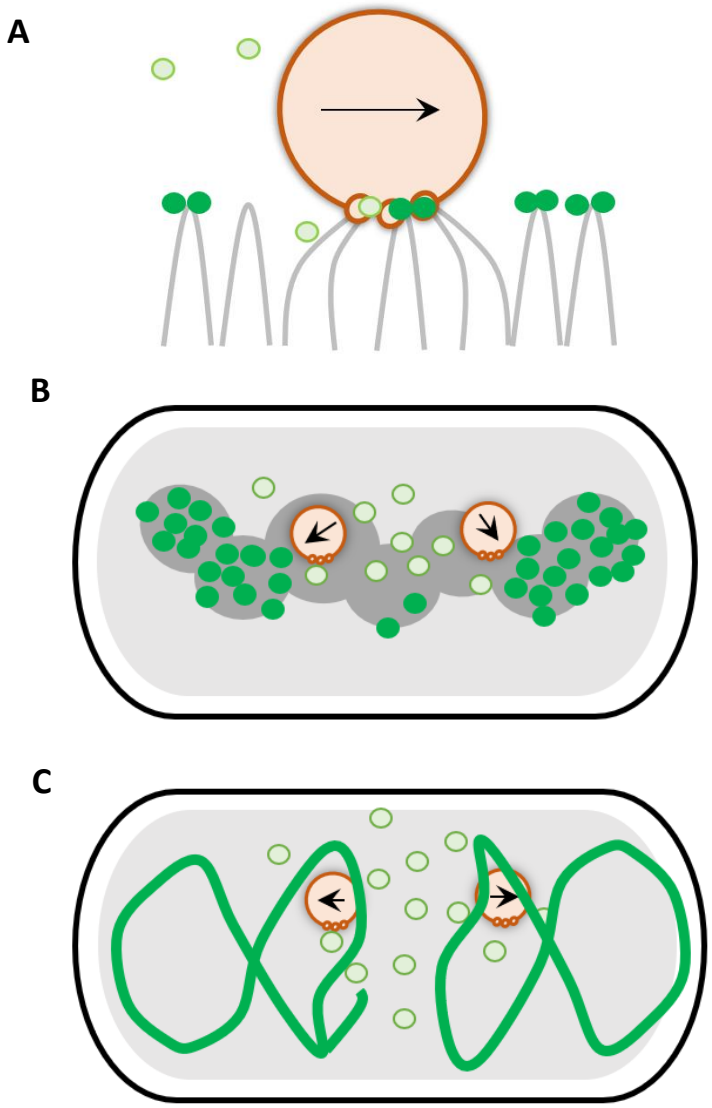

Figure 1.9. Variations and alternatives to the Brownian-ratchet model. A) DNA relay model as proposed for *C. crescentus* chromosome segregation. As in Figure 1.8, green circles represent ParA-ATP with active nsDNA-binding, whereas light green circles represent ParA-ADP. Grey loops depict the parameter of DNA elasticity with segments of the nucleoid that loop and 'relay' ParB-*parS* complexes to ParA-ATP tethers. For details, see text. **B)** Schematic of 'hitching-hiking' model after investigations of plasmid F and *B. subtilis* chromosome segregation. High density regions (HDRs) of the nucleoid are used by ParA-ATP for nsDNA-binding and in turn, the transport route of partition complexes across the cell is defined. The same biochemical basis applies between Par components for (**A**) and (**B**). **C)** The 'venus-fly trap' model. A TP228 ParF filaments (dark green) entrap partition complexes and translocates them to opposing cell poles. There are some similarities to the Brownian-ratchet model as the filament dissociates to ParF-ADP monomers (light green) upon stimulation of ParF ATPase activity by ParB. Adapted from **Lim et al., 2014, Le Gall et al., 2016, McLeod et al., 2017**.

The DNA-relay model was tested in a modeling study to account for differential spatial patterns of P1 ParA that lead to equi-positioning of DNA cargo (**Surovtsev et al., 2016b**). A DNA-relay mechanism was proposed without the constraints of a PopZ-mediated spontaneous ParA distribution, or a single retracting ParA-ATP cloud. The model resulted in ParA oscillatory behaviour and equi-positioning of cargos. When chromosomal fluctuations were not incorporated, the influence of ParABS could barely be deciphered. Crucially, the quantitative model for both the Brownian-ratchet and DNA-relay models are independent of changing chromosome topology through the cell-cycle and entropic demixing. A more comprehensive understanding of DNA segregation will be attained as these models are developed (**Lim et al., 2014; Hu et al., 2017b**).

1.6.2.2 The 'hitch-hiking' model

The third variation of the Brownian-ratchet model incorporates the volumetric distribution of Par components within the nucleoid as opposed to being constrained to the 2D outer surface of the nucleoid (**Figure 1.9B**) (**Le Gall et al., 2016**). The biochemical basis is based on the Brownian-diffusion chemophoresis model, as the stimulated ATPase activity of ParA weakens the tethers of the partition complex to the nucleoid. Super-resolution microscopy was used to determine localised ParA and segregating partition complexes. It was found that *E. coli* F plasmid and *B. subtilis* chromosome Par components located to within the nucleoid interior, and specifically to high-density chromosomal regions (HDRs), a feature described in earlier sections. Given that ParA proteins have been shown to bind DNA cooperatively, the model suggested a new mechanism by which Par components could become enriched at the HDRs for proper segregation. The partition complex cargo would be required to 'hitch-hike' on the high DNA-density regions of the nucleoid (**Le Gall et al., 2016**).

So far, this model has not been quantitatively analysed and hence it is unclear how the Brownian-ratchet model is affected by the 3D substrate. It can be immediately inferred that the confinement required for the Brownian-ratchet model to proceed is in fact provided by the interior of the nucleoid, although persistent and directed motion of the partition complex may rely on a more complex mechanism in a higher dimension. It could be that the nucleoid architecture plays a more integral role for Par components to reposition to HDRs (**Hu et al., 2017b**). A computational model of pB171 ParA demonstrated that dynamic ParA oscillations translated to a quite stable local ParA concentration difference across plasmids to bring about plasmid translocation, regardless of the exact mechanism of plasmid movement. It was determined that chromosomal architecture is used to constrain regions of DNA-associated ParA mini-filaments, which in turn supported directed motion. The model was stated to be a

robust mechanistic basis for self-organising DNA cargo positioning and unites previously contradicting models for plasmid segregation (**Ietswaart et al., 2014**).

1.6.3 The 'Venus-flytrap' as an alternative model

A completely novel mechanism was recently proposed for the multidrug resistant plasmid TP228, found in *Salmonella newport* and *E. coli*, which has a type I Par system (ParFGH) that unusually translocates duplicated plasmids to opposing poles (**Figure 1.9C**) (**McLeod et al., 2017**). The ParA analogue, ParF, is a well characterised dimer that can form a dimer-dimer structure in the presence of ATP as a base unit for polymerisation with multiple interfaces (**Schumacher et al., 2012; Zhang and Schumacher, 2017**). Intriguingly, *in vivo* plasmid stability studies showed that mutation to the polymerisation interfaces abrogated plasmid stability. Super-resolution microscopy was utilised to identify a three-dimensional ParF meshwork within the nucleoid of *E. coli* (**McLeod et al., 2017**). ParF was shown to dynamically relocate along the length of the nucleoid every 4-6 min. There was also synchronous tracking of the ParB proteins complex, ParGH, in the wake of ParF. As with Brownian-ratchet models, the ParGH complex stimulates ParF ATPase to drive ParF oscillations. While ParF has similar nsDNA-binding activities to other ParA proteins *in vitro*, the characterised self-sustaining filaments gave rise to the premise of a 'Venus flytrap' that ensures ParGH complexes are captured more efficiently than random encounters with single ParA tethers (**McLeod et al., 2017**).

A recently characterised feature of ParF is a residue change in the ATP-binding pocket to fine-tune ATPase activity (**Caccamo et al., 2020**). The interaction with ParG is also affected so that ATPase activity is stimulated less, and segregation is also inhibited. This could be a specific feature of ParF that enables self-sustaining filament formation *in vivo* to trap partition complexes and gradually translocate them to the poles (**Caccamo et al., 2020**). It is also worth noting that the observed filaments had a helical pitch and it was acknowledged that this could potentially correspond to the ellipsoid and helical HDR regions of the *E. coli* nucleoid, pending further investigations (**Fisher et al., 2013; McLeod et al., 2017**).

The pervasiveness of the type I system is a testament to the underlying mechanism being evolutionarily conserved and is an energetically favoured spatial regulator of protein clusters (**Murray and Sourjik, 2017**). This is corroborated by the fact that Brownian-ratchet mechanisms are attributed to other deviant Walker A motif ATPases, in MinD and McdA (carboxysome translocation), as well as to the Walker A ATPase, MukB (**Meinhaerdt and de Boer, 2001; MacCready et al., 2018; Hofmann et al., 2019**). There are consistent physical properties involving minimal systems that display dynamic patterns from self-organisation.

Computational models have shown that type I Par systems in general exhibit oscillatory dynamics that enable geometry sensing, or 'centre finding', which pertains to equi-positioning (or polar localisations in concert with polar proteins) of DNA cargos (**Surovtsev et al., 2016b; Murray and Sourjik, 2017; Hu et al., 2017a**).

The differences among the models described in this section relate to: how asymmetric ParA distributions are established and employed to drive cargo translocations; the basis of confinement; and apparent biochemical idiosyncrasies. While these point toward a high likelihood of evolution driving specificity for individual systems and species, it is also clear that there is a need for ongoing investigations. Some of the remaining questions from the models and computational analyses involve the different spatiotemporal patterns of ParA and ParB-associated cargos identified using super-resolution microscopy approaches. This will also aid in elucidating the role of nucleoid remodelling for plasmid and chromosome segregation. What is more, characterisation of species-specific Par components as well as interactions with other subcellular organisation systems are needed to finetune models with suitably distinct constraints (**Hu et al., 2017b**).

1.7 THESIS RATIONALE

Much of the research into type 1 partition systems has been carried out on *E. coli* plasmids due to the extensive knowledge on the species and the established experimental procedures. *V. cholerae* is an ideal candidate organism to study chromosomal segregation systems because it has a *parABS* locus on each of its two chromosomes and is closely related to *E. coli*. Furthermore, whilst the primary chromosome is classed as a type 1b system, the secondary chromosome is in fact classed as a type 1a system. This means that investigation of chromosome 2 (*Vc*Chr2) segregation could benefit from the prior research on plasmids.

As outlined above, the ParABS-mediated positioning of *Vc*Chr2 is indeed plasmid-like in that it is equi-positioned along the lateral axis of the cell. *Vc*ParABS2 functions in the absence of (known) interactions with other systems, such as SMC/condensin complexes or polar-tethering proteins. Corroborating this is the fact that ParA2 and *parS*2 deletions cause chromosome segregation defects with high chance of anucleate cells and subsequent cell death. Furthermore, Chr2 lateral positioning in parallel with Chr1 may interfere with entropic demixing properties. ParA2 pole-to-pole oscillations have been observed *in vivo* (**Fogel and Waldor, 2006**), and are somehow involved in Chr2 segregation. It is not clear how the Par component interactions differ from plasmid systems to accommodate a much larger DNA cargo or how its kinetics coordinate with the cell cycle.

The objective of this thesis was to characterise ParA2 ATPase and DNA-binding activities and the ParABS2 complex assembly, to elucidate the mechanism of action of Par complexes in *V. cholerae* Chr2 segregation.

Investigation of each step of the ParA2-ATPase cycle using various biochemical and biophysical techniques showed that ParA2 is similar to plasmid ParA proteins and very likely functions in a Brownian-ratchet like mechanism (**Chapter 2**). However, there are key differences in the rates of conformational change upon ATP-binding and DNA-binding. The cooperative binding of ParA2 to DNA and rates of nucleotide exchange have also been characterised for the first time for ParA proteins. These results indicate that ParA2 is inherently more dynamic on DNA compared to plasmid ParA proteins, and this could be exploited to drive the segregation of a chromosome.

Investigation of the assembly dynamics of the *Vc*Chr2 partition complex and ParA2 using light scattering assays showed that ParA2-DNA and ParB2-DNA-binding activities could be individually detected before a systematic examination of *Vc*ParABS2 assembly kinetics (**Chapter 3**). Several large ParABS2 complexes were characterised, and the introduction of CTP caused an oscillatory dynamics with *parS*2. Based on these results, a new model was proposed for the mechanism of CTP-mediated partition complex assembly in chromosome segregation.

A general discussion to summarise the results obtained from Chapters 2 and 3, and to state the importance to the field of bacterial chromosome segregation is provided in **Chapter 4**. To aid in this effort, supplementary data is presented in the **APPENDIX**. Finally, future experiments to further our understanding of the ParABS2 mechanism of action are outlined.

CHAPTER 2

A FAST ATPase CYCLE MEDIATES DYNAMIC ParA2 GRADIENT FORMATION ON DNA

A version of this chapter is being prepared for publication as:

Chodha, S.S., Brooks, A.C., Davis, P., Ramachandran, R., Chattoraj, D., Hwang, L-C. Kinetic Control of ParA2 Dynamic Patterning by ATP Cycling in *Vibrio cholerae* Chromosome 2 Segregation.

SEC-MALS experiments were performed in collaboration with Peter Davis (University of Sheffield). Peter Davis performed the SEC-MALS analyses and prepared the graphs (Figure 2.2). Alexandra Parker (University of Sheffield) performed ParA2 ATPase assays in the presence of CTP (Figure 2.1F).

2.1 INTRODUCTION

ParA proteins bind nsDNA that makes up the nucleoid, with different ParA patterning dynamics observed (**Castaing et al., 2008; Soberón et al, 2011; Chu et al., 2019**). Many chromosomal ParA proteins form a concentration gradient that retracts toward the new pole to effect chromosome segregation. Polar tethers are commonly recruited to facilitate asymmetric chromosome segregation, whereby the original chromosome origin is held at the old pole and the replicated chromosome origin is translocated to the new pole (**Yamaichi et al., 2012; Toro et al., 2008**). Alternatively, *V. cholerae* ParA2 was shown to oscillate from pole-to-pole several times in a cell-cycle, behaviour seen more typically for plasmid ParA proteins such as pB171 ParA, F SopA, and pSM19035 δ (**Fogel and Waldor, 2006; Quisel et al., 1999; Hatano et al., 2007; Pratto et al., 2008**). In the absence of polar proteins, partition complexes have relatively small excursions on the nucleoid, as the respective ParA dynamics bring about DNA cargo equi-positioning along the long axis.

Some ParA patterns were interpreted as filaments, or helical-bundles that undergo polymerising and depolymerising phases to drive proper localisation of the cognate partition complex. Plasmid pB171 oscillations were thought to be caused by ParA mini-filaments pushing replicated plasmids apart (**Ringgaard et al., 2009**). Plasmid P1 ParA showed a dense spot co-localising with the partition complex (**Hatano and Niki, 2010**). Another P1 ParA study investigated interactions with ATP and DNA and described how the nucleoid could act as a scaffold in the Brownian-ratchet Par mechanism and was said to account for ParA patterns on the nucleoid (**Vecchiarelli et al., 2010**). Specifically, ParA-ATP dimers bind the nucleoid and transiently tethers the ParB-*parS* partition complex. ParA ATP hydrolysis is stimulated by the partition complex itself and ParA loses DNA-binding activity. Key to the mechanism is the formation of a ParA depletion zone in the wake of the partition complex movement, as dissociated ParA resets in the time required to reach its DNA-binding state again. This has been suggested to be due to a slow conformation change but could feasibly be facilitated by any rate-limiting step in the DNA-binding process. The partition complex then tethers to an adjacent ParA-ATP on the nucleoid resulting in directed motion (**Vecchiarelli et al., 2010**).

The P1 and F plasmid Par systems were recapitulated in cell-free reconstitution and imaging experiments to show ParB-*parS* plasmids tethering to a DNA carpet (representing the nucleoid), causing ParA depletion zone formation and finally untethering from the carpet (**Hwang et al., 2013; Vecchiarelli et al., 2013**). Magnetic beads were then used to track motion along the carpet (**Vecchiarelli et al., 2014a**). No large, self-supporting filaments were detected in these experiments. Importantly, two plasmids with markedly different ParA nucleoid patterning were found to operate a similar partitioning mechanism. A super-resolution

imaging study also showed ParA occupied the entire nucleoid, and not just the surface, while observing no extended and self-supporting filaments. Moreover, the nucleoid was found to have high-density-regions (HDRs) that could account for the helical structures observed in early studies and interpreted as filaments or helical bundles (**Le Gall et al., 2016**). Modeling studies showed the Brownian-ratchet model can be tuned for ParA-replenishment rate, which affects depletion zone formation. DNA cargo trajectories evolved from diffusion, oscillations, local movement, and finally immobility (**Hu et al., 2015; 2017**). ParA polymerisations were not strictly precluded from the model as ParA proteins form filaments *in vitro*, albeit with higher than physiologically relevant ParA concentrations (**Ebersbach and Gerdes, 2006; Ringgaard et al., 2009**). *Vc*ParA2 can only form filaments on DNA and does so via an N-terminal helix-turn-helix domain, which is not present on other chromosomal ParA proteins. Moreover, different adenosine nucleotides result in distinct filaments, showing that ParA2 can adopt different conformations in the presence of DNA (**Hui et al., 2010**).

Chromosomes are much larger DNA cargo to manoeuvre than plasmids, whilst still using the nucleoid itself as a scaffold. Approximately 10% of bacteria have genomes on multiple chromosomes, of which *V. cholerae* is the foremost model for chromosome maintenance. The *V. cholerae* secondary chromosome (*Vc*Chr2) has a dedicated Par system classed closely with plasmids (**Espinosa et al., 2017)**. Chromosome Par systems must also adhere to cell-cycle timings and the exact Brownian-ratchet mechanism is therefore likely to vary between plasmid and chromosome Par systems.

To investigate how the distinct ParA2-DNA filaments might influence *Vc*Chr2 segregation, various kinetic analyses were performed to make direct comparisons to plasmid ParA proteins. ParA2 was found to exist as a dimer prior to nucleotide-binding, and to have a faster transition to the DNA-binding state compared to plasmid ParA proteins. ParA2 was confirmed to bind DNA with high affinity and cooperativity in the presence of ATP. ParA2-DNA-binding was shown without nucleotide, and in the presence of ADP, but these conditions resulted in low affinity interactions. Nucleotide exchange kinetics were also shown for the first time for a ParA protein. The new data support a Brownian-ratchet mechanism for *Vc*Chr2 segregation and a model for the ATPase cycle of ParA2 is presented, with key parameters that differ from plasmid ParA proteins highlighted.

2.2 EXPERIMENTAL PROCEDURES

2.2.1 Strains and plasmids

The strains and plasmids used and/or constructed during this work are detailed in the following tables:

Table 1. *E.coli* Strains and plasmids

E. coli	**Genotype**	**Supplier**
NEB 5-alpha	*fhuA2 Δ(argF-lacZ)U169 phoA glnV44 Φ80 Δ(lacZ)M15 gyrA96 recA1 relA1 endA1 thi-1 hsdR17*	New England Biolabs
BL21(DE3)	*fhuA2 [lon] ompT gal (λ DE3) [dcm] ΔhsdS λ DE3 = λ sBamHIo ΔEcoRI-B int::(lacI::PlacUV5::T7 gene1) i21 Δnin5*	New England Biolabs

Plasmid	**Description**	**Construction**
pBKSII	pBluescript KSII+	from Stratagene
*pUC57-*parA2-GFP*	pUC57 bearing *parA2-gfp*	from Genescript
pLCH02	pET15 b (+) bearing *parA2-gfp-his*	a) PCR amplification of *pUC57-parA2-gfp* with primers *parA2gfp*-W1 and *parA2gfp*-W2 b) Digestion of product with Nco1 and EcoR1 c) Ligation of fragment into pET15 b (+) cut with Nco1 and BamH1
pLCH04	pET15 b (+) bearing *parB2-his*	from Genescript
**pMBD02	pET28 b (+) bearing *his-parA2*	a) PCR amplification of pUC57-parA2-gfp with primers his-ParA2-fwd and his-ParA2-rev b) Digestion of product with Nde1 and BamH1 c) Ligation of fragment into pET28 b (+) cut with Nde1 and BamH1
pSC01	pET28 b (+) bearing *parA2*	a) PCR amplification of pMBD02 with LCH11-*parA2-gfp*-fwd and MBD02-*parA2-his*-rev b) Phosphorylation and ligation of product
**pLCH08	pBAD/His B bearing *parA2-gfp-his*	a) PCR amplification of *pUC57-parA2-gfp* with primers *parA2gfp*-W1 and *parA2gfp*-W2 b) Digestion of product with Nco1 and EcoR1 c) Ligation of fragment into pBAD/His B cut with Nco1 and EcoR1
***pLCH10	pBAD/His B bearing *parA2-gfp-his*	Insert KanR into pLCH08 at bla site (cut at Sca1)
***pLCH11	pBAD/His B bearing *parA2-K124R -gfp-his*	Site directed mutagenesis of pLCH10 with primers LCH19-*parA2(K124R)*-rev and LCH20-*parA2(K124R)*-fwd
***pLCH12	pBAD/His B bearing *parA2-K124Q-gfp-his*	Site directed mutagenesis of pLCH10 with primers LCH21-*parA2(K124Q)*-rev and LCH22-*parA2(K124Q)*-fwd
***pLCH13	pBAD/His B bearing *parA2-K124E-gfp-his*	Site directed mutagenesis of pLCH10 with primers LCH21-*parA2(K124E)*-rev and LCH22-*parA2(K124E)*-fwd

pRCT01	pBAD/His B bearing *parA2-K124Q*	a) PCR amplification of pLCH12 with LCH22-*parA2*-K124Q-fwd and RCT01-*parA2*-rev-EcoR1 b) Digestion of product with Nco1 and EcoR1 c) Ligation of fragment into pBAD/His B cut with Nco1 and EcoR1
pRCT02	pBAD/His B bearing *parA2-K124E*	a) PCR amplification of pLCH11 with LCH21-*parA2-K124E*-fwd and RCT01-*parA2*-rev-EcoR1 b) Digestion of product with Nco1 and EcoR1 c) Ligation of fragment into pBAD/His B cut with Nco1 and EcoR1
pRCT03	pBAD/His B bearing *parA2-K124R*	a) PCR amplification of pLCH11 with LCH20-*parA2-K124R*-fwd and RCT01-*parA2*-rev-EcoR1 b) Digestion of product with Nco1 and EcoR1 c) Ligation of fragment into pBAD/His B cut with Nco1 and EcoR1

NEB 5-alpha was used as host for cloning purposes. All plasmids were verified by DNA sequencing.

* Template for pLCH02, pSC01

** Template for pSC01

*** Templates for pRCT01, 2, 3

2.2.2 Oligonucleotides

Oligonucleotide primers used for construction of plasmids, and for amplifying DNA fragments used in experimental assays are listed in the Table 2.

Table 2. Oligonucleotides

Oligo	Sequence (5'-3')
his-parA2-fwd	CTAGCTAGCGCAATGAAACGTGAACAAAC
his-parA2-rev	GCGGATCCTTAGCCCTGATTCAGAGAG
LCH11-*parA2gfp*-fwd	ATACCATGGCAATGAAACG
MBD02-*parA2*-rev	GCGGATCCTTAGCCCTGATTCAGAGAG
parA2gfp-W1	TTTCACTGGCCGAACATACC
parA2gfp-W2	CCTGACCGTGAATGATTTCG
LCH19-*parA2(K124R*)-rev	CAGATGAACAGCCGTCATACTGCGGCCGGTACCGCCTTTTTGATT
LCH20-*parA2(K124R*)-fwd	AATCAAAAAGGCGGTACCGGCCGCAGTATGACGGCCTGTTCATCTG
LCH21-*parA2(K124Q*)-rev	ATGAACAGCCGTCATACTCTGGCCGGTACCGCCTTTTTG
LCH22-*parA2(K124Q*)-fwd	CAAAAAGGCGGTACCGGCCAGAGTATGACGGCTGTTCAT
LCH23-*parA2(K124E)*-rev	CAGCCGTCATACTTTCGCCGGTACCGCCT
LCH24-*parA2(K124E)*-fwd	AGGCGGTACCGGCGAAAGTATGACGGCTG
RCT01-*parA2*-EcoR1-rev	CTAGAATTCTTAGCCCTGATTCAGAGAG

Oligo	Sequence (5'-3')	Used for amplifying
M13-fwd-Cy5	Cy5-GTAAAACGACGGCCAGT	Cy5-labelled 144 bp nsDNA from pBKSII
KS-rev	CGAGGTCGACGGTATCG	

SK-fwd	GCTCTAGAACTAGTGGATCC	Cy3-labelled 62 bp nsDNA from pBKSII
KS-rev-Cy3	Cy3-CGAGGTCGACGGTATCG	

2.2.3 Buffers

Buffer A: 50 mM Tris-HCl pH 7.5, 100 mM NaCl, 10 mM $MgCl_2$, 10% glycerol, 100 mg/ml BSA, and 1 mM DTT. **Buffer B**: 50 mM Tris-HCl pH 7.5, 150 mM NaCl, 5 mM $MgCl_2$.

2.2.4 ParA2 protein expression and purification

Ten ml of LB medium with 50 µg/ml kanamycin (Kan) was inoculated with *E. coli* BL21(DE3) transformed with pSC01-*parA2* and grown overnight at 37 °C and shaking at 200 rpm. Culture was added to 2x500 ml fresh LB/Kan to an OD_{600} 0.55. Cultures were cooled to 25 °C and expression was induced with 1 mM isopropyl β-D-thiogalactoside (IPTG) for 2 h at 25 °C. Cells were harvested by centrifugation for 20 min at 4,000x*g* and stored at -80 °C. Cells obtained from a 1 L culture were defrosted and suspended in 10 ml per gram of pellet of 50 mM Tris-HCl pH 8.0, 0.1 M NaCl, along with ½ protease inhibitor tablet (Roche) and 1 mg/ml of lysozyme. Cells were placed on ice and disrupted by sonication using medium probe on a Soniprep 150 using 3 cycles of 20 s at 16-micron amplitude. Cell debris was removed by centrifugation at 72,000x*g* for 10 min and the supernatant fraction (cell-free extract, CFE) was used for purification. ParA2 purification was performed on an FPLC AKTA system (GE Healthcare). The CFE was applied on a 5 ml Heparin-HP cartridge (GE Healthcare) equilibrated in 50 mM Tris-HCl pH 8.0. Protein sample was eluted by a 50 ml gradient of 0--0.5 M NaCl in 50 mM Tris-HCl pH 8.0, and 2.5 ml fractions were collected. The main peak containing protein was eluted at 0.25 M NaCl and 3-4 peak fractions were combined for further purification by anion exchange chromatography and gel filtration. The protein sample was diluted 2.5-fold with water to 0.1 M NaCl and applied on a 6 ml Resource Q column (GE Healthcare) equilibrated with 50 mM Tris-HCl pH 8.0. Elution was performed at 6 ml/min with 60 ml 50 mM Tris-HCl pH 8.0 with a gradient of 0.1-0.7 M NaCl and 2.5 ml fractions collected. ParA2 was eluted at 0.35 M NaCl. Two peak fractions were combined and concentrated to 1 ml (Vivaspin 50,000 MWCO) and loaded on a 1.6x60 HiLoad Superdex 200 column equilibrated in 0.5 M NaCl 50mM Tris-HCl pH 8.0. Gel filtration was performed at 1.5 ml/min flow rate. Peak fractions were combined and concentrated. Before storage, 2 mM DTT, 0.1 mM EDTA and 10 % glycerol were added, and samples were held at -80 °C until further use. SDS-PAGE suggested the ParA2 was 98% pure. Protein sequence of ParA2 was confirmed with mass spectrometry.

2.2.5 ParA2-GFP purification

Ten ml of LB medium with 100 µg/ml ampicillin (Amp) was inoculated with *E. coli* BL21(DE3) transformed with pLCH02 and grown as in section 2.2.4. Culture was added to 2 x 500 ml fresh LB/Amp to an OD_{600} 0.5. Cultures were cooled to 16 °C and expression was induced with 1 mM isopropyl β-D-thiogalactoside (IPTG) overnight at 16 °C. Cells were harvested as described above for ParA2. CFE was applied to a 5 ml His-Trap HP column (GE Healthcare) equilibrated in 50 mM Tris-HCl pH 8.0, 0.1 M NaCl, with an AKTA purifier system with a flow rate of 5ml/min. Bound protein was eluted by a 50 ml gradient of imidazole from 0 to 0.5 M in 50 mM Tris-HCl pH 8.0, 0.1 M NaCl. Peak fractions were combined, and the volume of the protein sample was reduced to <2 ml (Vivaspin 50,000 MWCO). Sample was applied to 1.6 x 60 ml HiLoad Superdex 200 column equilibrated in 0.5 M NaCl 50mM Tris-HCl pH 8.0. Gel filtration was performed at 1.5 ml/min flow rate and 2 ml fractions were collected after void volume. Peak fractions were combined and concentrated (Vivaspin 50,000 MWCO). TEV protease (0.3 mg per 1 mg ParA2-GFP-His) was added in 50 mM Tris pH 8.0, 150 mM NaCl and left overnight at 16 °C. The sample was added to 25 mM Tris pH 8.0, 500 mM NaCl, 20 mM imidazole, 10% glycerol and 2 mM BME and loaded onto a 5 ml HisTrap column, eluting over a 12 CV 0.5 M imidazole gradient. The flow through was collected and reloaded onto the column to run once more. Protein was eluted with 25 mM Tris pH 8.0, 500 mM NaCl, 1 M imidazole, 10% glycerol and 2 mM BME. Peak fractions were collected, concentrated to <2 ml and buffer exchanged into 50 mM Tris pH 8.0, 500 mM NaCl, 10% glycerol, 2 mM DTT, and 0.1 mM EDTA using a VivaSpin column. The sample was then loaded onto a Superdex 200 16/600 and eluted over a 1.2 CV isocratic gradient. Peak fractions were pooled, concentrated, and stored at -80 °C.

2.2.6 ParA2 K124R/Q/E purification

Five ml of LB medium with 100 µg/ml ampicilin (Amp) was inoculated with *E. coli* BL21(DE3) transformed with pRCT01 or pRCT03, and grown as in section 2.2.4. This culture was added to 500 ml fresh LB/Amp to an OD_{600} 0.55. Cultures were cooled to 25 °C and expression was induced with 1 mM IPTG for 2 h at 25 °C. Cells were harvested by centrifugation for 20 min at 4,000x*g* and stored at -80 °C. For each mutant, a 0.5 L culture pellet was thawed, and re-suspended in 10 ml per gram of pellet in sonication buffer (50 mM Tris-HCl pH 8.0, 50 mM $(NH_4)_2SO_4$, 1 mM EDTA) along with ½ a protease inhibitor tablet (Roche) and 1 mg/ml of lysozyme. The cells were lysed by sonication for a total of 6 min at 30 s intervals at 12-micron amplitude and then centrifuged at 60,000x*g* at 4 °C for 25 min. Discarding the pellet, 0.35 g of ammonium sulphate was added per ml of supernatant before being centrifuged again at 60,000x*g* for 25 min at 4 °C. The supernatant was discarded, and the pellet was resuspended (in 10 ml) and left to dialyse overnight against 50 mM Tris-HCl pH

8.0, 100 mM NaCl, 10% glycerol, 0.1 mM EDTA, 2 mM DTT. The cell free extract was loaded onto a 5 ml HiTrap Heparin column and eluted against 50 mM Tris-HCl pH 8.0, 1 M NaCl, 10% glycerol, 0.1 mM EDTA, 2 mM DTT over a 12 CV gradient (0.1 M NaCl to 1 M NaCl); pooled fractions were then loaded onto a 1 ml Mono Q column and eluted against 50 mM Tris-HCl pH 8.0, 1 M NaCl, 10% glycerol, 0.1 mM EDTA, 2 mM DTT over a 20 CV gradient. Peak fractions were pooled and concentrated to <2 ml, before loading onto a Superdex 200 16/600 and eluted against 1.2 CV of storage buffer (30 mM Tris-HCl pH 7.5, 0.5M NaCl, 10% glycerol, 0.1 mM EDTA, 2 mM DTT). Peak fractions were pooled, concentrated, and stored at -80 °C.

2.2.7 ParB2 purification

Five ml of LB medium with 100 µg/ml ampicilin (Amp) was inoculated with *E. coli* BL21(DE3) transformed with pLCH04 and grown as in section 2.2.4. Culture was added to 500 ml fresh LB/Amp to an OD_{600} 0.55. Cultures were cooled to 25 °C and expression was induced with 1 mM IPTG for 4 h at 25 °C. Cells were harvested as described for ParA2, in section 2.2.4. CFE was applied on a 5 ml His-Trap HP column (GE Healthcare) equilibrated in 50 mM Tris-HCl pH 8.0, 0.1 M NaCl at flow rate 5ml/min. Bound protein was eluted by a 50 ml gradient of imidazole from 0 to 0.35 M in 50 mM Tris-HCl pH 8.0, 0.1 M NaCl. Peak fractions were combined, and the volume of the protein sample was reduced to <2 ml (Vivaspin 50,000 MWCO). Sample was applied to 1.6 x 60 ml HiLoad Superdex 200 column equilibrated in 0.5 M NaCl 50mM Tris-HCl pH 8.0. Gel filtration was performed at 1.5 ml/min flow rate and 2 ml fractions were collected after void volume. Peak fractions were combined and concentrated (Vivaspin 50,000 MWCO). The TEV-cleavage protocol for ParB2-His was performed as for ParA2-GFP-His in section 2.2.5. Protein was concentrated, and stored at -80 °C.

2.2.8 Size-Exclusion Chromatography-Multi Angle Light Scattering (SEC-MALS)

Samples of 40 µM ParA2 were incubated with or without 1.0 mM ATP or ADP, in 50 mM Tris-HCl pH 7.5, 210 mM NaCl, 5.0 mM $MgCl_2$, 0.1 mM EDTA, 1.0 mM DTT, 1.0 mM NaN_3, for 20 min at 37 °C. SEC-MALS of ParA2 was performed with 15 µl injections into a GE Superdex 200 10/300 GL SEC column at 0.75 ml/min equilibrated and run in 50 mM Tris-HCl pH 7.5 buffer (100 mM NaCl, 5.0 mM $MgCl_2$, 0.1 mM EDTA, 1.0 mM DTT, 1.0 mM NaN_3) using a Postnova AF2000 system with PN5300 autosampler. Protein elution was monitored with a Shimadzu Prominence SPD-20AV (PN3212) UV absorbance detector, PN3621b MALS detector and PN3150 Refractive Index Detector. Data analysis was conducted with NovaFFF AF2000 2.1.0.1 (Postnova Analytics, UK Ltd.) software and values plotted in Graphpad Prism 8.0.2. For protein concentration determination, a molar extinction coefficient at 280 nm of 1.03 M^{-1} cm^{-1} was used and absolute molecular weights were calculated using Zimm fits. Data was averaged in triplicate.

2.2.9 Electrophoretic mobility shift assays (EMSA)

A standard reaction mixture (20 µl) was prepared in Buffer A with 5 nM Cyanine 3-labeled 62 bp DNA and 2 mM of ATP, ADP, ATPγS or without nucleotide, with increasing concentrations of ParA2 as indicated. The reactions were assembled on ice, incubated for 30 min at 30 °C (unless stated otherwise) and analysed by gel electrophoresis in 5% polyacrylamide gels in TBM (90 mM Tris, 150 mM Borate, 10 mM $MgCl_2$). Gel electrophoresis was pre-run at 120 V for 30 min, at 4 °C, in a Mini-PROTEAN Tetra Cell, and then run at 120 V for 1 h, at 4 °C. Gels were imaged using a Bio-Rad ChemiDoc™ MP Imaging System using the Cy3 channel with 2 min exposure. Images were analysed with ImageJ (National Institute of Health, NIH).

2.2.10 Circular dichroism spectroscopy (CD)

CD experiments were performed in 10 mM Tris pH 8.0, 5 mM $MgCl_2$, which was filtered and degassed to prevent oxidation in the absence of DTT. Reaction mixtures were prepared by adding 5 µM ParA2 with 2 mM ATP, ADP, AMPPnP, ATPγS, or without nucleotide, to a final volume of 230 µl. An additional sample of ATP in the absence of $MgCl_2$ was prepared as above but in 10 mM Tris pH 8.0 , 2 mM EDTA. Each sample was filtered by centrifugation using a 0.2 µm Generon Proteus Clarification Mini Spin Column (GENMSF-500), at 14,000x*g* for 2 min. The 210 µl sample volume in the collection tube was incubated at 23 °C for 15 min. Spectra were measured using a Jasco J-810 Spectropolarimeter in a 1 mm Hellma Analytics QS High Precision Cell. Measurements were collected from 300 to 200 nm +/- 2.5 nm, in 1 nm intervals with an 8 s integration time. The spectrum of a buffer blank with or without 2 mM nucleotide was subtracted from the ParA2 spectrum with or without the corresponding nucleotide. Each spectrum recorded was an average of 3 scans and experiments were repeated at least twice. ParA2 secondary conformation was monitored by CD at 220 nm+/-2.5 nm with 8 s integration time, from 23 °C to 63 °C. The temperature was increased in 2 °C increments, with samples equilibrated for 1 min before measurement of the signal.

2.2.11 ATPase activity

For ATP hydrolysis time course measurements, 1.5 µM ParA2, 100 µM ATP and 64 nM [α-^{32}P]-ATP were incubated in Buffer A. Where indicated, 1.5 µM ParB2 and/or 0.1 mg/ml sonicated salmon sperm DNA were added. Reactions (10 µl) were assembled on ice, incubated for the indicated time periods at 37 °C and quenched by the addition of 10 µl 1% SDS, 20 mM EDTA. Single time point activity assays, indicated concentrations of ParA2 were incubated in reactions set up as described above, at 37 °C for 30 min. Aliquots (1 µl) from each sample was spotted onto a POLYGRAM CEL 300 PEI-TLC plate (Macherey-Nagel), and developed with 0.5 M LiCl (Sigma) in 1 M formic acid (Alfa Aeser). Dried plates were exposed

to a storage Phosphor screen and scanned with a phosphoimager (Typhoon FLA7000 IP) for quantification using ImageJ (NIH).

2.2.12 Nucleotide-binding, dissociation, and exchange assays

Stopped flow measurements with MANT (*N*-methylanthraniloyl)-labeled nucleotides (Jena) were performed at 23 °C using an Applied Photophysics SX20' system. The excitation monochromator wavelength was set to 356 nm±1.2 nm. The emission filter on the PMT was BLP01-405R-25 (Semrock). Nucleotide binding, dissociation, and exchange experiments were performed in Buffer B with 0.5 ml samples prepared on ice. For nucleotide binding assays, 0.6, 1.25, or 2.5 µM ParA2 was rapidly mixed with 25 µM MANT-AXP and fluorescence increase was monitored over time (integration time 0.1 s). For pseudo-first order reaction, 0.3125, 6.25, or 1.25, or 2.5 µM ParA2 was rapidly mixed with 3.125, 6.25, 12.5, or 25 µM MANT-AXP in buffer B and their fluorescence increase monitored. The observed binding curves were fitted with single exponential increase to determine observed rate of bindingk_{obs}. Using the equation $k_{obs} = k_{on}$. [MANT-AXP] + k_{off} (**Hulme and Trevethick, 2010**), plots of k_{obs} *vs.* substrate concentration yielded k_{on} and k_{off} from the slopes and y-intercepts, respectively. For nucleotide dissociation assay, 2.5 µM ParA2 and 5 µM MANT-AXP were pre-incubated at 23 °C for 3 min, then rapidly mixed with 1 mM unlabelled AXP and their fluorescence decrease monitored. For nucleotide exchange assay, 0.625, 1.25, or 2.5 µM ParA2 was preincubated at a 1:5 ratio with 3.125, 6.25, or 12.5 µM unlabelled AXP, respectively, then rapidly mixed with 15.625, 31.25, or 62.5 µM MANT-AXP at 5x higher concentrations than AXP. All data were means of at least two experiments. Values were reported as relative fluorescence increase or decrease.

2.2.13 Tryptophan fluorescence spectroscopy

For equilibrium binding assays, 0.6 µM ParA2 with 1 mM ATP, ADP or ATPγS were incubated at 23 °C for 15 min in Buffer B. In the absence of $MgCl_2$, a separate buffer was prepared with 0.1 mM EDTA and without $MgCl_2$. Tryptophan fluorescence was measured using a 'SpectraACQ' spectrafluorimeter set at 356 nm±1.2 nm in a 'HellmaAnalytics High Precision Cell'. FluorEssence V3.5' software was used for plotting data and GraphPad Prism for data analysis. Stopped-flow measurements were performed at 23 °C using an 'Applied Photophysics SX20' system. The excitation monochromator was set to 295 nm. The emission filter on the PMT was BLP01-325R-25 (Semrock). For kinetics experiment, 1.2 µM ParA2 was rapidly mixed with 2 mM MANT-AXP in buffer B and when present, 0.2 mg/ml DNA and 1.2 µM ParB2. Final concentrations after mixing were half of initial concentrations. All results are means of at least two experiments. Values were reported as relative fluorescence increase or decrease.

2.3 RESULTS

2.3.1 ParA2 ATP hydrolysis rate is potentially faster than plasmidal ParA proteins

The first step in characterising ParA2 was to confirm and quantify ATPase activity and this was achieved using thin layer chromatography with ATP spiked with [α-^{32}P]-ATP. 1.5 µM ParA2 was found to be a suitable concentration to compare the rate of ATP hydrolysis for the different reaction conditions within the designated time-period. ParA2 alone was shown to be a weak ATPase, with low levels of hydrolysis product detected but consistently above background level (**Figure 2.1A**). Sonicated salmon sperm DNA (sssDNA) (0.1 mg/ml), and ParB2 (1.5 µM), stimulated basal ParA2 ATPase activity by over 2-fold and 3-fold, respectively. There was a greater-than-additive effect for when ParB2 and sssDNA were both present, with activity stimulated at least 8-fold (**Figure 2.1A**). The effect of varying ParA2 concentration relative to fixed ParB2 and DNA can be seen in **Figure 2.1B**. The rate of hydrolysis remained linear over 30 min because the ATP was not used up under the conditions tested. Specific ATPase activity showed the stimulation of ATP hydrolysis did not change across the range of ParA2 concentrations in the presence of DNA (**Figure 2.1C**). It can be seen that the specific ParA2 ATPase activity is comparably higher than that of plasmid ParA proteins, both with and without DNA (**Figure 2.1D**). The plasmidal data was obtained from a separate study but the comparison potentially shows a slightly faster ATPase rate for ParA2. Specific ATPase activity also indicated that there was a pronounced difference in stimulated ATPase activity at sub-stoichiometric concentrations of ParA2 when in the presence of ParB2 where there was over a 10-fold stimulation at 0.5 µM ParA2:1.5 µM ParB2 (**Figure 2.1E**). This figure also shows that the stoichiometric effect was amplified when DNA was also present, with over a 20-fold stimulation at ParA2 concentrations below 1 µM.

The effect of *parS2* did not appear to have significant effect on ParA2 ATPase activity, as shown when pBKSII-*parS2* was used in place of sssDNA (**Figures 10A, 10F**). This finding could be due to high ParB2 availability in the assay. The effect of CTP was also considered as it was shown that ParB-CTP can load onto *parS*-DNA with high efficiency (**Soh et al., 2019; Jalal et al., 2020a**). CTP could play a role in the ParA2-ParB2 interaction, and stimulation of ParA ATPase activity (**Osorio-Valeriano et al., 2019**). There was, however, no discernible stimulation of ParA2 ATPase stimulation beyond what was observed with ParB2 and pBKSII-*parS2* (**Figure 2.1F**).

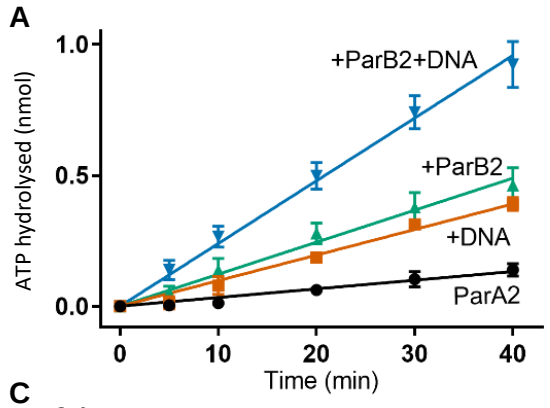

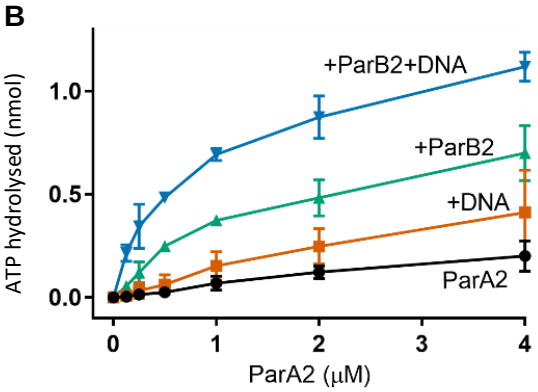

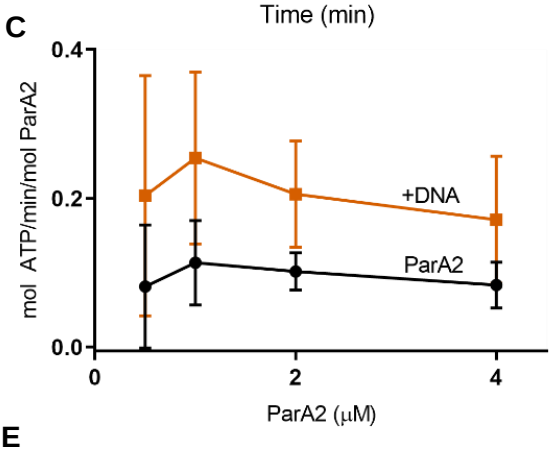

D

Specific activity (mol ATP/min/mol ParA)

	Alone	+ DNA
ParA2	0.1 ± 0.01	0.2 ± 0.03
SopA-His	0.06 ± 0.01	0.09 ± 0.02
P1 ParA	0.05 ± 0.01	0.09 ± 0.01

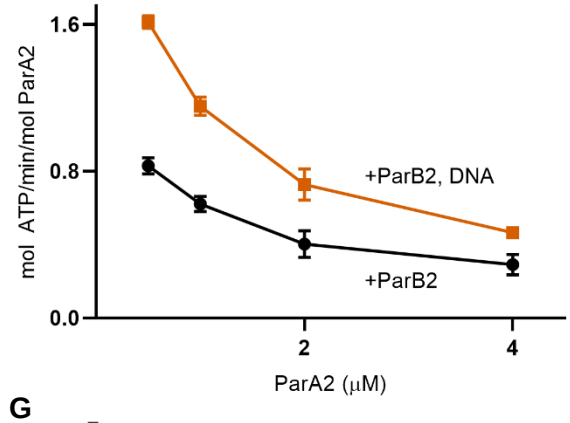

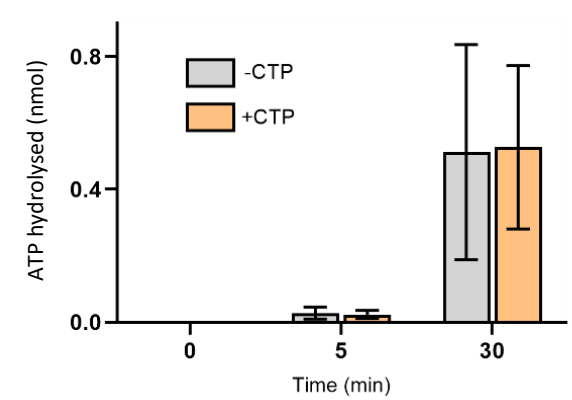

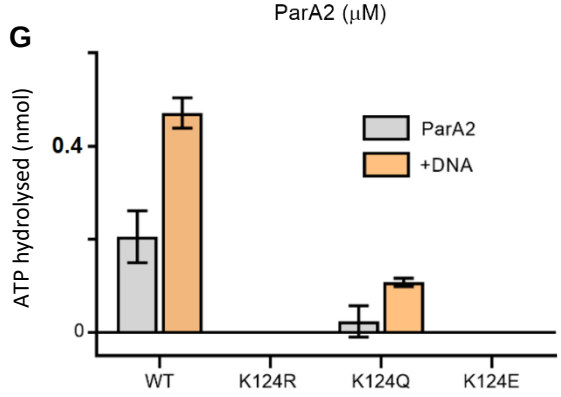

Figure 2.1. ATPase activity of ParA2. A) ParA2 ATP hydrolysis time courses. 1.5 µM ParA2 was mixed in buffer A with 200 µM ATP spiked with 64 nM [α-^{32}P]-ATP. 1.5 µM ParB2 and 100 µg ml^{-1} sonicated salmon sperm DNA were added as indicated. The hydrolysis product was measured after the indicated reaction time at 23 °C. **B)** Stoichiometric effects on ParA2 ATP hydrolysis**.** As in (**A**), except with indicated concentrations of ParA2 and hydrolysis product measured after 30 min. **C)** Specific ATPase activity of ParA2 with and without sssDNA (this study). **D)** Relative specific ATPase activity of ParA2 compared to the F SopA and P1 ParA proteins, with and without DNA (**MacCready et al., 2018**). ParA2 shows potentially higher specific ATPase activity and is stimulated more by the presence of DNA. **E)** As in **(C)** but with ParB2, and with both ParB2 and DNA **F)** Single time-point ParA2 ATP hydrolysis measurements in the presence of 1.5 µM ParB2 and 20 ng/µl pBKSII-*parS2*. With and without CTP conditions were tested, all other components as in (**A**). Experiment performed by Alexandra Parker (University of Sheffield). **G)** ATP hydrolysis measurements of ParA2 K124 mutants after 40 min incubations, with component concentrations as in (**A**).

Three ParA2 mutants were constructed by substituting the conserved lysine residue in the Walker-A box for glutamine (K124Q, uncharged side chain), glutamic acid (K124E, negatively charged side chain), and arginine (K124R, positively charged side chain). These mutagenesis products were expected to underscore the importance of the conserved lysine in ParA2 interactions with adenine nucleotides as well as ATP hydrolysis activity, and therefore overall ParA2 functionality. Indeed, all mutants showed distinct defects in ATP hydrolysis (**Figure 2.1G**). ParA2 K124Q retained some ATPase activity and the relative stimulation in the presence of DNA was much more pronounced compared to native ParA2 (**Figure 2.1G**). The K124R and K124E mutants displayed no ATPase activity and no stimulation was detected with DNA. These mutants were used in subsequent functional experiments.

2.3.2 ParA2 forms a dimer prior to interacting with ATP

It was next necessary to characterise the oligomeric state of ParA2 in the presence of different adenosine nucleotides prior to interacting with ATP. SEC-MALS showed that ParA (45 kDa) was already a majority dimer in the absence of nucleotide, with a calculated eluted protein molecular weight of 91.1 ± 0.27 kDa (**Figure 2.2**). There was no significant deviation from the majority dimer fraction in the presence of ADP (86.2 ± 0.36 kDa) or ATP (86.1 ± 0.35 kDa). Crucially, there was no sign that ParA2 oligomerises to form self-sustaining filaments, as has been seen for many plasmid ParA proteins.

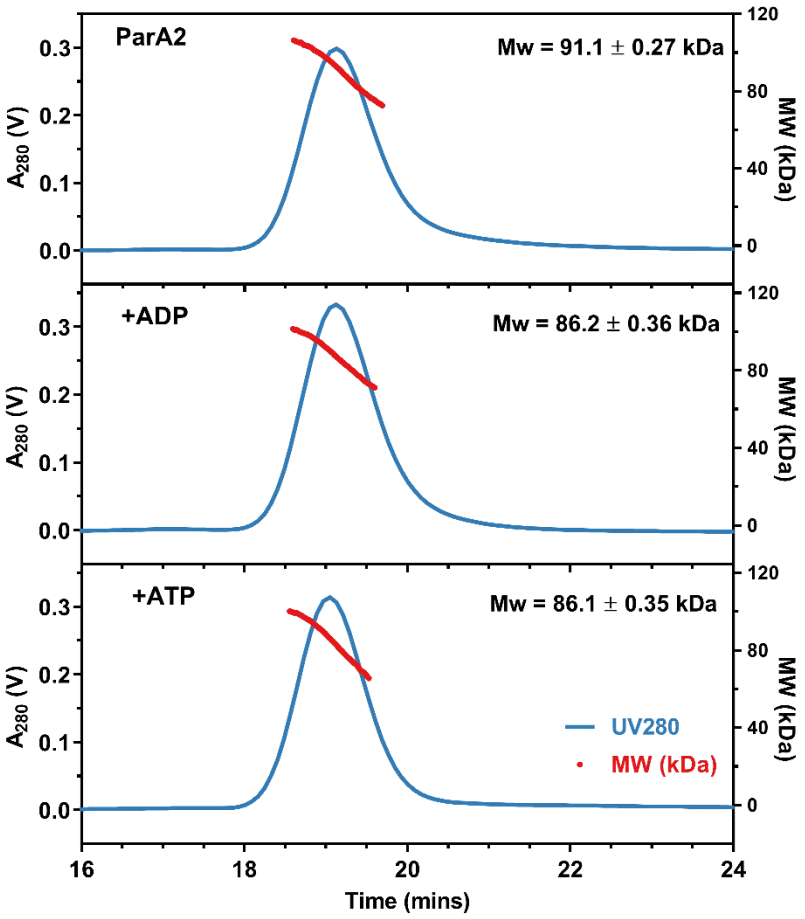

Figure 2.2. ParA2 dimerisation under different adenosine nucleotide conditions. SEC-MALS profiles of ParA2 in absence of nucleotide (top), in the presence of ADP (middle), and ATP (bottom). 40 µM ParA2 was pre-incubated with 2 mM nucleotide for 15 min, when present. Running buffer contained 0.5 mM nucleotide. Experiments performed in collaboration with Peter Davis (University of Sheffield). Analyses and graphs prepared by Peter Davis.

2.3.3 ParA2 binds nucleotide in multiple steps

In order to find the rate-limiting steps in the ParA2 ATPase cycle that would contribute to its dynamic subcellular behaviour (**Fogel and Waldor, 2006**), ParA2 interactions with adenine nucleotides were next investigated. Fluorescent adenosine nucleotide analogues, 2′(3′)-O-*N*′-methylaniloyl-aminoade-nosine-5′-triphosphate (MANT-ATP), and 2′(3′)-O-*N*′-methylaniloyl-aminoadenosine-5′-diphosphate (MANT-ADP), were used to monitor ParA2-nucleotide interactions. An equilibrium binding assay was first performed, with ParA2 at 5 µM and increasing MANT-nucleotide concentrations (**Figure 2.3A**), to show that ParA2 has very similar affinities for MANT-ATP (K_D = 11.83 µM) and MANT-ADP (K_D = 11.04 µM). The value was relatively close to that obtained with [α^{32}P]-ATP (22 µM) (**Hui et al., 2010**), and was also in the same order of magnitude to the noted K_Ds for P1 ParA (30 µM), SopA (74 µM), TP228 ParF (100 µM), and the chromosomal *C. crescentus* ParA (50–60 µM) (**Davey and Funnell, 1997; Bouet et al., 2007; Barilla et al., 2005; Easter and Gober, 2002**)., Walker A box mutants exhibited some MANT-ATP-binding activities. Single time-point measurements showed that K124R could bind MANT-ATP while K124Q, however, showed some quenching of signal which is suggestive of an interaction with MANT-ATP (**Figure 2.3B**). K124E did not cause any significant MANT-ATP fluorescence change. However, it was not clear if the signal change was a result of the mutations themselves or MANT-nucleotide binding.

The adenosine nucleotide-binding kinetics of ParA2 were then investigated using stopped-flow fluorometry. The extent of MANT-AXP-binding increased with higher ParA2 concentrations (0.6-2.5 µM) (**Figures 2.3C** and **2.3D**). The rates were consistent across the concentration range tested, demonstrating the reaction was not pseudo-first order (**Table 3**). ParA2-MANT-AXP binding kinetics took around 30 s to reach equilibrium. As for plasmid P1 ParA, this is slower than would be expected for simple nucleotide docking (**Vecchiarelli et al., 2010**). ParA2 is a dimer prior to ATP-binding and so the multiphasic timescale for binding MANT-AXP is suggestive of a slow conformational change, as examined in the next section. MANT-AXP was next varied to derive kinetic plots of the pseudo-first order ParA2 binding kinetics to MANT-ATP and MANT-ADP (**Figures 2.3E** and **2.3F**), where the observed rate constant (k_{obs}) was plotted against concentrations of MANT-nucleotides for ParA2. The k_{obs} increased linearly as the concentration of MANT-nucleotide increased. The fixed dissociation rate constant (k_{off}) was extrapolated from k_{obs} at the origins and the second-order rate constant, k_{on}, was determined from the slopes. The calculated K_Ds (=k_{off}/k_{on}) were 8.73 µM (MANT-ATP) and 8.2 µM (MANT-ADP). These were very similar to those obtained from the saturation binding assay (**Figure 2.3A**) and once again similar between the MANT-nucleotide conditions. The k_{off} for MANT-ADP (0.0365 s^{-1}) was higher than for MANT-ATP showing that ParA2 was more tightly bound to MANT-ATP (**Figures 2.3E**, **F**).

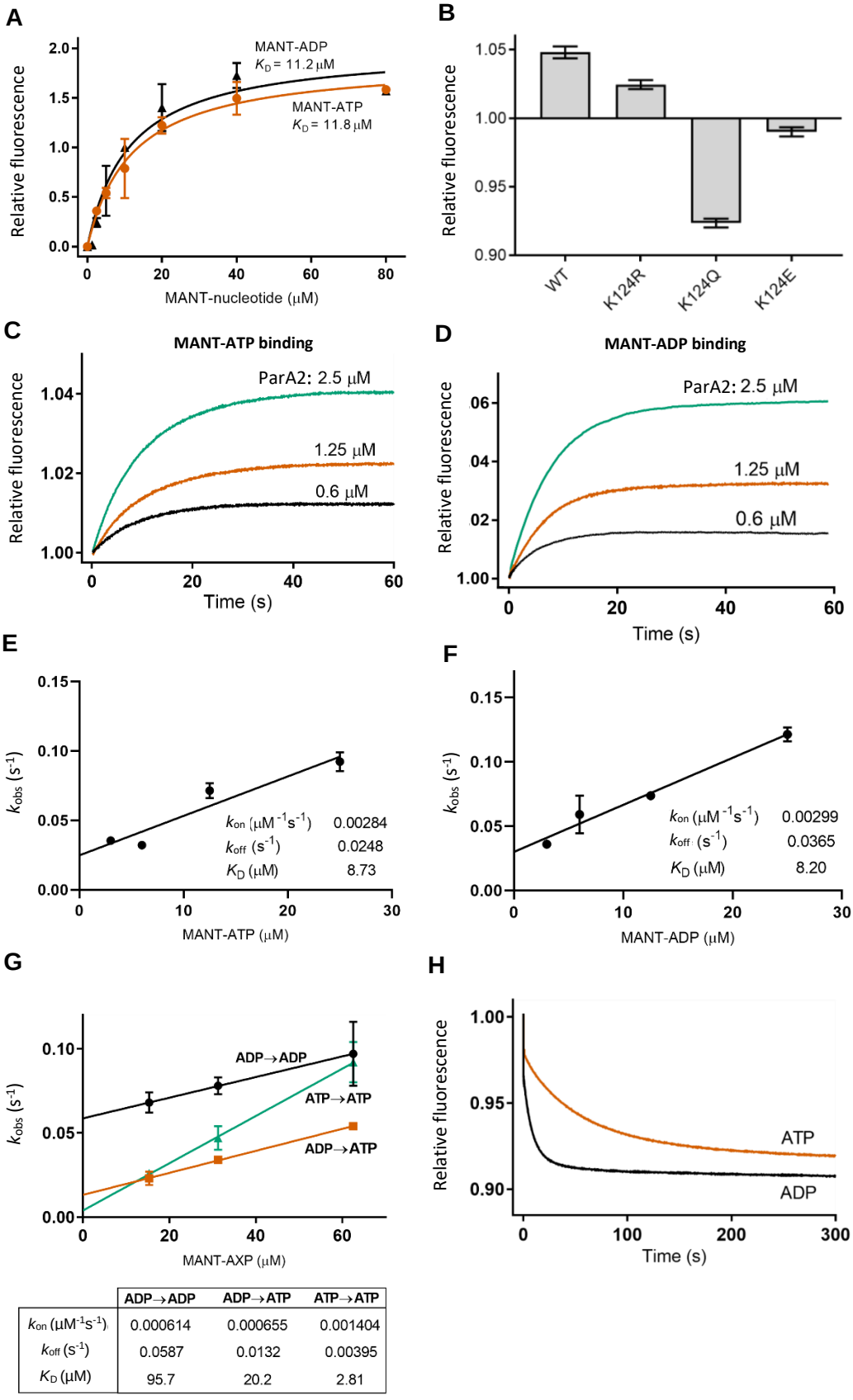

	ADP→ADP	ADP→ATP	ATP→ATP
k_{on} ($\mu M^{-1}s^{-1}$)	0.000614	0.000655	0.001404
k_{off} (s^{-1})	0.0587	0.0132	0.00395
K_D (μM)	95.7	20.2	2.81

Figure 2.3. Interaction of ParA2 and Walker box K124 variants with adenosine nucleotides. A) Equilibrium binding curves of ParA2 and MANT-AXP. 1.5 µM ParA2 was prepared with indicated concentrations of MANT-ATP or MANT-ADP in Buffer B (see section 2.2.3) on ice. An initial fluorescence measurement was taken for each sample before incubating at 37 °C for 20 min. The fluorescence change was then measured for each sample. Readings were acquired using a Fluorolog®-3 spectrofluorometer (Horiba Scientific) and a 'SpectraACQ' controller set at 356 nm ± 1.2 nm, in a 'HellmaAnalytics High Precision Cell'. Experiments were repeated twice. The relative fluorescence change (AU) was fitted in GraphPad Prism 8, with a saturation, one-site specific binding equation, to derive K_D. **B)** Fluorescence changes at saturating concentrations of MANT-ATP binding (for WT) to ParA2 K124 mutants. Experiment set up as in (**A**). A measurement was taken upon addition of all components and then after 2 min for each sample. **C)** ParA2-MANT-ATP-binding kinetics. ParA2 at indicated concentrations and 25 µM MANT-ATP were prepared separately in Buffer B (see section 2.2.3). Stopped-flow fluorescence spectroscopy was used to mix rapidly and monitor the change in relative MANT fluorescence. **D)** ParA2-MANT-ADP binding kinetics. As in (**A**), except with MANT-ADP. **E)** Plot of pseudo-first order rate constant k_{obs} against MANT-ATP concentration. Samples were prepared as in (**A**), except MANT-ATP was 10x higher concentration than ParA2. **F)** Plot of pseudo-first order rate constant k_{obs} against MANT-ADP concentration. Samples were prepared as in (**C**), except MANT-ADP was 10x higher concentration than ParA2. **G)** ParA2-AXP exchange kinetics plot. k_{obs} plotted against MANT-AXP concentration. ParA2 and AXP were prepared at the indicated concentrations, in a 1:5 ratio, while MANT-AXP was prepared separately and at a 5x higher concentration than AXP. **H)** ParA2-MANT-AXP dissociation kinetics. ParA2, at indicated concentrations, was prepared with MANT-AXP in a 1:2 ratio, while 1 mM AXP was prepared separately**.** ParA2 and MANT-AXP were pre-incubated at 23 °C for 3 min, then rapidly mixed with AXP. Dissociation kinetics were subsequently measured as a decrease in relative MANT fluorescence.

Table 3. Rates of ParA2 interactions in the presence of MANT-AXP

[ParA2]	0.6 μM	1.25 μM	2.5 μM
ATP association			
k **(s^{-1})**	0.132 ± 0.031	0.093 ± 0.013	0.093 ± 0.005
τ (s)	7.8 ± 1.8	11.7 ± 0.8	10.7 ± 0.6
ATP dissociation			
k **(s^{-1})**	0.019 ± 0.001	0.019 ± 0.003	0.015 ± 0.002
τ (s)	51.0 ± 2.3	52.4 ± 0.9	60.6 ± 6.7
ADP association			
k **(s^{-1})**	0.162 ± 0.024	0.140 ± 0.008	0.121 ± 0.004
τ (s)	6.2 ± 0.9	7.2 ± 0.4	8.3 ± 0.3
ADP dissociation			
k **(s^{-1})**	0.072 ± 0.002	0.081 ± 0.004	0.081 ± 0.002
τ (s)	13.8 ± 0.4	12.4 ± 0.7	12.3 ± 0.3

Source of data: Figures 2.1C, D, and F

Table 4. Rates of ParA2 conformational change under different conditions

[ParA2]	0.6 μM	1.25 μM	2.5 μM
ParA2			
k **(s^{-1})**	0.0177 ± 0.0016	0.0147 ± 0.0006	0.0156 ± 0.0015
τ (s)	56.76 ± 5.25	68.20 ± 2.75	64.22 ± 6.20
ParA2 + DNA			
k **(s^{-1})**	0.0328 ± 0.0015	0.0670 ± 0.0007	0.0684 ± 0.0006
τ (s)	30.53 ± 1.43	14.94 ± 0.16	14.63 ± 0.13
ParA2 + ParB2			
k **(s^{-1})**	0.0191 ± 0.0009	0.0149 ± 0.0001	0.0150 ± 0.0019
T (s)	52.43 ± 2.55	66.70 ± 0.23	67.17 ± 8.54
ParA2 + ParB2 + DNA			
k **(s^{-1})**	0.0361 ± 0.0015	0.0613 ± 0.0011	0.0702 ± 0.0007
τ (s)	27.69 ± 1.12	16.32 ± 0.30	14.31 ± 0.08

Source of data: Figure 2.5B

Errors are ± SD

A dissociation binding kinetics experiment was performed where ParA2 could bind MANT-nucleotide until equilibrium was reached, and excess unlabelled nucleotide was then added to initiate dissociation kinetics (**Figure 2.3H**). Unlabelled nucleotide could displace MANT-labelled counterparts, as shown by fast multiphasic dissociation kinetics that fitted well to a one-phase exponential decay model. There was a similar k_{off} for MANT-ATP (0.019 s^{-1}) to that obtained from the k_{obs} versus MANT-ATP plot (**Figure 2.3E**). Alternatively, the k_{off} value for MANT-ADP was slightly higher to that obtained prior, at 0.081 s^{-1} (**Table 3**).

Lastly, nucleotide exchange was investigated by preincubating ParA2 with unlabelled nucleotide and then competing with excess MANT-nucleotide (**Figure 2.3G**). Compared to MANT-AXP association, there were relatively low k_{on} values for all nucleotide exchange conditions tested (**Figure 2.3G**). The slow rates for nucleotide exchange likely correspond to ADP release and subsequent MANT-AXP binding kinetics (**Figures 2.3E, F**). High k_{off} values indicate that MANT-nucleotides less readily displace their unlabelled counterparts, and that ParA2 is stabilised as a sandwich dimer in the presence of unlabelled ATP and ADP.

2.3.4 ParA2 conformation is dependent on nucleotide binding

To determine how ParA2 structure and stability changed with nucleotide binding, and specifically the difference between the ATP- and ADP-bound states, circular dichroism (CD) was utilised to determine surface level (secondary structure) changes to the ParA2 dimer. A spectral analysis provided specific information on the ratio of α-helicity to β-sheets, with signals at 208 nm and from 218-224 nm providing the most information in the form of mean residue ellipticity (degree cm^2 $dmol^{-1}$). **Figure 2.4A** shows the spectra of ParA2 in the presence of various adenosine nucleotides. The spectrum for ParA2 alone has peaks at 208 nm and 220 nm and is consistent with a high α-helix content at the surface of the protein (39.3%). The signal at 208 nm increased (so that the peak decreased) to show a transition to lower helicity in the presence of ATP (29.2%) and ATPγS (24.0%). ADP caused a decrease to 19.9% and was perhaps suggestive of a more pronounced conformational change. Nevertheless, both ATP and ADP resulted in clear changes in ParA2 structure at the surface level. The peaks from 218-224 nm for all conditions did not diminish as was seen previously for the P1 ParA protein (**Davey and Funnell, 1997**).

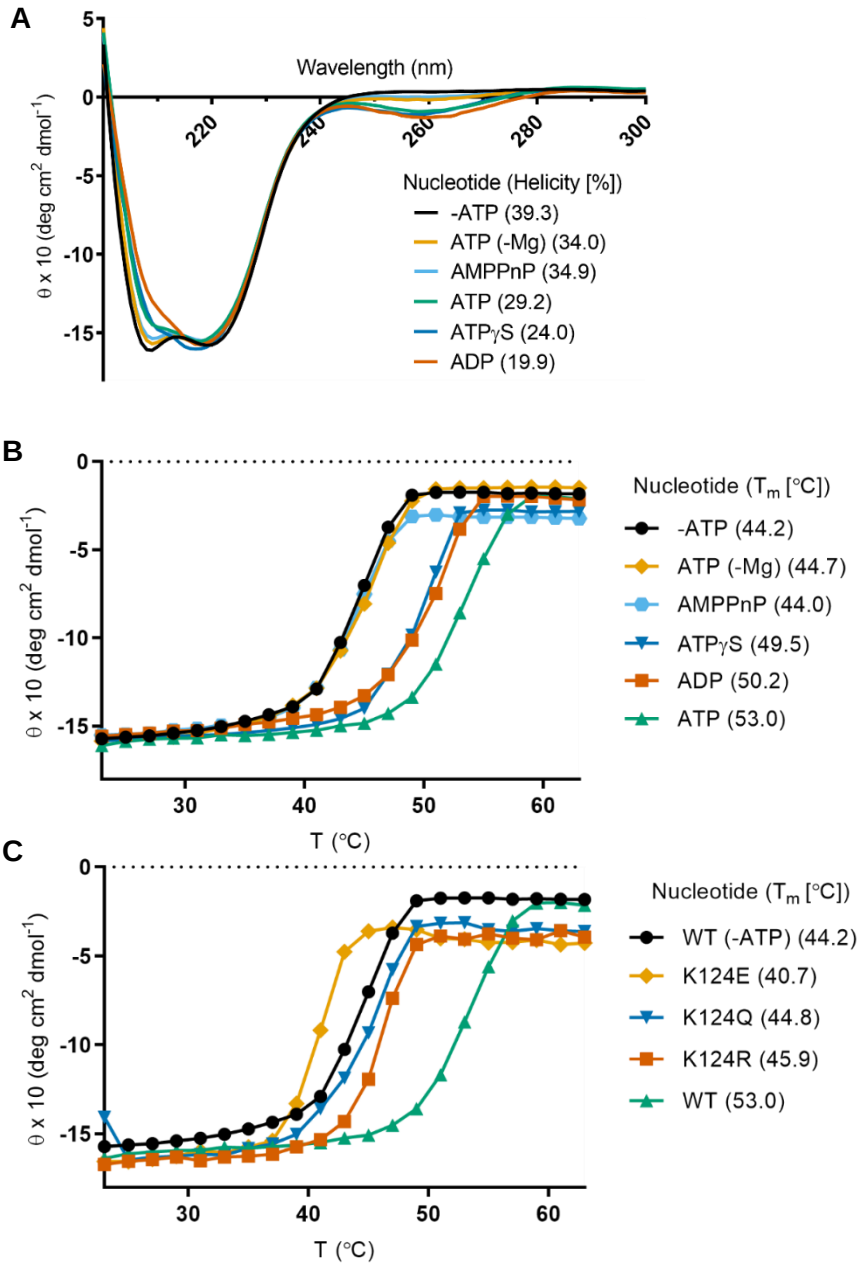

Figure 2.4. ParA2 conformational changes under different nucleotide conditions as monitored by circular dichroism spectroscopy. A) CD spectra of ParA2 under different nucleotide conditions. Surface helicity (%) for each condition is indicated. 5 µM ParA2 was prepared in 10 mM Tris-HCl pH 8, 5 mM $MgCl_2$, and 1 mM adenosine nucleotide when present. **B)** The effects of adenosine nucleotides on ParA2 stability. ParA2 changes in secondary structure monitored by CD at 220 nm (θ_{220}), with an averaging time of 8 s, from 24 °C to 63 °C. Samples preparation as in (**A**). Samples were equilibrated for 1 min prior to measurement with 2 °C increments. Relative ParA2 T_m values under different nucleotide conditions are shown in the table. **C)** As in (**B**), but for ParA2 K124 mutants in the presence of ATP, relative to wild-type ParA2 with ATP (WT), and without ATP (WT (-ATP)).

The change in the ParA2 CD spectra at 208 nm was next monitored in a thermal melt experiment that gave information on ParA2 stability with each adenosine nucleotide condition. Samples were gradually heated in increments of 2 °C and an increase in signal was observed to indicate a loss of overall protein structure, with melting temperature (T_m) determined. It was not possible to observe re-folding of ParA2 and this is perhaps due to the low NaCl concentration required for CD experiments leading to ParA2 precipitation upon heating. ParA2 alone had a T_m of 44.2 °C (**Figure 2.4B**). The non-hydrolysable ATP analague, AMPPnP did not support a significant change in either the spectra or stability and this was also the case for ATP (-Mg^{2+}) condition. ParA2 in the presence of ADP had an increased T_m of 49.5 °C, and 50.2 °C in the presence of ATPγS. ATP supported the transition to the most stable conformation, with a T_m of 53.0 °C. The Walker A box mutants displayed varying degrees of stability as seen in **Figure 2.4C**. ATP conferred some stability to ParA2 K124R but this was diminished compared to native ParA2 and a similar effect was seen for K124Q. Although control samples (-ATP) were not performed for each mutant, K124E had markedly less overall structural stability relative to even ParA2 alone.

2.3.5 ParA2 undergoes a slow conformation change

A rate-limiting step in the ParA2 ATPase cycle for slow DNA-rebinding would be involved in ParA2 gradient formation. This was shown for plasmid P1 ParA but no other ParA proteins, and it is not known if chromosomal ParAs also use a Brownian-ratchet mechanism for patterning and translocation. Therefore, the inherent tryptophan fluorescence of ParA2 was next utilised to look into the conformation change upon nucleotide-binding in more detail. A ParA2 monomer has six tryptophan residues, of which one is located close to the dimer interface and away from the Walker-A box region. The remaining tryptophan residues are buried based on comparisons to the P1 ParA structure (**Dunham et al., 2009**). Equilibrium ParA2 tryptophan fluorescence was measured in the presence of different adenosine nucleotides to determine which cofactors caused a conformation change (**Figure 2.5A**). A tryptophan fluorescence signal increase was detected with ATP (with Mg^{2+} also present) relative to the no nucleotide condition ('Mg' condition) and is presented as a relative fluorescence change. The signal change elicited with ATP was increased significantly with the addition of sssDNA. In the presence of DNA and ParB2 however the stimulatory effect of DNA was slightly diminished. ParB2 did not affect the tryptophan fluorescence signal relative to ATP condition. ParB2 itself has two tryptophan residues but there was no change in fluorescence, with or without DNA. ADP, and notably ATPγS, did not promote a ParA2 tryptophan fluorescence change alone. There was, however, a measurable increase with

ATPγS when DNA was also present. Of the Walker A box mutants, K124Q elicited a slight signal increase in the presence of both ATP but was not significantly above the margin of error. These results show that ParA2 assumes a wide range of distinct conformations under different conditions, and indicates the subtle characteristics required with being fully functional.

The kinetics of the ATP-specific tryptophan fluorescence increase was next investigated. The required experimental settings to attain kinetics across the various conditions and ParA2 concentrations, resulted in an appreciable rate of tryptophan fluorescence photobleaching, as demonstrated for ParA2 alone (**Figure 2.5B**). The addition of ATP caused a slow ParA2 tryptophan fluorescence signal increase. The rate of signal change was not shown to be dependent on ParA2 concentration, as shown in **Table 4**. The relative fluorescence change plateaued at around 180 s and was much slower than MANT-ATP-binding kinetics. Consistent with equilibrium measurements, the introduction of ParB2 showed no effect on the overall intensity, and there was also no effect on the rate. In the presence of ATP and DNA, there was a significant increase in overall intensity. The initial kinetics were similar to without DNA but the rate of fluorescence change quickly increased by around 8-fold (**Table 4**). This resulted in an apparent lag phase and the kinetics went on to reach a maximum intensity at around 80 s. The lag phase was most likely due to initial nucleotide-binding, after which it was not immediately clear if there was an additional structural change with DNA. Since the ATP hydrolysis kinetics showed a steady-state rate from the beginning, this demonstrates ATP hydrolysis was not affected by the slow conformation change, and there is likely no further structural change with DNA. It was thought that the greatly enhanced rate of fluorescence change was aiding in overcoming the high rate of photobleaching, and therefore higher intensities were possible. The kinetics were therefore fitted to a single exponential binding model to estimate the rates of conformation change between conditions (**Table 4**); this required the exclusion of the initial lag phase. Lastly, the addition of ParB2 to the ATP and DNA condition showed a lower overall equilibrium intensity but a comparable rate of signal change. Concentration effects on rates of change only occurred when in the presence of DNA or with DNA and ParB2, as represented by the τ time constant: a maximum rate of change was reached between both conditions from 0.6 μM (30.53 s and 27.69 s, respectively), to 1.25 μM (14.94 s and 16.32 s, respectively).

The conformational change was unexpectedly slow upon ATP binding, since the latter only required 30 s (**Figure 2.3C**). Although this slow conformational change was sped up with DNA, it was determined to be the rate-limiting step in the ParA2-ATPase cycle for slow DNA rebinding.

2.3.6 ParA2-ATP binds DNA with high affinity and cooperativity

Non-specific DNA-binding is a critical feature of type I ParA function. It is unclear how the distinctive ParA2 higher-order helical structures on DNA or *in vivo* gradient formation contribute to the mechanism of action. EMSAs were therefore utilised to investigate and quantify the ParA2-DNA interaction and its nucleotide dependence. ParA2 binding affinities to a 62 bp Cyanine-5 (Cy5) -labelled nsDNA fragment were elucidated in the presence of different adenosine nucleotides. **Figure 2.6A** shows the highest DNA-binding affinities were in the presence of ATP (K_D = 45.9 nM) and the slowly hydrolysable analogue, ATPγS (K_D = 34.1 nM). While ADP facilitated an EMSA shift, the DNA-binding affinity was around 8-fold lower than that with ATP (K_D = 378 nM), and 100% DNA-binding was not achieved. The characteristic DNA-binding activity in the absence of nucleotide was shown to require relatively high ParA2 concentrations (K_D = 1 µM). Moreover, less than 80% binding was achieved, even at ParA2 concentrations above 3 µM (**Figure 2.6B**).

The DNA-binding activities of the ParA2 K124 mutants were also determined in the presence of ATP (**Figure 2.6C**). ParA2 K124R had a similar affinity for DNA as native ParA2 (K_D = 47.1 nM) and this along with the result with ATPγS, confirms that ATP hydrolysis is decoupled from DNA-binding, as is the case with other characterised ParA proteins. To further support this, K124Q was the only mutant that maintained some ATPase activity, yet exhibited a 3-fold decrease in DNA affinity (K_D = 137.5 nM). This reduced affinity could be attributed to aberrant ATP-binding capability and in a similar manner, K124E had a 6-fold decrease in affinity for DNA (K_D = 452 nM). All of the mutants attained 100% DNA-binding. The results of ParA2 DNA-binding activities thus far are therefore suggestive of ATP facilitating a more stable conformation for not only ParA2, but also the ParA2 K124 mutants.

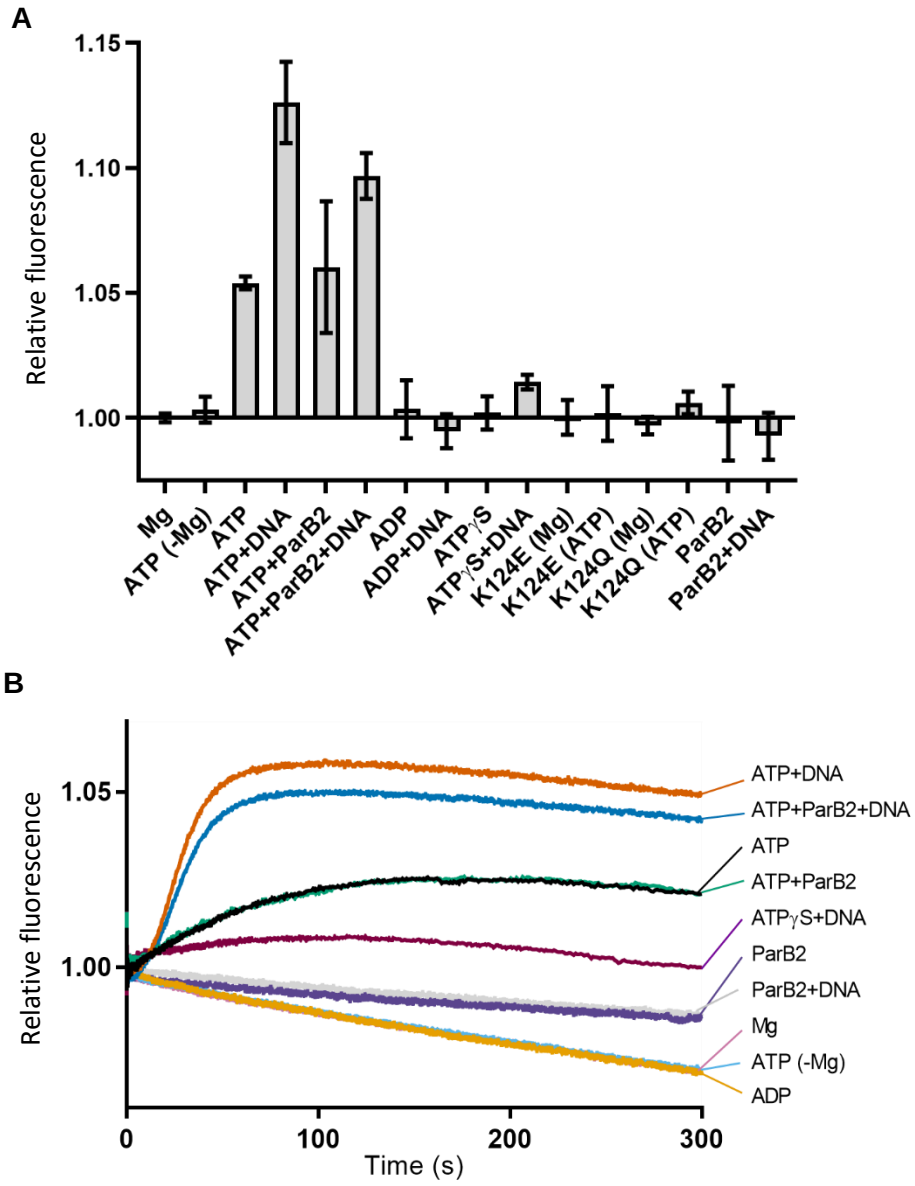

Figure 2.5. Intrinsic tryptophan fluorescence spectroscopy reveals changes in ParA2 conformation mediated by adenosine nucleotides, DNA, Mg^{2+} and ParB2. A) ParA2 steady-state tryptophan fluorescence change. ParA2 (0.6 µM) incubated in Buffer B (section 2.2.3) with nucleotide (1 mM) at 23 °C for 400 s before relative fluorescence change measured. In absence of $MgCl_2$, a separate buffer was prepared with 0.1 mM EDTA and without $MgCl_2$**. B)** ParA2 tryptophan fluorescence change kinetics. ParA2 (0.6 µM) set up in Buffer B in the stopped flow apparatus at 2x final concentration was mixed with (when present) nucleotide (1 mM), sssDNA (0.1 mg/ml), and ParB2 (0.6 µM) prepared in Buffer B at 2x final concentration in the second syringe, at 23 °C.

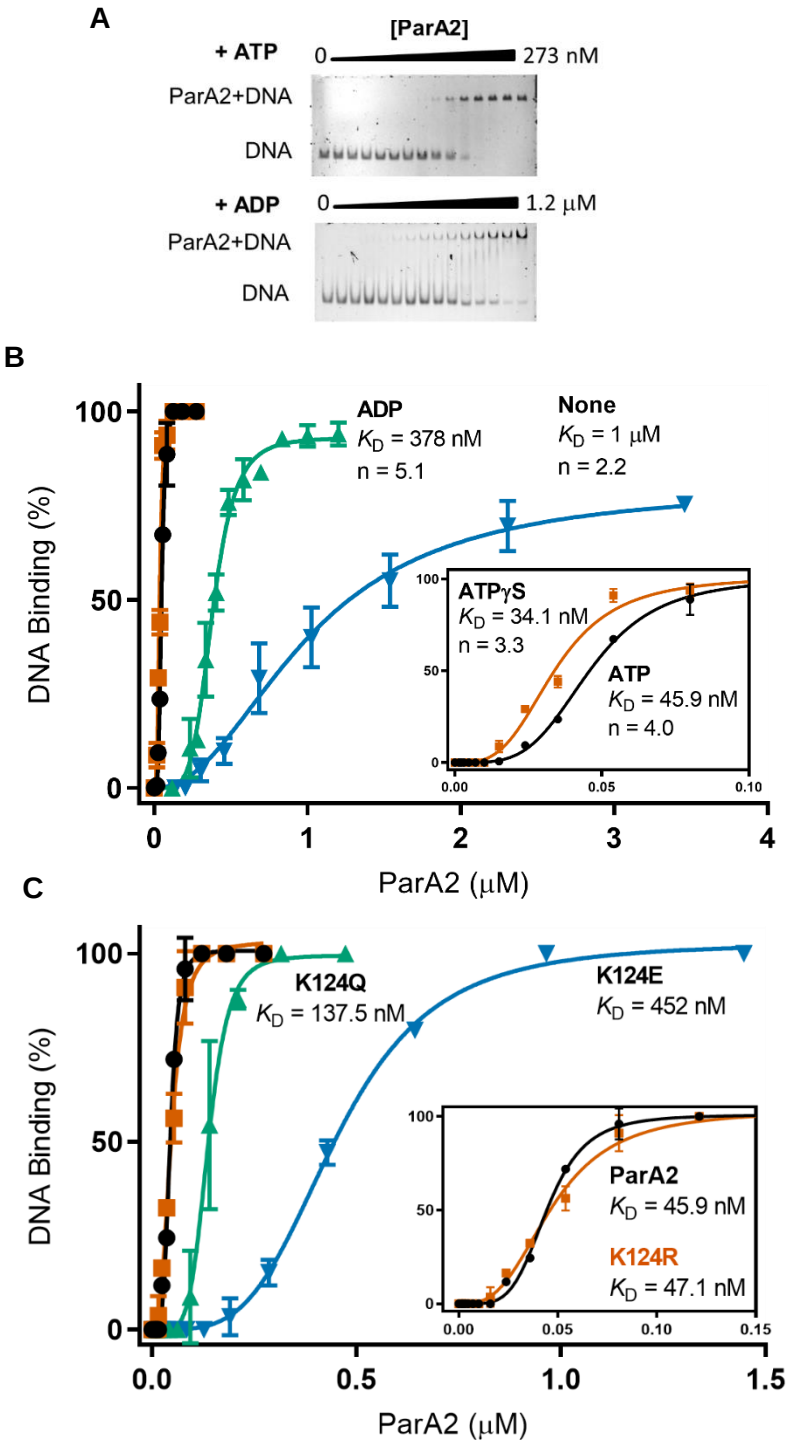

Figure 2.6. ParA2 binds DNA cooperatively with ATP. A) EMSAs of ParA2 DNA-binding. Cy3-62 bp DNA (5 nM) in the presence of 2 mM ATP (top), or ADP (bottom). Gels were run in a 5% polyacrylamide gel in TBM buffer **B)** ParA2-DNA-binding affinity. DNA-binding (%) was calculated using ImageJ. Data were plotted, with indicated K_Ds and Hill coefficients for each condition. **C)** K124R, K124Q, and K124E ParA2 variants binding to DNA with ATP. Reactions were set up and experiments run as in (**A**). Analysis performed as in (**B**).

The ParA2 DNA-binding curves for different nucleotides were sigmoidal and fitted curves for each condition showed high cooperative binding (n > 2). Hill coefficients were highest for ADP (n = 5.1), followed by ATP (n = 4.0) and ATPγS (n = 3.3), and finally no nucleotide (n = 2.2). This suggest that AXP facilitates efficient DNA interaction for native ParA2 over no nucleotide.

The stability of the ParA2-ATP-DNA structure was investigated further, by introducing competing DNA into the reaction to test how ParA2-ATP exchanges on DNA. A concentration of ParA2 (300 nM) was selected as an upper limit of the interaction with DNA, such that there was 100% binding (**Figure 2.7A**). Where the standard protocol required a 15 min incubation time for the nucleoprotein complex to form, here, unlabelled sssDNA was subsequently added in increasing amounts (in adjacent wells) for an additional 2 min incubation period. sssDNA (0.5 mg/ml) facilitated disassembly of the complex and this was more apparent with 2 mg/ml. A lower ATP concentration was tested (**Figure 2.7A**, lane 11) but the extent of dissociation remained constant. ParA2-DNA dissociation was observed in the presence of ATPγS to a comparable extent to the ATP condition. The ParA2 ATPase mutants were also tested where K124R and K124Q showed some dissociation, while K124E dissociated almost completely (**Figure 2.7B**). These findings indicate that DNA dissociation was not due to DNA-stimulated ATPase activity. ParA2-ATP is thus able to exchange on DNA without hydrolysing ATP. The C-terminally tagged ParA2-GFP-His was tested for similar functionality to native ParA2 for use in later experiments (Chapter 4).

Finally, it is known that ParA2 binds and coats DNA to form distinct, higher-order left-handed helical structures with different adenosine nucleotides (**Hui et al., 2010**). The highly cooperative binding as characterised here suggests that DNA topology could influence the ParA2 binding affinity for DNA. Indeed, as DNA length was increased from 62 bp to 144 bp and 232 bp, EMSA shifts were observed immediately in the ParA2 titration (data not shown). However, in using 62 bp substrate, useful comparisons could be made between nucleotide conditions to elucidate high affinity DNA-binding that is applicable to a Brownian-ratchet mechanism of action.

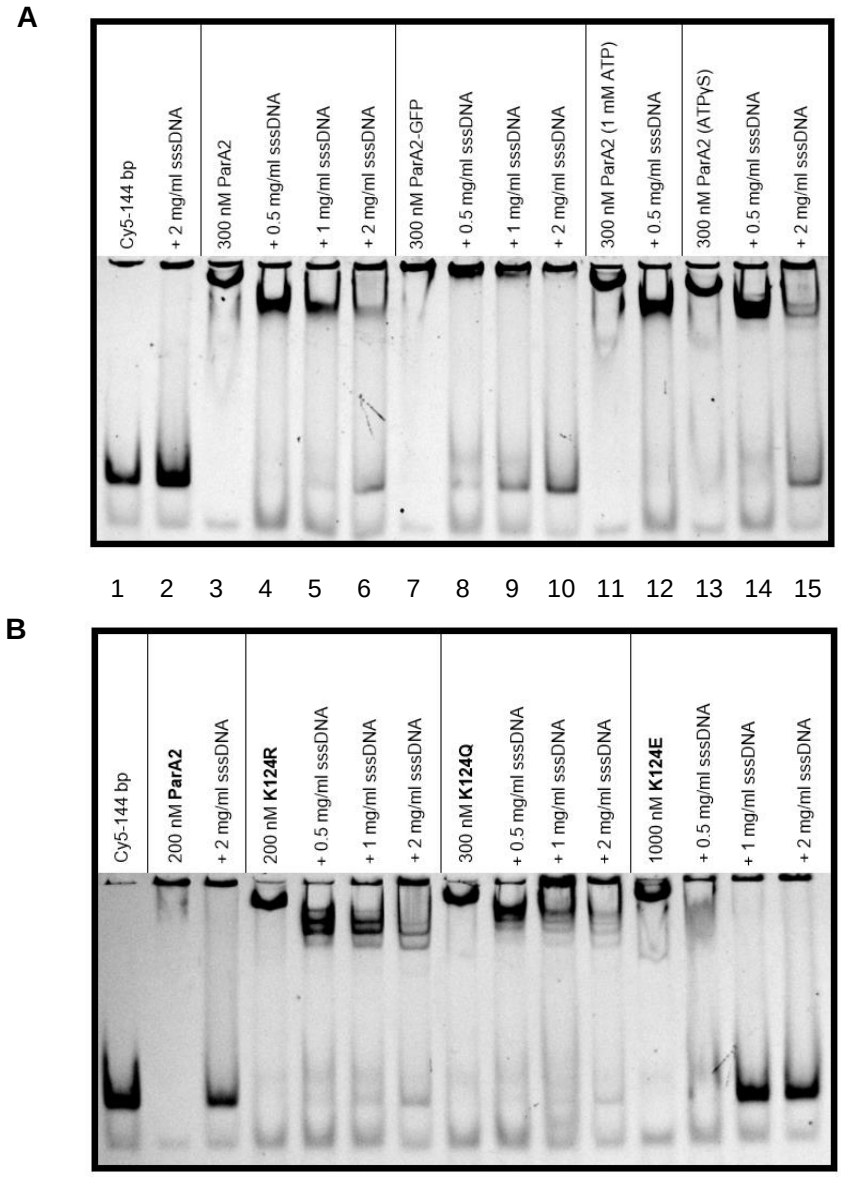

Figure 2.7. Dissociation of ParA2-DNA complex. A) EMSA of ParA2 dissociation from DNA. After an initial 15 min incubation of ParA2, DNA, and ATP, sssDNA was added for a further 2 min incubation in a competition binding experiment. ParA2-DNA complexes were pre-formed in lanes 3, 7, 11 and 13, by incubating 300 nM protein, 5 nM Cy3-labeled 144 bp nsDNA, and 2 mM ATP, unless stated otherwise. Control lanes 1 and 2 show a dark band, with a faint lower band to be disregarded and is an artefact fragment from PCR preparation. Increasing concentrations (as indicated) of added sssDNA showed competition with bound DNA substrate. There is increasing dissociation of complexes to free DNA (lower dark band) (lane 6). Complexes formed with ParA2-GFP-His showed similar levels of dissociation as WT ParA2 (lane 10). A lower ATP concentration was tested (1 mM) and showed the same dissociation (lane 12 relative to 4). Reactions incubated with 1 mM ATPγS also exhibited

dissociation (lane 15). **B)** ParA2 K124 variants bind and dissociate from DNA. Experiment set up as in (**A**) with distinctions as indicated. The ParA2 K124R and K124Q variants did not dissociate from DNA to the same degree as WT ParA2. Complex formation with ParA2 K124E required a much higher concentration but dissociated with half the amount of competing DNA (lane 14).

2.4 DISCUSSION

ParA2 is part of a prototypical Walker-box DNA partitioning system, which are generally used in both plasmid and chromosome segregation whereby the nucleoid is used as a support matrix to transport replicated DNA cargo. This feature is mediated by ParA-DNA-binding activity (**Corrales-Guerrero et al., 2020**), and manifests as dynamic polar gradients during segregation that vary for different ParA proteins. ParA2, however, exhibits an oscillatory pattern *in vivo* (**Fogel and Waldor, 2006**) whilst also oligomerising to form distinct filament structures around DNA with different adenosine nucleotides (**Hui et al., 2010**). It is not clear how these activities are linked to contribute to the mechanism of DNA segregation. Additional parameters that are incorporated in chromosome-specific segregation, are a much larger DNA cargo relative to plasmids and strict coordination with cell-cycle timings. In this chapter, the ParA2 ATPase cycle was investigated (**Figure 2.8**) by probing the direct interactions with adenosine nucleotides and the downstream activities. ParA2 was shown to be dynamic on DNA and there is evidence of a similar mode of action to that proposed for plasmid ParA proteins, in a Brownian-ratchet mechanism but with faster rates for individual activities to address the additional required parameters.

2.4.1 ParA2 oligomers are part of a Brownian-ratchet-like mechanism

The previously characterised ParA2-DNA filament structure prompted a posited mechanism that only one end of a filament would contact ParB2 (**Hui et al., 2010**). This would lead to polar-filament depolymerisation in a retracting, spindle-type mechanism as ParA2-ATPase activity was stimulated by the partition complex (ParB2 and DNA) (**Hui et al., 2010**). However, since ParA2 cannot form self-sustaining filaments, a retracting filament would require well-defined and positioned DNA ‘tracks’ from which to direct DNA segregation. A filament model in this regard would therefore be an ineffective concept, since the ratio of cell-to-genome length requires that the nucleoid is in fact comprised of numerous, compacted, high-density chromosomal regions (HDRs) (**Marbouty et al, 2015**).

Here, ParA2 has been shown to bind DNA with high cooperativity for all the adenosine nucleotide conditions tested (**Figure 2.6B**). It is very likely that the DNA-binding characterised here are the same as the characterised ParA2-DNA filaments, since comparable concentration ranges were used across the conditions in both studies (**Hui et al., 2010**). The Brownian-ratchet model does not state where the partition components localise within the cell, beyond postulating that segregation could occur in the confined spacing between the nucleoid surface and the inner-membrane (**Vecchiarelli et al., 2014b**). Super-resolution microscopy has previously been used to locate patches of ParA within the nucleoid volume (**Le Gall et al.,**

2016). Furthermore, it was shown that partition complexes also colocalised with HDRs, and 'hitch-hiked' to adjacent HDRs via interaction with ParA. ParA2 then, may preferentially form oligomers at HDRs with this high cooperative DNA-binding activity. In EMSAs, increasing DNA fragment length from 62 bp to 244 bp increased ParA2-ATP affinity for DNA and suggests that cooperative binding is enough to form short oligomers (data not shown). As an aside, it is not immediately clear what the physiological relevance of the DNA-binding activities are for ParA2 alone, or in the presence of ADP, as higher relative concentrations were required to promote DNA-binding (**Figure 2.6B**). Indeed, the previous filament structures of ParA2 were determined to be less ordered and stable relative to ParA2 in the presence of ATP (**Hui et al., 2010**).

Interestingly, ParA2 was shown here to be able to exchange on DNA in the presence of ATP, and this was also seen with ATPγS, which reveals that ATP hydrolysis is not essential for this dynamicity on DNA (**Figure 2.7A**). Moreover, it is perhaps sensible to say that rigid, polar filaments would not correspond to the observed ParA2 *in vivo*, which exhibits pole-to-pole oscillations. The features of highly cooperative DNA-binding and exchange on DNA could more readily contribute to this phenomenon. For instance, many ParA2 small oligomers could cooperatively nucleate at one end of the cell – maybe recruited to high density DNA regions corresponding to origin regions at the poles (**Marbouty et al., 2016**) – to then give rise to a dynamically exchanging gradient within the nucleoid volume. Interactions with the partition complex could then initiate ParA2 redistribution.

The dynamic ParA2-DNA oligomers formed via highly cooperative binding are part of a mechanism where ATP-mediated ParA2-DNA-binding occurs stochastically on the nucleoid, in a variation of a Brownian-ratchet mechanism **(Vecchiarelli et al, 2014**). Results of a cell-free reconstitution of the *Vc*ParABS2 system are presented in the Appendix (**Figure 5.1**). ParA2-GFP was shown to have similar DNA-binding activity to native ParA2 and was able to dissociate from DNA in EMSAs (**Figure 2.7A**). ParA2-GFP was subsequently used in the reconstitution, with the experiment largely performed as it was for the plasmid F SopABC system (**Vecchiarelli et al., 2014a**). ParA2-GFP-ATP bound to a surface coated with DNA (DNA carpet) within a microfluidics device; meanwhile, magnetic beads coated with *parS2* DNA were bound by ParB2. A magnet confined the reconstitution to 2D and depletion zones formed at a ParA2:ParB2 concentration ratio of 1:8 μM. Removal of the magnet showed that the beads did not adequately clear ParA2-GFP-ATP tethers and the beads remained static. Nevertheless, the initial reconstitution experiment and the dissociation EMSAs demonstrate that ParA2-GFP oligomers are dynamic on DNA, and they interact with ParB2-*parS2* complexes in a Brownian-ratchet mechanism.

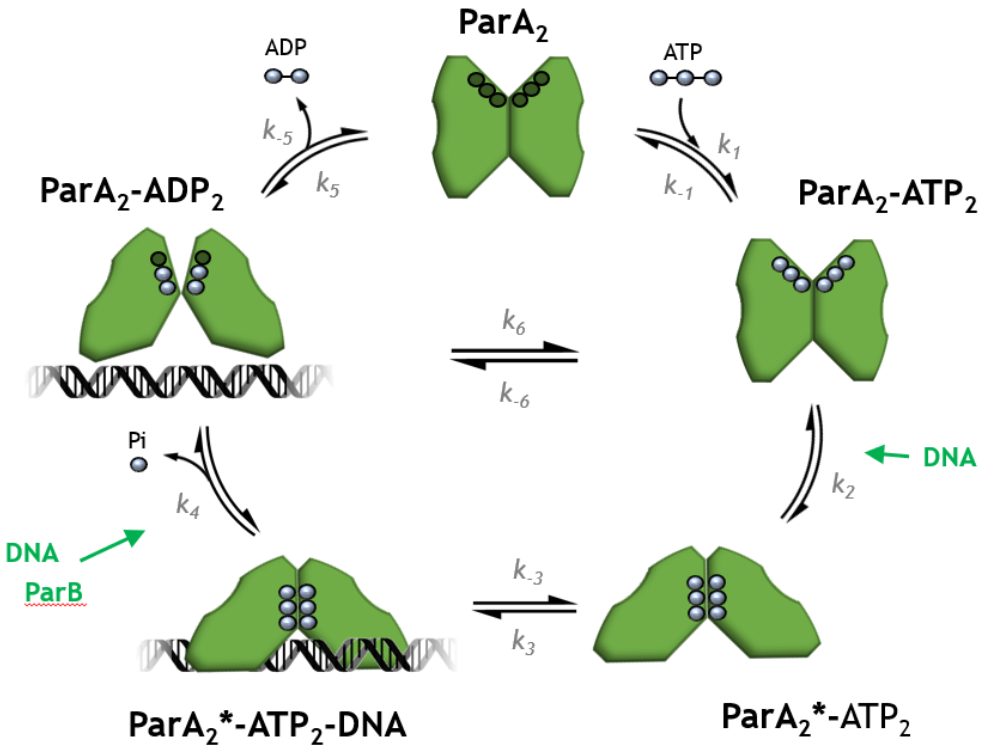

Table 5. Rate constants in ParA2 ATPase cycle

	Rate constant	Reference		Rate constant	Reference
k_1	0.003 $\mu M^{-1}s^{-1}$	Figure 2.3E	k_4	0.1 – 0.15 s^{-1}	Figure 2.1D
k_{-1}	0.025 s^{-1}	Figure 2.3E	k_5	0.0365 $\mu M^{-1}s^{-1}$	Figure 2.3F
k_2	0.0147 ± 0.0006 s^{-1} 0.0670 ± 0.0007 s^{-1} (+DNA)	Table 4	k_{-5}	0.003 s^{-1}	Figure 2.3F
k_3	0.015 ± 0.006 s^{-1}	*	k_6	0.0007 $\mu M^{-1}s^{-1}$	Figure 2.3G
k_{-3}	0.12 ± 0.03 s^{-1}	*	k_{-6}	0.0132 s^{-1}	Figure 2.3G

Figure 2.8. ATPase cycle of ParA2. The ParA2 dimer ($ParA2_2$) binds 2 ATP molecules (k_1, k_{-1}), and undergoes a slow conformational change to $ParA2_2$*-ATP_2 (k_2), the active nsDNA-binding state. This slow transition is significantly accelerated by DNA. $ParA2_2$*-ATP_2 loads onto DNA cooperatively to form oligomers on DNA (k_3, k_{-3}). $ParA2_2$-ADP_2 dissociates from DNA (k_4) upon ATP hydrolysis, which is stimulated by DNA and ParB2. ADP dissociates from ParA2 (k_5, k_{-5}), and the cycle restarts. ParA2 dimers diffuse away from the initial DNA-binding region until the $ParA2_2$*-ATP_2 state is attained again. ParA2 dimers undergo nucleotide exchange (k_6, k_{-6}) at faster rates than ATP-binding without dissociating to monomers. The rate of ParA2 rebinding to DNA is thus accelerated with higher ParA2 concentrations. Appropriate Figures and Tables are referenced. DNA-binding and dissociation rates are derived from cell-free reconstitution experiments performed by Adam Brooks (University of Sheffield) (*).

2.4.2 Depletion zone formation of a chromosomal ParA

ParA2 ATPase activity was previously shown to be stimulated by DNA and ParB2 (**Hui et al, 2010**). Here, the fold-stimulation of ParA2 ATPase activity has been determined directly for these conditions, as well as for when stimulation was highest, in the presence of both components. These activities have proven to be very similar to plasmid ParA proteins (**Davis et al., 1992; Libante et al., 2001; Barilla et al., 2005**) from which the Brownian-ratchet model was conceived (**Vecchiarelli et al, 2010; 2013; Hwang et al., 2013**), and other chromosomal ParA proteins (**Easter and Gober, 2003; Lee and Grossman, 2006**). In a Brownian-ratchet mechanism, this result equates to a dense partition complex stimulating the ATPase activity of nucleoid-associated ParA such that its DNA-binding conformation is lost.

The next step in the mechanism would be free ParA undergoing Brownian diffusion to form a depletion zone around the partition complex, which is enabled by a time-delayed re-acquisition of the DNA-bound state (**Vecchiarelli et al, 2010**). Here, ParA2 exhibited a clear conformation variation between ADP- and ATP-bound states, as represented by CD data. Interestingly, ParA2 helicity (39.3%) decreased with ADP (19.9%) and ATP (34%), in an apparent disparity with data acquired for plasmid P1 ParA (**Davey and Funnell, 1997**). In fact, the P1 ParA study utilised a relatively high NaCl concentration (150 mM) to keep the protein stable and meant that wavelengths below 220 nm were excluded, ultimately compromising the spectral analysis. Similar to ParA2, CD data for F SopA displayed a loss of signal at 208 nm with ATP and indicated a decrease in helicity (**Libante et al., 2001**). Nonetheless, there was an increase in stability with ATP for both P1 ParA and ParA2 in thermal melt experiments. An additional insight is that, for both proteins, the conformational change with ATP occurs before interaction with DNA. Indeed, the tryptophan fluorescence kinetics assays demonstrated that this conformation was attained slowly and represents the physiologically relevant DNA-binding species, referred to as $ParA2_2$*-ATP_2 (**Figure 2.8**).

ParA2 had an affinity for MANT-labelled ATP that was in the same order of magnitude to plasmid ParA proteins (**Davey and Funnell, 1997; Bouet et al., 2007; Barilla et al., 2005**). Interestingly though, ParA2 had a similar affinity for MANT-labelled ADP and ATP (11 µM). Intracellular ADP is maintained at a five-fold lower concentration to ATP (1.54±1.22 mM, mean ± SD), in order to favour ATP-dependent enzymes that are competitively inhibited by ADP (**Berg et al., 2002; Yaginuma et al., 2014**). As shown in Chapter 3, the addition of a large excess of ADP acts to disassemble ParA2-ATP from DNA, as well as from the partition complex. The ADP concentration most relevant to ParA2 within the cell would conceptually be within the vicinity of the partition complex, since ParA2 ATPase activity is stimulated most by ParB2 and DNA. Accordingly, the similar affinities for MANT-ADP and -ATP suggests that a

newly released ParA2-ADP dimer would have to diffuse further away from the partition complex before it could more readily encounter ATP; or even to exchange ADP for ATP, based on the finding that the k_{on} for ADP to MANT-ADP exchange, and ADP to MANT-ATP, were very comparable (**Figure 2.3G**). What is more, the partition complex would encounter many ParA2 units at one time owing to the nature of ParA2-DNA oligomer formation, and so many ParA2-ADP dimers would be released at a point in time. These events could contribute to a small overall effect in accentuating the formation of a ParA2 depletion zone around the partition complex. Adenosine nucleotide exchange data is not available for other ParA proteins to make more conclusive comparisons, but this feature could be a key difference to plasmid ParA depletion zones.

The steady-state relative tryptophan fluorescence change for ParA2 in the presence of ATP and DNA, was slightly higher than with ATP, DNA and ParB2. This indicates that less ParA2 was undergoing a conformation change for the latter condition and this could be because ParB2 was competing with ParA2-ATP for DNA. This represents the high concentration of ParB2 exchanging on and around the partition complex, competing with ParA2 for DNA and is another small effect that could accentuate depletion zone formation for the *Vc*Chr2 partition complex. This activity would most likely occur least when the local ParB2 concentration is vastly higher than ParA2, and the protein concentration ratio at the partition complex has been suggested to be up to 1:500 in favour of ParB (**Lim et al., 2014**).

2.4.3 The ParA2 ATPase cycle is faster than for plasmids

In a Brownian-ratchet mechanism, it is necessary to ascertain the ParA2-rebinding rate on DNA, as it would give a detailed insight into how *V. cholerae* Chr2 can be segregated as a much larger DNA cargo than plasmids, and with only a third of the cell to correctly do so. Individual activities in the ParA2 ATPase cycle have been characterised here to facilitate this objective (**Figure 2.8**). Firstly, ParA2 bound MANT-ATP in a similar manner to plasmid P1 ParA, and took approximately 30 s to reach a steady-state intensity (**Figure 2.3C**). This is quite slow for simple nucleotide-docking and suggested a conformational change. Unlike P1 ParA and SopA, SEC-MALS showed that ParA2 dimerisation was not a factor in these kinetics. The high concentration required for SEC-MALS did not allow for testing of lower concentration effects on ParA2 dimerisation. Interestingly, the rate of tryptophan fluorescence change with ATP was similar across the concentration range tested, indicating that ParA2 is also a dimer at these lower concentrations. The chromosomal ParA proteins (Soj) from *B. subtilis*, *H. pylori*, and *T. thermophilus* all exhibited a transition from monomer to dimer with ATP (**Scholefield et al., 2011; Lee and Grossman, 2006; Leonard et al., 2004**). ParA2 readily forming a dimer

before binding adenosine nucleotides is one less step to undergo in the ATPase cycle and could be a critical reason why it can direct chromosomal segregation in a shorter time-period.

Tryptophan fluorescence kinetics revealed that ParA2 proceeded to reach a steady-state intensity only slightly faster than plasmid P1 ParA when ATP and DNA were both present, but was up to five-fold faster to reach steady-state when only ATP was present (**Vecchiarelli et al., 2010**). The latter could represent an aspect of how ParA2 is able to oscillate from pole-to-pole, as it reaches the DNA-bound state more readily, even at regions within the nucleoid lacking HDRs, with less freely available DNA. The rate of tryptophan fluorescence change in the presence of DNA reached an apparent saturation when increasing ParA2 concentration from 0.6 to 1.25 µM (**Table 4**). This potentially indicates that cooperative binding on DNA prior to ATP-binding has a role in the rate of conformational change. In support of this possibility is the finding that ParA2 has a K_D of 1 µM on DNA in the absence of ATP (**Figure 2.6B**). ParA2-GFP DNA-binding and dissociation kinetics were determined by Adam Brooks in cell-free reconstitution assays (data not shown), with slightly faster k_{on} rates with ATP compared to P1 ParA, and the relevant rates are shown in **Figure 2.8**. Crucially, although the initial binding was slow, there was no lag time in binding DNA as opposed to what was observed for P1 ParA (**Vecchiarelli et al., 2010**).

ParA2 ATPase activity was potentially faster than the plasmidal ParA proteins, P1 ParA and F SopA, both with and without DNA (**MacCready et al., 2018**). The fold-stimulation by ParB2 and DNA was also much higher than the chromosomal Soj from *H. pylori* (**Lee and Grossman, 2006**). This demonstrates that the preceding steps in the ParA2 ATPase cycle being equivalent or quicker than ParA homologues, culminating with a faster ATPase activity. The final step to consider in the comparatively quicker ATPase cycle for ParA2 is ADP turnover, where ParA2 was determined to have a higher k_{off} for ADP than ATP (**Figure 2.3E** and **2.3F**). In the cell, this would perhaps be facilitated by the innately less stable structure of ParA2-ADP relative to ParA2-ATP (**Figure 2.4B**). Moreover, ParA2 undergoing ADP to ATP exchange demonstrates that the non-nucleotide-bound state can be relatively short with available nucleotide and could represent its bypassing completely. In any case, ParA2 is already a dimer as a base unit in the ATPase cycle and has therefore one less activity to undergo. ParA2 dynamicity within the cell is thus likely a result of a faster ATPase cycle. An applicable analogy can be made with TP228 ParF where a hyperactive ATPase mutant was able to oscillate more often *in vivo* (every 2-3 min) compared to WT ParF (every 4-6 min) (**McLeod et al., 2017**).

The results presented in this chapter point strongly towards a Brownian-ratchet-like mechanism for Chr2 segregation, as opposed to a filament-pulling model as proposed when

ParA2-DNA filaments were first characterised (**Hui et al., 2010**). ParA2 has similar properties to other ParA proteins, but the individual activities are faster. It has been shown that a ParA2-GFP depletion zone forms upon interaction with ParB2-*parS2* complexes. The time-delayed conformational change is long enough for ParA2 to diffuse away from the partition complex. In fact, a high diffusion constant of ~1 $\mu m^2 s^{-1}$ within cells is a key parameter for self-assembly of ParB into clusters (**Debaugny et al., 2018**). However, a faster ParA2-GFP rebinding rate on DNA means that a higher concentration of ParB2 is required to adequately clear ParA2-GFP oligomers from the vicinity of the partition complex. The kinetic model for the ParA2 ATPase cycle (**Figure 2.8**) illustrates how ParA2 is already a dimer prior to binding ATP. While MANT-ATP association was similar to plasmid ParA homologues, the subsequent slow conformational change was appreciably quicker. Finally, the innately weak ParA2 ATPase activity is in fact faster than other documented ParA homologues. Although the exact mechanism for ParA2 oscillations is still elusive, it has been demonstrated that this is mediated by highly cooperative DNA-binding, and fast exchange on DNA. These results are consistent with what would be expected for driving a large DNA cargo that is also to coordinated with shorter replication and cell division timings, where ParA2 is part of a Brownian-ratchet-like mechanism, but with a much faster rebinding rate on the DNA scaffold.

CHAPTER 3

KINETICS OF V. cholerae ParABS2 COMPLEX ASSEMBLY

A version of the chapter is being prepared for publication as:

Chodha, S.S., Tufail, F., Parker., A., Hwang., L-C. Self-Assembly of the *Vibrio cholerae* Chromosome 2 ParABS Complex is Mediated by ATP and CXP. *Frontiers in Molecular Biosciences.*

3.1 INTRODUCTION

ParB dimers binds *parS* and surrounding DNA to form a dense partition complex demarcated for segregation (**Funnell, 2016**). The initial binding of ParB to *parS* proceeds in a sequence-specific manner, via a conserved HTH-motif located within a central DNA-binding domain (DBD) (**Chen et al., 2015; Schumacher et al., 2010**). ParB also exhibits nsDNA-binding via the DBD (**Fisher et al., 2017**). The nsDNA-binding initiates 1D-spreading from *parS*, and subsequent 3D-bridging, with interactions between ParB dimer N-terminal domains (NTD) in an open 'Y' conformation (**Graham et al., 2014; Song et al., 2017**).

An additional Type I Par system element was recently revealed as ParB has been shown to bind and hydrolyse cytidine triphosphate (CTP) to CDP (**Osorio-Valeriano et al., 2019, Soh et al., 2019**). The missing element was foreshadowed as biochemical reconstitutions of ParB spreading and bridging corresponding to the level of DNA condensation that would be necessary *in vivo*, proved unsuccessful (**Sanchez et al., 2015**). ParB proteins homodimerise at the CTD. Co-crystal structures of *B. subtilis* ParB with CDP (**Soh et al., 2019**), and a ParB analogue from *M. xanthus* (PadC) with CTP (**Osorio-Valeriano et al., 2019**), showed a second dimer-interface acting as the catalytic-centre on interlocking NTDs. This closes the ParB dimer into a ring conformation. Single-molecule imaging and biochemical assays showed *B. subtilis* SpoOJ DNA sliding clamps assembling at *parS* enclosed substrates in the presence of CTP, in a mechanism that recruits numerous ParB dimers at a single site (**Soh et al., 2019**). This study was supported by a label-free reconstitution of *C. crescentus* ParB spreading on enclosed DNA substrate with CTP and, interestingly, a transcriptional regulator was shown to act as a roadblock to attenuate ParB spreading, (**Jalal et al., 2020a**). Both CTP-binding and hydrolysis were required for proper partition complex formation and chromosome segregation in *M. xanthus* (**Osorio-Valeriano et al., 2019**). The CTP-binding domain is conserved across canonical ParB proteins and is likely a fundamental factor for Type I Par systems.

ParA2 forms nucleoprotein filaments alone and with adenosine nucleotides (**Hui et al., 2010**). Formation of the filaments is due to highly cooperative binding to DNA and are most stable in the presence ATP, as shown in Chapter 2 (section 2.3.6). High affinity nsDNA-binding was observed in the presence of ATP, and represents ParA2 on the nucleoid primed for the tethering interaction for the partition complex as defined by the Brownian-ratchet model (**Vecchiarelli et al., 2015**). Interactions between ParA and ParB have been characterised and CTP has been shown to enhance this interaction (**Leonard et al., 2004; Volante and Alonso, 2015; Osorio-Valeriano et al., 2019**).

In this chapter, light scattering assays were used to characterise *V. cholerae* Chr2 Par system complex assembly dynamics. A large ParA2-DNA complex was detected in the presence of ATP and represents ParA2 filaments. ParB2-DNA-binding was only detected in light scattering assays in the presence of CTP and on *parS2*-DNA. ParA2-ATP and ParB2 formed an even larger complex on DNA compared to their individual binding activities, and the complex was stabilised by *parS2*. These interactions are thought to represent partition complex assembly and ParA2-mediated nucleoid tethering. The addition of CTP resulted in a dynamic oscillation in partition complex assembly kinetics and could have a direct influence on the final subcellular localisation of *Vc*Chr2 partition complexes within the cell.

3.2 EXPERIMENTAL PROCEDURES

3.2.1 Strains and plasmids

The strains and plasmids used and/or constructed during this work are detailed in the table below.

Table 6. *E.coli* Strains and plasmids

E. coli	**Genotype**	**Supplier**
NEB 5-alpha	*fhuA2 Δ(argF-lacZ)U169 phoA glnV44 Φ80 Δ(lacZ)M15 gyrA96 recA1 relA1 endA1 thi-1 hsdR17*	New England Biolabs
BL21(DE3)	*fhuA2 [lon] ompT gal (λ DE3) [dcm] ΔhsdS λ DE3 = λ sBamHIo ΔEcoRI-B int::(lacI::PlacUV5::T7 gene1) i21 Δnin5*	New England Biolabs

Plasmid	**Description**	**Construction**
pLCH04	pET15 b (+) bearing *parB2-his*	from Genescript
pSC01	pET28 b (+) bearing *parA2*	a) PCR amplification of pMBD02 (see **Table 1**) with LCH11-*parA2-gfp*-fwd and MBD02-*parA2-his*-rev b) Phosphorylation and ligation of product
pRCT01	pBAD/His B bearing *parA2-K124Q*	a) PCR amplification of pLCH12 (see **Table 1**) with LCH22-*parA2*-K124Q-fwd and RCT01-*parA2*-rev-EcoR1 b) Digestion of product with Nco1 and EcoR1 c) Ligation of fragment into pBAD/His B cut with Nco1 and EcoR1
pRCT03	pBAD/His B bearing *parA2-K124R*	a) PCR amplification of pLCH11 (see **Table 1**) with LCH20-*parA2-K124R*-fwd and RCT01-*parA2*-rev-EcoR1 b) Digestion of product with Nco1 and EcoR1 c) Ligation of fragment into pBAD/His B cut with Nco1 and EcoR1
pBKSII	pBluescript KSII+	from Stratagene
pBKSII-*parS2*	pBKSII bearing one *parS2* site	a) Annealed oligonucleotides LCH04-*parS2*-T and LCH05-*parS2*-B as top and bottom strands of *parS2B* site b) Digest product with BamHI and EcoR1 c) Ligation of fragment into pBKSII cut with BamHI and EcoR1
pSC04	pBKSII bearing two *parS2* sites	a) PCR amplification of pBKSII using primers SC09-*parS2*-fwd and SC10-*parS2*-rev b) Phosphorylation and ligation of product
pSC05	pBKSII bearing six *parS2* sites	from Genewiz
pSC06	pBKSII bearing nine *parS2* sites	from Genewiz
pSC07	pBKSII bearing three *parS2* sites	a) PCR amplification of pSC05 using primers SC11-3x*parS2*-rev and SC12-3x*parS2*-fwd b) Phosphorylation and ligation of product

NEB 5-alpha was used as host for cloning. All plasmids were verified by DNA sequencing.

3.2.2 Oligonucleotides

Oligonucleotide primers used for construction of plasmids, and for amplifying DNA fragments used in experimental assays, are listed in the table below.

Table 7. Oligonucleotides

Oligo	Sequence (5'-3')
his-parA2-fwd	CTAGCTAGCGCAATGAAACGTGAACAAAC
his-parA2-rev	GCGGATCCTTAGCCCTGATTCAGAGAG
LCH11-*parA2gfp*-fwd	ATACCATGGCAATGAAACG
MBD02-*parA2*-rev	GCGGATCCTTAGCCCTGATTCAGAGAG
parA2gfp-W1	TTTCACTGGCCGAACATACC
parA2gfp-W2	CCTGACCGTGAATGATTTCG
LCH19-*parA2(K124R*)-rev	CAGATGAACAGCCGTCATACTGCGGCCGGTACCGCCTTTTTGATT
LCH20-*parA2(K124R*)-fwd	AATCAAAAAGGCGGTACCGGCCGCAGTATGACGGCCTGTTCATCTG
LCH21-*parA2(K124Q*)-rev	ATGAACAGCCGTCATACTCTGGCCGGTACCGCCTTTTTG
LCH22-*parA2(K124Q*)-fwd	CAAAAAGGCGGTACCGGCCAGAGTATGACGGCTGTTCAT
RCT01-*parA2*-EcoR1-rev	CTAGAATTCTTAGCCCTGATTCAGAGAG
LCH04-*parS2*-T	CGCGGATCCATTTACAATGTAAAGGAATTCCGG
LCH05-*parS2*-B	CCGGAATTCCTTTACATTGTAAATGGATCCGCG
SC09-2x*parS2*-fwd	TGTAAATATATCAAGCTTATCGAT
SC10-2x*parS2*-rev	CTGTAAACATTCCTTTACATTGTAAA
SC11-3x*parS2*-rev	CATCGCAGGATGCTCTTT
SC12-3x*parS2*-fwd	GAATTCGATATCAAGCTTATCG

Oligo	Sequence (5'-3')	Used for amplifying
M13-fwd-Cy5	Cy5-GTAAAACGACGGCCAGT	Cy5-labelled 144 bp nsDNA (from pBKSII) and 147 bp *parS2* DNA (from pBKSII-*parS2*)
KS-rev	CGAGGTCGACGGTATCG	

3.2.3 Buffers

Buffer A: see section 2.2.3. **Buffer B**: see section 2.2.3. Buffer B filtered using 0.1 µm filter, then degassed.

3.2.4 ParA2, ParA2 K124R/Q, and ParB2 purification

As described in Chapter 2.

3.2.5 Light scattering assays

All experiments were performed in a Fluorolog®-3 spectrofluorometer (Horiba Scientific) using a 'SpectraACQ' controller set at 467 nm, in a 'HellmaAnalytics High Precision Cell'. Reaction Buffer B (see section 3.2.3) was degassed and filtered (0.1 µm). Reaction premixes containing combinations of ParA2, ParB2, pBKSII with an indicated number of *parS2* sites,

ATP, and CTP, were prepared on ice, and then pre-incubated at 23 °C for 15 min. Component concentrations are stated for each individual experiment. A short period (10 ± 2 s) was required for rapid sample mixing, and to position the cuvette before the sample was illuminated using 467 nm light, and 90° scattered light was measured every 0.5 s at room temperature. For sequential and competition assays the acquisition was paused, the relevant component(s) added, the cuvette was repositioned, and measurements were resumed (15 ± 2 s dead time). All measurements are given as arbitrary units (AU). 'FluorEssence V3.5' software was used for plotting data and 'GraphPad Prism' was used to analyse data.

3.2.6 EMSAs

A standard reaction mixture (20 µl) was prepared in Buffer A (see section 3.2.3) with 5 nM Cyanine 5-labeled 144 bp nsDNA or 147 bp *parS2*-DNA, 2 mM of ATP, ADP, ATPγS or no nucleotide, with indicated final concentrations of ParB2. The reactions were assembled on ice, incubated for 30 min at 30 °C, and analysed by gel electrophoresis in 5% polyacrylamide gels in TBM (90 mM Tris, 150 mM Borate, 10 mM $MgCl_2$). Gel electrophoresis was pre-run at 120 V for 30 min, at 4 °C, in a Mini-PROTEAN Tetra Cell, and then run at 120 V for 1 h, at 4 °C. Gels were imaged using a Bio-Rad ChemiDoc™ MP Imaging System using the Cy5 channel with 2 min exposure. Images were analysed with ImageJ (NIH).

3.3 RESULTS

3.3.1 CTP facilitates ParB2-binding at *parS2* sites

V. cholerae Chr2 has nine 15 bp palindromic *parS2* sites, with six located closer to *oriC2* than the *ter* (**Yamaichi et al., 2007a; Figure 1.6C**). The number of ParB protein foci commonly observed within cells is lower than the available *parS* sites (**Erdman et al., 1999; Fogel and Waldor, 2006; Broedersz et al., 2014; Sanchez et al., 2015**). Propagation of ParB dimers to DNA flanking *parS*-sites is dependent on stochastic interactions on DNA (**Graham et al., 2014; Sanchez et al., 2015; Taylor et al., 2015**). A time-based, 90° light scattering assay was used to detect the formation of large ParB2-DNA complexes in solution. The method provided flexibility in the preparation of pre-mixed components, and the order of addition in reactions. Nucleoprotein complexes were only detected in the presence of *parS2* and CXP (**Figure 3.1A, B**). Increasing the number of *parS2* sites resulted in increased light scattering, indicative of larger complex formation. A slightly less-than-stepwise intensity increase was observed which suggests that a single *parS2* site is enough to load many ParB2 dimers onto the plasmid DNA utilised, while the presence of up to six *parS2* sites increased loading efficiency (**Figure 3.1C**). ParB2 also bound DNA containing *parS2* sites in the presence of CDP, but the relative intensity change was ~3-fold lower compared to with CTP (**Figure 3.1A**). Recent studies show ParB dimers to adopt a sliding clamp conformation with CTP that enables high-affinity binding at *parS* and propagation to flanking DNA regions. The CDP-bound conformation was proposed to confer instability to ParB-DNA-binding (**Soh et al., 2019**; **Osorio-Valeriano et al., 2019; Jalal et al., 2020a**). Accordingly, these light scattering data suggest that CTP facilitates ParB2 accumulation on *parS2*-DNA enclosed substrate, and CDP confers a less stable DNA association.

3.3.2 ParA2 interacts with DNA in the presence of ATP to form large nucleoprotein complexes

ParA DNA-binding activity in the presence of ATP facilitates colocalization with the nucleoid (**Sengupta et al., 2010; Fogel and Waldor, 2006)**, and ParA2 forms distinct structures on DNA with different nucleotide cofactors (**Hui et al., 2010; section 2.3.6)**. Here, assembly of a *V. cholerae* ParA2-DNA complex was observed in the presence of ATP (**Figure 3.1D**). The greatest amount of ParA2-DNA complex was observed with the slowly hydrolysing analogue, ATPγS, suggesting that ATP hydrolysis causes disassembly of the complex. Complex formation with ATPγS was not observed for plasmid P1 ParA and supports previous findings that ParA2 can interact with DNA in the presence of different adenosine nucleotides (**Havey et al., 2011; Hui et al., 2010**). ATP-binding (K124Q) and hydrolysis (K124R) defective

mutants showed abolished and diminished DNA-binding activities, respectively (**Figure 3.1E**). Permanent binding was expected for K124R, and native ParA2-ATP therefore has a specific conformation with ATP that facilitates a DNA-binding activity that was not accessible to ParA2 K124R.

ParA2 DNA-binding activities in the absence of nucleotide or with ADP were also not detected (**Figure 3.1B**). However, preincubation of ParA2 with DNA prior to the addition of ATP lead to a lower overall extent in intensity change, indicating ParA2 was maybe already partially bound to DNA, and less overall ATP-mediated DNA-binding was possible due to steric-hindrance (**Figure 3.1F**). ATP to ADP exchange lead to complex disassembly, which was recyclable upon re-addition of ATP. ATP was limited to 0.2 mM (five times lower) for complex assembly and a lower relative intensity change was attained. Addition of 0.5 mM ADP to the steady-state to challenge the stability of the ParA2-DNA complex, resulted in a slow disassembly over 1000 s before the rate slowed somewhat as the intensity approached that of t=0 (**Figure 3.1G**). Upon subsequent addition of 1 mM ATP, ParA2 re-bound DNA to a similar extent of the first round of assembly. This demonstrates that ParA2 is not aggregating, and its nucleotide exchange activities facilitate recyclable DNA interactions. ParA2 has been shown to bind DNA with high cooperativity and this has been shown for other ParA proteins (**Leonard et al., 2004**). Moreover, the ParA2-DNA structure formed with ATP was previously found to be large enough to be detected in pelleting assays (**Hui et al., 2010**). Disassembly of this nucleoprotein complex upon challenging with ADP, indicates that ParA2 is innately dynamic on DNA substrate. The slow rate of disassembly however demonstrates that, at the protein concentrations used, ParA2-ATP-DNA exchanges slowly with ParA2-ADP. The fact that ParA2 is likely already associated to DNA is probably the reason that ParA2 was able to re-form the large complex upon ATP addition, as it exchanged with the less well-ordered ParA2-ADP subunits on DNA (**Hui et al., 2010**). These observations indicate that the ATP-bound form of ParA2 is critical for forming a large nucleoprotein complex with DNA and that this activity can be impeded or reversed depending on available nucleotide conditions.

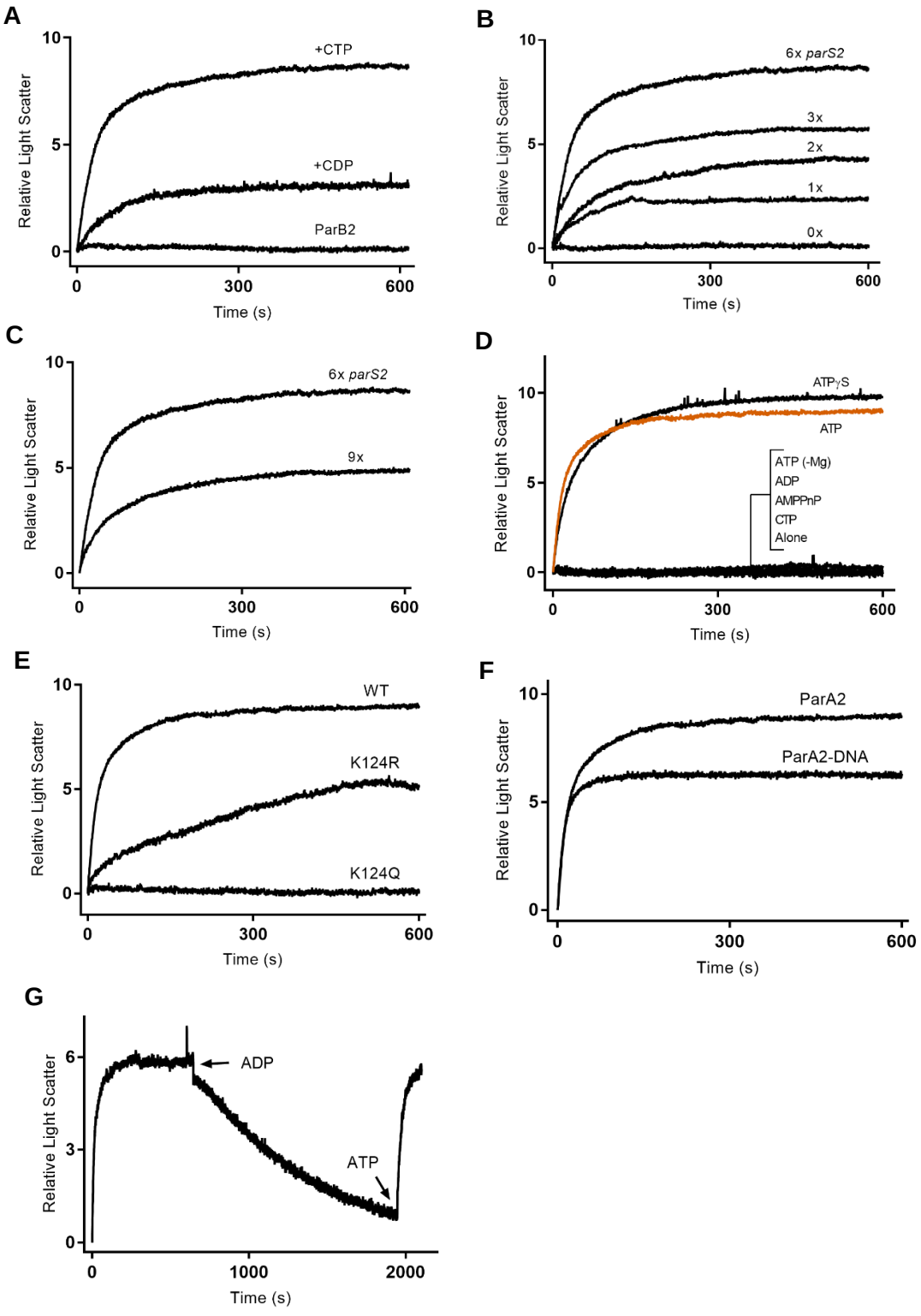
A
Relative Light Scatter
+CTP
+CDP
ParB2
Time (s)
B
6x parS2
3x
2x
1x
0x
C
6x parS2
9x
D
ATPγS
ATP
ATP (-Mg)
ADP
AMPPnP
CTP
Alone
E
WT
K124R
K124Q
F
ParA2
ParA2-DNA
G
ADP
ATP

Figure 3.1. ParA2 and ParB2 DNA-binding kinetics as detected by light scattering. A) ParB2 binding to pBKSII-*parS2* DNA alone, with CDP, and with CTP, indicated. 1 µM ParB2, 5 ng/µl pBKSII, and 1 mM nucleotide where indicated, were prepared in separate premixes. Premix 1 contained ParB2, while pBKSII and nucleotide were prepared in premix 2. Premixes were incubated for 15 min at 23 °C. Light scattering was measured after a 10 ± 2 s mixing time. 'Relative Light Scatter' was obtained by normalising individual data sets against initial intensities. **B)** ParB2 binding to pBKSII with an indicated number of *parS2* sites, in the presence of CTP. Reactions prepared as in (A). **C)** ParB2 binding to pBKSII-9x*parS2* relative to pBKSII-6x*parS2*. **D)** ParA2 binding to pBKSII with different adenosine nucleotides. Reaction scheme as in (**A**) but with ParA2 and adenosine nucleotides. For 'ATP (-Mg)' condition, reaction buffer was prepared with 2 mM EDTA and in the absence of Mg. **E)** DNA-binding kinetics in the presence of ATP of ATP-hydrolysis deficient ParA2 mutant variants, K124R and K124Q. Reactions set up as in (**D**). The reference curve is ParA2-DNA-binding with ATP from (**D**). **F)** Indirect demonstration of ParA2-DNA-binding prior to ATP-docking. There was reduced binding upon ATP addition possibly due to steric hindrance. For 'ParA2-DNA': 1 µM ParA2 and 5 ng/µl pBKSII were preincubated in premix 1, and ATP was prepared in premix 2. The reference curve is as in (**E**). **(G)** Nucleotide exchange effects on ParA2-ATP DNA-binding kinetics. 0.2 mM ATP was used for initial assembly. 0.5 mM ADP was added at steady-state to initiate disassembly. ATP was re-added at 1 mM as a steady-state was approached, as indicated with arrows.

3.3.3 ParA2-ParB2-DNA complex assembly is dependent on ATP, but not *parS2*

Next, ParA2-ParB2-DNA complex assembly kinetics were investigated. In an iterative approach, different combinations of ParA2, ParB2, DNA, and ATP were prepared. Two responses were evident in the data (**Figure 3.2B**). The assigned 'Group 1 (Gr.1)' response was observed when ATP was separated from ParA2 in pre-incubations, while the 'Gr.2' response was seen when ATP was pre-incubated with ParA2. Gr.1 was characterised by three-phase assembly kinetics, whereas only two phases were observed for Gr.2 (**Figure 3.2B**)**;** all curves are shown in **Figure 3.3**. A fast, initial phase was present for Gr.1 and corresponds to ParA2 binding ATP and quickly associating with DNA. This phase was missing in Gr.2 where ATP and ParA2 were pre-mixed; the higher initial intensity was attributed to the pre-formation of ParA2-ATP facilitating a higher initial extent of DNA-binding. Steady-state intensities were reached slowly for both groups (and relative to ParA2-ATP association with DNA). This is indicative of progressive interactions between ParA2, ParB2, and DNA.

A

	Reaction	Premix 1	Premix 2
Gr.1	1	ParA	ParB, DNA, ATP
	2	ParA, ParB	DNA, ATP
	3	ParA, DNA	ParB, ATP
	4	ParA, ParB, DNA	ATP
Gr.2	5	ParA, ATP	ParB, DNA
	6	ParA, ParB, ATP	DNA
	7	ParA, DNA, ATP	ParB

B

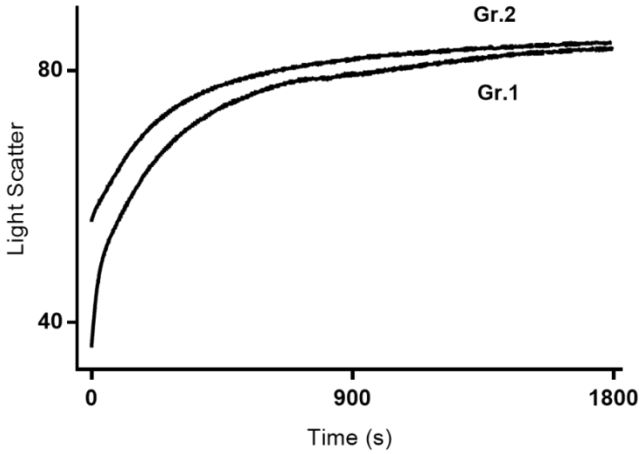

Figure 3.2. Order-of-addition effects on ParA2-ParB2-DNA complex assembly. A) Combinations of 1 μM ParA2, 1 μM ParB2, 5 ng/μl DNA (pBKSII), and 1 mM ATP were prepared in separate premixes, with ParA2 fixed to premix 1. Group 1 (Gr.1) and Gr.2 comprise combinations where ParA2 and ATP were either separate or together, respectively. **B)** Representative curves of changes in light scattering for Gr1 and Gr2 combinations. 'Light Scatter' represents raw light scattering intensities for appropriate comparisons to be made. All curves are shown in **Figure 3.3**.

Reaction		Premix 1	Premix 2
Gr.1	1	ParA	ParB, DNA, ATP
	2	ParA, ParB	DNA, ATP
	3	ParA, DNA	ParB, ATP
	4	ParA, ParB, DNA	ATP
Gr.2	5	ParA, ATP	ParB, DNA
	6	ParA, ParB, ATP	DNA
	7	ParA, DNA, ATP	ParB

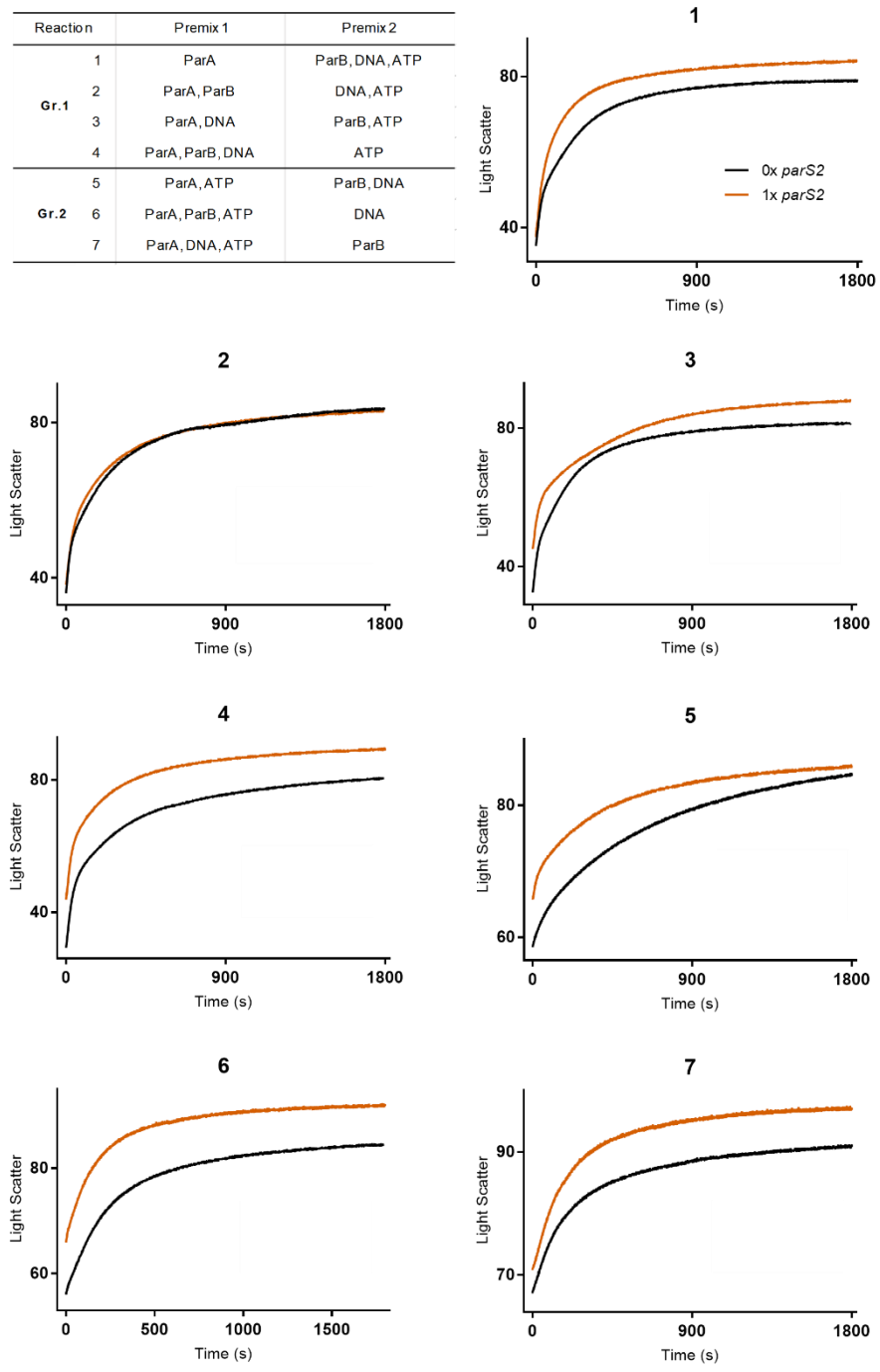

Figure 3.3. Order-of-addition effects on ParA2-ParB2-DNA complex assembly (all reactions). There are two curves for each reaction. Premixes were coloured to depict when pBKSII (black) or pBKSII-*parS2* (orange) was used. 1 μM ParA2, 1 μM ParB2, 5 ng/μl DNA and 1 mM nucleotide used throughout. Numbers on top of graphs indicate corresponding reaction from table.

A sequential acquisition displayed the additive effects of ParA2-DNA-binding in the presence of ATP, followed by ParB2 addition (**Figure 3.4A**). Protein-protein interactions, as well as individual DNA-binding activities, therefore contributed to complex assembly. As expected, sequential addition of DNA, ParB2, and then ParA2 showed no noticeable increase in light scattering until the addition of ATP (**Figure 3.4B**). Interestingly, upon addition of ATP, there was a rapid increase in light scattering that was missed during component addition and mixing (15 ± 2 s). This was largely attributed to ParA2-ATP being recruited to the already DNA-bound ParB2, which itself does not form a large enough complex for detection. Thus, in addition to high-affinity DNA-binding activity, ParA2-ATP is required for protein-protein interactions with ParB2 that leads to large nucleoprotein complex formation (DNA-ParA2-ParB2-DNA).

The ParA2-ParB2-DNA complex was innately stable with the component concentrations used and there was no sign of disassembly over the duration of the experiments. Assembly kinetics were very similar in the presence of *parS2* (pBKSII-*parS2*), but higher overall intensities were reached for all conditions (**Figure 3.3**). As with most studied ParA proteins, ParA2-ATP hydrolysis is weak and stimulated by ParB2 and DNA (**section 2.3.1; Lim et al., 2014; McLeod et al., 2017; MacCready et al., 2018**). By restricting ATP concentration (0.1 mM instead of 1 mM), the available ATP diminished as it was turned over due to ATP hydrolysis, resulting in slow complex disassembly over 3000 s (**Figure 3.4C**). ParA2-ParB2-DNA complex formation in the presence of ATPγS at the same concentration for comparison, showed no noticeable decrease in signal (**Figure 3.4D**). The complex formed in the presence of ATPγS was also larger, again signifying the role of ongoing ParA2-ATP hydrolysis in complex disassembly. As with ParA2-ATP DNA-binding, ATP to ADP exchange lead to rapid complex disassembly (**Figure 3.4E**). When 0.5 mM ATP was used initially to reach a steady-state intensity, disassembly could be initiated with 1 mM ADP. This was followed by addition of 2 mM ATP for complex reassembly to a similar extent achieved in the first round of assembly. A multi-phasic disassembly was observed, with an initial fast phase followed by a much slower second phase, before reaching a steady-state intensity. The fast phase is indicative of ParA2 losing protein-protein interactions with ParB2 as the former was exchanged with ParA2-ADP. The slower phase corresponds to disassembly of stable ParA2-ATP-DNA complexes with ADP exchange. Since ParB2 and DNA both stimulate ParA2-ATP hydrolysis up to 8-fold, this likely enhanced DNA disassembly. ParA2 therefore loses protein-protein interactions with ParB2 faster than dissociating from DNA when the stability of the ParA2-ParB2-DNA complex is challenged with ADP (**Havey et al., 2012; Osorio-Valeriano et al., 2019**).

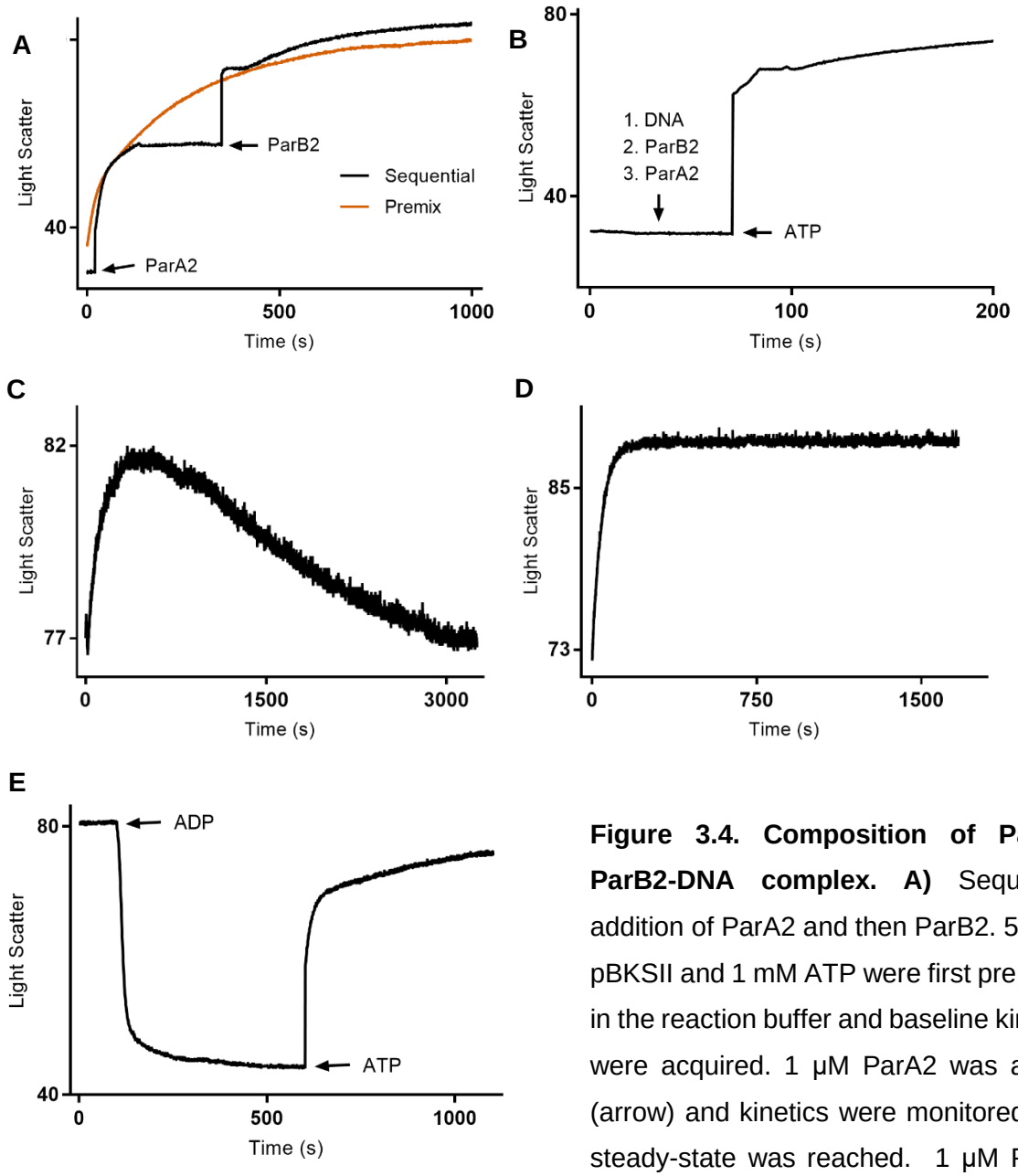

Figure 3.4. Composition of ParA2-ParB2-DNA complex. A) Sequential addition of ParA2 and then ParB2. 5 ng/µl pBKSII and 1 mM ATP were first prepared in the reaction buffer and baseline kinetics were acquired. 1 µM ParA2 was added (arrow) and kinetics were monitored until steady-state was reached. 1 µM ParB2 was then added and reaction monitoring was resumed. A 15 ± 2 s mixing time was required for component addition events. **B)** Sequential addition of ParB2 and then ParA2. 5 ng/µl DNA was first prepared in the reaction buffer and baseline kinetics were acquired. 1 µM ParB2 and then 1 µM ParA2 were added (arrow) and the reaction was monitored. 1 mM ATP was then added. **C)** The effect of ATP hydrolysis on the Par complex. Sample was prepared as in 'Reaction 1' from **Figure 3.2A**, but with 0.1 mM ATP. **D)** ATPγS stabilises the Par complex. As in (C), but with ATPγS. **E)** Nucleotide exchange causes complex disassembly. 0.5 mM ATP was used for initial assembly with 1 µM ParA2, 1 µM ParB2, and 5 ng/µl DNA (pBKSII). 1 mM ADP was added as indicated at steady-state to initiate disassembly. 2 mM ATP was introduced as indicated for complex reassembly.

3.3.4 Absolute and relative component concentrations affect complex size

The individual effects of ParA2, ParB2, and DNA concentrations on the extent of the assembled complex were examined. For each condition, ParA2-ParB2-DNA assembly kinetics were acquired upon addition of ATP, and end-point light scattering intensities were plotted (**Figure 3.5A-C**). A low level of ParA2 (0.5 µM) supported a small signal change, while there was an apparent saturation of ParA2 interacting with ParB2 and DNA by 2 µM (**Figure 3.5A**). There were similar end-point intensities for 1 µM and 2 µM ParA2. Due to the slightly slower kinetics, 1 µM ParA2 was viewed as the optimal concentration, as less of the initial kinetics were missed during the required reaction mixing time (binding curves not shown).

As already determined, a ParA2-ATP-DNA complex forms in the absence of ParB2 (**Figure 3.5B**), and the addition of even a sub-stoichiometric concentration of ParB2 (0.5 µM) was enough to form a significantly larger complex. Lower end-point intensities were attained for concentrations above 1 µM ParB2. A likely contributing factor of higher ParB2 apparently destabilising the ParA2 interactions that facilitate ParA2-ParB2-DNA complex formation, is increased stimulation of ParA2 ATPase activity, as seen in section 2.3.1. A key difference was observed compared to plasmid P1 ParB, with a small increase in end-point intensity as ParB2 was increased to 8 µM (**Figure 3.5B**) (**Havey et al., 2012**). This result suggests the destabilising effects are overcome as ParB2 itself begins to contribute more to the overall complex assembly.

Increasing DNA concentration caused a general, albeit slight, decrease in complex size and can be explained by DNA being more sparsely populated by ParA2 and ParB2, and in turn affecting protein-protein interactions (**Figure 3.5C**). This would also affect the NTD bridging interactions of ParB2. The component concentrations to produce the largest complex, along with optimal assembly kinetics were 1 µM ParA2, 1 µM ParB2, and 5 ng/µl DNA (1 ParA2 dimer: 1 ParB2 dimer: 15 bp DNA). While ParA2 at low concentration interacts with ParB2 and DNA, an optimal saturation point is quickly reached as ParA2 is increased. Meanwhile, complex assembly was shown to be sensitive to sub-stoichiometric or high ParB2 levels, as has been demonstrated for plasmid P1 partition complex assembly (**Funnell and Bouet, 1999; Easter and Gober, 2002; Havey et al., 2012**). Intracellular ParA and ParB concentrations are also reportedly in the 1-2 µM range and deviations perturb partition (**Lim et al., 2014; Graham et al., 2014**). The absolute, as well as relative, concentrations of ParA2 and ParB2, are important for overall complex assembly, and a high protein to DNA ratio was optimal with this technique.

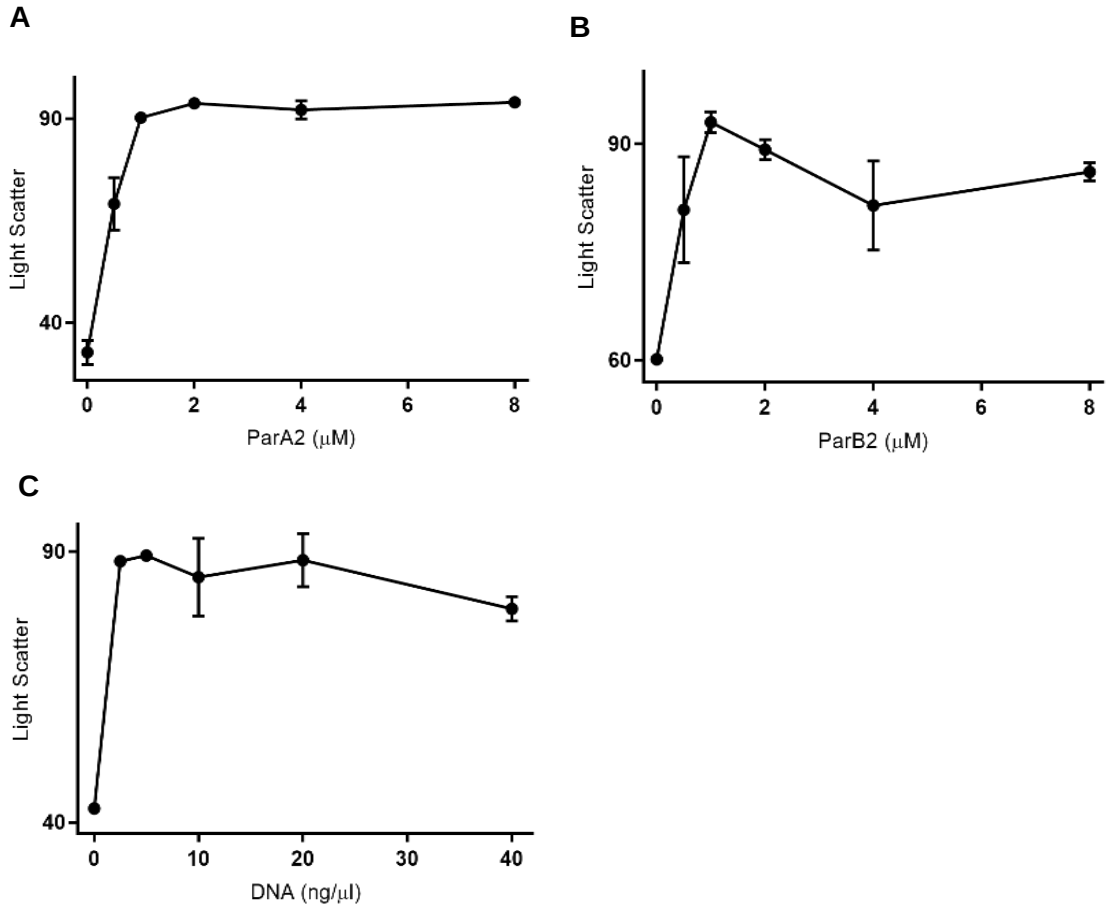

Figure 3.5. Stoichiometric effects on ParA2-ParB2-DNA complex assembly kinetics. A) Effect of varying ParA2 concentration on total relative light scattered in ParA2-ParB2-DNA complex assembly. Indicated concentrations of ParA were prepared with 1 μM ParB2, 5 ng/μl pBKSII. A 15 ± 2 s mixing time was required to add 1 mM ATP and mix to begin date acquisitions. End-point measurements after 2000 s are shown. **B)** As in (**A**) except for varying ParB2. 1 μM ParA2 used throughout. **C)** As in (**A**) except for varying pBKSII. 1 μM ParA2 and ParB2 used.

3.3.5 ParA2-ParB2-DNA complex assembly with CTP is sensitive to order of component addition

Next, the intention was to incorporate CTP into the partition complex assembly in a way that would enable comparisons to be made between conditions with relative ease. In utilising the reaction scheme in section 3.3.3 (**Figure 3.2A)**, CTP was systematically added to each individual premix in order to acquire a range of conditions, which would give an informed insight into the effect on assembly kinetics. NsDNA was first tested to reveal visibly faster assembly rates and higher initial intensities for Gr.1 reactions in the presence of CTP (**Figure 3.6**). It is likely that ParB2 could bind nsDNA with higher affinity in the presence of CTP, even though this did not produce a detectable complex when examined in isolation (**Figure 3.1B**). Alternatively, protein-protein interactions with ParA2 may be augmented for ParB2 in the presence of CTP such that a faster assembly rate ensues. In support of this, the conserved CTP-binding domain of the ParB-like protein, PadC from *M. xanthus*, was shown to be sufficient for the interaction with ParA in the presence of CTP (**Osorio-Valeriano et al., 2019**).

Both Gr.1 and Gr.2 reactions could be further sub-categorised into curves that reached higher or lower end point intensities depending on how CTP was incorporated into reactions (**Figure 3.7A**). Accordingly, curves categorised into Gr.1A and Gr.2A are representative of when ParB2 and CTP were pre-incubated separately, and these reactions reached the lower end-point intensities. Alternatively, Gr.1B and Gr.2B curves represent ParB2 and CTP being pre-incubated together, and reached the higher relative end-point intensities (**Figures 3.6** and **3.7A**). These data show that CTP augments ParB2-nsDNA-binding activity. For Gr.1A and Gr.2A reactions, this would have resulted in ParB2 contributing less to the overall complex assembly relative to conditions with pre-formed ParB2-CTP. ParA2-ATP would be able to occupy more DNA during the additional time required for ParB2 to bind CTP, and subsequently commence DNA-binding and protein-protein interactions. There would therefore be less be less DNA freely available for ParB2-CTP in Gr.1A and Gr.2A reactions compared to the Gr.1B and Gr.2B reactions. The influence of pre-formed ParB2-CTP on partition complex assembly with nsDNA was clear as the largest complexes detected over the duration of the experiments were for the two conditions where ParB2, CTP, and DNA were incubated together (**Figures 3.6** and **3.7A**).

Reaction		Premix 1	Premix 2
Gr.1	1	ParA	ParB, DNA, ATP
	2	ParA, ParB	DNA, ATP
	3	ParA, DNA	ParB, ATP
	4	ParA, ParB, DNA	ATP
Gr.2	5	ParA, ATP	ParB, DNA
	6	ParA, ParB, ATP	DNA
	7	ParA, DNA, ATP	ParB

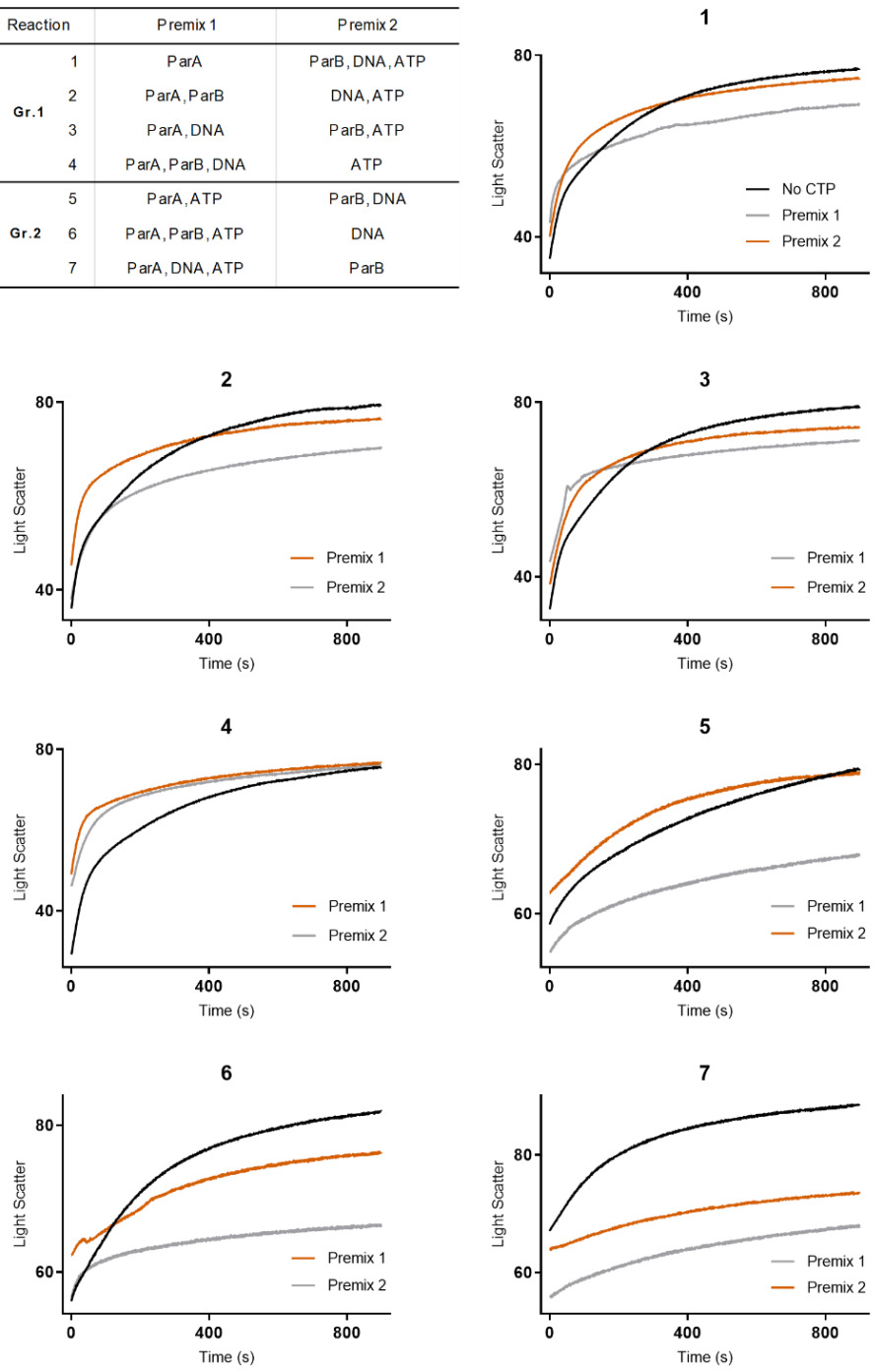

Figure 3.6. Order-of-addition effects on ParA2-ParB2-DNA complex assembly kinetics with CTP (all reactions). There are two curves for each reaction with CTP added to individual premixes as well as a reference reaction in the absence of CTP (black). Premixes were coloured to depict when ParB2 and *parS2* were separate (grey) or together (orange). 1 μM ParA2, ParB2, 5 ng/μl pBKSII and 1 mM nucleotide used throughout.

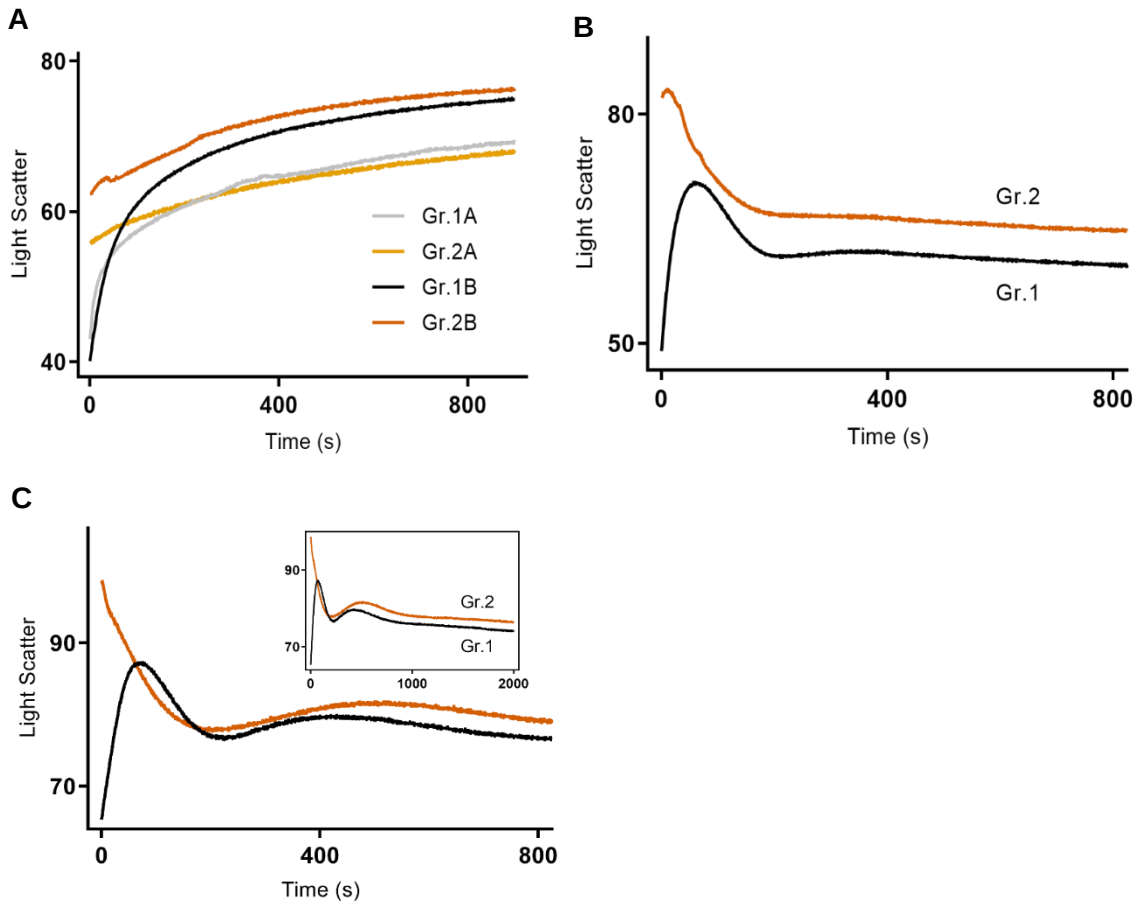

Figure 3.7. The effect of CTP on ParA-ParB-DNA complex assembly. A) A larger Par complex is attained when ParB2 is preincubated with CTP. The reaction scheme in **Figure 3.2** was used to iteratively add CTP. Four representative curves show CTP addition for Gr.1 and Gr.2 reactions (nsDNA). All curves are shown in **Figure 3.6**. Gr.1 reactions: when ParB2 was pre-incubated separately from CTP (Gr.1A), a lower steady-state intensity was observed relative to when ParB2 was with CTP (Gr.1B). Similarly, for Gr.2 reactions: when ParB2 was pre-incubated separately from CTP (Gr.2A), lower initial and steady-state intensities were observed relative to when ParB2 was pre-incubated with CTP (Gr.2B). As in **Figure 3.2**, 1 μM ParA2, ParB2, 5 ng/μl pBKSII, and 1 mM nucleotide were used throughout. **B)** CTP causes complex disassembly to a lower steady-state intensity with *parS2* DNA. As in (**A**) but with pBKSII-*parS2* and only Gr.1B and Gr.2B conditions are shown. All curves are shown in **Figure 3.8**. **C**) An oscillatory dynamic occurs with increased number of *parS*2 sites. The inset shows a prolonged acquisition with a pronounced initial oscillation. As in (**B**) but pBKSII-6x*parS2* was utilised. Black and orange curves for all plots are representative Gr.1B and Gr.2B reactions.

3.3.6 CTP facilitates a dampened protein oscillation on *parS2* DNA

In order to investigate the effects of ParB2-CTP binding to *parS2* DNA, the same reaction scheme described in section 3.3.5 was used, but pBKSII-*parS2* was utilised in place of pBKSII. Intriguingly, most experiments exhibited a striking disassembly to a lower steady-state intensity (**Figure 3.8**), and the most dynamic conditions are shown as Gr.1B and Gr.2B curves (**Figures 3.7B**) for direct comparison with nsDNA (pBKSII) (**Figure 3.7A**). As described earlier, ParB-CDP is more likely than ParB-CTP to spontaneously dissociate from nucleotide and DNA (**Soh et al., 2019**). In general, there was a propensity for faster disassembly kinetics when ParB2 was preincubated with CTP for each reaction (**Figure 3.8,** orange curves). The fastest disassembly kinetics were observed with preformed ParB2-CTP-*parS* (**Figure 3.7B**). These conditions would lead to ParB2-CDP being reached quickest as the closed ring ParB-CTP conformation at *parS* forms the catalytic site for CTP hydrolysis. Instability of ParB2-CDP on DNA is a possible feature of the observed disassembly kinetics to a lower steady-state.

Prior to the disassembly event, higher intensities were reached with pBKSII-*parS2* than with pBKSII. This was attributed to greater ParB2 enrichment on DNA comprising *parS2* (**Figure 3.1B**), and in turn an increased number of CXP-mediated interactions between ParB2 and ParA2-ATP, as was indicated with nsDNA. The influence of these interactions was demonstrated further as the Gr.2 condition (with higher available ParA2-ATP) reached a significantly higher initial intensity (**Figure 3.7B**). Interestingly, disassembly also began earlier on for the Gr.2 condition and is suggestive of ParA2-ATP activity also driving disassembly. Interestingly, the addition of more *parS2* sites lead to apparent dampened oscillatory kinetics (**Figure 3.7C**). pBKSII-6x*parS2* was used to show that both Gr.1 and Gr.2 conditions decreased to a similar, lower threshold intensity before a slight reassembly and disassembly event. With regards to the slight reassembly phase, it was thought that the higher number of available *parS2* sites could transiently increase the rate of ParB2-CXP nucleation on DNA as the steady-state intensity was approached, with interactions with ParA2-ATP also pertinent.

Reaction		Premix 1	Premix 2
Gr.1	1	ParA	ParB, DNA, ATP
	2	ParA, ParB	DNA, ATP
	3	ParA, DNA	ParB, ATP
	4	ParA, ParB, DNA	ATP
Gr.2	5	ParA, ATP	ParB, DNA
	6	ParA, ParB, ATP	DNA
	7	ParA, DNA, ATP	ParB

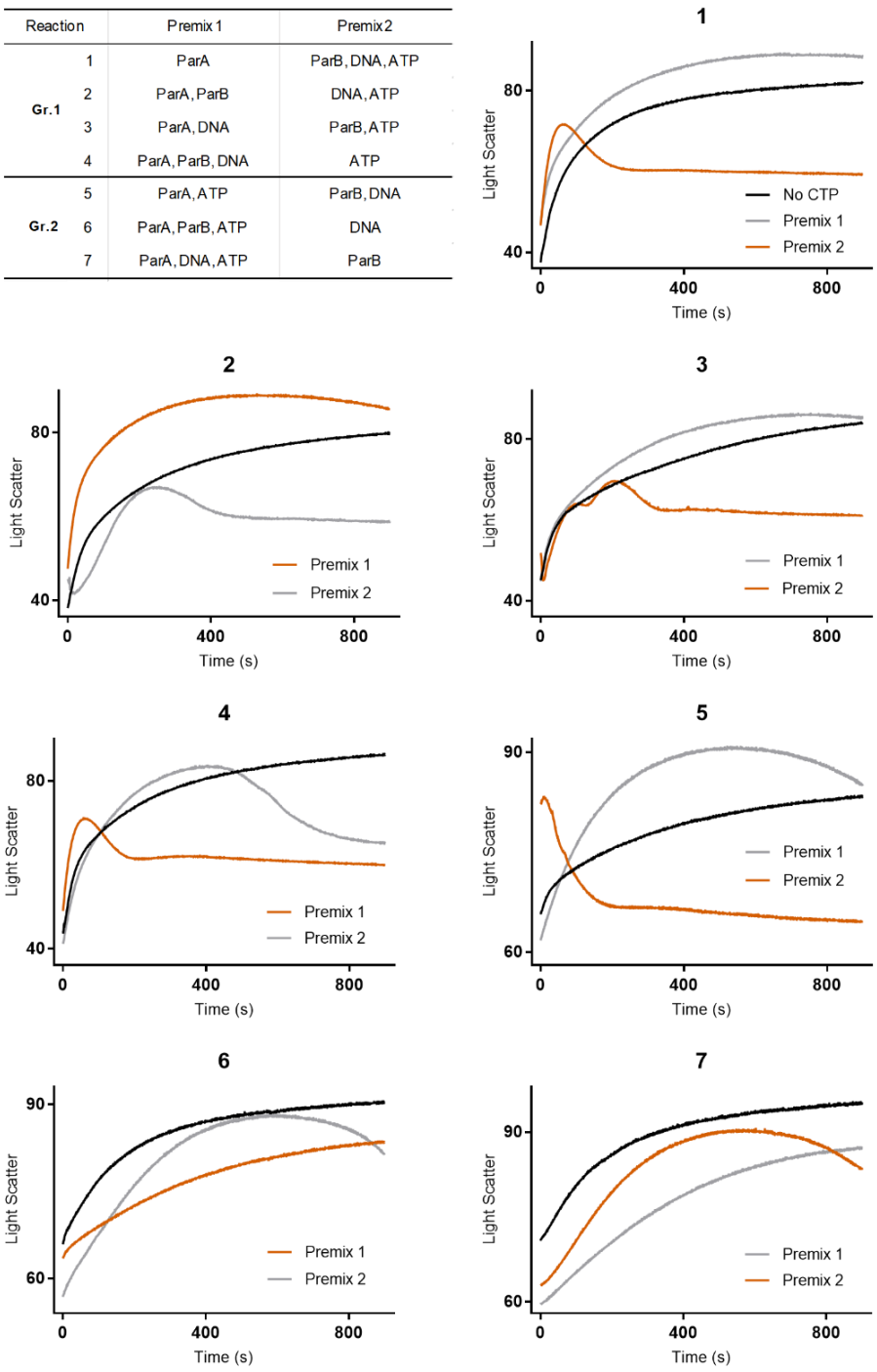

Figure 3.8. Order-of-addition effects on ParA2-ParB2-parS2 complex assembly kinetics with CTP (all reactions). There are two curves for each reaction as CTP was added to individual premixes and curves were plotted against a reference of the same reaction in the absence of CTP (black). Premixes were coloured to depict when ParB2 and *parS2* were separate (grey) or together (orange). 1 μM ParA2, ParB2, 5 ng/μl pBKSII-*parS2*, and 1 mM nucleotide used throughout.

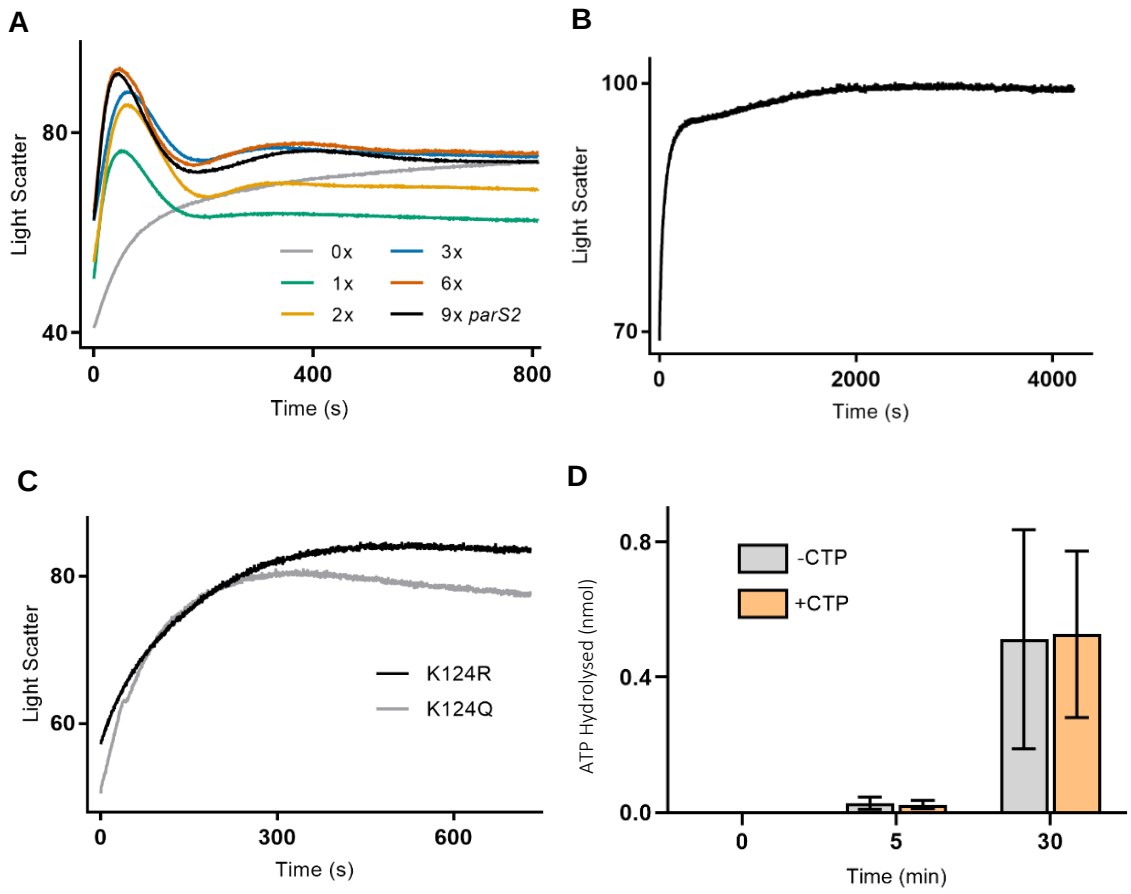

Figure 3.9. Examining oscillatory kinetics. A) Increasing *parS2* site number enhances oscillatory kinetics. Curves for pBKSII with an indicated number of *parS2* sites are shown. Samples were otherwise prepared as in 'Reaction 1', orange curve from **Figure 3.8**. **B**) ParA2-ATPγS does not support partition complex oscillation dynamics**.** Reaction set up as in (A) but only for pBKSII-6x*parS2* and in the presence of ATPγS in place of ATP. **C)** ParA2 K124R and K124Q proteins do not support oscillation complex dynamics. Reaction set up as in (A) but only for pBKSII-6x*parS2*. **D)** ParA2-ATPase activity in the presence of ParB2-*parS2*-CTP is not stimulated beyond that seen with ParB2-*parS2*. ParA2 was incubated with ParB2, pBKSII-*parS2*, CTP, 0.2 mM ATP, and 32 nM radiolabelled [α-^{32}P]-ATP. Reactions were quenched at the indicated time points and thin layer chromatography was used to separate hydrolysis product. A phosphor screen was used to quantify the hydrolysis product.

Oscillatory dynamics were dependent on native ParA2 activities with ATP. Assembly with ATPγS instead of ATP abolished disassembly (**Figure 3.9B**), and both ParA2 K124Q and K124R in the presence of ATP facilitated assembly of a more stable complex than native ParA2 (**Figure 3.9C**). Stimulated ParA2 ATPase activity was not thought to be a feature of the oscillations as there was no detectable difference in ATPase activity when CTP was present than when in the presence of ParB2 and *parS2* alone (**Figure 3.9D**). Alternatively, when fitted to a single exponential equation, the rate of ParA2 DNA association with ATP (0.074 s^{-1}) was much faster than ParB2 association to 6x*parS2* DNA (0.039 s^{-1}). ParA2 DNA association with ATPγS (0.048 s^{-1}) was also faster, but by a much smaller margin. The apparent instability of ParB2-CDP, coupled to the stable formation of ParA2-ATP complexes with DNA, could account for the disassembly kinetics observed.

The composition of the lower intensity complex was still not clear, as well as the full extent of disassembly. A sequential acquisition was subsequently performed where ParA2 first formed a complex with pBKSII-6x*parS2* DNA in the presence of both ATP and CTP, and ParB2 was then added. It was shown that the end point intensity was larger than the ParA2-ATP-DNA complex (**Figure 3.10A**). ParA2 nucleotide exchange experiments gave further insight. 0.5 mM ATP and 1 mM CTP were used to reach a steady-state intensity, upon which, 1 mM ADP was added. Dissociation was visibly slower than ParA2-ParB2-DNA complex dissociation (**Figure 3.10B**). This is maybe indicative of less ParA2-ParB2 interactions being interrupted and an apparent slower rate of dissociation supports the idea that ParA2 contributes a larger proportion of this complex. The addition of 2 mM ATP showed that the oscillatory assembly is recyclable (**Figure 3.10B**). Consistent with previous order of addition results, a slower oscillation was attained upon addition of CTP when the ParA2-ParB2-*parS2* complex was first formed and disassembled (**Figure 3.10C**). An important finding was that this was also seen upon the addition of CDP and in fact was slightly faster to resume oscillatory behaviour (**Figure 3.10D**). The timing of disassembly kinetics is therefore controlled by ParB2 reaching the CDP-bound state and the smaller complex size is a result of (incomplete) disassembly of ParB2-CDP such that it contributes less to the overall *Vc*ParABS2 complex.

The Par protein oscillations were investigated in more detail by varying nucleotide and protein concentrations. Varying parameter effects on kinetics were compared against the Gr.1 reference curve in **Figure 3.7C**. CTP concentration was first lowered to a ratio of 1 mM ATP: 0.1 mM CTP. The higher proportion of available ParA2-ATP caused a higher initial intensity to be reached (t=0), while a slightly lower peak (and less overall disassembly) showed the effect of less ParB2-CXP contribution (**Figure 3.11A**). The fact that disassembly began before the reference curve corroborates the previous notion that ParA2-ATP activity appears to drive disassembly. There was a similar extent of reassembly to the reference curve, and potentially

shows that ParB2-CXP rebinding at *parS2* sites reinstates interactions between ParB2, and ParA2-ATP associated with DNA. In comparison, lower ATP (0.1 mM ATP: 1 mM CTP) yielded a lower starting intensity and a delayed disassembly relative to the reference curve (**Figure 3.11B**). There was a reduced extent of reassembly with less available ParA2-ATP. As expected, increasing ParA2 concentration to 2 µM resulted in a significantly higher starting intensity and almost immediate disassembly (**Figure 3.11C**). Thereafter, there was a lesser extent of disassembly and only a very slight reassembly event. This was attributed to ParA2-ATP coating more *parS2* sites and effectively inhibiting ParB2 reaching the CDP state. ParB2-CTP was further inhibited from binding at *parS2* sites when ParA2 was increased to 4 µM, such that disassembly was more subtle (**Figure 3.11C**). These data match the stoichiometry data in **Figure 3.5A** showing increased ParA2 concentrations stabilises the Par complex. Increasing ParB2 to 2 µM and 4 µM did little to change the overall kinetics apart from a general increase in intensity (**Figure 3.11D**). 8 µM ParB2 was also tested with roughly the same kinetics as for 4 µM (data not shown), and suggests saturation of binding to the available *parS2* sites. Alternatively, if stimulated ParA2-ATPase activity caused disassembly, the kinetics would theoretically be sensitive to the concentration of ParB2. Reassembly was slightly affected with ParB2 at 4 µM, as ParB2-CTP would outcompete ParA2-ATP for DNA-binding. This would cause less ParA2-ATP-DNA interaction with ParB2-CTP-DNA. Finally, for most of the conditions, a steady-state between ParA2 and ParB2 activities was reached after around 600 s. Taken together, these results could suggest that the oscillatory behaviour on *parS2* DNA is caused by an intricate interplay between DNA association activities of ParA2-ATP and ParB2-CDP, with protein-protein interactions displaying the oscillations.

In order of addition experiments, the observed number of different disassembly timings between all conditions highlighted the influence of protein-protein and protein-DNA interactions in inhibiting oscillatory complex dynamics (**Figure 3.8**). Moreover, ParB2 binding to nsDNA and *parS2* in the absence of CTP was confirmed with EMSAs (**Figure 3.12**). There was a shift at relatively low ParB2 concentrations denoting specific binding species in contrast to with nsDNA, where there was a gradient of complexes. There was a large complex formed that was immobile as ParB2 was increased to 300 nM and this was also observed with *parS2*. There was, however, incomplete binding to nsDNA at even at high concentrations, whereas no free *parS2* DNA was detected.

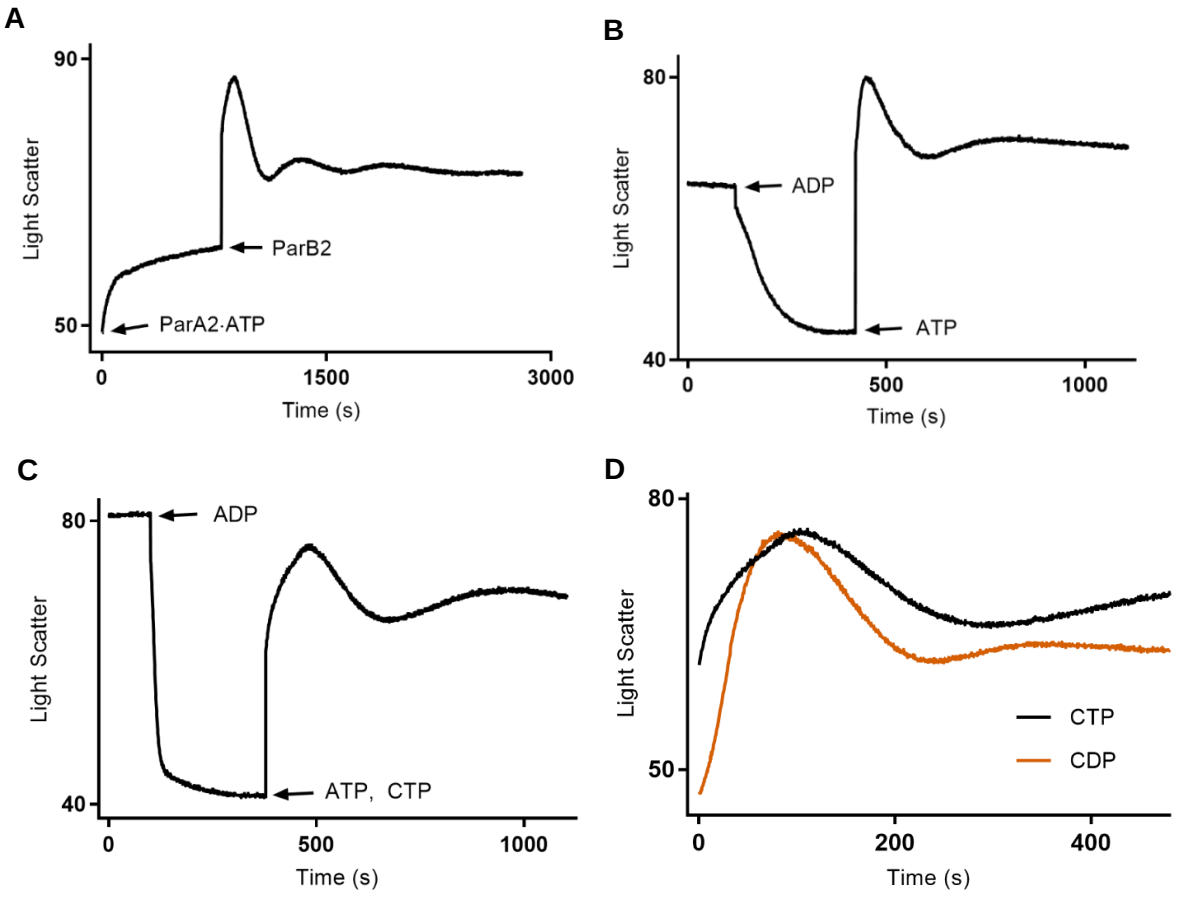

Figure 3.10. Sequential addition effects on oscillatory kinetics. A) ParA2 assembly on DNA followed by ParB2 addition. 1 μM ParA2 was added to 5 ng/μl pBKSII-6x*parS2*, 1 mM ATP and CTP. Kinetics were acquired until a steady-state was approached. 1 μM ParB2 was then added as indicated. A 15 ± 2 s mixing time was required for component addition events. **B)** Nucleotide exchange causes disassembly. 0.5 mM ATP was used for initial (oscillatory) assembly of 1 μM ParA2, 1 μM ParB2, and 5 ng/μl pBKSII-6x*parS2*, and 1 mM CTP. 1 mM ADP was added at steady-state to initiate disassembly. ATP (2 mM) was re-added, as indicated. **C)** Slower oscillation arises from disassembly of a previously non-oscillatory complex. 0.5 mM ATP was used for initial assembly 1 μM ParA2, 1 μM ParB2, and 5 ng/μl pBKSII-6x*parS2*. 1 mM ADP was added at steady-state to initiate disassembly. ATP (2 mM) was re-added, along with 1 mM CTP, as indicated by the arrow. **D)** Nucleotide exchange-mediated reassembly in the presence of CDP results in faster oscillation kinetics than with CTP. As in (**C**), but only reassembly shown with CDP. Reassembly kinetics from (**C**) used as a reference.

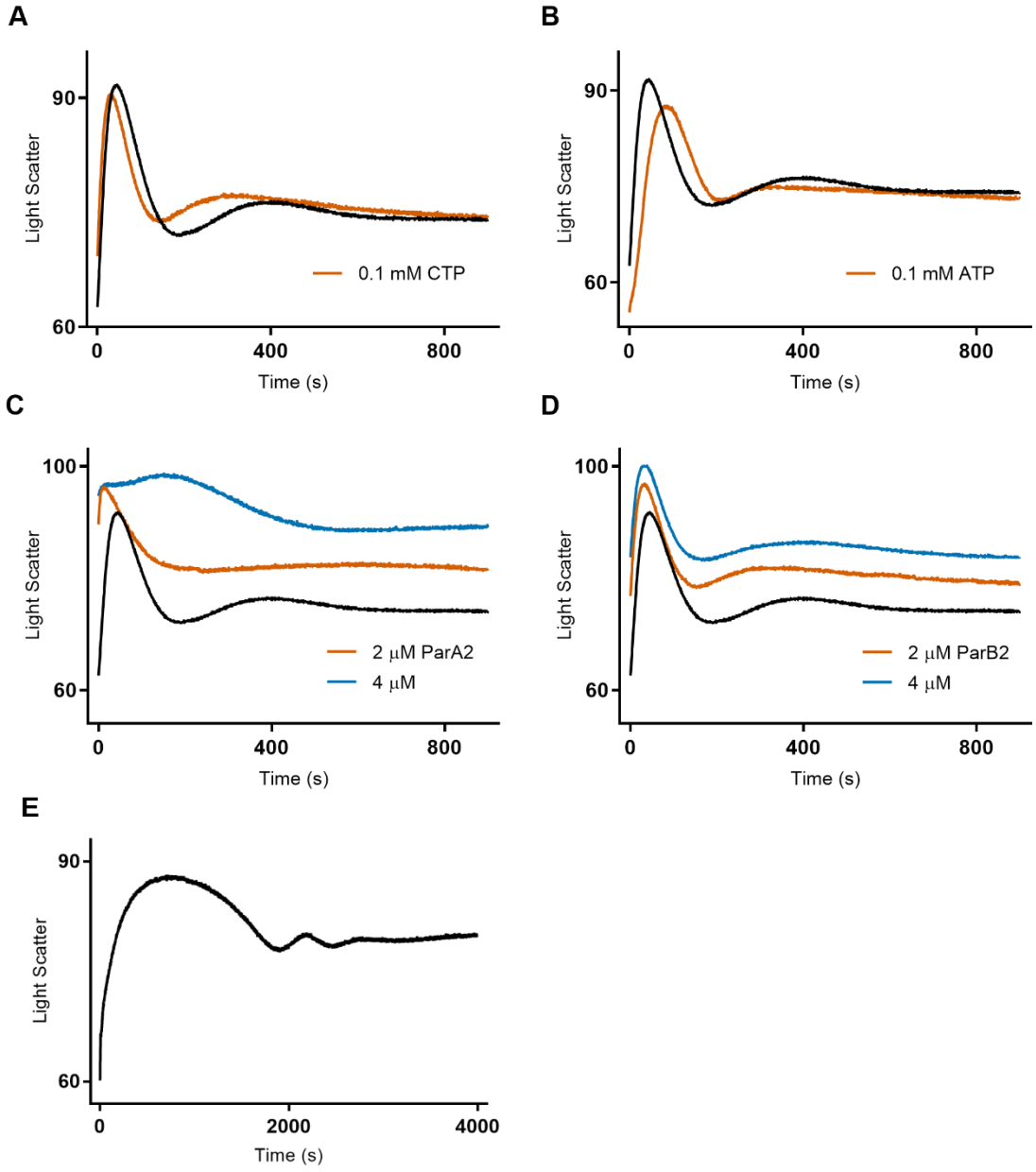

Figure 3.11. Component concentration effects on ParA2-ParB2-*parS2* complex oscillations. A) Lower CTP concentration causes visibly faster initial complex assembly. ParA2 prepared alone in premix 1. 1 μM ParB2 incubated with 5 ng/μl DNA (pBKSII-6x*parS2*), 1 mM ATP, and 0.1 mM CTP in premix 2. Kinetics plotted against a reference curve from **Figure 3.9A** (6x*parS2*). **B)** Lower ATP leads to slower initial assembly, and less reassembly. As in (**A**) but with 0.1 mM ATP and 1 mM CTP. **C)** Higher ParA2 concentrations leads to very fast initial assembly and less subsequent disassembly. As in (**A**) but with indicated ParA2 concentrations, 1 mM ATP, and 1 mM CTP. **D)** Higher ParB2 causes a general increase in light scattering intensity. As in (**A**) except with indicated ParB2 concentrations, 1 mM ATP and 1 mM CTP. **E)** pBKSII-6x*parS* used in a prolonged acquisition to show eventual disassembly dynamics of 'Reaction 1', grey curve from **Figure 3.8**.

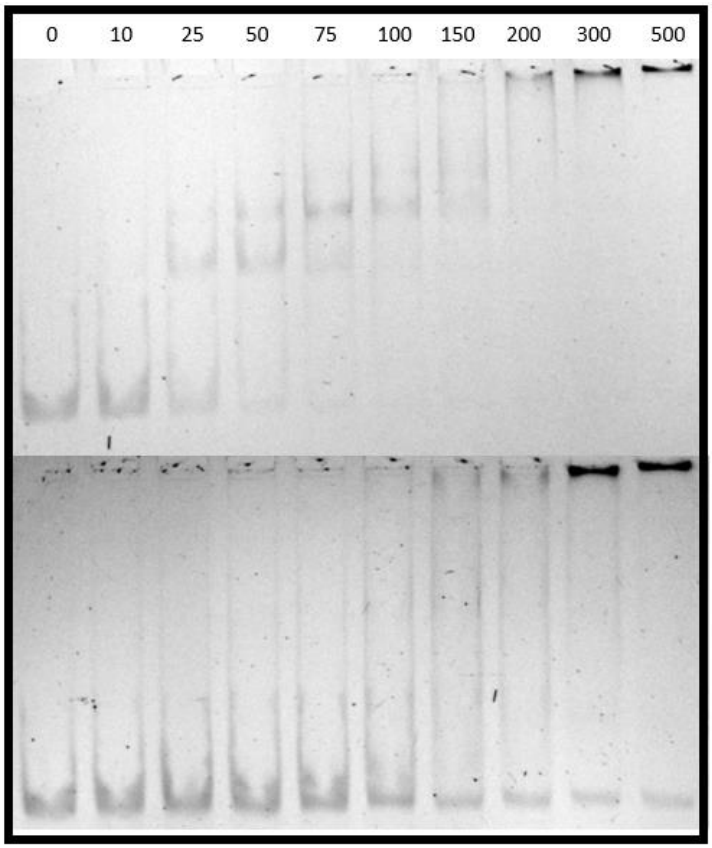

Figure 3.12. ParB2 DNA-binding activity as detected by gel-mobility shift assay. Top panel: Indicated concentrations of ParB2 (nM) binding to 5 nM Cy5-labelled 147 bp *parS2* DNA. Specific parS2-binding species can be seen from 10-150 nM ParB2. A complete shift (immobile complexes in the well) was seen from 300 nM and represents ParB2 binding all available DNA. **Bottom panel:** As in top panel but with 144 bp nsDNA. A gradient of ParB2-nsDNA-binding species was seen from 100-200 nM ParB2. As with (**A**), an immobile complex was observed from 300 nM ParB2. Incomplete binding was shown with free-nsDNA at the bottom of the gel for 300 and 500 nM ParB2.

3.4 DISCUSSION

3.4.1 Self-assembly of the *Vc*ParABS2 partition complex

Light scattering has been used to show real-time partition complex assembly for a chromosomal ParABS system. *V. cholerae* ParABS2 is classed similarly to plasmid systems and correspondingly shows the same basic assembly requirements whereby ParA2 and ParB2 were able to interact with DNA, and each other, in an ATP-dependent manner (**Bouet and Funnell, 1999; Pratto et al., 2008; Havey et al., 2012**). Crucially, a distinct feature with this method is individual Par protein DNA-binding activities were detected and it was therefore possible to probe the influence each had on overall complex formation (**Figure 3.1**). Recent studies have comprehensively demonstrated that canonical ParB proteins have a CTP-binding domain that is critical for ParB DNA-binding activities, as well as for interaction with ParA (**Soh et al., 2019; Osorio-Valeriano et al., 2019; Jalal et al., 2020a**). Indeed, ParB2 binding to *parS2*-DNA was only detected with CTP. Remarkably, *Vc*ParABS2 complex kinetics exhibited oscillatory behaviour with ATP and CTP. This iteration of *Vc*ParABS2 complex kinetics is thought to be a pronounced example of dynamic interplay between Par components on DNA that is present for all conditions tested.

ParA dimers co-localise on the nucleoid via ATP-mediated DNA-interaction, and variations of the Brownian-ratchet model for plasmid partition define a subsequent interaction between ParA and the ParB-*parS* partition complex (**Lim et al., 2014; Vecchiarelli et al., 2014b**). This interaction is thought to occur at a central ParA dimer region and the NTDs of ParB (**Surtees and Funnell, 1999; Volante et al., 2015**). This is therefore referred to as the nucleoid-adaptor-complex (NAC) for both plasmid and chromosomal Par systems (**Havey et al., 2012; Chu et al., 2019**). Recent *in vivo* studies have determined chromosomal partition complex formation only requires *parS* and ParB (**Ginda et al., 2017; Debaugny et al., 2018; and Bohm et al., 2020**), while structural studies have depicted ParA-ParB-DNA interactions are facilitated when a *parS* site is present on the DNA (**Volante et al., 2015; Chu et al., 2019**). Here, the *Vc*ParABS2 complex was significantly larger than ParA2-DNA-binding with ATP, and is indicative of protein-protein interactions that bridge DNA (**Figure 3.4A** and **3.7A**). A ParA2 ATPase-deficient mutant (K124R) was expected to support a similarly stable complex as ATPase activity is ablated (**Kaur et al., 2011**). The complex however was noticeably less stable, with a similar result for K124Q. These results show that native ParA2 can adopt a specific conformation for interaction with ParB2. The basis of the *Vc*ParABS2 complex assembly identified in this study is therefore likely based on ParB2-*parS2* clusters being recruited to nsDNA-bound ParA2.

A key feature that has emerged for the ParA-ATPase superfamily is self-organising behaviour. DNA acts as a reaction matrix for ParA (**Hwang et al., 2013; Vecchiarelli et al., 2014a**), in a similar manner as MinD forms dynamic patterns on the membrane in the presence of MinE (**Hu et al., 2002**). In the Brownian-ratchet model, ParB-DNA stimulates ParA-ATPase activity and a ParA depletion zone forms on the nucleoid around the partition complex. It is thought ParA diffuses away during a slow conformation change to the DNA-binding state upon ATP-binding (**Vecchiarelli et al., 2010**), and ParB-*parS* immediately binds an adjacent nucleoid ParA-ATP dimer. Accordingly, chromosomal ParB-*parS* clusters have been shown to determine ParA localisation in live-cell imaging (**Marston and Errington, 1999**; **Iniesta, 2014; Ginda et al., 2017**). Here, ParA2-ATPase activity caused slow ParA2-ParB2-DNA disassembly that was only revealed with a restricted ATP concentration (**Figure 3.4C**). Stimulated ATPase activity could also account for why high ParB2 concentrations supported a smaller ParA2-ParB2-DNA complex (**Figure 3.5B**). As discussed below, CTP provides an additional energy source that mediates partition complex dynamics. This study shows that ParA2 and ParB2 are part of a self-organising system and undergo change due to energy dissipation during complex formation that causes an ongoing dynamic behaviour at steady-state (**Halley and Winkler, 2008**).

3.4.2 ATP and CDP mediate protein composition of the partition complex

Although not detected outright with light scattering, ParB2-DNA-binding activity in the absence of CXP was shown to support rapid partition complex formation via protein-protein interactions with ParA2 (**Figure 3.4B**). EMSAs also showed large ParB2-DNA complexes (**Figure 3.12**). It is likely the influence of a ParB2-ParB2 bridging interaction was not directly detected due to a lower level of ParB2 on DNA without CTP. The ParB NTD has widely been recognised for ParA2 interaction and to promote ParA ATPase activity (**Libante et al., 2001; Ah-Seng et al., 2009; Leonard et al., 2004; Chen et al., 2015; Volante et al., 2015; Chu et al., 2019**; **Osorio-Valeriano et al., 2019**). Based on the crystal structure of the *H. pylori* chromosomal ParB (Spo0J)-*parS* complex, it was thought that the NTD might be more exposed than unbound *Hp*SpoOJ dimers (**Chen et al., 2015**). A follow up structural study with ParA (Soj) showed a Spo0J-Soj-DNA NAC complex that was promoted by Soj and facilitated by *parS* (**Chu et al., 2019**). Similarly, *B. subtilis* Soj and SpoOJ interacting domains were mapped to show a DNA-ParA-ParB-*parS* interaction (**Volante et al., 2015**). Data presented in order of addition experiments demonstrated a higher signal intensity with *parS2* DNA compared to nsDNA (**Figure 3.3**). This large partition complex is therefore most likely attributed to more ParB2 binding to pBKSII-*parS2* relative to pBKSII.

Direct detection of a large ParB2-DNA partition complex with light scattering was dependent on *parS2* and CXP. Studies have shown ParB dimers to adopt different conformations with CDP and CTP and a model summarising the prospective ParB2 CTPase cycle is shown in **Figure 3.13**. The plasmid P1 ParB NTD was implicated for ParB-ParB interactions (**Surtees and Funnell, 1999**). Later, *B. subtilis* ParB was shown to bind CTP at a conserved arginine patch within the NTD that then acted as a second dimer interface to form a closed, sliding clamp conformation at *parS* (**Soh et al., 2019**). Structural comparisons between CTP-binding domains of the ParB-like protein, PadC from *M. xanthus*, and *T. thermophilus* ParB also showed that CTP stabilised ParB NTDs in a closed conformation (**Osorio-Valeriano et al., 2019**). Furthermore *Bs*ParB, *Mx*ParB, and *Cc*ParB CTPase activities are stimulated in the presence of *parS* (**Soh et al., 2019**; **Osorio-Valeriano et al., 2019; Jalal et al., 2020a**), and crystal structures of the *Bs*ParB sliding clamp conformation could only be obtained with CDP. It was inferred that *parS* catalyses the closure of ParB-CTP and quickly stimulates CTPase activity. Although there was a slightly differing model for *Mx*ParB-CTP nucleation onto DNA, the consensus was that ParB has a relatively weak association with CDP, and so the CDP-bound state is considered to confer instability to ParB on DNA (**Soh et al., 2019**; **Osorio-Valeriano et al., 2019**). *Mx*ParB-CDP was in fact suggested to adopt an open conformation (**Osorio-Valeriano et al., 2019**). Based on these insights, the unstable ParB2-CDP state is quickly attained upon CTP-mediated ParB2 nucleation at *parS2*. A high loading rate of ParB2-CTP at *parS2* could thus describe the relatively high steady-state intensity seen here.

Addition of *parS2* sites facilitated larger complex formation in an almost step-wise fashion with CTP. Interestingly, this pattern ended when a much lower steady-state intensity with nine *parS2* sites was observed (**Figure 3.1C**). An explanation for the lower intensity with nine *parS2* sites is that there is a shift in the rate of unstable ParB2-CDP formation, such that it is perhaps higher than ParB2-CTP nucleation on the available *parS2* with this substrate. Alternatively, it could be that non-CTP-bound ParB2 facilitates greater ParB2-ParB2 bridging activity via the NTD, subject to adequate DNA-binding (**Surtees and Funnell, 1999**; **Taylor et al, 2014; Sanchez et al., 2015; Fisher et al., 2017**). As *parS* supports cooperative ParB-CTP binding (**Soh et al, 2019**), nine-*parS2* sites could represent a threshold for switching the ParB2 population to CXP-bound over unbound, thereby disrupting overall bridging activity. *Vc*ParABS2 complex formation was observed to be similar for six and nine *parS2* sites and suggests ParB2 is in fact equally saturated on both substrates (**Figure 3.9A**). However, it is currently not known how CTP affects ParB bridging activity and bridging could be unaffected or even enhanced.

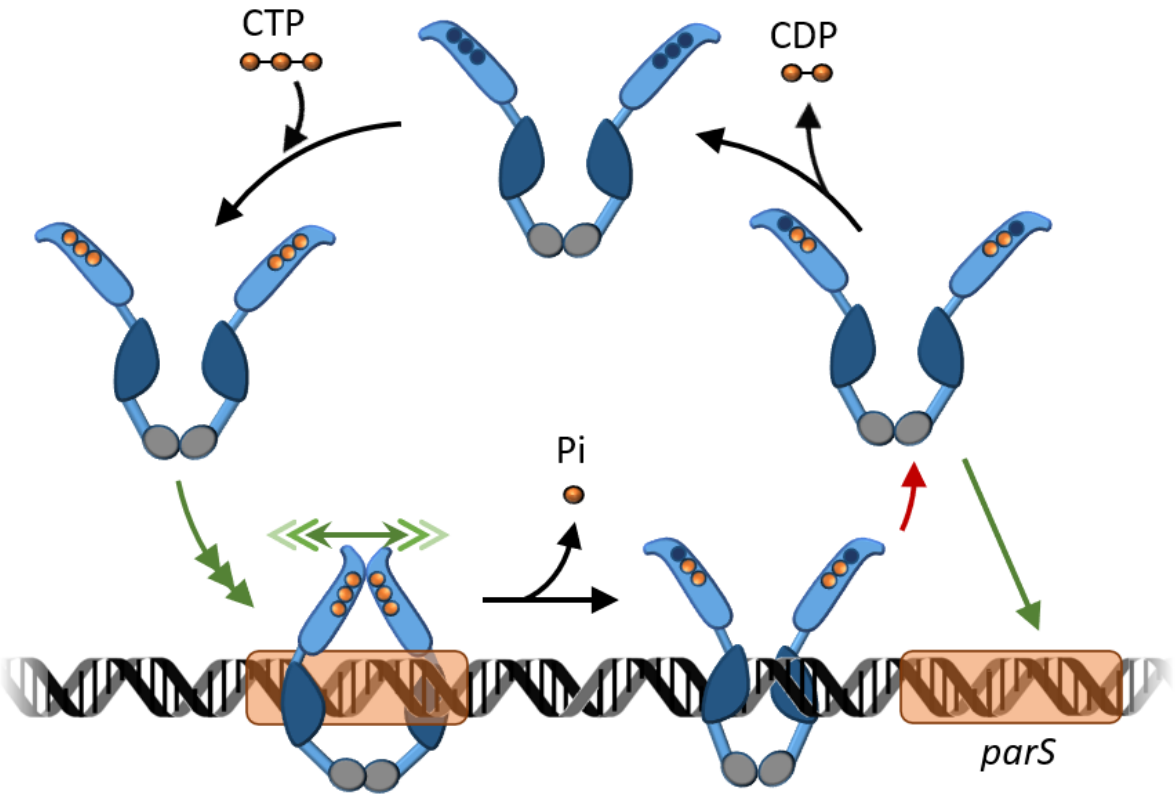

Figure 3.13. Summary of the potential ParB2 CTPase cycle on *parS2* DNA. A ParB2 dimer binds CTP. ParB2 is able to bind parS2 in the absence of CTP with the helix-turn-helix (HTH) -motif located within the DNA-binding domain (DBD) (dark blue). However, ParB2 undergoes 'gate closure' as the N-terminal domain (NTD) forms a second dimer interface akin to the sandwich dimer for ParA2 proteins. Each monomer makes contacts with the opposing γ-phosphate of CTP. Steric hindrance with the change of conformation causes DBDs to dissociate from *parS2*, such that the ParB2 sliding clamp spreads away. This facilitates high ParB2 recruitment at a single *parS2* site. In turn, the sandwich dimer formed at *parS2* is the active site for CTP hydrolysis and ParB2 hydrolyses CTP to CDP. The CDP (open) conformation is assumed and is unstable on DNA. CDP dissociates and the cycle restarts. Adapted from **Soh et al., 2019**; **Osorio-Valeriano et al., 2019; Jalal and Le, 2020; and Kawalek et al., 2020**.

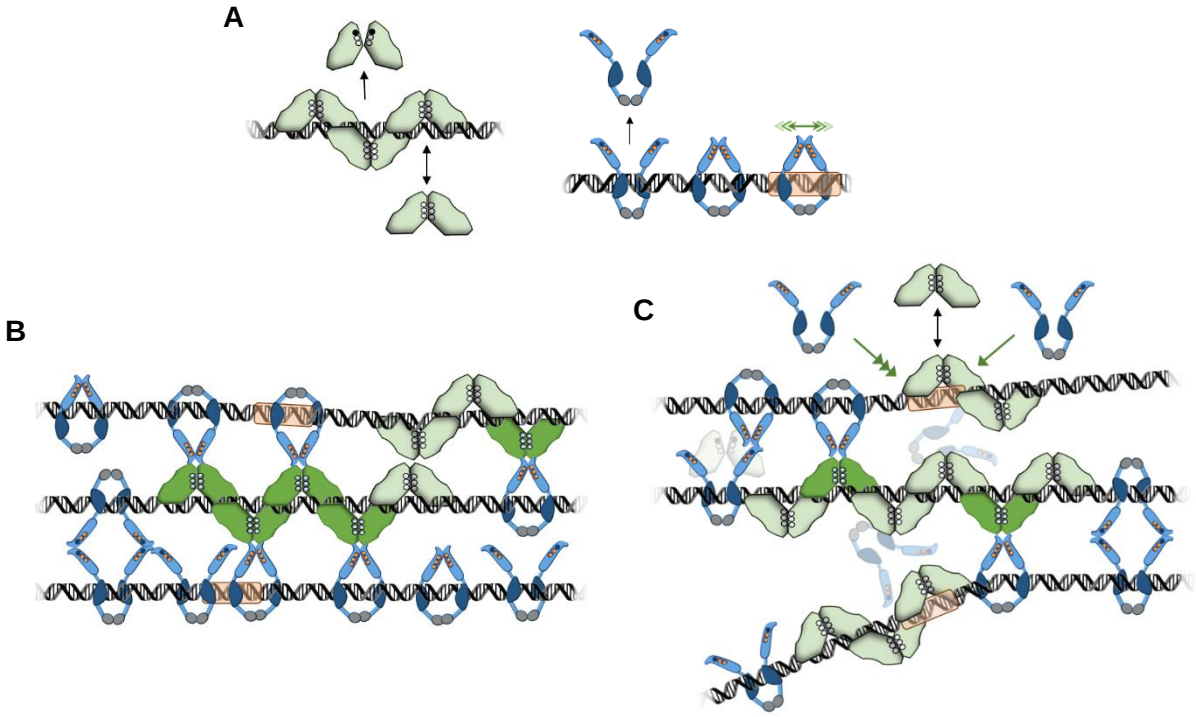

Figure 3.14. Model for the oscillatory kinetics of *Vc*ParABS2 complex assembly. A) Individual DNA-binding activities of Par proteins. ParA2-ATP forms large nucleoprotein filaments. ParA2-ATP can exchange on DNA and ATP hydrolysis is stimulated 2-fold beyond the basal low activity in the presence of DNA. Meanwhile ParB2 nucleates at *parS2* with high efficiency facilitated by spreading from *parS2.* ParB2-CDP is the open conformation and is innately more unstable on DNA than ParB2-CTP. ParB2 undergoes stochastic spreading and bridging activities to form a partition complex. **B)** *Vc*ParABS2 initial complex assembly. There is a pre-steady-state overaccumulation of Par proteins within the Par complex. Dark green ParA2-ATP represents active interactions with DNA bound ParB2. ParA2-ParB2 interactions and ParB2 bridging activities condense DNA for the formation of a large DNA-ParA2-ParB2-*parS2* complex. This represents the tethering of the partition complex to the nucleoid via ParA2-ParB2 interactions. The interaction also occurs in the absence of CTP but with less ParB2 initially recruited. **C)** ParA2 cooperative binding outcompetes ParB2 for available DNA. First disassembly event: ParA2-ATP cooperative binding accentuates ParB2-CDP instability on DNA and occupies more of the available DNA as it does not discriminate for DNA substrate. This leads to fewer DNA-ParA2-ParB2-*parS2* complexes. Transient reassembly: ParB2-CXP rebinds at available *parS2* sites as ParA2-ATP exchanges on DNA. Approaching the steady-state complex: An equilibrium of self-assembly is reached and the complex is comprised of less overall DNA-ParA2-ParB2-*parS2* interactions, as represented by less dark green ParA2-ATP dimers. ATPase activity is stimulated up to 8-fold by the presence of both ParB2 and DNA and ParA2-ADP dissociates from the complex for a slow steady-state decrease.

ParAB2 complex formation on nsDNA with CTP was notably slower than with *parS2* because of less ParB2 nucleation on DNA (**Figure 3.9A**). Moreover, since ParB2 did not elicit an intensity change on nsDNA for when in the presence or absence of CTP, an initially suggested a similar overall extent of DNA-binding for both conditions (**Figures 3.1A** and **3.1B**). Crucially, however, initial ParA2-ParB2-DNA complex kinetics were faster with CTP and is suggestive of a higher level of nsDNA-binding for ParB2-CTP. As alluded to previously, this would result in a greater number of ParA2-ParB2 interactions.

Alternatively, the extent of nsDNA-binding could be similar between the two conditions and it is the interaction with ParA2 that is enhanced by CTP. Indeed, the canonical ParB NTD of PadC was found to interact with *Mx*ParA in the CTP-bound state (**Osorio-Valeriano et al., 2019).** Order of addition experiments on *parS2* showed pre-formation of ParB2-CTP leads to faster initial assembly kinetics for each condition (**Figure 3.8** – orange curves). In testing component stoichiometry, a higher available ParA2-ATP population (via higher relative ATP to CTP concentration, or a directly higher ParA2 concentration) was shown to be the dominant factor in discerning faster initial kinetics. This was shown as a clear shift left from the reference curve (**Figure 3.10A, 3.7C**). These kinetics can be summarised as the rapid accumulation of ParA2-ATP on DNA and ParB2-CXP on *parS2*, in addition to the subsequent formation of CXP-mediated ParA2-ParB2 interactions.

The conditions where disassembly kinetics proceeded quickest were observed with preformed ParB2-CTP-*parS2* (**Figure 3.7B** and **3.8**), as the main rate-limiting factor appears to be attainment of the ParB2-CDP state. A sequential acquisition corroborates this as disassembly kinetics were markedly faster in the presence of CDP (**Figure 3.10D**). Available ParA2-ATP also played a significant part in driving faster disassembly kinetics. ParA2-ATPase activity was similar when in the presence of ParB2-*parS2* and ParB2-CTP-*parS2*. ParA2 would thus remain largely unchanged in this small window of *Vc*ParABS2 complex kinetics. A model for the proposed self-assembly of Par components is provided in **Figure 3.14**. As described in section 1.6.1, 'self-organisation' is defined as arising from transient interactions between individual components of a system which consumes energy (for example GTP or ATP). 'Self-assembly' on the other hand is the association of a set of components into a stable structure without dissipation of energy (**Ramm et al., 2019**). As the DNA becomes saturated with components, there would be competition for substrate between ParA2 and ParB2. ParA2-ATP would be able to bind all available ~3 kb DNA, whereas high-affinity ParB2-CTP DNA-binding would be restricted to the six, 15 bp *parS2* sites, and ParB2-CDP showed reduced nucleation on *parS2* DNA. There was also less rebinding in the oscillations with CDP in **Figure 3.10D**. ParA2 would therefore make up a larger proportion of the lower steady-state intensity attained during oscillations, along with less ParA2-ParB2 interactions.

Preformation of ParA2-ATP (Gr.2) generally yielded some of the more stable acquisitions, with ParA2-ATP rapidly binding DNA and restricting ParB2-CTP association with *parS2* if they are not allowed to interact beforehand. A surprising result that prevented the establishment of an over-arching category defining preincubation of ParB2 with CTP as the prerequisite for oscillation kinetics, was that when ParA2 (alone or with ATP) was preincubated with ParB2-CTP, the expected faster disassembly kinetics for those reactions did not materialise (**Figure 3.8,** reactions 2 and 6 – orange curves). A ParB2-CTP interaction with ParA2 prior to nucleation on *parS2* DNA seems to inhibit the specific activities seemingly responsible for disassembly, and could be because ParB2 CTPase activity is inhibited, or because ParB2-CDP was stabilised on DNA by the preformed protein-protein interaction. ParB2 CTPase activity must therefore be characterised to gain further insight. Protein-DNA interactions in the absence of nucleotide are not detected outright but affect complex dynamics. Another condition, with ParA2 and ParB2 incubated together but separate from nucleotide and *parS2*-DNA, showed immediate oscillatory behaviour (**Figure 3.8,** reaction 2 – grey curve). Upon component mixing, ParA2 and ParB2 would both be in 'nucleotide start' conditions. ParB2 would encounter CTP (present at one-thousand-fold excess to ParB2). Indeed, *Bs*ParB, *Mx*ParB, and *Cc*ParB exhibited cooperative CTP-binding in the presence of *parS*-DNA (**Soh et al., 2019**; **Osorio-Valeriano et al., 2019; Jalal et al., 2020a**). Similar conditions with ParB2 separate from CTP resulted in more stable kinetics (**Figure 3.8,** reactions 1, 3, and 4, – grey curves), where a prolonged acquisition for reaction 1 (with pBKSII-6x*parS2*) was required to show an eventual oscillation (**Figure 3.11E**). These additional protein-protein and protein-DNA interactions appear to inhibit the formation of ParB2-CDP, whether by directly inhibiting ParB2 CTPase activity, or inhibiting ParB2-CTP from binding at *parS2* which would lead to initial assembly kinetics as on nsDNA (**Figure 3.3**) until *parS2* becomes available.

The rebinding phase of the oscillatory kinetics was more pronounced with increased *parS2* number (**Figure 3.9A**). A higher CTP to ATP concentration caused diminished rebinding (**Figure 3.11B**), while a higher ATP-CTP ratio had the opposite effect (**Figure 3.11A**). Taken together, these results suggest that increased nucleation of ParB2 on the additional *parS2* sites and adequate level of ParA2-ATP are required for ParA2-ParB2 DNA bridging. The intricate nature of these dynamics was shown however, as kinetics with increased ParA2 lead to less rebinding and indicated that ParB2 was inhibited from binding at *parS2*; as expected, increased ParB2 concentration still exhibited rebinding, with DNA-binding likely restricted to *parS2* sites (**Figure 3.11D**).

3.4.3 Implications for *V. cholerae* chromosome 2 segregation

The *V. cholerae* nucleoid is comprised of two chromosomes, each of which utilises the nucleoid itself as a scaffold to drive their own segregation via distinct Par systems prior to cell division. Chr1 lies along the length of the cell, with the origin and terminus at opposite poles. Chr2 lies parallel to Chr1, with the origin at mid cell, and the terminus in close proximity to that of Chr1. Segregation is coupled to replication, and as Chr2 is a third of the size of Chr1, activities are coordinated as such (**Espinosa et al., 2017**). Chr2 replication initiation, and copy number, is intrinsically coupled to the duplication of a site on Chr1, *crtS*, that is reached two thirds of the way into Chr1 replication (**de Lemos Martins et al., 2018**). For Chr1, only the replicated origin is moved asymmetrically to the new pole, while Chr2 origins are moved symmetrically to the quarter position (**Espinosa et al., 2017**). Relative to plasmid Par systems then, the *Vc*Chr2 partition system not only has two copies of a much larger cargo but it only has a third of the total time available to correctly equi-position them. Rapid and precise partitioning is therefore required.

In this study, ParA2 formed large complexes on DNA with ATP and likely represents the filaments previously reported (**Hui et al., 2010**). Binding was fast and with none of the observed lag-time (up to 30 s) seen for plasmids P1 ParA, F SopA, and pSM19035 δ (**Havey et al., 2012; Hwang et al., 2013; Vecchiarelli et al., 2013, Pratto et al., 2008**). A modeling study between plasmid F SopA and *B. subtilis* Soj nucleoid dynamics found that increasing the available ParA could capture the subtleties of a chromosomal Par system (**Jindal and Emberley, 2019**). Indeed, the reaction was defined by more overall partition complex contacts with nucleoid-bound ParA proteins. The DNA-ParA2-ParB2-*parS2*, NAC, complex was slow to reach steady-state intensity (**Figure 3.2**), compared to P1 Par system under similar experimental conditions, which displayed either sigmoidal (Gr.1) or hyperbolic curves (Gr.2) and both reached similar steady-state intensities after ~75 s (**Havey et al., 2012**), Notably, there was a disassembly dynamic for the P1 Par system, similar to that seen in this study for *Vc*ParABS2 with CTP, albeit without the oscillatory behaviour. These results suggest that the *Vc*Chr2 Par system forms an innately more stable partition complex appropriate for a much larger cargo, and is corroborated by the fact that ParB2-*parS2* magnetic beads were static even with the formation of clear ParA2 depletion zones (**Figure 5.1**).

Generally, *in vivo* ParA and ParB concentrations are in the µM range (**Surtees and Funnell, 2003**), though the partition complex consists of ParB molecules with a theorized ParA:ParB stoichiometry of ~1:500 µM (**Lim et al., 2014**). In the cell, ParA2 pole-to-pole oscillations result in the lowest average ParA2 concentration at mid cell, which is where partition complex assembly would occur upon replication initiation, (**Fogel and Waldor, 2006**). *Vc*Chr2 partition complex assembly would therefore predominantly comprise of ParB2 binding

the six *parS2* sites located close to the origin with high affinity, and CTP would facilitate loading efficiency. The plasmid NAC includes plasmid pairing, but this is not required for chromosomes and sister snapping is more relevant (**Pratto et al., 2008; Chu et al., 2019; Joshi et al., 2013**). In diffusing away relative to each other due to steric hindrance, the two Chr2 partition complexes would begin to interact with different ParA2 oscillation phases to assume opposite quarter cell positions. The NAC interaction will be dominated by more transient ParA2 interactions with a high rate of stimulated ATPase activity. This moment in Chr2 partitioning is therefore best represented by the experimental condition with restricted ATP level (**Figure 3.4C**) which affected the available ParA2-ATP at the partition complex assembly.

The nucleoid itself has been posited to contribute to the motive force of the partition complex, in terms of its innate elasticity and the formation of HDRs (**Lim et al., 2014, Le Gall et al., 2016**). Cellular processes such as chromosome replication were believed to control nucleoid morphology throughout the cell-cycle. ParA was shown to distribute throughout the nucleoid, as opposed to just the surface, and the partition complex was speculated to be manoeuvred from adjacent ParA-rich HDRs. Localisation of partition complexes within the nucleoid was dependent on ParA-DNA-binding and stimulation of ATPase activity by ParB (**Le Gall et al., 2016**). For *Vc*Chr2, the ability for ParA2 to form oligomers on DNA could be mediated by HDRs in the cell, as a high ParA2 concentration (~1 µM) was required for filament formation (**Hui et al., 2010**). In this study, ParA2-ParB2-DNA stoichiometry experiments showed a large end-point intensity increase between 0.5 and 1 µM ParA2 (**Figure 3.4A**). While the slow rate of ParA2-DNA disassembly with ATP to ADP exchange (**Figure 3.1G**) does not correlate with fast oscillations on the nucleoid, the local subcellular ParA2 concentrations are likely to be well below the concentrations used in this study (**Lim et al., 2014**).

*Vc*ParABS2 kinetics in the presence of CTP showed an oscillatory decrease to a lower steady-state intensity, and as described earlier, these dynamics most likely modulate the overall partition complex size due to the unstable conformation of ParB2-CDP on DNA. In addition, as the partition complexes move further up the ParA2 concentration gradient, ParA2-ATP would naturally contribute more to the NAC (**Figure 3.14**). It could be that the oscillatory kinetics characterised in this study play out at the quarter cell position, such that a threshold ParA2-ATP concentration overcomes the ParB2-*parS2* stimulated ATPase activity. The ParA2-ATP concentration and ParB2-CDP instability would therefore act to phase-lock the partition complexes at these positions. **Figure 3.11D** shows that a high ParB2 concentration relative to ParA2 maintains dynamic self-assembly of Par proteins on parS2 DNA. The higher concentration of ParA2-ATP at the quarter cell positions could shift the *in vivo* partition complex ParA2-ParB2 ratio from 1:500 and more towards what is characterised in this chapter. It is not clear what causes ParA2 oscillations because the *Vc*Chr2 partition complex does not

reach the cell poles. Speculating about an interplay between the oscillatory behaviour of the partition complex size and the ParA2 pole-to-pole oscillations is therefore difficult. Further ParA2-ParB2 interaction studies will help elucidate further details of this mechanism.

CHAPTER 4

GENERAL DISCUSSION

4.1 GENERAL DISCUSSION

4.1.1 The different DNA-binding modes of ParB2

In Chapter 3, partition complex assembly on both specific- and nsDNA was characterised. EMSAs illustrated specific nucleoprotein binding species with *parS2* DNA. Large, immobile complexes formed at a threshold concentration of ParB2, with both *parS2* and nsDNA. Crystal structures of chromosomal CTD-truncated ParB monomers showed binding to *parS* sites in an open conformation and bridging interactions between NTDs (**Leonard et al., 2004; Chen et al., 2015; Song et al, 2017**). It was also determined that full-length ParB, with dimerisation at the CTD, is needed for DNA condensation and the formation of coherent partition complexes on *parS*-proximal DNA. In utilising plasmid DNA in light scattering assays, bridging between DNA-bound ParB molecules would theoretically cause clustering of plasmids. Critically, however, ParB2 DNA-binding with subsequent bridging interactions were not detected by the light scattering assay. This was also observed for plasmid P1 ParB and indicates weak inter-NTD interactions that are incapable of stably bridging large DNA molecules, and/or insufficient nucleation on the available DNA (**Havey et al., 2012**).

The addition of CTP caused an increase in light scattering and is representative of a different DNA-binding mode with ParB2-CTP in a closed sliding-clamp conformation spreading along DNA, as described for *Bs*SpoOJ and *Cc*ParB on enclosed DNA substrates (**Soh et al., 2019; Jalal et al., 2020a**). The requirement for *parS* corroborates these studies whereby a high nucleation of ParB on DNA is facilitated by dimer sliding clamp formation at *parS*, followed by lateral spreading supporting the recruitment of numerous ParB molecules at a single site. Most *parS* sites are distributed within the Ori domain and together support a better-defined partition complex demarcated for segregation. Further *in vitro* characterisation will help to elucidate how much ParB-mediated DNA bridging contributes to formation of this complex in the presence of CTP, or whether it is based solely on spreading activity, which is perhaps the less likely scenario (**Soh et al., 2019; Sanchez et al., 2015**).

4.1.2 ParA2 cooperative DNA-binding is part of a Brownian-ratchet mechanism

ParA2 binding to nsDNA was characterised in Chapter 2 with EMSAs in the presence of different adenosine nucleotides. Nucleoprotein filaments were originally identified in an *in vitro* structural study showing distinct filaments on DNA under different nucleotide conditions, with a more regular, and apparently more stable, filament being observed in the presence of ATP (**Hui et al., 2010**). Similarly, in this study, ParA2 nucleoprotein complexes were detected

in the absence of nucleotide, and with ADP, but a high-affinity DNA interaction was only found with ATP or ATPγS. What is more, light scattering assays performed in Chapter 3 showed that DNA-binding by ParA2 was only detected with ATP or ATPγS. The observation of nucleoprotein filaments both in the absence of nucleotide and with ADP are thus far unique to ParA2. Based on biochemical characterisations in this study, a high ParA2 concentration to DNA availability is required for DNA-binding to be detected in the absence of adenosine nucleotide. The *Cc*ParA cytosolic concentration was determined from quantitative western blots to be around 1 µM (**Lim et al., 2014**). A similar concentration of ParA2 was consistently utilised in this study, however, there is much more available DNA within the cell relative to that required for nucleoprotein detection in EMSAs. It is therefore probable that DNA comprising the nucleoid acts as a competitive substrate for ADP-bound and nucleotide-free ParA2 dimers to prevent significant nucleoprotein complexes from forming.

Perhaps more significantly, ParA2-ATP cooperative DNA-binding indicates that the less well-ordered nucleoprotein structures for other conditions are likely very dynamic on the nucleoid and most probably only transiently formed. Light scattering assays, with a higher concentration of DNA utilised, showed that ParA2-DNA-binding with ATP was reversed with the addition of a higher concentration of competing ADP. This indicates that ParA2 dimers on DNA can exchange nucleotide with an open nucleotide-binding pocket, as defined for pSM19035 δ (**Pratto et al., 2008**). ParA2 can exchange nucleotide without dissociating to monomers, and then in turn dissociates from DNA. High affinity DNA-binding, as was apparent in EMSAs, therefore would only occur with ATP bound to ParA2 *in vivo*. Cooperative DNA-binding of ParA-ATP has also been inferred for *Bs*Soj, *Hp*Soj, as well as P1 ParA and F SopA (**Hester and Lutkenhaus, 2007; Chu et al., 2019; Castaing et al., 2008; Hui et al., 2010**). This could therefore be a conserved feature of all type I ParA proteins in order to coat DNA within nucleoid HDRs (**Le Gall et al., 2016**).

In Chapter 2, a slow conformational change upon ATP-binding was observed for a chromosomal ParA for the first time and corresponds to the active DNA-binding state integral to a Brownian-ratchet mechanism. The transition was found to be around 5-fold faster than plasmid P1 ParA (**Vecchiarelli et al., 2010**). The presence of DNA increased the rate of conformational change for both P1 ParA and ParA2, with ParA2 maintaining a slightly faster transition to the DNA-binding state. Cell-free reconstitutions with fluorescently tagged plasmid F SopA showed an initial lag-time before binding to a DNA carpet (**Hwang et al., 2013**). Moreover, ATP did not support P1 ParA DNA-binding detection by light scattering but there was a lag-time for P1 ParABS assembly that was attributed to reaching the competent DNA-binding state (**Havey et al., 2012**). There was no equivalent lag-time for ParA2 observed in experiments reported in Chapter 3. The combination of a base dimer unit, a faster

conformational change, and the pre-association with DNA prior ATP-binding could contribute to the absence of such a lag-time.

Plasmid ParA proteins have been comprehensively biochemically characterised, and data is now steadily accumulating for chromosomal ParA proteins. *Cc*ParA exhibits a slower relative ATPase rate than plasmid ParA proteins, with a 5-fold higher concentration of ParB required to adequately stimulate ATPase activity (**Lim et al., 2014**). Studies on *Bs*Soj, *Hp*Soj, and *Tt*Soj have presented basal and stimulated ATPase rates as fold-changes and are not easily comparable. However, it was suggested that *Bs*Soj ATPase activity is prematurely stimulated relative to *Cc*ParA (**MacCready et al., 2018; Lim et al., 2014**). In Chapter 2, ParA2 was systematically characterised biochemically for direct comparisons to be made at each stage of the ATPase cycle, and it has been determined that ParA2 has a faster ATPase cycle than plasmid ParA proteins (**MacCready et al., 2018**).

The impact of ParA2 being quicker than other ParA proteins to assume the active DNA-binding conformation is presented in the Appendix, with a cell-free 2D reconstitution of the *Vc*ParABS2 system (**Figure 5.1**). ParA2-GFP-ATP bound a DNA carpet within a microfluidics device that acted as a biomimetic nucleoid surface. Magnetic beads coated with *parS2* DNA were incubated with ParB2, after which they were also introduced into the microfluidics device. An integral feature of the Brownian-ratchet model as proposed for plasmids is confinement, either by the inner membrane, or the interior of the nucleoid itself, and a magnet positioned beneath the DNA carpet constrained the beads to the DNA carpet. The interaction between ParA2 and ParB2 represented the nsDNA-ParA2-ParB2-*parS2* complex, as characterised in Chapter 3. A 1:1 concentration ratio (μM) of ParA2:ParB2 was initially utilised and the beads were immobilised. This was increased to 1:8 ratio to elicit a clear ParA2-GFP depletion zone around the beads, although they remained immobilised, even with the complete removal of the magnet constraining 2D movement. It was observed that ParA2-GFP was not adequately cleared from the beads and they therefore remained tethered to the DNA carpet. However, analysis of various beads in the acquisition showed clearance of ParA2-GFP from the bead was indirectly proportional to depletion zone formation (**Figure 5.1B**). A similar ratio of SopA:SopB was used to show directed motion (**Vecchiarelli et al., 2014a**). A local subcellular ParA2 asymmetry on nucleoid is therefore determined by ParB2-*parS2* and in turn drives segregation, as demonstrated for P1 and F plasmid ParABS systems (**Hwang et al., 2013; Vecchiarelli et al., 2014a**). This initial finding suggests that a higher concentration of ParB2 is required to release the beads from the DNA carpet. In effect, a larger depletion zone is required to prevail over the ability of ParA2 to bind DNA, with no apparent lag-time that arises from a relatively fast overall ATPase cycle.

4.1.3 ParA2 subcellular oscillations and equi-positioning of DNA cargo

Moving beyond local ParA2 concentration gradients, ParA2 displays *in vivo* pole-to-pole oscillations and this property is more commonly seen for plasmid ParA proteins (**Fogel and Waldor, 2006**). ParA2 is classed as similar to plasmid ParA proteins, and Chr2 is derived from a mega-plasmid. Indeed, another significant analogy with plasmid segregation is equi-positioning along the lateral cell axis. It is not clear why some ParA proteins oscillate whereas others are less overtly dynamic. Plasmid P1 ParA, for example, is quite stable on the nucleoid with only minor concentration perturbations appearing to drive segregation of plasmids, although the rate of ATP hydrolysis is very similar to plasmid F SopA, which does oscillate *in vivo* (**Sengupta and Austin, 2011**). Nevertheless, some informed speculations are made below.

Nucleoid remodelling during the cell-cycle has been postulated to play a role in ParA oscillations. Plasmid F SopA *in vivo* distributions, referred to as maxima, were located at the edges of the nucleoid where Ori domains were determined to be at high density relative to the centre of the cell (**Le Gall et al., 2016; Marbouty et al., 2015**). This was deemed consistent with SopA oscillatory behaviour. As the DNA replication cycle subsequently ensued, the duplicated Ori domain concomitantly relocated along the cell, following the SopA gradient (**Le Gall et al., 2016**). Thus, it could be that the replicated Ori domain is highly condensed until the DNA replication cycle shifts the HDRs from one pole to the other (**Marbouty et al., 2015**). SopA could transition to the opposing pole with cooperative binding. In the same light, ParA2 cooperative DNA-binding could feasibly contribute to observed *in vivo* ParA2 pole-to-pole oscillations (**Fogel & Waldor, 2006**). The capacity for oscillatory behaviour could be facilitated further by ParA2 exchange on DNA, as characterised in Chapter 2 with DNA competition gel shift assays, to gradually and stably relocate to prominent HDRs located at the ends of segregating nucleoids near the poles.

The best evaluation of subcellular ParA dynamicity has been via computational modelling of the initial Brownian-ratchet model, which has characterised motility patterns classed as completely diffusive, pole-to pole oscillations, minimal excursions, and static. For a single partition complex, or for two-partition complex motility, parameter ranges for ATP hydrolysis and DNA-binding rates were characterised such that there was a significant window of opportunity that supported pole-to-pole oscillations akin to those seen *in vivo* (**Hu et al., 2017a**). Another study incorporated available ParA and ParB, substrate length, and the length of time between ParA-ParB interactions before ParB stimulates of ParA ATPase activity (**Jindal and Emberly, 2019**). Modifying ParA availability or the size of the depletion zone recapitulated some of the differences between partition complex segregation for plasmids and

chromosomes. It was suggested that chromosome segregation is fine-tuned to be in line with idiosyncrasies of host cell physiology and environmental requirements (**Jindal and Emberly, 2019**).

Most primary chromosomes have a longer time-period for segregation to occur compared to *Vc*Chr2. For example, of the studied chromosomal Par systems, *P. aeruginosa* has a doubling time that is at least twice as long as *V. cholerae* (18 min) (**Lasocki et al., 2007; Rasmussen et al., 2007**). Meanwhile, *C. crescentus*, *M. xanthus*, *Mycobacterium smegmatis*, *B. cenocepacia*, *S. coelicolor*, and *P. putida* all have minimal doubling times of at least 89 min (**Boutte et al., 2008**; **Vaksman et al., 2015; Klann et al., 1998; MacDonald et al., 2008; Chen and Qin, 2011; and Munna et al., 2015**). The exception is *B. subtilis,* which has a vegetative cell-cycle doubling time similar to *V. cholerae* (**Pandey et al., 2013**). *B. subtilis* has the only other known oscillating chromosomal ParA and this suggests that faster segregation is mediated by a more dynamic ParA behaviour *in vivo*. This corresponds to modeling studies that have determined faster ATP hydrolysis rates and overall ParA availability correlate with *in vivo* oscillations (**Hu et al., 2017a; Jindal and Emberly, 2019**). As an aside, a highly conserved polar tether in Gram positive organisms, DivIVA, is used by *B. subtilis* for polar localisation of partition complexes (**Hammond et al., 2019**). Alternatively, TP228 ParF is able to oscillate and direct partition complexes to the poles without polar tethers. This was determined to be facilitated by a tuned, slower rate of ATPase activity relative to P1 and F plasmid ParA proteins. Here, biochemical parameters have been defined for potential use in a future species-specific computational model of chromosome segregation for *V. cholerae*.

Computational models have been largely derived from biochemical data and are simpler for plasmids compared to primary chromosomes, by means of additional segregation machinery such as SMC/condensins and polar tethers for the latter. *Vc*Chr2 is a third of the size of the primary chromosome and as such, equi-positioning appears to be sufficient for appropriate separation of Ter domains by MatP and for cell division to be licenced to proceed. Without the polar tether complex, HubP, Chr1 *oriC* localised on average 16% of the total cell length away from the cell pole as opposed to just 4% on average with HubP (**Yamaichi et al., 2012**). As the chromosome inhabits the entire length of the cell, in the absence of HubP, the cell would need to grow by a suitable amount to facilitate separation of Chr1 Ter domains and the rate of cell proliferation would effectively be reduced (**Kadoya et al., 2011**).

4.1.4 *Vc*ParABS2 complex assembly with CTP could influence Chr2 equi-positioning

Equi-positioning of DNA cargos has been described by a Brownian-ratchet model and intrinsic to this is a ParA-ParB interaction with subsequent stimulation of ATP hydrolysis. CTP-

binding by the ParB-like protein, PadC, was found to augment interaction with *Mx*ParA (**Osorio-Valeriano et al., 2019**). *Hp*Soj was tested for ATPase stimulation with DNA-bound *Hp*Spo0J (ParB) and it was suggested that the N-terminal regions of a ParB dimer could be brought together to insert into the appropriate two regions of a *Hp*Soj dimer (**Chu et al., 2019**). The binding of an arginine residue on a ParB helix close to the ParA active site could act as an arginine finger to further stabilise ATP-binding, and thus stimulate ATPase activity. (**Caccamo et al., 2020**). In Chapter 2, there was no apparent context for ParB2 NTD-mediated stimulation of ParA2 ATPase activity, as there was no difference in stimulation with and without CTP. This could be due to the high protein concentrations utilised.

Alternatively, the ParA2-ParB2 interaction was integral to the formation of higher order complexes characterised in Chapter 3. In the presence of CTP, an oscillatory dynamic ensued before reaching a lower steady-state intensity. The oscillatory behaviour likely arose from dynamic self-assembly of ParA2-ATP and ParB2-CXP on *parS2* DNA (**Figure 3.14**). Conditions that favoured CTP hydrolysis to CDP resulted in earlier oscillatory dynamics. CTPase activity was not characterised in this study, however slightly faster oscillations were seen with CDP. Furthermore, the lower steady-state intensity complex was deemed to be a result of ParA2-ATP outcompeting ParB2-CDP for DNA such that there is a higher proportion of ParA2 to ParB2 on the available DNA. In this scenario, ParA2 is able to cooperatively bind to all of the available enclosed DNA substrate, whereas ParB2 only nucleates onto the few *parS2* sites.

The 2D reconstitution has demonstrated that a 1:8 molar ratio of ParA2:ParB2 causes the formation of a depletion zone, but it is insufficient to completely release the partition complexes on the magnetic beads. The *Vc*ParABS2 steady-state complex with CTP suggests the molar ratio would in fact have to be even higher in favour of ParB2 to facilitate an adequate ParA2-GFP depletion zone formation. *In vivo*, the local concentration ratio of ParA:ParB on *C. crescentus* partition complexes has been determined to be around 1:500 µM (**Lim et al., 2014**). Here, however, as *Vc*Chr2 partition complexes move up the ParA2 concentration gradient, the concentration ratio would move more towards what was utilised in Chapter 3. The ¼ and ¾ cell positions could correspond to a ParA2 concentration whereby ParA2 would thus work to effectively tether-lock the partition complex (**Figure 4.1**). Therefore, taking the assembly of the *Vc*ParABS2 complex with CTP into consideration, there could be a locking mechanism that also contributes to equi-positioning of sister *Vc*Chr2 *oriC*s.

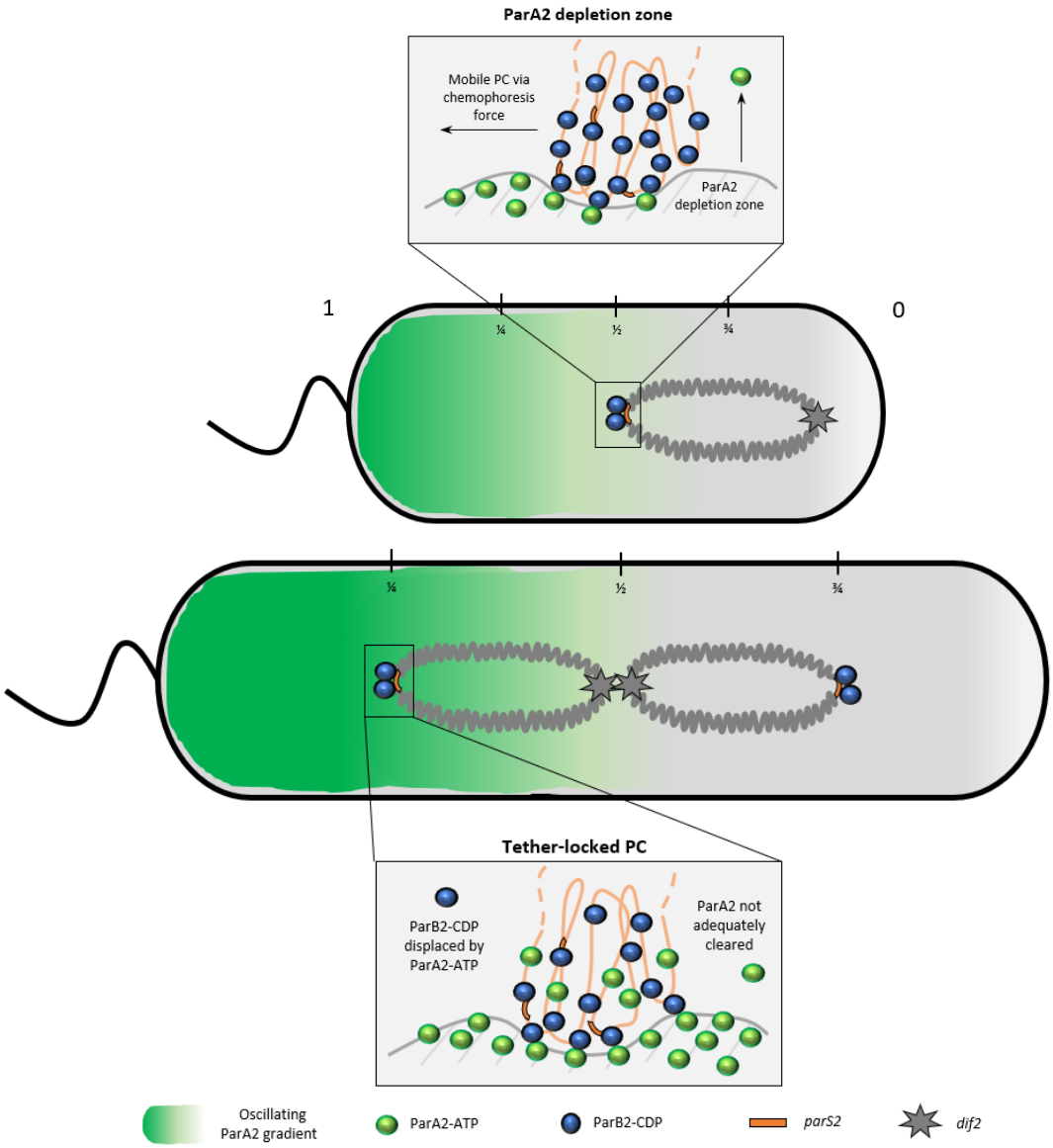

Figure 4.1. Model for the tether-locking mechanism of the partition complex (PC) arising from self-assembly of ParA2-ATP and ParB2-CDP at quarter-cell positions. As in **Figure 1.3**, the old pole and new poles are denoted by '1' and '0', respectively. Grey represents the region of the cell taken up by the entire nucleoid while Chr2 is in dark grey. Windows depict how the ParA2:ParB2 concentration ratios change at ¼, ½, and ¾ cell positions to affect PC mobility. Within the windows, the partition complex is in orange while the nucleoid is grey. Segregation of replicated Chr2 by Brownian-ratchet mechanism (top): at mid-cell, the ParA2:ParB2 concentration ratio is up to a 1:500 µM, and ParB2 initiates a ParA2 depletion zone at the trailing edge of the PC. This is 'self-organisation' and uses energy (ATP hydrolysis). Segregated PCs reach quarter-cell positions in a growing cell (bottom): local ParA2 concentration increases, and ParB2-CDP fails to clear an adequate depletion zone. Due to ParA2-ATP cooperative DNA binding, there is a persistent nsDNA-ParA2-ParB2-*parS2* interaction which locks the PCs to these positions. This is 'self-assembly' of Par components and relies on Brownian diffusion (see **Figure 3.14** for dynamics).

4.1.5 Summary of findings

A comprehensive biochemical characterisation of the *Vc*ParABS2 system has been performed in an attempt to determine how nucleoprotein filaments fit into the larger scheme of ParA2-mediated chromosome segregation. ATP-binding and dissociation kinetics have only previously been performed for plasmid P1 ParA. In Chapter 2, this was done for ParA2, and nucleotide exchange kinetics were also examined. Dimerisation upon nucleotide-binding has been determined for chromosomal ParA proteins of various species. Furthermore, the kinetics of ATP-linked ParA2 conformational changes to the DNA-binding state, have been characterised here for only the second time, following that of plasmid P1 ParA. ParA2 DNA-binding was analysed to investigate cooperative binding activity with ATP, which could apply to other ParA proteins. The rate of ParA2 ATPase activity has been found to be fast relative to those measured for other ParA proteins. The effect of CTP on ParABS assembly has been characterised for the first time. Additionally, initial data from a cell-free reconstitution supported a Brownian-ratchet-like mechanism of action for *Vc*ParABS2. The exact cause of ParA2 oscillations has not been deciphered but contributing factors have been proposed. Finally, this thesis set out the differences between 'self-organisation' of the Par system, which constitutes the Brownian-ratchet mechanism, and 'self-assembly' of ParA2-ATP and ParB2-CDP on DNA comprising *parS2* sites. The latter potentially contributes to the final positioning of the Par complexes at quarter-cell positions and further reconstitutions can show this definitively.

4.2 FUTURE PROSPECTIVES

4.2.1 ParB2 binding to alternate *parS2* sites

There are 15 putative *parS2* sites in the *V. cholerae* genome. YFP-ParB2 formed foci on 9 *parS2* sites located on Chr2 and 1 site on Chr1 (**Yamaichi et al., 2007a**). The use of *parS2*-B throughout this study was based upon it being located directly downstream of the *parAB* operon. Additional *parS2* sites introduced for light scattering assays were also *parS2*-B and this was for simplicity in introducing a single variable at a time, and for consistency in interpretation of results, given that only ParB2-binding to *parS2*-B was characterised in EMSAs. Plasmid F SopB was previously found to bind 16 bp *parS* sites with no steric hindrance. In contrast, adjacent *parS2*-B sites inhibited ParB2 nucleation and this was avoided by maintaining at least 15 bp between sites in light scattering assays (data not shown). There may be further idiosyncrasies of ParB2 specific DNA-binding that can be evaluated with EMSAs. First, binding to the distinct *parS2* sites can be determined. There are single base pair differences outside of the 7 bp inverted repeat for verified *parS2* sites. The remaining *parS2* sites have differences within this region. Binding affinities can be calculated to indicate

functionality and/or redundancy. ParB2-CTP spread off linearised plasmid DNA as detected with light scattering (data not shown). Short plasmid substrates could thus be utilised in EMSAs for direct comparisons to be made with CTP and without CTP. Imaging is achievable via fluorescently tagged plasmids via nick translation, or by a standardised DNA staining protocol with SYBRsafe cyanine dye.

Light scattering has been a valuable tool to determine ParB2-CTP-binding to *parS2* DNA. The different DNA-binding modes for ParB2 can be investigated to determine the extent of bridging interactions of ParB2 alone and of CTP-bound ParB2. Up to 9 *parS2* sites were used to show no increase in the absence of CTP. However, distribution of the sites around the plasmid could influence bridging interactions, given that steric hindrance has already been hinted at. *Pa*ParB has been speculated to bind half *parS* sites to alter the nucleoid architecture. EMSAs and light scattering assays can be used to determine a similar activity for ParB2.

4.2.2 Cell-free reconstitutions

Experiments with magnetic beads (**Figure 4.2**) can continue with determining the concentration of ParB2 required to release the bead from the ParA2-GFP-ATP tethers on the DNA carpet. Observed directed motion akin to that seen for reconstitutions of plasmid F SopABC would follow, with the goal of optimising the height of the perpendicularly placed magnet acting to confine motion to 2D. In order to introduce CTP to the experiments, double tethered DNA is needed for beads to enclose ParB2-CTP sliding clamp dimers (**Figure 4.2C**). The DNA needs to be biotinylated on each end, and so the cyanine-5 label will be lost. Instead, a nick-translation methodology can be utilised to label the enclosed DNA substrate before coating the beads. Alternatively, ParB2 can be fluorescently labelled with a small fluorophore to minimise perturbations to functionality, given that both dimerisation and NTD interactions are crucial for DNA condensation.

ParA2:ParB2 concentration ratios can be compared in the absence and presence of CTP to look into any parallels drawn from light scattering assays regarding the ParA2 tether-lock mechanism proposed (**Figure 4.2D**). A range of concentration ratios of ParA2-ATP on the DNA carpet and ParB2 on the beads can be used to show the effects of CXP on both the Brownian-ratchet (self-organisation) and the final locking mechanism (self-assembly) (**Figure 4.2D**). Specifically, surface chemistry approaches (termed photocatalytic nanolithography) can be utilised to construct regions devoid of DNA within the microfluidics device (**Ul-Haq et al., 2013**). One approach is to have a checkered-type DNA carpet pattern, to demonstrate partition complexes tracking more clearly along these regions.

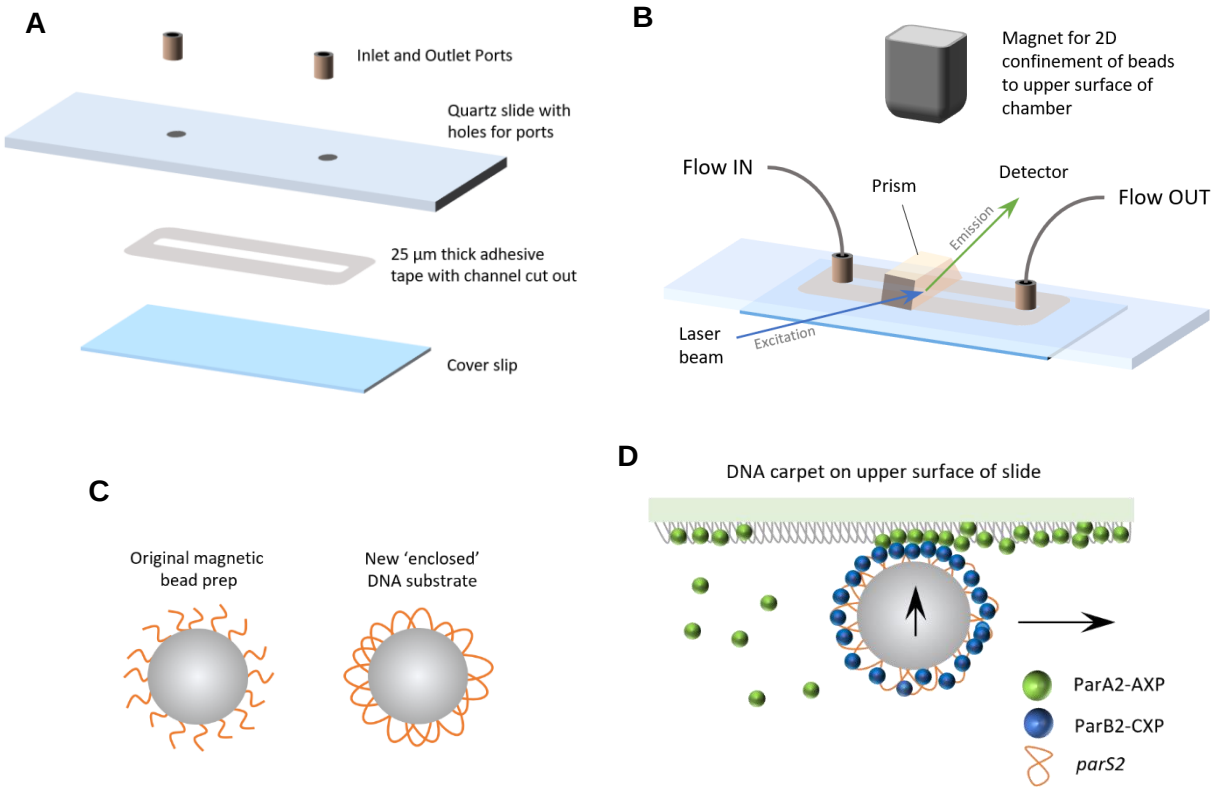

Figure 4.2. Reconstitutions to investigate dynamic self-assembly in more detail, with enclosed DNA substrate on magnetic beads for ParB2-CXP. A) Assembly of microfluidics chamber for cell-free ParABS experiments. A thin adhesive tape sandwiched between two slides forms the chamber and inlet and outlet ports are used for preparation of the DNA carpet, and for flowing in samples (ParA2-GFP, ParB2, magnetic beads with *parS2*, ATP, and CXP). **B)** A prism-TIRF microscope for imaging Par interactions in real time. **C)** Magnetic beads need to have double-tethered DNA substrate by biotinylation of both free ends so that ParB2-CXP sliding clamps do not fall off. **D)** Interaction of ParB2-*parS2* complexes on magnetic beads with ParA2-GFP on the DNA carpet in a Brownian-ratchet mechanism. A higher concentration of ParB2-CXP is likely required to clear a ParA2 depletion zone in future experiments, relative to what was observed in Figure 5.1, in the absence of CXP.

Another interesting experiment to conduct would be the replication of HDRs in a 2D manner. In this experimental set up, increased DNA carpet density at the ends of the microfluidics chamber can be complemented with a sparsely populated mid-region. *Vc*ParABS2 interactions could be monitored in real time to finetune assembly dynamics and then determine conditions that recapitulate *in vivo* observations of ParA2 oscillations. There is also scope for 3D reconstitutions with use of self-assembling 3D DNA origami structures within the microfluidics chamber (**Endo et al., 2013**).

4.2.3 Final perspectives

Considerable progress has been made in understanding ParABS-mediated bacterial chromosome segregation. However, many mechanistic features are missing, or are just being revealed, as demonstrated with the discovery of ParB-CTP-binding activity. Further characterisation of individual Par protein activities will give more insight into the mechanistic features underlying DNA segregation, for example potential ParB-bridging activities conferred from CTP-binding. Moreover, 69% of bacterial species encode a *par* locus and up to 75% have at least one Par system component (**Livny et al., 2007**). This indicates evolution between species for the ParABS system and bacterial chromosome segregation, to meet the requirements of the mother-organism and its environment(s) (**Jalal and Le, 2020**). There are still many unknowns between species, such as the reason for varying number of *parS* sites and different Par system partners (**Kawalek et al., 2020**).

As described in Chapter 1, deletion of *par* locus genes on primary chromosomes can result in significant segregation defects and affect growth rates. In general, primary chromosome Par systems are not essential but are required for accurate *oriC* segregation after the bulk is segregated via SMC/MukB and the mechanism of entropic demixing (**Kawalek et al., 2020; Jun & Wright, 2010**). Rod-shaped cells greatly improve the efficiency of entropic demixing of bacterial chromosomes, and the actin-homologue, MreB, enables the maintenance of this geometry (**Shi et al., 2018; Wu et al., 2020**). However, the variability of chromosome segregation between species has been shown as *C. crescentus* encodes for both SMC and MreB but the Par system is still essential for generational cell viability (**Sundararajan and Goley, 2017**). Furthermore, while *Vc*ParABS1 is not essential, simultaneous *mukB* and *par* locus deletions were said to cause no significant defect to *Vc*Chr1 segregation (data not shown in paper) (**David et al., 2014**). This perhaps shows a reliance on entropic demixing, or that there is further redundancy built in for *Vc*Chr1 segregation. Crucially, however, Par systems have the capacity to translocate whole chromosomes, as the essential activity of *Vc*ParABS2 shows that bulk-segregation systems are insufficient for translocation of *Vc*Chr2 (**Yamaichi et al. 2007b**). Research on *Vc*ParABS2 as a model chromosomal Par system is therefore warranted to further findings presented in this study, and could contribute to a better understanding of the complexities involved in large DNA cargo translocation.

It is also becoming clearer that Brownian-ratchet mechanisms are conserved as spatial regulators of protein clusters (**Murray and Sourjik, 2017; Hu et al., 2017a; MacCready et al., 2018**). Since there are no Walker-type P-loop ATPases in eukaryotes, they are an ideal target for antibiotics (**Matano et al., 2017**). Potential antibiotics could be developed to target the ESKAPE pathogens, of which *Enterococcus faecium*, *Staphylococcus aureus*,

Acinetobacter species, *P. aeruginosa*, and *Enterobacter* species encode *par* genes (**Livny et al., 2007**).

Further experiments to investigate chromosome segregation within the nucleoid is also required (**Marbouty et al., 2015; Le Gall et al., 2016**). While in principle, the changing architecture of the nucleoid during the cell-cycle likely contributes to ParA dynamicity and to translocation of partition complexes, the exact events in time have not been experimentally examined. Single-molecule imaging can contribute to this endeavour. Novel molecular biology and biophysics methodologies, as well as traditional biochemical and genetic approaches, will reveal more details of the exact mechanisms responsible for bacterial chromosome segregation.

Finally, Par systems can be utilised in new approaches and synthetic biology. Plasmid ParB fluorescent fusion proteins have already been utilised as markers of chromosomal loci, with *parS* inserted throughout both *V. cholerae* chromosomes (**Fiebig et al., 2006; David et al., 2014**). Furthermore, ParB-*parS* complexes have been integrated into an *E. coli* genetic circuit to achieve a greater complexity of cell types through asymmetric cell division and cell differentiation (**Mushnikov et al., 2019**). There is also scope for implementation of Par systems into synthetic cells for faithful segregation of minimal genomes; *E. coli* is being used for construction of large Mb plasmids and secondary chromosomes by using new bacterial artificial chromosome (BAC) vectors in bottom-up synthetic biology, with potential uses in biotechnology and medicine (**Mukai et al., 2020**). *E. coli* was previously believed to be unsuitable for this undertaking as traditional plasmid vectors lack some of the regulatory DNA elements required for stable maintenance of such a large DNA cargo. The *oriC* and *par* locus from a *Vibrio* secondary chromosome was introduced for even distribution of duplicated DNA material prior to cell division at mid-cell (**Mukai et al., 2020**). This could potentially be taken further, as there are around 40 genes needed for general chromosome maintenance, and some with unknown function (**Hutchison et al., 2016**). A more complete understanding of global chromosome segregation, and maintenance, can facilitate refactoring of the genes required, including *par* genes, into a final operon(s) for their optimal utilisation in minimal genomes (**Temme et al., 2012**). Ongoing research into ParABS systems will therefore benefit from newly emerging methodologies, and the obtained insights will give a more complete understanding of subcellular bacterial spatiotemporal organisation. The insights could subsequently be used in prospective real-world and novel applications.

APPENDIX

2D CELL-FREE RECONSTITUTION OF THE *Vc*ParABS2 SYSTEM

Experiments were prepared and run in collaboration with Adam Brooks (University of Sheffield). Adam Brooks performed TIRF microscopy imaging.

5.1 EXPERIMENTAL PROCEDURES

5.1.1 Strains and plasmids

The strains and plasmids used and/or constructed during this work are detailed in the table below.

Table 8. *E. coli* strains and plasmids

E. coli	**Genotype**	**Supplier**
NEB 5-alpha	*fhuA2 Δ(argF-lacZ)U169 phoA glnV44 Φ80 Δ(lacZ)M15 gyrA96 recA1 relA1 endA1 thi-1 hsdR17*	New England Biolabs
BL21(DE3)	*fhuA2 [lon] ompT gal (λ DE3) [dcm] ΔhsdS λ DE3 = λ sBamHIo ΔEcoRI-B int::(lacI::PlacUV5::T7 gene1) i21 Δnin5*	New England Biolabs

Plasmid	**Description**	**Construction**
pBKSII	pBluescript KSII+	from Stratagene
pBKSII-*parS2*	pBKSII bearing *parS2* site	a) Annealed oligonucleotides LCH04-*parS2*-T and LCH05-*parS2*-B as top and bottom strands of *parS2B* site b) Digest product with BamHI and EcoRI c) Ligation of fragment into pBKSII cut with BamHI and EcoRI

5.1.2 Oligonucleotides

Oligonucleotide primers used for construction of plasmids, and for amplifying DNA fragments used in experimental assays, are listed in the table below.

Table 9. Oligonucleotides

Oligo	**Sequence (5'-3')**	**Used for amplifying**
SC05-pBKSII_fwd_Biotin	[Btn]GTCTGACAGTTACCAATGC	Biotinylated and Cy5-labelled 3 kb DNA with a *parS2* site
SC07-pBKSII_rev_Cy5	[Cy5]GATAATCTCATGACCAAAATCCC	

5.1.3 Buffers

Buffer A: see section 2.2.3. **TE**: Tris-HCl pH 8.0, 2 mM EDTA. **TN100**: 10 mM Tris-HCl pH 8.0, 100 mM NaCl. **TN100 + Mg**: 10 mM Tris-HCl pH 8.0, 100 mM NaCl, 10 mM $MgCl_2$

5.1.4 Protein purification

As in Chapter 2.

5.1.5 Microfluidics device preparation

The flow cell was assembled from a quartz slide (VWR) with drilled inlet and outlet ports, a glass coverslip (Fisher Scientific), and 25 µm-thick acrylic adhesive tape (3M).The chamber

was made by laser cutting the relevant region from the acrylic tape. Inlet and outlet port fixtures (Upchurch Scientific) were attached using a liquid photopolymer (Norland Optical Adhesive 61) (Thorlabs) and curing by exposing to UV light. Slides and cover slips were cleaned prior to assembly with an overnight 5 M sulphuric acid bath. The slides were washed with double-distilled water (milli-Q), and dried with nitrogen/argon gas, before plasma-cleaning. Flow cells were assembled, and oven baked for 1 h at 100 °C for curing of adhesive tape.

5.1.6 Biotinylated liposomes

DOPC (1,2-dioleoyl-*sn*-glycero-3-phosphocholine) was mixed with 1% biotin-PE (1-oleoyl-2-(12-biotinyl(aminododecanoyl))-*sn*-glycero-3-phosphoethanolamine) (Avanti Polar Lipids), and chloroform was lyophilised from solution by heating for 1 h at 50 °C. TN100 was used to resuspend lipids and the solution was degassed with argon gas, sealed, and stored at 4 °C for up to 1 month.

5.1.7 Biotinylated sssDNA

10 mg/ml ~1 kb sssDNA (Sigma) was biotinylated using 40 µM biotin-14-dCTP (Jena) and 20 U/µl terminal transferase (NEB) and incubated at 37 °C for 30 min before purifying with S200 microspin columns (GE Healthcare) and ethanol precipitation. The acquired DNA pellet was resuspended in TE buffer.

5.1.8 Coating magnetic beads with biotinylated Cy5-labelled 3kb *parS2*-DNA

40 µl of 10 mg/ml MyOne Streptavidin C1 Dynabeads (Invitrogen) were washed in wash buffer (10 mM Tris-HC pH 8, 1 mM NaCl, 1 mM EDTA). Beads were resuspended in 1.3 ml of wash buffer and 3 µl Tween 20. The bead suspension was then placed on a magnet and the supernatant discarded. Beads were then resuspended in the same wash buffer with Tween 20 solution. This was repeated for a total of 3 washes. 3 kb Cy5-labelled and biotinylated *parS2* (8 pM in 50 µl) was added to the bead suspension and incubated while shaking at 193 rpm for 1 h. The beads were washed in 1 .5 ml of wash buffer a further 3 times. Beads were resuspended in 40 µl elution buffer (30 mM Tris-HCl pH7, 100 mM KCl, 1 mM EDTA) and stored at 4 °C .

5.1.9 Coating of DNA carpet within microfluidics device

Lipids were diluted to 1 mg/ml for a total volume of 500 µl and injected into flow cell using tubing attached to the inlet port. The prepared flow cell was incubated at 30 °C for 1 h. Excess lipids were washed with TN100 by withdrawing from the outlet port at a rate of 80 µl/min using a syringe pump. 1 mg/ml NeutrAvidin protein (ThermoFisher) was flowed into the flow cell at 80 µl/min and incubated for 1 h at room temperature and pressure (rtp). Excess protein was washed with TN100 at 80 µl/min. Biotinylated sssDNA was diluted to 1 mg/ml in TN100 +

$MgCl_2$. The solution was introduced into the flow cell at 20 µl/min, and the flow cell was incubated overnight at 4 °C. Unbound biotinylated sssDNA was washed from the flow cell with TN100 + $MgCl_2$ at 50 µl/min.

5.1.10 Reconstitution of the *Vc*ParABS2 complex

5 µM ParA2-GFP was pre-incubated in reaction buffer (Buffer A, 2 mM ATP, 0.1 mg/ml α-casein, and 2 mM DTT) with a total volume of 20 µl, for 15 min at 30 °C. In parallel, ParB2 was pre-incubated with 2 mg/ml *parS2*-DNA beads, in the same reaction buffer to a volume of 20 µl, for 30 min at rtp. 5 µM ParB2 was used for a 1:1 molar ratio, and 40 µM ParB2 was used for a 1:8 molar ratio. A magnet was used to pull down the beads and 15 µl of reaction was aspirated. The ParA2-GFP pre-incubation was added to 175 µl of new reaction buffer. The ParB2-*parS2* bead preincubation was then added for a 1:1 or 1:8 molar ratio of ParA2 to ParB2-*parS2* beads.

The 200 µl samples were injected into the inlet port of the microfluidic device prepared with a DNA carpet, using a syringe pump at a rate of 80 µl/min. TIRF-microscopy imaging was carried out by Adam Brooks (University of Sheffield). Images were processed and analysed using ImageJ software (NIH).

5.2 RESULTS

A

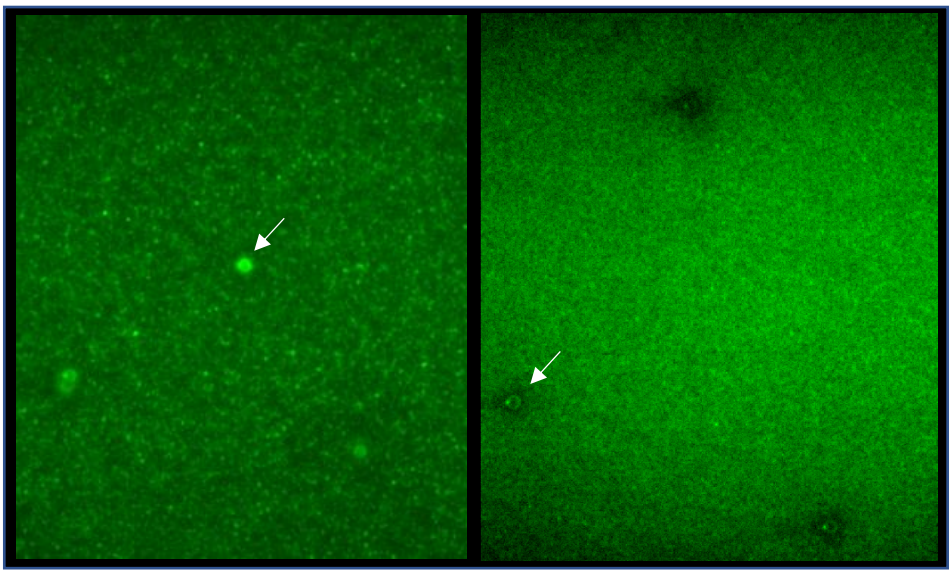

B

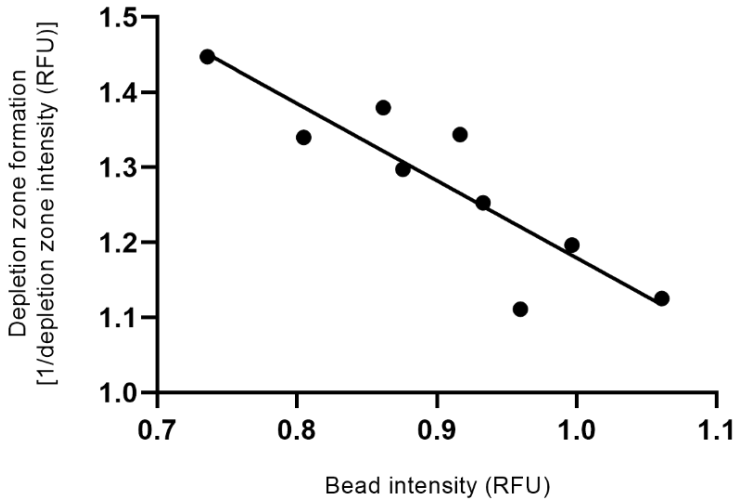

Figure 5.1 2D reconstitution of *Vc*ParABS2 complex. A) ParA2-GFP is visualised on a DNA-carpet, interacting with ParB2-*parS2* complexes on magnetic beads. The left panel has a ratio of ParA2:ParB2 of 1:1 µM, while the right panel a 1:8 µM ratio. Arrowheads show representative beads in both conditions. ParA2-GFP is cleared from the beads more considerably in the right panel, with a pronounced depletion zone visible around the beads relative to the left panel. **B)** Depletion zone formation is indirectly proportional to ParA2-GFP clearance from the beads.

REFERENCES

Adams, D.W., Wu, L.J., Errington, J. (2014). Cell-cycle regulation by the bacterial nucleoid. Curr. Opin. Microbiol. *22*, 94–101. https://doi.org/10.1016/j.mib.2014.09.020

Ah-Seng, Y., Lopez, F., Pasta, F., Lane, D., Bouet, J.-Y. (2009). Dual Role of DNA in Regulating ATP Hydrolysis by the SopA Partition Protein. J Biol Chem *284*, 30067–30075. https://doi.org/10.1074/jbc.M109.044800

Attaiech, L., Minnen, A., Kjos, M., Gruber, S., Veening, J.-W. (2015). The ParB-parS Chromosome Segregation System Modulates Competence Development in Streptococcus pneumoniae. mBio *6*, e00662. https://doi.org/10.1128/mBio.00662-15

Aylett, C.H.S., Wang, Q., Michie, K.A., Amos, L.A., Löwe, J. (2010). Filament structure of bacterial tubulin homologue TubZ. Proc. Natl. Acad. Sci. U.S.A. *107*, 19766–19771. https://doi.org/10.1073/pnas.1010176107

Azam, T.A., Ishihama, A. (1999). Twelve species of the nucleoid-associated protein from Escherichia coli. Sequence recognition specificity and DNA-binding affinity. J. Biol. Chem. *274*, 33105–33113. https://doi.org/10.1074/jbc.274.46.33105

Badrinarayanan, A., Le, T.B.K., Laub, M.T. (2015). Bacterial chromosome organization and segregation. Annu Rev Cell Dev Biol *31*, 171–199. https://doi.org/10.1146/annurev-cellbio-100814-125211

Baek, J.H., Rajagopala, S.V., Chattoraj, D.K. (2014). Chromosome segregation proteins of Vibrio cholerae as transcription regulators. mBio *5*, e01061-01014. https://doi.org/10.1128/mBio.01061-14

Barillà, D., Rosenberg, M.F., Nobbmann, U., Hayes, F. (2005). Bacterial DNA segregation dynamics mediated by the polymerizing protein ParF. EMBO J *24*, 1453–1464. https://doi.org/10.1038/sj.emboj.7600619

Bartosik, A.A., Glabski, K., Jecz, P., Lasocki, K., Mikosa, M., Plochocka, D., Thomas, C.M., Jagura-Burdzy, G. (2014). Dissection of the region of Pseudomonas aeruginosa ParA that is important for dimerisation and interactions with its partner ParB. Microbiology (Reading) *160*, 2406–2420. https://doi.org/10.1099/mic.0.081216-0

Bartosik, A.A., Lasocki, K., Mierzejewska, J., Thomas, C.M., Jagura-Burdzy, G. (2004). ParB of Pseudomonas aeruginosa: Interactions with Its Partner ParA and Its Target parS and Specific Effects on Bacterial Growth. Journal of Bacteriology *186*, 6983–6998. https://doi.org/10.1128/JB.186.20.6983-6998.2004

Bartosik, A.A., Mierzejewska, J., Thomas, C.M., Jagura-Burdzy, G. (2009). ParB deficiency in Pseudomonas aeruginosa destabilizes the partner protein ParA and affects a variety of physiological parameters. Microbiology (Reading) *155*, 1080–1092. https://doi.org/10.1099/mic.0.024661-0

Bates, D., (2008). The bacterial replisome: back on track? Mol Microbiol *69*, 1341–1348. https://doi.org/10.1111/j.1365-2958.2008.06378.x

Baxter, J., Oliver, A.W., Schalbetter, S.A. (2019). Are SMC Complexes Loop Extruding Factors? Linking Theory With Fact. BioEssays *41*, 1800182. https://doi.org/10.1002/bies.201800182

Berg, J.M., Tymoczko, J.L., Stryer, L., Berg, J.M., Tymoczko, J.L., Stryer, L. (2002). Biochemistry, 5th ed. W H Freeman.

Bernhardt, T.G., de Boer, P.A.J. (2005). SlmA, a nucleoid-associated, FtsZ binding protein required for blocking septal ring assembly over Chromosomes in E. coli. Mol. Cell *18*, 555–564. https://doi.org/10.1016/j.molcel.2005.04.012

Böhm, K., Giacomelli, G., Schmidt, A., Imhof, A., Koszul, R., Marbouty, M., Bramkamp, M. (2020). Chromosome organization by a conserved condensin-ParB system in the actinobacterium Corynebacterium glutamicum. Nat Commun *11*, 1485. https://doi.org/10.1038/s41467-020-15238-4

Bouet, J.-Y., Funnell, B.E. (1999). P1 ParA interacts with the P1 partition complex at parS and an ATP-ADP switch controls ParA activities. EMBO J *18*, 1415–1424. https://doi.org/10.1093/emboj/18.5.1415

Bouet, J.-Y., Ah-Seng, Y., Benmeradi, N., Lane, D. (2007). Polymerization of SopA partition ATPase: regulation by DNA-binding and SopB. Molecular Microbiology *63*, 468–481. https://doi.org/10.1111/j.1365-2958.2006.05537.x

Booker, B.M., Deng, S., Higgins, N.P. (2010). DNA topology of highly transcribed operons in Salmonella enterica serovar Typhimurium. Molecular Microbiology *78*, 1348–1364. https://doi.org/10.1111/j.1365-2958.2010.07394.x

Bouet, J.-Y., Stouf, M., Lebailly, E., Cornet, F. (2014). Mechanisms for chromosome segregation. Curr Opin Microbiol *22*, 60–65. https://doi.org/10.1016/j.mib.2014.09.013

Boutte, C.C., Srinivasan, B.S., Flannick, J.A., Novak, A.F., Martens, A.T., Batzoglou, S., Viollier, P.H., Crosson, S. (2008). Genetic and Computational Identification of a Conserved Bacterial Metabolic Module. PLoS Genet *4*, e1000310. https://doi.org/10.1371/journal.pgen.1000310

Breier, A.M., Grossman, A.D. (2007). Whole-genome analysis of the chromosome partitioning and sporulation protein Spo0J (ParB) reveals spreading and origin-distal sites on the Bacillus subtilis chromosome. Mol Microbiol *64*, 703–718. https://doi.org/10.1111/j.1365-2958.2007.05690.x

Broedersz, C.P., Wang, X., Meir, Y., Loparo, J.J., Rudner, D.Z., Wingreen, N.S. (2014). Condensation and localization of the partitioning protein ParB on the bacterial chromosome. Proc Natl Acad Sci U S A *111*, 8809–8814. https://doi.org/10.1073/pnas.1402529111

Brooks, A.C., Hwang, L.C. (2017). Reconstitutions of plasmid partition systems and their mechanisms. Plasmid, *91*, 37–41. https://doi.org/10.1016/j.plasmid.2017.03.004

Caccamo, M., Dobruk-Serkowska, A., Rodríguez-Castañeda, F., Pennica, C., Barillà, D., Hayes, F. (2020). Genome Segregation by the Venus Flytrap Mechanism: Probing the Interaction Between the ParF ATPase and the ParG Centromere Binding Protein. Front. Mol. Biosci. *7*. https://doi.org/10.3389/fmolb.2020.00108

Campbell, C.S., Mullins, R.D. (2007). In vivo visualization of type II plasmid segregation: bacterial actin filaments pushing plasmids. J. Cell. Biol. *179*, 1059–1066. https://doi.org/10.1083/jcb.200708206

Castaing, J.-P., Bouet, J.-Y., Lane, D. (2008). F plasmid partition depends on interaction of SopA with non-specific DNA. Molecular Microbiology *70*, 1000–1011.

https://doi.org/10.1111/j.1365-2958.2008.06465.x

Chattoraj, D., Cordes, K., Abeles, A. (1984). Plasmid P1 replication: negative control by repeated DNA sequences. PNAS *81*, 6456–6460. https://doi.org/10.1073/pnas.81.20.6456

Chen, B.-W., Lin, M.-H., Chu, C.-H., Hsu, C.-E., Sun, Y.-J. (2015). Insights into ParB spreading from the complex structure of Spo0J and parS. Proc. Natl. Acad. Sci. U.S.A. *112*, 6613–6618. https://doi.org/10.1073/pnas.1421927112

Chen, W., Qin, Z. (2011). Development of a gene cloning system in a fast-growing and moderately thermophilic Streptomyces species and heterologous expression of Streptomyces antibiotic biosynthetic gene clusters. BMC Microbiol. *11*, 243. https://doi.org/10.1186/1471-2180-11-243

Chu, C.-H., Yen, C.-Y., Chen, B.-W., Lin, M.-G., Wang, L.-H., Tang, K.-Z., Hsiao, C.-D., Sun, Y.-J. (2019). Crystal structures of HpSoj-DNA complexes and the nucleoid-adaptor complex formation in chromosome segregation. Nucleic Acids Res. *47*, 2113–2129. https://doi.org/10.1093/nar/gky1251

Corrales-Guerrero, L., He, B., Refes, Y., Panis, G., Bange, G., Viollier, P.H., Steinchen, W., Thanbichler, M. (2020). Molecular architecture of the DNA-binding sites of the P-loop ATPases MipZ and ParA from Caulobacter crescentus. Nucleic Acids Res *48*, 4769–4779. https://doi.org/10.1093/nar/gkaa192

Dame, R.T., Rashid, F.-Z.M., Grainger, D.C. (2020). Chromosome organization in bacteria: mechanistic insights into genome structure and function. Nat Rev Genet *21*, 227–242. https://doi.org/10.1038/s41576-019-0185-4

Das, B. (2014). Mechanistic insights into filamentous phage integration in Vibrio cholerae. Front. Microbiol. *5*. https://doi.org/10.3389/fmicb.2014.00650

Davey, M.J., Funnell, B.E. (1997). Modulation of the P1 Plasmid Partition Protein ParA by ATP, ADP, and P1 ParB. J. Biol. Chem. *272*, 15286–15292. https://doi.org/10.1074/jbc.272.24.15286

David, A., Demarre, G., Muresan, L., Paly, E., Barre, F.-X., Possoz, C. (2014). The Two Cis-Acting Sites, parS1 and oriC1, Contribute to the Longitudinal Organisation of Vibrio cholerae Chromosome I. PLOS Genetics *10*, e1004448. https://doi.org/10.1371/journal.pgen.1004448

Davis, M.A., Martin, K.A., Austin, S.J. (1992). Biochemical activities of the ParA partition protein of the P1 plasmid. Molecular Microbiology *6*, 1141–1147. https://doi.org/10.1111/j.1365-2958.1992.tb01552.x

Davis, M.A., Radnedge, L., Martin, K.A., Hayes, F., Youngren, B., Austin, S.J. (1996). The P1 ParA protein and its ATPase activity play a direct role in the segregation of plasmid copies to daughter cells. Mol. Microbiol. *21*, 1029–1036. https://doi.org/10.1046/j.1365-2958.1996.721423.x

de Lemos Martins, F., Fournes, F., Mazzuoli, M.-V., Mazel, D., Val, M.-E. (2018). Vibrio cholerae chromosome 2 copy number is controlled by the methylation-independent binding of its monomeric initiator to the chromosome 1 crtS site. Nucleic Acids Res. *46*, 10145–10156. https://doi.org/10.1093/nar/gky790

Debaugny, R.E., Sanchez, A., Rech, J., Labourdette, D., Dorignac, J., Geniet, F., Palmeri, J., Parmeggiani, A., Boudsocq, F., Anton Leberre, V., Walter, J.-C., Bouet, J.-Y. (2018). A

conserved mechanism drives partition complex assembly on bacterial chromosomes and plasmids. Mol. Syst. Biol. *14*, e8516. https://doi.org/10.15252/msb.20188516

Dekker, J., Rippe, K., Dekker, M., Kleckner, N. (2002). Capturing Chromosome Conformation. Science *295*, 1306–1311. https://doi.org/10.1126/science.1067799

Demarre, G., Galli, E., Muresan, L., Paly, E., David, A., Possoz, C., Barre, F.-X. (2014). Differential Management of the Replication Terminus Regions of the Two Vibrio cholerae Chromosomes during Cell Division. PLoS Genet. *10*. https://doi.org/10.1371/journal.pgen.1004557

diCenzo, G.C., Finan, T.M. (2017). The Divided Bacterial Genome: Structure, Function, and Evolution. Microbiol Mol. Biol. Rev. *81*. https://doi.org/10.1128/MMBR.00019-17

Dingman, C.W. (1974). Bidirectional chromosome replication: some topological considerations. J. Theor. Biol. *43*, 187–195. https://doi.org/10.1016/s0022-5193(74)80052-4

Dobruk-Serkowska, A., Caccamo, M., Rodríguez-Castañeda, F., Wu, M., Bryce, K., Ng, I., Schumacher, M.A., Barillà, D., Hayes, F. (2012). Uncoupling of Nucleotide Hydrolysis and Polymerization in the ParA Protein Superfamily Disrupts DNA Segregation Dynamics. J. Biol. Chem. *287*, 42545–42553. https://doi.org/10.1074/jbc.M112.410324

Dubarry, N., Pasta, F., Lane, D. (2006). ParABS Systems of the Four Replicons of Burkholderia cenocepacia: New Chromosome Centromeres Confer Partition Specificity. J. BACTERIOL. *188*, 9.

Duigou, S., Boccard, F. (2017). Long range chromosome organization in Escherichia coli: The position of the replication origin defines the non-structured regions and the Right and Left macrodomains. PLOS Genetics *13*, e1006758. https://doi.org/10.1371/journal.pgen.1006758

Dunham, T.D., Xu, W., Funnell, B.E., Schumacher, M.A. (2009). Structural basis for ADP-mediated transcriptional regulation by P1 and P7 ParA. EMBO J. *28*, 1792–1802. https://doi.org/10.1038/emboj.2009.120

Easter, J., Gober, J.W. (2002). ParB-stimulated nucleotide exchange regulates a switch in functionally distinct ParA activities. Mol Cell 10, 427–434. https://doi.org/10.1016/s1097-2765(02)00594-4

Ebersbach, G., Ringgaard, S., Møller-Jensen, J., Wang, Q., Sherratt, D.J., Gerdes, K. (2006). Regular cellular distribution of plasmids by oscillating and filament-forming ParA ATPase of plasmid pB171. Mol. Microbiol. *61*, 1428–1442. https://doi.org/10.1111/j.1365-2958.2006.05322.x

Echeverria, P., Murphy, J.R. (1980). Enterotoxigenic *Escherichia coli* Carrying Plasmids Coding for Antibiotic Resistance and Enterotoxin Production. The Journal of Infectious Diseases *142*, 273–278.

Edlin, G., Lin, L., Bitner, R. (1977). Reproductive fitness of P1, P2, and Mu lysogens of *Escherichia coli*. Journal of Virology *21*, 560–564. https://doi.org/10.1128/JVI.21.2.560-564.1977

Egan, E.S., Fogel, M.A., Waldor, M.K. (2005). MicroReview: Divided genomes: negotiating the cell-cycle in prokaryotes with multiple chromosomes. Molecular Microbiology *56*, 1129–1138. https://doi.org/10.1111/j.1365-2958.2005.04622.x

Egan, E.S., Waldor, M.K. (2003). Distinct replication requirements for the two *Vibrio cholerae* chromosomes. Cell *114*, 521–530. https://doi.org/10.1016/s0092-8674(03)00611-1

Endo, M., Yang, Y., Sugiyama, H. (2013). DNA origami technology for biomaterials applications. Biomater. Sci. *1*, 347–360. https://doi.org/10.1039/C2BM00154C

Erdmann, N., Petroff, T., Funnell, B.E. (1999). Intracellular localization of P1 ParB protein depends on ParA and parS. PNAS *96*, 14905–14910. https://doi.org/10.1073/pnas.96.26.14905

Espinosa, E., Barre, F.-X., Galli, E. (2017). Coordination between replication, segregation and cell division in multi-chromosomal bacteria: lessons from Vibrio cholerae. Int. Microbiol. *20*, 121–129. https://doi.org/10.2436/20.1501.01.293

Espinosa, E., Paly, E., Barre, F.-X. (2020). High-Resolution Whole-Genome Analysis of Sister-Chromatid Contacts. Molecular Cell. https://doi.org/10.1016/j.molcel.2020.06.033

Fiebig, A., Keren, K., Theriot, J.A. (2006). Fine-scale time-lapse analysis of the biphasic, dynamic behaviour of the two Vibrio cholerae chromosomes. Molecular Microbiology *60*, 1164–1178. https://doi.org/10.1111/j.1365-2958.2006.05175.x

Figge, R.M., Easter, J., Gober, J.W. (2003). Productive interaction between the chromosome partitioning proteins, ParA and ParB, is required for the progression of the cell-cycle in Caulobacter crescentus. Mol Microbiol *47*, 1225–1237. https://doi.org/10.1046/j.1365-2958.2003.03367.x

Fink, G., Löwe, J. (2015). Reconstitution of a prokaryotic minus end-tracking system using TubRC centromeric complexes and tubulin-like protein TubZ filaments. PNAS *112*, E1845–E1850. https://doi.org/10.1073/pnas.1423746112

Fisher, G.L., Pastrana, C.L., Higman, V.A., Koh, A., Taylor, J.A., Butterer, A., Craggs, T., Sobott, F., Murray, H., Crump, M.P., Moreno-Herrero, F., Dillingham, M.S. (2017). The structural basis for dynamic DNA-binding and bridging interactions which condense the bacterial centromere. eLife *6*, e28086. https://doi.org/10.7554/eLife.28086

Fisher, J.K., Bourniquel, A., Witz, G., Weiner, B., Prentiss, M., Kleckner, N. (2013). Four-Dimensional Imaging of *E. coli* Nucleoid Organization and Dynamics in Living Cells. Cell *153*, 882–895. https://doi.org/10.1016/j.cell.2013.04.006

Fogel, M.A., Waldor, M.K. (2005). Distinct segregation dynamics of the two *Vibrio cholerae* chromosomes. Mol. Microbiol. *55*, 125–136. https://doi.org/10.1111/j.1365-2958.2004.04379.x

Fogel, M.A., Waldor, M.K. (2006). A dynamic, mitotic-like mechanism for bacterial chromosome segregation. Genes Dev. *20*, 3269–3282. https://doi.org/10.1101/gad.1496506

Fung, E. (2001). Probing the ATP-binding site of P1 ParA: partition and repression have different requirements for ATP-binding and hydrolysis. The EMBO Journal *20*, 4901–4911. https://doi.org/10.1093/emboj/20.17.4901

Funnell, B.E. (2016). ParB Partition Proteins: Complex Formation and Spreading at Bacterial and Plasmid Centromeres. Front. Mol. Biosci. *3*, 44. https://doi.org/10.3389/fmolb.2016.00044

Funnell, B.E. (1991). The P1 plasmid partition complex at parS. The influence of *Escherichia coli* integration host factor and of substrate topology. J. Biol. Chem. *266*, 14328–14337.

Galli, E., Paly, E., Barre, F.X. (2017). Late assembly of the *Vibrio cholerae* cell division machinery postpones septation to the last 10% of the cell-cycle. Scientific Reports *7*, 44505. https://doi.org/10.1038/srep44505

Galli, E., Poidevin, M., Le Bars, R., Desfontaines, J.-M., Muresan, L., Paly, E., Yamaichi, Y., Barre, F.X. (2016). Cell division licensing in the multi-chromosomal Vibrio cholerae bacterium. Nature Microbiology *1*, 1–5. https://doi.org/10.1038/nmicrobiol.2016.94

Garner, E. C., Campbell, C. S., & Mullins, R. D. (2004). Dynamic instability in a DNA-segregating prokaryotic actin homolog. Science (New York, N.Y.), 306(5698), 1021–1025. https://doi.org/10.1126/science.1101313

Gayathri, P., Fujii, T., Møller-Jensen, J., van den Ent, F., Namba, K., Löwe, J. (2012). A bipolar spindle of antiparallel ParM filaments drives bacterial plasmid segregation. Science *338*, 1334–1337. https://doi.org/10.1126/science.1229091

Gerdes, K., Howard, M., Szardenings, F. (2010). Pushing and Pulling in Prokaryotic DNA Segregation. Cell *141*, 927–942. https://doi.org/10.1016/j.cell.2010.05.033

Gerdes, K., Molin, S. (1986). Partitioning of plasmid R1. Structural and functional analysis of the parA locus. J. Mol. Biol. *190*, 269–279. https://doi.org/10.1016/0022-2836(86)90001-x

Gerdes, K., Møller-Jensen, J., Jensen, R.B. (2000). Plasmid and chromosome partitioning: surprises from phylogeny. Molecular Microbiology *37*, 455–466. https://doi.org/10.1046/j.1365-2958.2000.01975.x

Ginda, K., Santi, I., Bousbaine, D., Zakrzewska-Czerwińska, J., Jakimowicz, D., McKinney, J., (2017). The studies of ParA and ParB dynamics reveal asymmetry of chromosome segregation in mycobacteria. Mol. Microbiol. *105*, 453–468. https://doi.org/10.1111/mmi.13712

Godfrin-Estevenon, A.-M., Pasta, F., Lane, D. (2002). The *parAB* gene products of *Pseudomonas putida* exhibit partition activity in both *P. putida* and *Escherichia coli*. Molecular Microbiology *43*, 39–49. https://doi.org/10.1046/j.1365-2958.2002.02735.x

Goodman, S. D., Velten, N. J., Gao, Q., Robinson, S., & Segall, A. M. (1999). In vitro selection of integration host factor binding sites. Journal of bacteriology, 181(10), 3246–3255. https://doi.org/10.1128/JB.181.10.3246-3255.1999

Graham, T.G.W., Wang, X., Song, D., Etson, C.M., van Oijen, A.M., Rudner, D.Z., Loparo, J.J. (2014). ParB spreading requires DNA bridging. Genes Dev. *28*, 1228–1238. https://doi.org/10.1101/gad.242206.114

Halley, J.D., Winkler, D.A. (2008). Consistent concepts of self-organization and self-assembly. Complexity *14*, 10–17. https://doi.org/10.1002/cplx.20235

Hammel, M., Amlanjyoti, D., Reyes, F.E., Chen, J.-H., Parpana, R., Tang, H.Y.H., Larabell, C.A., Tainer, J.A., Adhya, S. (2016). HU multimerization shift controls nucleoid compaction. Science Advances *2*, e1600650. https://doi.org/10.1126/sciadv.1600650

Hammond, L.R., White, M.L., Eswara, P.J. (2019). ¡vIVA la DivIVA! J. Bacteriol. *201*. https://doi.org/10.1128/JB.00245-19

Harrison, P.W., Lower, R.P.J., Kim, N.K.D., Young, J.P.W. (2010). Introducing the bacterial "chromid": not a chromosome, not a plasmid. Trends Microbiol. *18*, 141–148.

https://doi.org/10.1016/j.tim.2009.12.010

Hatano, T., Niki, H. (2010). Partitioning of P1 plasmids by gradual distribution of the ATPase ParA. Mol. Microbiol. *78*, 1182–1198. https://doi.org/10.1111/j.1365-2958.2010.07398.x

Hatano, T., Yamaichi, Y., Niki, H. (2007). Oscillating focus of SopA associated with filamentous structure guides partitioning of F plasmid. Molecular Microbiology *64*, 1198–1213. https://doi.org/10.1111/j.1365-2958.2007.05728.x

Havey, J.C., Vecchiarelli, A.G., Funnell, B.E. (2012). ATP-regulated interactions between P1 ParA, ParB and non-specific DNA that are stabilized by the plasmid partition site, parS. Nucleic Acids Res. *40*, 801–812. https://doi.org/10.1093/nar/gkr747

Hester, C.M., Lutkenhaus, J. (2007). Soj (ParA) DNA-binding is mediated by conserved arginines and is essential for plasmid segregation. PNAS *104*, 20326–20331. https://doi.org/10.1073/pnas.0705196105

Hofmann, A., Mäkelä, J., Sherratt, D.J., Heermann, D., Murray, S.M. (2019). Self-organised segregation of bacterial chromosomal origins. eLife *8*, e46564. https://doi.org/10.7554/eLife.46564

Hoischen, C., Bussiek, M., Langowski, J., Diekmann, S. (2008). Escherichia coli low-copy-number plasmid R1 centromere parC forms a U-shaped complex with its binding protein ParR. Nucleic Acids Res. *36*, 607–615. https://doi.org/10.1093/nar/gkm672

Hu, L., Vecchiarelli, A.G., Mizuuchi, K., Neuman, K.C., Liu, J. (2015). Directed and persistent movement arises from mechanochemistry of the ParA/ParB system. PNAS *112*, E7055–E7064. https://doi.org/10.1073/pnas.1505147112

Hu, L., Vecchiarelli, A.G., Mizuuchi, K., Neuman, K.C., Liu, J. (2017a). Brownian Ratchet Mechanism for Faithful Segregation of Low-Copy-Number Plasmids. Biophys. J. *112*, 1489–1502. https://doi.org/10.1016/j.bpj.2017.02.039

Hu, L., Vecchiarelli, A.G., Mizuuchi, K., Neuman, K.C., Liu, J. (2017b). Brownian ratchet mechanisms of ParA-mediated partitioning. Plasmid *92*, 12–16. https://doi.org/10.1016/j.plasmid.2017.05.002

Hu, Z., Gogol, E.P., Lutkenhaus, J. (2002). Dynamic assembly of MinD on phospholipid vesicles regulated by ATP and MinE. Proc Natl Acad Sci U S A *99*, 6761–6766. https://doi.org/10.1073/pnas.102059099

Hui, M.P., Galkin, V.E., Yu, X., Stasiak, A.Z., Stasiak, A., Waldor, M.K., Egelman, E.H. (2010). ParA2, a *Vibrio cholerae* chromosome partitioning protein, forms left-handed helical filaments on DNA. Proc Natl Acad Sci U S A *107*, 4590–4595. https://doi.org/10.1073/pnas.0913060107

Hulme, E.C., Trevethick., M. A. (2010). Ligand binding assays at equilibrium: validation and interpretation. British Journal of Pharmacology *161*, 1219-1237

Hutchison, C. A., 3rd, Chuang, R. Y., Noskov, V. N., Assad-Garcia, N., Deerinck, T. J., Ellisman, M. H., Gill, J., Kannan, K., Karas, B. J., Ma, L., Pelletier, J. F., Qi, Z. Q., Richter, R. A., Strychalski, E. A., Sun, L., Suzuki, Y., Tsvetanova, B., Wise, K. S., Smith, H. O., Glass, J. I., Venter, J. C. (2016). Design and synthesis of a minimal bacterial genome. Science *351*, 6253-6280. https://doi.org/10.1126/science.aad6253

Hwang, L.C., Vecchiarelli, A.G., Han, Y.-W., Mizuuchi, M., Harada, Y., Funnell, B.E., Mizuuchi,

K. (2013). ParA-mediated plasmid partition driven by protein pattern self-organization. EMBO J. *32*, 1238–1249. https://doi.org/10.1038/emboj.2013.34

Ietswaart, R., Szardenings, F., Gerdes, K., Howard, M. (2014). Competing ParA Structures Space Bacterial Plasmids Equally over the Nucleoid. PLoS Comput. Biol. *10*, e1004009. https://doi.org/10.1371/journal.pcbi.1004009

Iniesta, A.A. (2014). ParABS System in Chromosome Partitioning in the Bacterium *Myxococcus xanthus*. PLOS ONE *9*, e86897. https://doi.org/10.1371/journal.pone.0086897

Jakimowicz, D., Chater, K., Zakrzewska-Czerwi´nska, J. (2002). The ParB protein of *Streptomyces coelicolor* A3(2) recognizes a cluster of *parS* sequences within the origin-proximal region of the linear chromosome. Molecular Microbiology *45*, 1365–1377. https://doi.org/10.1046/j.1365-2958.2002.03102.x

Jalal, A.S., Tran, N.T., Le, T.B. (2020a). ParB spreading on DNA requires cytidine triphosphate in vitro. Elife *9*. https://doi.org/10.7554/eLife.53515

Jalal, A.S.B., Tran, N.T., Stevenson, C.E., Chan, E.W., Lo, R., Tan, X., Noy, A., Lawson, D.M., Le, T.B.K. (2020b). Diversification of DNA-Binding Specificity by Permissive and Specificity-Switching Mutations in the ParB/Noc Protein Family. Cell Reports *32*, 107928. https://doi.org/10.1016/j.celrep.2020.107928

Jalal, A.S.B., Le, T.B.K. (2020). Bacterial chromosome segregation by the ParABS system. Open Biol. *10*, 200097. https://doi.org/10.1098/rsob.200097

Jensen, R.B., Gerdes, K. (1999). Mechanism of DNA segregation in prokaryotes: ParM partitioning protein of plasmid R1 co-localizes with its replicon during the cell-cycle. EMBO J. *18*, 4076–4084. https://doi.org/10.1093/emboj/18.14.4076

Jindal, L., Emberly, E. (2019). DNA segregation under Par protein control. PLoS One *14*. https://doi.org/10.1371/journal.pone.0218520

Joshi, M.C., Magnan, D., Montminy, T.P., Lies, M., Stepankiw, N., Bates, D. (2013). Regulation of Sister Chromosome Cohesion by the Replication Fork Tracking Protein SeqA. PLOS Genetics *9*, e1003673. https://doi.org/10.1371/journal.pgen.1003673

Jun, S., Wright, A. (2010). Entropy as the driver of chromosome segregation. Nat. Rev. Microbiol. *8*, 600–607. https://doi.org/10.1038/nrmicro2391

Jung, A., Raßbach, A., Pulpetta, R.L., van Teeseling, M.C.F., Heinrich, K., Sobetzko, P., Serrania, J., Becker, A., Thanbichler, M. (2019). Two-step chromosome segregation in the stalked budding bacterium *Hyphomonas neptunium*. Nat. Commun. *10*, 3290. https://doi.org/10.1038/s41467-019-11242-5

Junier, I., Martin, O., Képès, F. (2010). Spatial and Topological Organization of DNA Chains Induced by Gene Co-localization. PLOS Computational Biology *6*, e1000678. https://doi.org/10.1371/journal.pcbi.1000678

Kadoya, R., Baek, J.H., Sarker, A., Chattoraj, D.K. (2011). Participation of Chromosome Segregation Protein ParAI of *Vibrio cholerae* in Chromosome Replication. Journal of Bacteriology *193*, 1504–1514. https://doi.org/10.1128/JB.01067-10

Kadoya, R., Chattoraj, D.K. (2012). Insensitivity of Chromosome I and the Cell-cycle to Blockage of Replication and Segregation of *Vibrio cholerae* Chromosome II. mBio *3*, e00067-

12. https://doi.org/10.1128/mBio.00067-12

Kahng, L.S., Shapiro, L. (2003). Polar Localization of Replicon Origins in the Multipartite Genomes of *Agrobacterium tumefaciens* and *Sinorhizobium meliloti*. J. Bacteriol. *185*, 3384–3391. https://doi.org/10.1128/JB.185.11.3384-3391.2003

Kaur, T., Al Abdallah, Q., Nafissi, N., Wettig, S., Funnell, B.E., Slavcev, R.A. (2011). ParAB-mediated intermolecular association of plasmid P1 *parS* sites. Virology *421*, 192–201. https://doi.org/10.1016/j.virol.2011.09.027

Kawalek, A., Bartosik, A.A., Glabski, K., Jagura-Burdzy, G. (2018). *Pseudomonas aeruginosa* partitioning protein ParB acts as a nucleoid-associated protein binding to multiple copies of a *parS*-related motif. Nucleic Acids Res. *46*, 4592–4606. https://doi.org/10.1093/nar/gky257

Kawalek, A., Wawrzyniak, P., Bartosik, A.A., Jagura-Burdzy, G. (2020). Rules and Exceptions: The Role of Chromosomal ParB in DNA Segregation and Other Cellular Processes. Microorganisms *8*, 105. https://doi.org/10.3390/microorganisms8010105

Khare, D., Ziegelin, G., Lanka, E., Heinemann, U. (2004) Nat. Struct. Mol. Biol. 11, 656–663

Kim, H.J., Calcutt, M.J., Schmidt, F.J., Chater, K.F. (2000). Partitioning of the linear chromosome during sporulation of *Streptomyces coelicolor* A3(2) involves an *oriC*-linked *parAB* locus. J. Bacteriol. *182*, 1313–1320. https://doi.org/10.1128/jb.182.5.1313-1320.2000

Klann, A.G., Belanger, A.E., Abanes-De Mello, A., Lee, J.Y., Hatfull, G.F. (1998). Characterization of the *dnaG* Locus in *Mycobacterium smegmatis* Reveals Linkage of DNA Replication and Cell Division. J. Bacteriol. *180*, 65–72.

Kondo, S., Miura, T. (2010). Reaction-Diffusion Model as a Framework for Understanding Biological Pattern Formation. Science 329, 1616. https://doi.org/10.1126/science.1179047

Kono, N., Arakawa, K., Tomita, M. (2011). Comprehensive prediction of chromosome dimer resolution sites in bacterial genomes. BMC Genomics *12*, 19. https://doi.org/10.1186/1471-2164-12-19

Koonin, E.V. (1993a). A common set of conserved motifs in a vast variety of putative nucleic acid-dependent ATPases including MCM proteins involved in the initiation of eukaryotic DNA replication. Nucleic Acids Res. *21*, 2541–2547. https://doi.org/10.1093/nar/21.11.2541

Koonin, E.V. (1993b). A superfamily of ATPases with diverse functions containing either classical or deviant ATP-binding motif. J. Mol. Biol. *229*, 1165–1174. https://doi.org/10.1006/jmbi.1993.1115

Lasocki, K., Bartosik, A.A., Mierzejewska, J., Thomas, C.M., Jagura-Burdzy, G. (2007). Deletion of the parA (soj) Homologue in *Pseudomonas aeruginosa* Causes ParB Instability and Affects Growth Rate, Chromosome Segregation, and Motility. Journal of Bacteriology *189*, 5762–5772. https://doi.org/10.1128/JB.00371-07

Le Gall, A., Cattoni, D.I., Guilhas, B., Mathieu-Demazière, C., Oudjedi, L., Fiche, J.-B., Rech, J., Abrahamsson, S., Murray, H., Bouet, J.-Y., Nollmann, M. (2016). Bacterial partition complexes segregate within the volume of the nucleoid. Nature Communications *7*, 12107. https://doi.org/10.1038/ncomms12107

Lee, P.S., Grossman, A.D. (2006). The chromosome partitioning proteins Soj (ParA) and Spo0J (ParB) contribute to accurate chromosome partitioning, separation of replicated sister

origins, and regulation of replication initiation in *Bacillus subtilis*. Molecular Microbiology *60*, 853–869. https://doi.org/10.1111/j.1365-2958.2006.05140.x

Leonard, T.A., Butler, P.J.G., Löwe, J.(2004). Structural analysis of the chromosome segregation protein Spo0J from *Thermus thermophilus*. Mol. Microbiol. *53*, 419–432. https://doi.org/10.1111/j.1365-2958.2004.04133.x

Li, H., Angelov, A., Pham, V.T.T., Leis, B., Liebl, W. (2015). Characterization of chromosomal and megaplasmid partitioning loci in *Thermus thermophilus* HB27. BMC Genomics *16*. https://doi.org/10.1186/s12864-015-1523-3

Libante, V., Thion, L., Lane, D. (2001). Role of the ATP-binding site of SopA protein in partition of the F plasmid. Journal of Molecular Biology *314*, 387–399. https://doi.org/10.1006/jmbi.2001.5158

Lieberman-Aiden, E., Berkum, N.L. van, Williams, L., Imakaev, M., Ragoczy, T., Telling, A., Amit, I., Lajoie, B.R., Sabo, P.J., Dorschner, M.O., Sandstrom, R., Bernstein, B., Bender, M.A., Groudine, M., Gnirke, A., Stamatoyannopoulos, J., Mirny, L.A., Lander, E.S., Dekker, J. (2009). Comprehensive Mapping of Long-Range Interactions Reveals Folding Principles of the Human Genome. Science *326*, 289–293. https://doi.org/10.1126/science.1181369

Lim, G.E., Derman, A.I., Pogliano, J. (2005). Bacterial DNA segregation by dynamic SopA polymers. Proc Natl Acad Sci U S A *102*, 17658–17663. https://doi.org/10.1073/pnas.0507222102

Lim, H.C., Surovtsev, I.V., Beltran, B.G., Huang, F., Bewersdorf, J., Jacobs-Wagner, C. (2014). Evidence for a DNA-relay mechanism in ParABS-mediated chromosome segregation. Elife *3*, e02758. https://doi.org/10.7554/eLife.02758

Lin, D.C., Grossman, A.D. (1998). Identification and characterization of a bacterial chromosome partitioning site. Cell *92*, 675–685. https://doi.org/10.1016/s0092-8674(00)81135-6

Lin, L., Osorio Valeriano, M., Harms, A., Søgaard-Andersen, L., Thanbichler, M. (2017). Bactofilin-mediated organization of the ParAB S chromosome segregation system in *Myxococcus xanthus*. Nature Communications *8*, 1817. https://doi.org/10.1038/s41467-017-02015-z

Lioy, V.S., Cournac, A., Marbouty, M., Duigou, S., Mozziconacci, J., Espéli, O., Boccard, F., Koszul, R. (2018). Multiscale Structuring of the *E. coli* Chromosome by Nucleoid-Associated and Condensin Proteins. Cell *172*, 771-783.e18. https://doi.org/10.1016/j.cell.2017.12.027

Lioy, V.S., Volante, A., Soberón, N.E., Lurz, R., Ayora, S., Alonso, J.C. (2015). ParAB Partition Dynamics in Firmicutes: Nucleoid Bound ParA Captures and Tethers ParB-Plasmid Complexes. PLoS ONE *10*, e0131943. https://doi.org/10.1371/journal.pone.0131943

Livny, J., Yamaichi, Y., Waldor, M.K. (2007). Distribution of Centromere-Like *parS* Sites in Bacteria: Insights from Comparative Genomics. Journal of Bacteriology *189*, 8693–8703. https://doi.org/10.1128/JB.01239-07

Lu, M., Campbell, J.L., Boye, E., Kleckner, N. (1994). SeqA: A negative modulator of replication initiation in *E. coli*. Cell *77*, 413–426. https://doi.org/10.1016/0092-8674(94)90156-2

Lutkenhaus, J. (2007). Assembly dynamics of the bacterial MinCDE system and spatial

regulation of the Z ring. Annu. Rev. Biochem. *76*, 539–562. https://doi.org/10.1146/annurev.biochem.75.103004.142652

MacCready, J.S., Hakim, P., Young, E.J., Hu, L., Liu, J., Osteryoung, K.W., Vecchiarelli, A.G., Ducat, D.C. (2018). Protein gradients on the nucleoid position the carbon-fixing organelles of cyanobacteria. eLife *7*, e39723. https://doi.org/10.7554/eLife.39723

MacDonald, K.L., Speert, D.P. (2008). Differential modulation of innate immune cell functions by the *Burkholderia cepacia* complex: *Burkholderia cenocepacia* but not *Burkholderia multivorans* disrupts maturation and induces necrosis in human dendritic cells. Cellular Microbiology *10*, 2138–2149. https://doi.org/10.1111/j.1462-5822.2008.01197.x

Mäkelä, J., Sherratt, D. (2020). SMC complexes organize the bacterial chromosome by lengthwise compaction. Curr. Genet. https://doi.org/10.1007/s00294-020-01076-w

Marbouty, M., Le Gall, A., Cattoni, D.I., Cournac, A., Koh, A., Fiche, J.-B., Mozziconacci, J., Murray, H., Koszul, R., Nollmann, M. (2015). Condensin- and Replication-Mediated Bacterial Chromosome Folding and Origin Condensation Revealed by Hi-C and Super-resolution Imaging. Molecular Cell *59*, 588–602. https://doi.org/10.1016/j.molcel.2015.07.020

Marston, A.L., Errington, J. (1999). Selection of the midcell division site in *Bacillus subtilis* through MinD-dependent polar localization and activation of MinC. Mol. Microbiol. *33*, 84–96. https://doi.org/10.1046/j.1365-2958.1999.01450.x

Matano, L.M., Morris, H.G., Hesser, A.R., Martin, S.E.S., Lee, W., Owens, T.W., Laney, E., Nakaminami, H., Hooper, D., Meredith, T.C., Walker, S. (2017). An antibiotic that inhibits the ATPase activity of an ABC transporter by binding to a remote extracellular site. J. Am. Chem. Soc. *139*, 10597–10600. https://doi.org/10.1021/jacs.7b04726

McLeod, S. M., Burrus, V., & Waldor, M. K. (2006). Requirement for Vibrio cholerae integration host factor in conjugative DNA transfer. Journal of bacteriology, 188(16), 5704–5711. https://doi.org/10.1128/JB.00564-06

McLeod, B.N., Allison-Gamble, G.E., Barge, M.T., Tonthat, N.K., Schumacher, M.A., Hayes, F., Barillà, D. (2017). A three-dimensional ParF meshwork assembles through the nucleoid to mediate plasmid segregation. Nucleic Acids Res. *45*, 3158–3171. https://doi.org/10.1093/nar/gkw1302

Meinhardt, H., de Boer, P.A.J. (2001). Pattern formation in *Escherichia coli*: A model for the pole-to-pole oscillations of Min proteins and the localization of the division site. PNAS *98*, 14202–14207. https://doi.org/10.1073/pnas.251216598

Merrell, D.S., Butler, S.M., Qadri, F., Dolganov, N.A., Alam, A., Cohen, M.B., Calderwood, S.B., Schoolnik, G.K., Camilli, A. (2002). Host-induced epidemic spread of the cholera bacterium. Nature *417*, 642–645. https://doi.org/10.1038/nature00778

Milunovic, B., diCenzo, G.C., Morton, R.A., Finan, T.M. (2014). Cell Growth Inhibition upon Deletion of Four Toxin-Antitoxin Loci from the Megaplasmids of *Sinorhizobium meliloti*. Journal of Bacteriology *196*, 811–824. https://doi.org/10.1128/JB.01104-13

Minnen, A., Attaiech, L., Thon, M., Gruber, S., Veening, J.-W. (2011). SMC is recruited to *oriC* by ParB and promotes chromosome segregation in *Streptococcus pneumoniae.* Mol. Microbiol. *81*, 676–688. https://doi.org/10.1111/j.1365-2958.2011.07722.x

Mohl, D.A., Easter, J., Gober, J.W. (2001). The chromosome partitioning protein, ParB, is

required for cytokinesis in *Caulobacter crescentus*. Mol. Microbiol. *42*, 741–755. https://doi.org/10.1046/j.1365-2958.2001.02643.x

Mohl, D.A., Gober, J.W. (1997). Cell-cycle-dependent polar localization of chromosome partitioning proteins in *Caulobacter crescentus*. Cell *88*, 675–684. https://doi.org/10.1016/s0092-8674(00)81910-8

Mori, H., Kondo, A., Ohshima, A., Ogura, T., Hiraga, S. (1986). Structure and function of the F plasmid genes essential for partitioning. J Mol. Biol. *192*, 1–15. https://doi.org/10.1016/0022-2836(86)90459-6

Mukai, T., Yoneji, T., Yamada, K., Fujita, H., Nara, S., Su'etsugu, M. (2020). Overcoming the Challenges of Megabase-Sized Plasmid Construction in *Escherichia coli*. ACS Synthetic Biology. https://doi.org/10.1021/acssynbio.0c00008

Munna, M.S., Zeba, Z., Noor, R., (2015). Influence of temperature on the growth of *Pseudomonas putida*. Stamford Journal of Microbiology *5*, 9–12. https://doi.org/10.3329/sjm.v5i1.26912

Murayama, K., Orth, P., de la Hoz, A.B., Alonso, J.C., Saenger, W. (2001). Crystal structure of omega transcriptional repressor encoded by *Streptococcus pyogenes* plasmid pSM19035 at 1.5 A resolution. J. Mol. Biol. *314*, 789–796. https://doi.org/10.1006/jmbi.2001.5157

Murray, H., Ferreira, H., Errington, J. (2006). The bacterial chromosome segregation protein Spo0J spreads along DNA from *parS* nucleation sites. Mol. Microbiol. *61*, 1352–1361. https://doi.org/10.1111/j.1365-2958.2006.05316.x

Murray, S.M., Sourjik, V. (2017). Self-organization and positioning of bacterial protein clusters. Nature. Phys. *13*, 1006–1013. https://doi.org/10.1038/nphys4155

Mushnikov, N.V., Fomicheva, A., Gomelsky, M., Bowman, G.R. (2019). Inducible asymmetric cell division and cell differentiation in a bacterium. Nature Chemical Biology *15*, 925–931. https://doi.org/10.1038/s41589-019-0340-4

Ni, L., Xu, W., Kumaraswami, M., Schumacher, M.A. (2010). Plasmid protein TubR uses a distinct mode of HTH-DNA-binding and recruits the prokaryotic tubulin homolog TubZ to effect DNA partition. Proc. Natl. Acad. Sci. U.S.A. *107*, 11763–11768. https://doi.org/10.1073/pnas.1003817107

Osorio-Valeriano, M., Altegoer, F., Steinchen, W., Urban, S., Liu, Y., Bange, G., Thanbichler, M. (2019). ParB-type DNA Segregation Proteins Are CTP-Dependent Molecular Switches. Cell *179*, 1512-1524.e15. https://doi.org/10.1016/j.cell.2019.11.015

Pandey, R., Ter Beek, A., Vischer, N.O.E., Smelt, J.P.P.M., Brul, S., Manders, E.M.M. (2013). Live Cell Imaging of Germination and Outgrowth of Individual *Bacillus subtilis* Spores; the Effect of Heat Stress Quantitatively Analyzed with SporeTracker. PLoS One *8*. https://doi.org/10.1371/journal.pone.0058972

Park, K., Han, E., Paulsson, J., Chattoraj, D.K. (2001). Origin pairing ('handcuffing') as a mode of negative control of P1 plasmid copy number. EMBO J. *20*, 7323–7332. https://doi.org/10.1093/emboj/20.24.7323

Peskin, C.S., Odell, G.M., Oster, G.F. (1993). Cellular motions and thermal fluctuations: the Brownian ratchet. Biophys. J. *65*, 316–324.

Pratto, F., Cicek, A., Weihofen, W.A., Lurz, R., Saenger, W., Alonso, J.C. (2008). *Streptococcus pyogenes* pSM19035 requires dynamic assembly of ATP-bound ParA and ParB on *parS* DNA during plasmid segregation. Nucleic Acids Res. *36*, 3676–3689. https://doi.org/10.1093/nar/gkn170

Ptacin, J.L., Lee, S.F., Garner, E.C., Toro, E., Eckart, M., Comolli, L.R., Moerner, W.E., Shapiro, L. (2010). A spindle-like apparatus guides bacterial chromosome segregation. Nature Cell Biology *12*, 791–798. https://doi.org/10.1038/ncb2083

Quisel, J.D., Lin, D.C.-H., Grossman, A.D. (1999). Control of Development by Altered Localization of a Transcription Factor in *B. subtilis*. Molecular Cell *4*, 665–672. https://doi.org/10.1016/S1097-2765(00)80377-9

Radnedge, L., Youngren, B., Davis, M., Austin, S. (1998). Probing the structure of complex macromolecular interactions by homolog specificity scanning: the P1 and P7 plasmid partition systems. EMBO J. *17*, 6076–6085. https://doi.org/10.1093/emboj/17.20.6076

Ramachandran, R., Ciaccia, P.N., Filsuf, T.A., Jha, J.K., Chattoraj, D.K. (2018). Chromosome 1 licenses chromosome 2 replication in *Vibrio cholerae* by doubling the *crtS* gene dosage. PLoS Genet. *14*, e1007426. https://doi.org/10.1371/journal.pgen.1007426

Ramachandran, R., Jha, J., Paulsson, J., Chattoraj, D. (2017). Random versus Cell-cycle-Regulated Replication Initiation in Bacteria: Insights from Studying *Vibrio cholerae* Chromosome 2. Microbiol. Mol. Biol. Rev. *81*, e00033-16, e00033-16. https://doi.org/10.1128/MMBR.00033-16

Ramm, B., Heermann, T. & Schwille, P. (2019). The *E. coli* MinCDE system in the regulation of protein patterns and gradients. *Cell. Mol. Life Sci.* 76**,** 4245–4273. https://doi.org/10.1007/s00018-019-03218-x

Rasmussen, T., Jensen, R.B., Skovgaard, O. (2007). The two chromosomes of Vibrio cholerae are initiated at different time points in the cell-cycle. EMBO J. *26*, 3124–3131. https://doi.org/10.1038/sj.emboj.7601747

Reyes-Lamothe, R., Tran, T., Meas, D., Lee, L., Li, A.M., Sherratt, D.J., Tolmasky, M.E. (2014). High-copy bacterial plasmids diffuse in the nucleoid-free space, replicate stochastically and are randomly partitioned at cell division. Nucleic Acids Res. *42*, 1042–1051. https://doi.org/10.1093/nar/gkt918

Ringgaard, S., van Zon, J., Howard, M., Gerdes, K. (2009). Movement and equi-positioning of plasmids by ParA filament disassembly. Proc. Natl. Acad. Sci. U.S.A. *106*, 19369–19374. https://doi.org/10.1073/pnas.0908347106

Austin, S., Abeles, A. (1983). Partition of unit-copy miniplasmids to daughter cells. II. The partition region of miniplasmid P1 encodes an essential protein and a centromere-like site at which it acts. J. Mol. Biol. *169*, 373–387. https://doi.org/10.1016/s0022-2836(83)80056-4

Saint-Dic, D., Frushour, B.P., Kehrl, J.H., Kahng, L.S. (2006). A parA Homolog Selectively Influences Positioning of the Large Chromosome Origin in *Vibrio cholerae*. Journal of Bacteriology *188*, 5626–5631. https://doi.org/10.1128/JB.00250-06

Scholefield, G., Whiting, R., Errington, J., Murray, H. (2011). Spo0J regulates the oligomeric state of Soj to trigger its switch from an activator to an inhibitor of DNA replication initiation. Mol .Microbiol. *79*, 1089–1100. https://doi.org/10.1111/j.1365-2958.2010.07507.x

Schumacher, M.A., Mansoor, A., Funnell, B.E. (2007). Structure of a four-way bridged ParB-DNA complex provides insight into P1 segrosome assembly. J. Biol. Chem. *282*, 10456–10464. https://doi.org/10.1074/jbc.M610603200

Schumacher, M.A., Piro., K., Xu., W. (2010). Insight into F plasmid DNA segregation revealed by structures of SopB and SopB-DNA complexes. Nucleic Acids Research. *38*, 4514-4526

Schumacher, M.A. (2012). Bacterial plasmid partition machinery: a minimalist approach to survival. Curr. Opin. Struct. Biol. *22*, 72–79. https://doi.org/10.1016/j.sbi.2011.11.001

Sengupta, M., Austin, S. (2011). Prevalence and Significance of Plasmid Maintenance Functions in the Virulence Plasmids of Pathogenic Bacteria. Infection and Immunity *79*, 2502–2509. https://doi.org/10.1128/IAI.00127-11

Sengupta, M., Nielsen, H.J., Youngren, B., Austin, S. (2010). P1 Plasmid Segregation: Accurate Redistribution by Dynamic Plasmid Pairing and Separation. J.B. *192*, 1175–1183. https://doi.org/10.1128/JB.01245-09

Shebelut, C.W., Guberman, J.M., Teeffelen, S. van, Yakhnina, A.A., Gitai, Z. (2010). Caulobacter chromosome segregation is an ordered multistep process. PNAS *107*, 14194–14198. https://doi.org/10.1073/pnas.1005274107

Shi, H., Bratton, B. P., Gitai, Z., & Huang, K. C. (2018). MreB as the Foreman of *E. coli* Construction. *Cell*, *172*(6), 1294–1305. https://doi.org/10.1016/j.cell.2018.02.050

Soh, Y.-M., Davidson, I.F., Zamuner, S., Basquin, J., Bock, F.P., Taschner, M., Veening, J.-W., De Los Rios, P., Peters, J.-M., Gruber, S. (2019). Self-organization of *parS* centromeres by the ParB CTP hydrolase. Science *366*, 1129–1133. https://doi.org/10.1126/science.aay3965

Soler-Bistué, A., Aguilar-Pierlé, S., Garcia-Garcerá, M., Val, M.-E., Sismeiro, O., Varet, H., Sieira, R., Krin, E., Skovgaard, O., Comerci, D.J., Rocha, E.P.C., Mazel, D. (2020). Macromolecular crowding links ribosomal protein gene dosage to growth rate in *Vibrio cholerae.* BMC Biology *18*, 43. https://doi.org/10.1186/s12915-020-00777-5

Song, D., Rodrigues, K., Graham, T.G.W., Loparo, J.J. (2017). A network of cis and trans interactions is required for ParB spreading. Nucleic Acids Res. *45*, 7106–7117. https://doi.org/10.1093/nar/gkx271

Sozhamannan, S., Waldminghaus, T. (2020). Exception to the exception rule: synthetic and naturally occurring single chromosome *Vibrio cholerae*. Environ. Microbiol. https://doi.org/10.1111/1462-2920.15002

Srivastava, P., Chattoraj, D.K. (2007). Selective chromosome amplification in *Vibrio cholerae*. Molecular Microbiology *66*, 1016–1028. https://doi.org/10.1111/j.1365-2958.2007.05973.x

Srivastava, P., Fekete, R.A., Chattoraj, D.K. (2006). Segregation of the Replication Terminus of the Two *Vibrio cholerae* Chromosomes. Journal of Bacteriology *188*, 1060–1070. https://doi.org/10.1128/JB.188.3.1060-1070.2006

Stephens, C., Arismendi, T., Wright, M., Hartman, A., Gonzalez, A., Gill, M., Pandori, M., Hess, D. (2020). F Plasmids Are the Major Carriers of Antibiotic Resistance Genes in Human-Associated Commensal Escherichia coli. mSphere *5*. https://doi.org/10.1128/mSphere.00709-20

Sugawara, T., Kaneko, K. (2011). Chemophoresis as a driving force for intracellular organization: Theory and application to plasmid partitioning. Biophysics (Nagoya-shi) *7*, 77–88. https://doi.org/10.2142/biophysics.7.77

Sullivan, N.L., Marquis, K.A., Rudner, D.Z., (2009). Recruitment of SMC by ParB-parS organizes the origin region and promotes efficient chromosome segregation. Cell *137*, 697–707. https://doi.org/10.1016/j.cell.2009.04.044

Sundararajan, K., & Goley, E. D. (2017). Cytoskeletal Proteins in *Caulobacter crescentus*: Spatial Orchestrators of Cell Cycle Progression, Development, and Cell Shape. Sub-cellular biochemistry *84*, 103–137. https://doi.org/10.1007/978-3-319-53047-5_4

Surovtsev, Ivan V., Campos, M., Jacobs-Wagner, C. (2016). DNA-relay mechanism is sufficient to explain ParA-dependent intracellular transport and patterning of single and multiple cargos. PNAS *113*, E7268–E7276. https://doi.org/10.1073/pnas.1616118113

Surovtsev, Ivan V., Lim, H.C., Jacobs-Wagner, C. (2016). The Slow Mobility of the ParA Partitioning Protein Underlies Its Steady-State Patterning in *Caulobacter*. Biophys. J. *110*, 2790–2799. https://doi.org/10.1016/j.bpj.2016.05.014

Surtees, J.A., Funnell, B.E. (1999). P1 ParB Domain Structure Includes Two Independent Multimerization Domains. Journal of Bacteriology *181*, 5898–5908. https://doi.org/10.1128/JB.181.19.5898-5908.1999

Talukder, A., Ishihama, A. (2015). Growth phase dependent changes in the structure and protein composition of nucleoid in *Escherichia coli*. Sci. China Life Sci. *58*, 902–911. https://doi.org/10.1007/s11427-015-4898-0

Taylor, J.A., Pastrana, C.L., Butterer, A., Pernstich, C., Gwynn, E.J., Sobott, F., Moreno-Herrero, F., Dillingham, M.S. (2015). Specific and non-specific interactions of ParB with DNA: implications for chromosome segregation. Nucleic Acids Research *43*, 719–731. https://doi.org/10.1093/nar/gku1295

Temme, K., Zhao, D., & Voigt, C. A. (2012). Refactoring the nitrogen fixation gene cluster from *Klebsiella oxytoca*. Proceedings of the National Academy of Sciences of the United States of America *109*(18), 7085–7090. https://doi.org/10.1073/pnas.1120788109

Toro, E., Hong, S.-H., McAdams, H.H., Shapiro, L. (2008). *Caulobacter* requires a dedicated mechanism to initiate chromosome segregation. PNAS *105*, 15435–15440. https://doi.org/10.1073/pnas.0807448105

Toro-Nahuelpan, M., Corrales-Guerrero, L., Zwiener, T., Osorio-Valeriano, M., Müller, F.-D., Plitzko, J.M., Bramkamp, M., Thanbichler, M., Schüler, D. (2019). A gradient-forming MipZ protein mediating the control of cell division in the magnetotactic bacterium *Magnetospirillum gryphiswaldense*. Molecular Microbiology *112*, 1423–1439. https://doi.org/10.1111/mmi.14369

Trojanowski, D., Hołówka, J., Zakrzewska-Czerwińska, J. (2018). Where and When Bacterial Chromosome Replication Starts: A Single Cell Perspective. Front. Microbiol. *9*. https://doi.org/10.3389/fmicb.2018.02819

Turing, A. (1952). The chemical basis of morphogenesis. *Phil. Trans. R. Soc. Lond. B* 237:37–72. http://doi.org/10.1098/rstb.1952.0012

Ul-Haq, E., Patole, S., Moxey, M., Amstad, E., Vasilev, C., Hunter, C.N., Leggett, G.J.,

Spencer, N.D., Williams, N.H. (2013). Photocatalytic Nanolithography of Self-Assembled Monolayers and Proteins. ACS Nano *7*, 7610–7618. https://doi.org/10.1021/nn402063b

Vaksman, Z., Kaplan, H.B. (2015). *Myxococcus xanthus* Growth, Development, and Isolation. Current Protocols in Microbiology *39*, 7A.1.1-7A.1.21. https://doi.org/10.1002/9780471729259.mc07a01s39

Val, M.-E., Kennedy, S.P., El Karoui, M., Bonné, L., Chevalier, F., Barre, F.-X. (2008). FtsK-dependent dimer resolution on multiple chromosomes in the pathogen *Vibrio cholerae*. PLoS Genet. *4*, e1000201. https://doi.org/10.1371/journal.pgen.1000201

Val, M.-E., Marbouty, M., de Lemos Martins, F., Kennedy, S.P., Kemble, H., Bland, M.J., Possoz, C., Koszul, R., Skovgaard, O., Mazel, D. (2016). A checkpoint control orchestrates the replication of the two chromosomes of *Vibrio cholerae*. Sci. Adv. *2*, e1501914. https://doi.org/10.1126/sciadv.1501914

Vecchiarelli, A.G., Han, Y.-W., Tan, X., Mizuuchi, M., Ghirlando, R., Biertümpfel, C., Funnell, B.E., Mizuuchi, K. (2010). ATP control of dynamic P1 ParA–DNA interactions: a key role for the nucleoid in plasmid partition. Mol. Microbiol. *78*, 78–91. https://doi.org/10.1111/j.1365-2958.2010.07314.x

Vecchiarelli, A.G., Havey, J.C., Ing, L.L., Wong, E.O.Y., Waples, W.G., Funnell, B.E. (2013). Dissection of the ATPase Active Site of P1 ParA Reveals Multiple Active Forms Essential for Plasmid Partition. J. Biol. Chem. 288, 17823–17831. https://doi.org/10.1074/jbc.M113.469981

Vecchiarelli, A.G., Neuman, K.C., Mizuuchi, K. (2014a). A propagating ATPase gradient drives transport of surface-confined cellular cargo. Proc. Natl. Acad. Sci. USA *111*, 4880–4885. https://doi.org/10.1073/pnas.1401025111

Vecchiarelli, A.G., Seol, Y., Neuman, K.C., Mizuuchi, K. (2014b). A moving ParA gradient on the nucleoid directs subcellular cargo transport via a chemophoresis force. Bioarchitecture *4*, 154–159. https://doi.org/10.4161/19490992.2014.987581

Vecchiarelli, A.G., Taylor, J.A., Mizuuchi, K. (2015). Reconstituting ParA/ParB-mediated transport of DNA cargo. Methods Cell Biol. *128*, 243–269. https://doi.org/10.1016/bs.mcb.2015.01.021

Venkatesan, M.M., Goldberg, M.B., Rose, D.J., Grotbeck, E.J., Burland, V., Blattner, F.R. (2001). Complete DNA sequence and analysis of the large virulence plasmid of *Shigella flexneri.* Infect. Immun. *69*, 3271–3285. https://doi.org/10.1128/IAI.69.5.3271-3285.2001

Venkova-Canova, T., Srivastava, P., Chattoraj, D.K. (2006). Transcriptional inactivation of a regulatory site for replication of *Vibrio cholerae* chromosome II. PNAS *103*, 12051–12056. https://doi.org/10.1073/pnas.0605120103

Verma, S.C., Qian, Z., Adhya, S.L. (2019). Architecture of the *Escherichia coli* nucleoid. PLoS Genet *15*. https://doi.org/10.1371/journal.pgen.1008456

Viollier, P.H., Thanbichler, M., McGrath, P.T., West, L., Meewan, M., McAdams, H.H., Shapiro, L. (2004). Rapid and sequential movement of individual chromosomal loci to specific subcellular locations during bacterial DNA replication. Proc. Natl. Acad. Sci. U S A *101*, 9257–9262. https://doi.org/10.1073/pnas.0402606101

Wade, J.T., Grainger, D.C. (2017). Spurious transcription and its impact on cell function. Transcription *9*, 182–189. https://doi.org/10.1080/21541264.2017.1381794

Wagstaff, J., Löwe, J. (2018). Prokaryotic cytoskeletons: protein filaments organizing small cells. Nature Reviews Microbiology *16*, 187–201. https://doi.org/10.1038/nrmicro.2017.153

Walker, J.E., Saraste, M., Runswick, M.J., Gay, N.J. (1982). Distantly related sequences in the alpha- and beta-subunits of ATP synthase, myosin, kinases and other ATP-requiring enzymes and a common nucleotide binding fold. EMBO J *1*, 945–951.

Wang, X., Montero Llopis, P., Rudner, D.Z. (2014). *Bacillus subtilis* chromosome organization oscillates between two distinct patterns. Proceedings of the National Academy of Sciences *111*, 12877–12882. https://doi.org/10.1073/pnas.1407461111

Wertheim, K.Y., Roose, T. (2019). Can VEGFC Form Turing Patterns in the Zebrafish Embryo? *Bull Math Biol* 81, 1201–1237. https://doi.org/10.1007/s11538-018-00560-2

Wu, L.J., Lee, S., Park, S., Eland, L.E., Wipat, A., Holden, S., Errington, J. (2020). Geometric principles underlying the proliferation of a model cell system. Nat. Commun. *11*, 4149. https://doi.org/10.1038/s41467-020-17988-7

Xu, Q., Dziejman, M., Mekalanos, J.J. (2003). Determination of the transcriptome of Vibrio cholerae during intraintestinal growth and midexponential phase in vitro. Proc. Natl. Acad. Sci. U.S.A. *100*, 1286–1291. https://doi.org/10.1073/pnas.0337479100

Yaginuma, H., Kawai, S., Tabata, K.V., Tomiyama, K., Kakizuka, A., Komatsuzaki, T., Noji, H., Imamura, H. (2014). Diversity in ATP concentrations in a single bacterial cell population revealed by quantitative single-cell imaging. Scientific Reports *4*, 6522. https://doi.org/10.1038/srep06522

Yamaichi, Y., Niki, H. (2000). Active segregation by the *Bacillus subtilis* partitioning system in *Escherichia coli*. PNAS *97*, 14656–14661. https://doi.org/10.1073/pnas.97.26.14656

Yamaichi, Y., Fogel, M.A., McLeod, S.M., Hui, M.P., Waldor, M.K. (2007a). Distinct centromere-like *parS* sites on the two chromosomes of *Vibrio* spp. J. Bacteriol. *189*, 5314–5324. https://doi.org/10.1128/JB.00416-07

Yamaichi, Y., Fogel, M.A., Waldor, M.K. (2007b). par genes and the pathology of chromosome loss in *Vibrio cholerae*. PNAS *104*, 630–635. https://doi.org/10.1073/pnas.0608341104

Yamaichi, Y., Gerding, M.A., Davis, B.M., Waldor, M.K. (2011). Regulatory Cross-Talk Links *Vibrio cholerae Chromosome* II Replication and Segregation. PLOS Genetics *7*, e1002189. https://doi.org/10.1371/journal.pgen.1002189

Yamaichi, Y., Bruckner, R., Ringgaard, S., Möll, A., Cameron, D.E., Briegel, A., Jensen, G.J., Davis, B.M., Waldor, M.K. (2012). A multidomain hub anchors the chromosome segregation and chemotactic machinery to the bacterial pole. Genes Dev. *26*, 2348–2360. https://doi.org/10.1101/gad.199869.112

Youngren, B., Nielsen, H.J., Jun, S., Austin, S. (2014). The multifork *Escherichia coli* chromosome is a self-duplicating and self-segregating thermodynamic ring polymer. Genes Dev. *28*, 71–84. https://doi.org/10.1101/gad.231050.113

Yuan, J., Yamaichi, Y., Waldor, M.K. (2011). The Three *Vibrio cholerae* Chromosome II-Encoded ParE Toxins Degrade Chromosome I following Loss of Chromosome II. J. Bacteriol. *193*, 611–619. https://doi.org/10.1128/JB.01185-10

Zawadzki, P., Stracy, M., Ginda, K., Zawadzka, K., Lesterlin, C., Kapanidis, A.N., Sherratt,

D.J. (2015). The Localization and Action of Topoisomerase IV in *Escherichia coli* Chromosome Segregation Is Coordinated by the SMC Complex, MukBEF. Cell Rep. *13*, 2587–2596. https://doi.org/10.1016/j.celrep.2015.11.034

Zhang, H., Schumacher, M.A. (2017). Structures of partition protein ParA with nonspecific DNA and ParB effector reveal molecular insights into principles governing Walker-box DNA segregation. Genes Dev. *31*, 481–492. https://doi.org/10.1101/gad.296319.117